

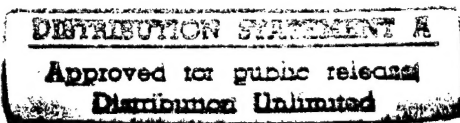
**INSTANTANEOUS VELOCITY
AND WALL PRESSURE FEATURES
IN A TURBULENT BOUNDARY LAYER**

Final Report
ONR N00014-93-1-0639

WILLIAM DE OJEDA & CANDACE E. WARK

Fluid Dynamics Research Center
Illinois Institute of Technology
Chicago, IL 60616

July 1997



DTIC QUALITY INSPECTED 4

19970806 063

REPORT DOCUMENTATION PAGE

Form Approved
OMB No. 0704-0188

Public reporting burden for this collection of information is estimated to average 1 hour per response, including the time for reviewing instructions, searching existing data sources, gathering and maintaining the data needed, and completing and reviewing the collection of information. Send comments regarding this burden estimate or any other aspect of this collection of information, including suggestions for reducing this burden to Washington Headquarters Services, Directorate for Information Operations and Reports, 1215 Jefferson Davis Highway, Suite 1204, Arlington, VA 22202-4302, and to the Office of Management and Budget, Paperwork Reduction Project (0704-0188), Washington, DC 20503.

1. AGENCY USE ONLY (Leave blank)	2. REPORT DATE 14 JULY 1997	3. REPORT TYPE AND DATES COVERED Final	
4. TITLE AND SUBTITLE Instantaneous Velocity and Wall Pressure Features in a Turbulent Boundary Layer		5. FUNDING NUMBERS G N00014-93-1-0639	
6. AUTHOR(S) William de Ojeda and Candace E. Wark			
7. PERFORMING ORGANIZATION NAMES(S) AND ADDRESS(ES) Illinois Institute of Technology MMAE Dept. 10 W. 32nd St. Chicago, IL 60616		8. PERFORMING ORGANIZATION REPORT NUMBER	
9. SPONSORING / MONITORING AGENCY NAMES(S) AND ADDRESS(ES) Office of Naval Research 800 North Quincy St. Arlington, VA 22217-5000		10. SPONSORING / MONITORING AGENCY REPORT NUMBER	
11. SUPPLEMENTARY NOTES			
a. DISTRIBUTION / AVAILABILITY STATEMENT Approved for Public Availability		12. DISTRIBUTION CODE	
13. ABSTRACT (Maximum 200 words) Instantaneous organized motions in a turbulent boundary layer are related to characteristic wall pressure signatures for $1500 < Re_\theta < 6000$ and are compared with structures extracted from conditional averaging. The conditional velocity and pressure fields were obtained from velocity measurements performed at 176 separate locations in the streamwise-wall normal plane, and from one microphone mounted flush with the boundary layer test plate. Instantaneous realizations of the velocity and pressure field were obtained through high-resolution particle image velocimetry and an array of 39 microphones. The instantaneous and conditional flow fields showed that an adverse pressure gradient associated with a positive wall pressure was present beneath a large-scale shear layer structure separating high speed flow upstream from low speed flow ($\partial u' / \partial x < 0$). Only the instantaneous measurements showed that an isolated negative wall pressure was associated with a shear layer of positive $\partial u' / \partial x$ denoted here as an "inverse" shear layer; the structure was washed out and therefore not observed in the conditional averaging calculations. The shear layer exhibited large vorticity with the same sense of rotation as the mean vorticity and localized regions of strong turbulence production along the interface, whereas the inverse shear layer did not.			
14. SUBJECT TERMS Turbulent boundary layers, Wall pressure fluctuations, Particle Image Velocimetry, PIV		15. NUMBER OF PAGES 171	
		16. PRICE CODE	
17. SECURITY CLASSIFICATION OF REPORT unclassified	18. SECURITY CLASSIFICATION OF THIS PAGE unclassified	19. SECURITY CLASSIFICATION OF ABSTRACT unclassified	20. LIMITATION OF ABSTRACT UL

ACKNOWLEDGMENT

The support of the Office of Naval Research under Grant N00014-93-1-0639 monitored by Dr. L. Patrick Purtell is greatly appreciated.

We thank many of the faculty, students and staff of the Fluid Dynamics Research Center for their suggestions, recommendations and review of this work. In particular, the advise of Professors Ahmed Naguib and Hassan Nagib were especially insightful and helpful. Our gratitude is also extended to Mr. Scott Ullrich who developed the PIV interrogation system used in this work; Mr. Steve Gravante who did most of the initial wall-pressure acquisition work; Mr. Oliver Juckenhoefel for his measurements of the conditionally-averaged velocity field and Mr. Alex Grossman for his help in displaying the data. Special thanks are extended to Ron Mashek and Craig Johnson, our very capable machinists, who, among many other things, built the intricate holder/array of miniature microphones. Their experience and suggestions were very valuable.

TABLE OF CONTENTS

	Page
ACKNOWLEDGMENT	iii
LIST OF TABLES	vi
LIST OF FIGURES	vii
LIST OF ABBREVIATIONS	xi
ABSTRACT	xiii
CHAPTER	
I. INTRODUCTION	
1.1 The Problem of Turbulence	1
1.2 Historical Background	2
II. ORGANIZED MOTION IN A TURBULENT BOUNDARY LAYER	6
2.1 The Turbulent Boundary Layer Profile	6
2.2 Turbulent Structures	7
2.3 Role of Wall Pressure Fluctuations on Turbulent Structures	9
2.4 Instantaneous Flow Features: Particle Image Velocimetry	12
2.5 Objectives	14
III. EXPERIMENTAL SET-UP	16
3.1 Flow Facility	16
3.2 Particle Image Velocimetry Measurements	16
3.3 Pressure Measurements	21
3.4 Synchronization of PIV and Pressure Measurements	30
3.5 Acquisition System	31

CHAPTER	Page
IV. DATA PROCESSING AND ERROR ANALYSIS	34
4.1 PIV Data Processing	33
4.2 Mean and RMS Velocity Profiles	38
4.3 Velocity, Vorticity and Reynolds Stresses	39
4.4 Pressure Profiles in Space	45
4.5 Conditional Averages and Spectra of Pressure	50
4.6 Spatial Filtering and Spectra of Pressure	52
V. INSTANTANEOUS VELOCITY AND PRESSURE FIELDS AND TEMPORAL EVOLUTION OF PRESSURE STRUCTURES . . .	57
5.1 Review of Conditional Pressure and Velocity Calculations .	57
5.2 Present Goals	58
5.3 Instantaneous Correlations	59
VI. WALL PRESSURE MEASUREMENTS	84
6.1 Conditional Averages	85
6.2 Long Time Sequence of Wall Pressure	99
VII. STRUCTURES IN THE TURBULENT BOUNDARY LAYER	107
7.1 Coherent Structures	107
7.2 Objectives of the Current Measurements	108
7.3 Selected Structural Features	110
7.4 Characteristic-Wall Pressure Fluctuations	132
VIII. CONCLUSIONS AND RECOMMENDATIONS	147
8.1 Conclusions	147
8.2 Recommendations	151
BIBLIOGRAPHY	153

LIST OF TABLES

Table	Page
4.1 Range of Flows	39

LIST OF FIGURES

Figure	Page
3. 1 Schematic of the Mark V. Morkovin Wind Tunnel	17
3. 2 Particle Image Velocimetry Set-up and Pressure Array	17
3. 3 Schematic Diagram of the Interrogation System	19
3. 4 Sample of a Single Frame, Double-Exposed Image Taken in the Turbulent Boundary Layer with a Single Interrogation Region Highlighted and Resultant Two-Dimensional Autocorrelation Field	20
3. 5 Microphone Array and Supporting Hardware	22
3. 6 Main Casing	23
3. 7 Miniature-Microphones Inserts	24
3. 8 Reference Microphone Insert and Plugs	25
3. 9 Assignment of Array Microphones to Reference Microphone	27
3. 10 Typical Miniature Microphone Calibration Curve (Top) and Knwoles Factory Calibration Curve (Bottom)	28
3. 11 Voltage Spectra of Microphone Signals with and without Analog Filtering	33
4. 1 Description of Vector Field and Calculation	34
4. 2 Vector Fields, (a) Raw Data and (b) After Clean-up Routine	38
4. 3 Wall Scaling of Boundary Layer Mean (Top) and Turbulent Intensity Profiles (Bottom)	40
4. 4 Line Average and RMS Profiles	41
4. 5 Fluctuating Velocity Fields: Top, $U_c = 0.7U_\infty$; Middle, $0.9U_\infty$; Bottom, Reynolds Decomposed. $Re_\theta = 3950$	43
4. 6 Contour of Integration around Data Point (i,j)	44
4. 7 Total (Top), Fluctuating (Middle) Non-dimensionalized Vorticity Fields $\omega^+ = \omega v / u_\tau^2$ and Reynolds Stresses uv / u_τ^2 (Bottom) for the Instantaneous Flow Field of Fig. 4.5	46
4. 8 Simple and Improved Concatenation for Three Rows of Microphones	48

Figure	Page
4. 9 Taylor's Hypothesis versus Spatial Distribution of Pressure	49
4. 10 Time Evolution of the Wall Pressure	51
4. 11 Conditional Average of Pressure for Positive ($p' \geq \kappa p_{rms}$) and Negative ($p' \leq -\kappa p_{rms}$) Events for an Individual Microphone, $\langle p'(\tau) \rangle$, and for the Concatenated Wall Pressure Signal, $\langle p'(x^+ = 0, \tau) \rangle$; $\kappa = 2.5$	53
4. 12 Power Spectra of Pressure for an Individual Microphone, $\phi_{p'(\tau)p'(\tau)}$, and for the Concatenated Wall Pressure Signal, $\phi_{p'(x^+ = 0, \tau)p'(x^+ = 0, \tau)}$	54
4. 13 Power Spectra of the Concatenated Spatial Pressure Profiles with and without Filtering	55
5. 1a Instantaneous Velocity and Pressure Fields, Event i, $Re_\theta = 1520$	61
5. 1b Detail of the Instantaneous Velocity Field and Contours of Wall Pressure Underneath from Event i	62
5. 2a Instantaneous Velocity and Pressure Fields, Event ii, $Re_\theta = 1520$	63
5. 2b Detail of the Instantaneous Velocity Field and Contours of Wall Pressure Underneath from Event ii	64
5. 3a Instantaneous Velocity and Pressure Fields, Event iii, $Re_\theta = 1520$	66
5. 3b Detail of the Instantaneous Velocity Field and Contours of Wall Pressure Underneath from Event iii	67
5. 4a Instantaneous Velocity and Pressure Fields, Event iv, $Re_\theta = 3950$	69
5. 4b Detail of the Instantaneous Velocity Field and Contours of Wall Pressure Underneath from Event iv	70
5. 5a Instantaneous Velocity and Pressure Fields, Event v, $Re_\theta = 3950$	72
5. 5b Detail of the Instantaneous Velocity Field and Contours of Wall Pressure Underneath from Event v	73
5. 6a Instantaneous Velocity and Pressure Fields, Event vi, $Re_\theta = 3950$	74
5. 6b Detail of the Instantaneous Velocity Field and Contours of Wall Pressure Underneath from Event vi	75
5. 7a Instantaneous Velocity and Pressure Fields, Event vii, $Re_\theta = 5790$	77

Figure	Page
5. 7b Detail of the Instantaneous Velocity Field and Contours of Wall Pressure Underneath from Event vii	78
5. 8a Instantaneous Velocity and Pressure Fields, Event viii, $Re_\theta=5790$	79
5. 8b Detail of the Instantaneous Velocity Field and Contours of Wall Pressure Underneath from Event viii	80
5. 9a Instantaneous Velocity and Pressure Fields, Event ix, $Re_\theta=5790$	82
5. 9b Detail of the Instantaneous Velocity Field and Contours of Wall Pressure Underneath from Event ix	83
6. 1 Illustration of Space-Time Averaging	86
6. 2 Time-Space Conditional Average for Negative (Top) and Positive (Bottom) Pressure Events. $Re_\theta=1520$ and Threshold $\kappa=2.5$	87
6. 3 Time-Space Conditional Average for Negative (Top) and Positive (Bottom) Pressure Events. $Re_\theta=3950$ and Threshold $\kappa=2.5$	88
6. 4 Time-Space Conditional Average for Negative (Top) and Positive (Bottom) Pressure Events. $Re_\theta=5790$ and Threshold $\kappa=2.5$	89
6. 5a Time-Space Average for Positive Pressures. $Re_\theta=1520$, $\kappa=2.5$	90
6. 5b Time-Space Average for Negative Pressures. $Re_\theta=1520$, $\kappa=2.5$	91
6. 6a Time-Space Average for Positive Pressures. $Re_\theta=3950$, $\kappa=2.5$	92
6. 6b Time-Space Average for Negative Pressures. $Re_\theta=3950$, $\kappa=2.5$	93
6. 7a Time-Space Average for Positive Pressures. $Re_\theta=5790$, $\kappa=2.5$	94
6. 7b Time-Space Average for Negative Pressures. $Re_\theta=5790$, $\kappa=2.5$	95
6. 8 History of Wall Pressure at $Re_\theta=3950$	101
7. 1 Near Wall Shear Layers (a) $Re_\theta=1520$, $U_c = 0.70 U_\infty$, (b) $Re_\theta=3950$, $U_c = 0.85 U_\infty$ (c) $Re_\theta=5790$, $U_c = 0.85 U_\infty$: Reynolds Decomposed Vector Field (Top) and Vector Field in a Plane Moving at U_c (Bottom)	112
7. 2 Instantaneous Spanwise Total Vorticity in the Same Velocity Fields as Fig. 7.1: $Re_\theta = 1520$ (Top), $Re_\theta = 3950$ (Middle), $Re_\theta = 5790$ (Bottom)	116

LIST OF ABBREVIATIONS

Abbreviation	Term
f	frequency
f'	wall scaled frequency = $f\nu/u_\tau^2$
$h(n)$	filter coefficients
k_g	global threshold in clean-up routine
k_l	local threshold in clean-up routine
k	wave number
k_c	extraneous wave number = $1/\Delta$
P	average (mean) pressure
p	wall pressure = $P+p'$
p'	fluctuating pressure component
\tilde{p}'	filtered fluctuating pressure component
p_{rms}	root mean square of p'
Re_θ	Reynolds number based on momentum thickness = $\theta U_\infty/\nu$
t	time or time delay
t'	non-dimensional time or time delay = tu_τ^2/ν
U	average (mean) streamwise velocity
\bar{U}	average (mean) streamwise velocity obtained with PIV measurements
$\langle U \rangle$	average (mean) streamwise velocity obtained with HW measurements
U_c	convective velocity of reference frame
U_∞	freestream velocity
U^+	non-dimensional mean streamwise velocity component = U/u_τ
u	streamwise velocity component = $\bar{U} + u'$
u'	fluctuating streamwise velocity component
u_{median}	local group median velocity calculated in the clean-up routine

Abbreviation	Term
u_{rms}	root mean square value of u'
u_{std}	local standard deviation calculated in the clean-up routine
u_τ	wall friction velocity = $\sqrt{\tau_w/\rho}$
\bar{V}	average (mean) wall normal velocity component
v	wall normal velocity component = $\bar{V} + v'$
v'	fluctuating wall normal velocity component
v_{median}	local group median velocity calculated in the clean-up routine
v_{std}	local standard deviation calculated in the clean-up routine
$u'v'$	shear product
$\overline{u'v'}$	Reynolds shear stress
x	streamwise coordinate or offset
x^+	non-dimensional streamwise coordinate or offset = xu/v
y	coordinate in direction normal to wall
y^+	non-dimensional normal coordinate = yu/v
z	spanwise coordinate or offset
z^+	non-dimensional spanwise coordinate = zu/v
χ	off-set distance in x-direction from the pressure detection
δ	boundary layer thickness
Δ	separation between microphones
ε	dissipation rate
ϕ	power spectra
μ	dynamic viscosity of fluid
ν	kinematic viscosity of fluid
θ	momentum thickness
τ	wall shear stress
τ	off-set time from the pressure dection point

Abbreviation	Term
ω	total vorticity (spanwise component)
ω^+	non-dimensional total vorticity (spanwise component) = $\omega v / u_\tau^2$

ABSTRACT

The instantaneous streamwise and wall normal velocity components, u and v , in a plane along the streamwise and wall normal directions, x and y , were measured by means of Particle Image Velocimetry in a turbulent boundary layer over a flat plate simultaneously with the wall pressure using a 13×3 array of microphones. The experiment was performed for $Re_\theta = 1520, 3950$ and 6790 . The field of velocity measurements spanned approximately two boundary layer thickness, 2δ , in the streamwise direction and from the buffer layer to nearly δ in the wall normal direction. The wall pressure was measured at 13 discrete locations spanning 1δ in the streamwise direction. The instantaneous velocity fields show organized motions also observed in the literature from data bases of Direct Numerical Simulations (DNS) performed at lower Reynolds numbers. Some of these structures consist of bulges in the outer interface, incursions of flow from the outer parts of the boundary layer towards the wall, and shear layers of various sizes and inclination angles. The shear layer structure is present in many of the realizations and the slope of the interface that divides low and high streamwise momentum flow ranges from 20° when the shear layer is confined to the near wall region ($y^+ < 100$) to 45° when spanning several hundred y^+ . Negative total vorticity, typically on the order of $\omega_z^+ < -0.07$, is distributed along the interface; however, only localized areas exist where there is significant levels of negative Reynolds Stress product, $u'v' < -3u_\tau^2$, and these areas are located nearby eddie-like structures. The shear layers in the present study extend further in the wall normal direction (normalized on wall units) when compared with the numerical simulations. Furthermore, the DNS results typically depict a single eddy associated with a shear layer; contrasted with the current investigation which reveals several eddies located along the shear layer interface. The characteristic wall pressure signature of a shear layer consists of consecutive negative and positive pressures composing an adverse $\partial p/\partial x$. The streamwise separation between the

negative and positive pressure peaks is typically 125 viscous units. It is estimated that this pressure “structure” convects at a speed of $0.5 U_\infty$ (12 u_τ) with the positive pressure peak preceding the negative pressure peak by some eight viscous time units ($t^+ = 8$). Tracking some of these structures shows that they may convect large distances, on the order of δ . Additionally, negative pressure events, distinct from the negative/positive pair discussed above, are associated with an eddy at $y^+ \approx 100$. This roll-up motion was observed to have a sense of rotation opposite to that of the mean spanwise vorticity. The flow downstream of this roll-up structure consists of an “inverse” shear layer characterized by a positive $\partial u' / \partial x$ gradient, whereas the flow upstream and above of the roll-up structure exhibits flow ejections.

CHAPTER I

INTRODUCTION

1.1 The Problem of Turbulence

Stating a problem is half solving it. It is difficult to provide a precise definition of turbulence, despite being a phenomenon commonly encountered in a wide range of technical disciplines. Most naturally occurring flows are turbulent; e.g., currents below the surface of the ocean, the rising air in developed cumulus clouds, jet streams in the troposphere, river flows, etc. The engineer's design often encounters turbulent flows. Turbulence occurs in the flow field over turbine blades, the wings and fuselage of an aircraft, in the fluid transported in pipelines, often with adverse results on performance. In other cases however, the designs themselves rely on the flows being turbulent, such as to enhance mixing, expedite chemical reactions and combustion or improve heat transfer. And all these flows, though apparently very different from one another, when observed more closely may be unified by a number of characteristics attributed to turbulence.

Turbulent flows are characterized by rapid irregular and seemingly apparent random fluctuations of flow properties. Their nature is three dimensional, responsible for rapid mixing and increased rates of momentum, heat and mass transfer. Consequently, they are highly diffusive, far more so than smooth, laminar flows where diffusion takes place at the molecular level. Additionally, turbulent flows are highly dissipative, where the kinetic energy of turbulence is dissipated through viscosity, raising the internal energy of the flow. For turbulence to persist energy must be supplied to the flow at a rate greater than or equal to the dissipation rate.

There is no general approach to the solution of turbulence. The complex nature of the equations of motion has discouraged a deterministic approach and favored one based on statistical methods. These methods in themselves are insufficient and rely on empirical data and oftentimes on ad hoc assumptions. A second and very effective approach uses

dimensional analysis. Though the equations of motion are not solved, the analysis identifies the independent variables required to determine the appropriate scaling variables. In conjunction with dimensional analysis, the asymptotic invariance approach relies in taking the limit as the Reynolds number approaches infinity: in this limit, the effects due to molecular viscosity are negligible. In flows with simple geometries, where both time and length scales vary slowly in the streamwise direction, turbulent quantities may be successfully non-dimensionalized by the local length and time scales (local invariance), and oftentimes the turbulence may be assumed to be dynamically similar everywhere in the flow.

To date, no one theory of turbulence has emerged. Direct, statistical and dimensional approaches have not been sufficient to unify the understanding of turbulence. With the passing of time, experiments and analysis have sought to increase the physical understanding of turbulence. Revealing the characteristic features in turbulent flows, the relevant structures found therein, their formation and breakdown, etc. could bridge the gap between the equations of motion and the actual flow dynamics. A historical review of the treatment of turbulence is presented next.

1.2 Historical Background

For a given unsteady turbulent field, Osborne Reynolds in 1895 suggested to decompose the instantaneous flow variables into their mean and fluctuating components, e.g. $u_i = U_i + u'_i$ where $i = 1, 2, 3$ denoting the x, y, z coordinates respectively. Substitution into the Navier-Stokes equations, followed by time averaging, yields the Reynolds averaged momentum equation. It takes the following form,

$$U_j \frac{\partial U_i}{\partial x_j} = \frac{1}{\rho} \frac{\partial}{\partial x_j} (\Sigma_{ij} - \rho \bar{u'_i u'_j}) \quad (1.1)$$

The mean stress tensor is given by $\Sigma_{ij} = -P\delta_{ij} + 2\mu S_{ij}$, where S_{ij} is the mean strain rate which is defined by,

$$S_{ij} = \frac{1}{2} \left(\frac{\partial U_i}{\partial x_j} + \frac{\partial U_j}{\partial x_i} \right) \quad (1.2)$$

Equation 1.1 contains six independent convective stress terms, $\overline{u'_i u'_j}$, which combine with U_i and the pressure P for a total of ten unknowns, with only three momentum equations and the continuity equation. Relationships between these stresses and mean velocity and/or pressure are needed to close the system of equations. Several have been proposed but unfortunately, to date, no universal constitutive relation has been found. Two popular relationships are described next.

In order to solve the system of equations early semi-empirical methods were introduced. Boussinesq (1877) introduced an effective turbulent eddy viscosity, ν_t , by analogy to laminar flow; that is, $\tau_t \equiv -\rho \overline{u' v'} = \nu_t (\partial U / \partial y)$. U is the average or mean streamwise velocity component and u' and v' are the streamwise and wall normal velocity fluctuation components respectively, with their averaged product being the Reynolds shear stress. Prandtl (1925) suggested the use of a mixing length, ℓ_m , to represent an effective interaction distance between turbulent "lumps", drawing an analogy with the mean free path between molecules. Prandtl's relation, $\tau_t = \rho \ell_m^2 |\partial u / \partial y| \partial u / \partial y$, requires a relationship for ℓ_m which is also flow dependent. Both the eddy viscosity and the mixing length are measured experimentally and may vary substantially according to the problem under consideration, thus prohibiting a unified approach.

Improvements upon these formulations were aimed at representing, more directly, the fluctuating character of turbulence. Rather than using mean flow properties, these models treated the turbulent kinetic energy (TKE) of the fluctuations, $K \equiv 1/2 \overline{(u'^2 + v'^2 + w'^2)}$. The turbulent kinetic energy equation is derived from the Navier-Stokes equations (see Tennekes and Lumley, 1972). The one-equation formulation involves one equation, which is the TKE equation, and K as the turbulent quantity. Other than K , turbulent quantities that appear in this formulation are patterned

after the semi-empirical models above. Bradshaw (1967) introduced the relation $\tau_t = a\rho K$ where a is an empirically determined constant. Prandtl (1945) invoked the eddy viscosity concept through $\mu_t = \rho\sqrt{K}\ell$ where ℓ still needs to be modeled. Launder and Spalding (1972) and Rodi (1980) proposed an independent equation for ℓ , of the form $Z \equiv K^m \ell^n$, which was to be used with the TKE equation; this formulation is known as the two-equation model. The choice of $m = 3/2, n = -1$ makes Z proportional to the dissipation rate, ε . These K - ε models are widely used in general-purpose computer codes, though predictions are not always reliable and depend on the fine tuning of the adjustable constants. Further details of these models may be found in Mansour et al. (1988).

The direct treatment of the turbulent flow field consists of solving numerically the time-dependent, three-dimensional Navier-Stokes equations through Direct Numerical Simulation (DNS). The resolution of the grid used in the simulation has to be on the order of the viscous length scale ν/u_τ , while encompassing the geometric parameters of the flow (e.g., boundary layer thickness δ , pipe diameter) in order to accurately resolve the range of turbulent scales. In the case of a turbulent boundary layer the range between these two scales, $\delta u_\tau / \nu$, increases with the Reynolds number of the flow. Consequently, application of these simulations are limited to low Reynolds number flows. Spalart (1988) used DNS in a turbulent boundary layer on a flat plate with zero pressure gradient up to $Re_\theta = 1410$, where Re_θ is Reynolds number based on momentum thickness ($Re_\theta = U_\infty \theta / \nu$). The low Reynolds number restriction may be lessened by means of Large Eddy Simulation (LES) by considering scales above a given threshold; below this threshold, the scales are modeled by a subgrid scale model. The larger scales, which are highly dependent on the flow under consideration, are thus treated directly. Direct and large-eddy simulations of turbulence are reviewed by Rogallo and Moin (1984).

The study of turbulence from a statistical point of view was initiated by Taylor (1935). Taylor studied homogeneous and isotropic decaying turbulence. Kolmogoroff (1941)

established, for sufficiently high Reynolds numbers, the existence of a range of high wave numbers where turbulence is statistically in equilibrium and uniquely determined by the dissipation and viscosity, ε and ν . These small scales of motion are assumed to be in local isotropic equilibrium and are mainly responsible for dissipation. On the other hand large scales, of much lower wave number, while not depending directly on the flow viscosity are mostly responsible for production of turbulence.

The concept of intermittency at the edges of turbulent shear flows was introduced by Corrsin (1943) and Townsend (1947). The outer edge of the turbulent layer is characterized by an alternating turbulent and non-turbulent interface. The consideration of large eddy motions was considered by Townsend (1956) and Hinze (1959). Long time averaged spatial correlations were used to deduce the features of these large eddy motions. Townsend (1970) inferred the double roller large eddy structure in the case of a free shear flow and later the double cone structure for wall bounded shear flows (Townsend 1976). These representations set the stage for the investigation of organized, non-random large scale motions. The following chapter considers these investigations as they pertain to turbulent boundary layers.

CHAPTER II

ORGANIZED MOTION IN A TURBULENT BOUNDARY LAYER

The specific features of organized, non-random structures in turbulent flows depends on the flow under consideration. A great deal of attention has been given to wall bounded turbulence due to its widespread application in technology (turbomachinery, aircraft, heating and cooling...) Much of the research has focused on the turbulent boundary layer formed by a steady, incompressible, two dimensional flow over a smooth flat plate with zero pressure gradient: the canonical turbulent boundary layer. The following sections consider important aspects of the turbulent boundary layer, beginning with its unique velocity profile and a review of the work performed to date to distinguish organized motions in the fluctuating field.

2.1 The Turbulent Boundary Layer Profile

The mean flow profile in a turbulent boundary layer exhibits three distinct regions, each with its own unique scaling. These are discussed below.

The Viscous Sublayer. Very close to the wall, the no-slip condition renders the inertia terms negligible and the turbulent stresses $\overline{u'v'}$ are small as compared to the viscous stress terms. These assumptions simplify the Reynolds averaged momentum equation (Eqn. 1.1) for a zero pressure gradient condition to the form,

$$0 = \nu \frac{\partial^2 U}{\partial y^2} \quad (2.1)$$

Integrating this equation yields,

$$u^+ = y^+ \quad (2.2)$$

where $u^+ \equiv u/u_\tau$, $y^+ \equiv yu_\tau/\nu$ and $u_\tau \equiv \sqrt{\tau_w/\rho}$. This constant stress layer is assumed valid for $0 \leq y^+ \leq 5$.

The Buffer Layer. Further away from the wall, encompassing $7 \lesssim y^+ \lesssim 30$, the viscous and turbulent stresses become equally important. An implicit formula valid in this region is given by Spalding (1961),

$$y^+ = u^+ + e^{-K\kappa} \left(e^{Ku^+} - 1 - Ku^+ - \frac{1}{2} (Ku^+)^2 - \frac{1}{6} (Ku^+)^3 \right) \quad (2.3)$$

The Logarithmic and Outer Layer. Extending from $30 \lesssim y^+ \lesssim 150$ to $y/\delta \lesssim 0.15$ the flow is fully turbulent and the turbulent stresses are much greater than the viscous stresses. Consequently the mean velocity follows a logarithmic profile,

$$u^+ = \frac{1}{\kappa} \ln y^+ + C \quad (2.4)$$

Examining experimental data, Clauser (1956) proposed $\kappa = 0.41$ and $C = 4.9$.

The turbulent boundary layer exhibits two unique features, which in addition to its practical applications, make it a specially interesting problem to consider. One of these is the universality of the logarithmic profile; it is observed regardless of pressure gradient, surface roughness or Reynolds number. Secondly, the largest production rate of turbulent energy occurs in the buffer region (production = $\overline{u'v'}\partial U/\partial y$). This was demonstrated by the measurements of Klebanoff (1954). Laufer (1954) found the same result in the case of pipe flows. More than half of the total turbulent energy production occurs within this region (see Hinze, 1959).

2.2 Turbulent Structures

A widely used tool for examining organized motions in a turbulent boundary layer are spatial and temporal correlations. The Eulerian spatial correlation method used by Townsend (1956) was expanded to a time-space correlation by Favre et al. (1957),

$$R_{ij}(\bar{x}, \bar{\xi}; t, \tau) = \overline{u_i(\bar{x}, t)u_j(\bar{x} + \bar{\xi}, t + \tau)} \quad (2.5)$$

Measurements were performed with two probes, and repeated for varying distances from the wall. The speed of propagation of the structure was calculated from the maximum

value of the correlation, which corresponds to a specific time shift for a given separation between probes. The calculated convection speeds reveal a structure that convects with the local mean speed and is inclined to the wall; also the magnitudes of the maximum correlation values in the streamwise direction were observed to be much larger than in the spanwise direction.

Time-space correlations of the pressure fluctuations along the streamwise direction, $R_{pp}(\tilde{\xi}, \tau)$, beneath a turbulent boundary layer were calculated using two wall flush mounted pressure transducers by Willmarth and Wooldridge (1962). The time shifts in the correlation maxima correspond to convection speeds of pressure producing eddies. These vary from 0.56 to 0.83 U_∞ , when correlating the high and low frequencies respectively, corresponding to small and large scale producing eddies respectively. The extent of the transverse pressure correlation is of the same order as the streamwise correlation, δ , in contrast with the velocity correlations of Favre. The authors then calculate pressure-velocity correlations, R_{pu} and R_{pv} , to estimate the velocity field associated with organized turbulent structures (Willmarth and Wooldridge, 1963). A picture of the flow is estimated from a vector field where the velocity components correspond to the pressure-velocity correlations R_{pu} and R_{pv} . The pattern is composed of a clockwise rotating structure elongated in the wall normal direction. Willmarth (1975) also examined the correlations between wall shear stress at the wall and measurements of velocity. Alike R_{pu} and R_{pv} , correlations of R_{pt} were highly correlated over a significant portion of the boundary layer.

The production of turbulence in the boundary layer was examined by Kline et al. (1970) by visualizing the flow with a hydrogen-bubble wire placed parallel to and at various distances from the wall. Very close to the wall the flow forms an alternating pattern of high and low-speed streaks. The streaks gradually rise, suddenly lift-up, oscillate and break up: this phenomenon has become known as bursting. Most of the turbulent energy production, in the range of $0 < y^+ < 100$, occurs during this bursting

process (Kim et al. 1971). Earlier, Corino and Brodkey (1969) observed low speed fluid lifting up away from the wall (ejections) succeeded by high speed upstream fluid moving towards the wall (sweeps), closely paralleling the bursting phenomenon.

The dynamics of bursting are not limited to the near wall region, but have been found to highly interact with the outer part of the boundary layer. Blackwelder and Kovasznay (1972) reported that strong events in the wall region associated with bursting remain highly correlated out to $y/\delta \approx 0.5$.

Flow visualization and hot-wire measurements led Head and Bandyopadhyay (1981) to suggest the existence of highly elongated structures inclined at 45° to the wall similar to the hairpin and horseshoe vortices proposed by Theodorsen in 1955. The hairpin structure is small in the streamwise direction but it is highly elongated along lines of 45° . A physical model based on the horseshoe-type, Λ -shaped, vortices was proposed by Perry and Chong (1982), and further developed by Perry et al. (1986). They show that a range of geometrically similar hierarchies of a random array of vortices at different stages of stretching yield the correct logarithmic mean velocity profile, the region of constant Reynolds shear stress and correct streamwise fluctuation velocity spectra.

2.3 Role of Wall Pressure Fluctuations on Turbulent Structures

Experiments concerning pressure have been limited to measurements beneath turbulent flows; i.e., at the wall, since by inserting a pressure measuring probe into a turbulent flow the resulting change in the velocity field would affect the measurement of pressure. A Poisson equation relating the turbulent pressure field to the turbulent velocity field can be derived by taking the divergence of the momentum equation. This relationship shows that the turbulent pressure fluctuations are an integral effect of the velocity field,

$$\frac{\partial^2 p}{\partial x_i^2} = -\rho q \quad (2.6)$$

where the source term q is given by,

$$q = 2 \frac{\partial U_i}{\partial x_j} \frac{\partial u_j}{\partial x_i} + \frac{\partial^2}{\partial x_i \partial x_j} (u_i u_j - \bar{u}_i \bar{u}_j) \quad (2.7)$$

The pressure fluctuations at a point \vec{x} on the wall is then given by,

$$p_w(\vec{x}) = \frac{\rho}{\pi} \int_{y>0} q(\vec{x}_s) \frac{dV(\vec{x}_s)}{\vec{x} - \vec{x}_s} \quad (2.8)$$

where the volume of integration is over the entire half-space containing the flow, $y > 0$, and \vec{x}_s is the dummy variable in the integration. Multiple sources therefore contribute to the wall pressure fluctuations. These contributions will decrease with increasing distance from \vec{x} .

Pressure fluctuations are commonly grouped into large scale (low frequency) structures that originate in the outer part of the boundary layer and small scale (high frequency) structures that are limited to the wall region and are often related to the bursting phenomenon. On the one hand, conditional space-time correlations of pressure and velocity measurements, R_{pu} and R_{pv} , from Panton et al. (1980) attest that large scale disturbances are linked with the intermittent character of the turbulent boundary layer. On the other hand, conditional sampling on the basis of high frequency pressure and (near wall) velocity activity led Thomas and Bull (1983) to identify a characteristic wall pressure pattern associated with the burst-sweep cycle. The pattern inferred by the authors consists of a large positive pressure in the streamwise direction with a region of negative pressure to either side. The pattern which was determined to convect at $0.67 U_\infty$ is closely coupled to an inclined shear layer and the bursting cycle.

Conditional sampling of simultaneous pressure and velocity measurements have shown strong relationships between large amplitude wall pressure events and shear layer structures. Johansson et al. (1987) performed conditional averages of the streamwise velocity at various positions from the wall directly above the pressure transducer in a flat plate turbulent boundary layer. The conditionally averaged streamwise velocity, for $p' > 3p_{rms}$, where p' is the fluctuating wall pressure, shows a distinctive shear layer of

low momentum fluid followed upstream by high momentum fluid for distances from the wall to $y^+ = 187$. Also when detecting on a shear layer, at various wall normal locations, the averaging yields a positive pressure peak. The authors did not find a relation between strong negative pressure peaks and a shear layer, but rather the conditional average of the streamwise velocity for $p' < -3p_{rms}$ revealed a high streamwise velocity occurring around the detection time.

In the comprehensive review by Eckelman (1990), conditional averages performed in pipe flows are shown to partially corroborate the findings of Johansson et al. (1987). In this review, measurements performed in pipe flows by Langeheineken (1981) and Dinkelacker and Langeheineken (1983) confirm the coupling between positive pressure peaks and the existence of a shear layer. Additionally, Sieber and Dinkelacker (1987) extended their velocity measurements in the streamwise direction to show there is a coupling between negative pressure peaks and a shear layer signature.

Jukenhoeffel (1995) measured the conditional velocity field in an extended grid on the xy plane representative of both large positive and negative pressure peaks ($p' > 2.5p_{rms}$, $p' < -2.5p_{rms}$) in a turbulent boundary layer over a smooth flat plate. A single microphone was positioned at the center of the grid, flush with the tunnel floor. Conditional averaging and quadratic stochastic estimates yielded similar results. The conditional velocity field representative of large positive and negative pressure peaks was consistent throughout the range of Reynolds numbers considered. A large positive pressure peak was found to be associated with a shear layer, where fluid with positive momentum was found upstream of fluid with a momentum deficit. The location of the shear layer in the region close to the wall coincides with the detection point in the conditional averaged wall pressure signal. A large negative pressure peak is likewise associated with a similar shear layer; though in this case the location of the shear layer near the wall occurs at a downstream location of approximately $x^+ = 400$. Additionally, large negative pressure peaks are associated with a small region of fluid which has a

slight momentum deficit just upstream of the pressure detection point; this region was observed to reside within the buffer layer with a streamwise extent of approximately 50 non-dimensionalized wall units.

One critical question which arises when investigating conditionally averaged fields is the correspondence between the instantaneous field and the conditionally averaged field. The process of conditional averaging “washes out” features in the instantaneous flow field. Secondly, a question which invariably arises is “Is the conditional field an artifact of the averaging process?” In other words, are the features highlighted by the conditional averaging present in the instantaneous flow field.

2.4 Instantaneous Flow Features: Particle Image Velocimetry

Traditionally, experiments have been performed where long time series of flow properties are measured at discrete points in space. These studies have identified significant common or basic patterns in the flow. The analysis relies on statistical processes which unfortunately suffer from a number of shortcomings as documented earlier. The relationship between the conditional and the instantaneous realization is of critical importance; secondly, it is very difficult to uncover the interactions between different structures when using a statistical approach. In addition introduction of instrumentation into the stream will disturb the flow.

Experimental methods have increasingly advanced to capture a more complete picture of the turbulent flow. Particle Image Velocimetry (PIV) was developed to yield the instantaneous velocity field over a fairly large two dimensional region of the flow. The standard planar PIV set-up yields two components of velocity, but it has more recently been extended to yield all three components of velocity (Prasad and Adrian, 1993) in a 2-D plane. It is possible to resolve accurately, for instance, some 20,000 velocity vectors at a given instant in time. A plane of the instantaneous turbulent flow can therefore be analyzed.

Planar velocimetry techniques grew from flow visualization. These rely on pulsed light to identify the position of tracing elements in the flow field. Well known illustrations of particle streak and stroboscopic photography were compiled by Van Dyke (1982). Falco (1977) used a high-powered laser flash to cause a light-sensitive chemical to fluoresce in the flow field. The fluorescent trace over the duration of the flash yielded the velocity. The origin of particulate marking techniques is found in solid mechanics where the pulsed light concept was used to create speckle patterns and relate these to displacements in solids under deformation. Analogously, in fluid mechanics, Laser Speckle Velocimetry or LSV can be used to determine velocity when a high concentration of particles is present. Speckle refers to the pattern that results when the light scattered by adjacent particles overlaps. Less dense seeding is required in PIV, where instead of speckle, individual particle images are recorded. Typically, the flow is illuminated twice with extremely short duration pulses, double exposing particles onto a film. Ideally a small area on the film (on the order of $1 \times 1 \text{ mm}^2$) contains a large number of particle pairs (10 to 20), which when correlated yields the average displacements of these particles. Meinhart (1994) and Westerweel (1993) used this technique extensively in studying and corroborating its effectiveness in turbulent flows over a flat plate and in a pipe flow respectively. A treatment of particle imaging techniques is the subject of the review by Adrian (1991).

It is important to stress the instantaneous character of the flow in the nature of these experiments. These contrast fundamentally with point measurements, whose analysis have mostly relied on averaging based techniques which yield average structures. Averaging however eliminates secondary motions and as stated the basic patterns that are documented with conditionally averaging point measurements may be an artifact of the averaging process and not an important flow structure. The use of PIV represents both, the structure which commonly appears from the averaging as well as other coherent

motions present at that instant. Unfortunately, one of the main disadvantages of PIV is that time information is not feasible for any practical turbulent flow field.

2.5 Objectives

The flow considered here is the turbulent boundary layer over a smooth flat plate with zero pressure gradient; that is, the canonical turbulent boundary layer. Experiments are performed to obtain accurate instantaneous images of the turbulent velocity field simultaneously with the wall pressure. The objective is to analyze the instantaneous turbulent flow for given wall pressure signatures. The effect of Reynolds number will be investigated by performing measurements over a range of $Re_\theta \equiv U_\infty \theta / \nu \equiv 1500$ to 6000, where θ is the momentum thickness.

A standard, two-velocity component, PIV experiment is set-up to record the instantaneous flow field ranging from the buffer layer through the outer layer. The PIV realizations are recorded in the xy plane and a 2-D grid (xz plane) of wall pressure sensors is centered underneath the photograph.

The instantaneous realization of the velocity field is used to analyze turbulent structures. The turbulent velocity field is considered from one of two different reference frames. First, the instantaneous total velocity is decomposed using the standard Reynolds decomposition ($u(x,y) = \bar{U}(y) + u'(x,y)$, $v(x,y) = \bar{V}(y) + v'(x,y)$). The local mean velocity $\bar{U}(y)$, $\bar{V}(y)$ is calculated for all x locations over all PIV realizations at a given Reynolds number. This line average $\bar{U}(y)$ profile is subsequently subtracted from each instantaneous velocity leaving the fluctuation $u'(x,y)$ field. Secondly, a constant convection velocity U_c is subtracted from the total velocity. U_c is chosen to be a fraction of the free stream velocity; typically in the range 0.6 to 0.9 U_∞ . In addition, the total and fluctuating vorticity and the Reynolds stress field $u'v'$ is also used in analyzing the turbulent structures.

The two dimensional array of microphones provides the pressure $p(x, z, t)$ and allows the investigation of the formation and convection of significant wall pressure imprints. The objectives of this investigation are to record a PIV realization of the flow simultaneously with the wall pressure signature. The combination of instantaneous, spatially resolved, velocity and pressure measurements allows a look at the turbulent flow field from a new perspective; it provides a more complete picture regarding the interaction between the velocity field and the wall pressure. Contrary to previous experiments, multiple organized turbulent motions in the velocity field may be identified at a given instant in time while simultaneous structures are identifiable in the spatially resolved pressure field. Special consideration has been given to characteristic events, among them, strong shear layers, bulges in the boundary layer interface, incursions of freestream flow into the boundary layer, large scale motions of constant momentum as well as the wall pressure signatures corresponding to each of these flow structures. Such events as these have been observed in the literature from data of numerical simulations performed at lower Reynolds numbers. Specific events that contribute to the production of turbulence through significant contributions to $u'v'$ and vorticity, and thus believed to play a major role in understanding the flow evolution, are also considered.

CHAPTER III

EXPERIMENTAL SET-UP

As stated in the Objectives the goal of this experiment is to capture the instantaneous velocity flow field by means of PIV while recording the pressure underneath at several locations using an array of miniature microphones. The following sections describe the flow facility and the instrumentation used for the velocity and pressure measurements.

3.1 Flow Facility

The experiments are performed in the Mark V. Morkovin closed-return windtunnel. The facility is shown in Figure 3.1. A 4:1 contraction leads to the high speed test section, which is $0.9 \times 0.61 \times 6$ m in height, width and length respectively. For the range of operating conditions, the turbulence intensity levels in the high speed test section are below 0.1%. The turbulent boundary layer develops along a mirror finish aluminum test plate placed 0.3 m above the test section floor. Transition to turbulence is triggered using a flush mounted 24-grit 0.2 m long sandpaper strip, located about 0.15 m downstream from the leading edge of the test plate. A zero streamwise pressure gradient is attained by adjusting the movable test section ceiling.

3.2 Particle Image Velocimetry Measurements

The optical system, lasers and camera, for the PIV measurements are shown with respect to the tunnel test section in Figure 3.1. Details of the laser forming optics are shown in Figure 3.2. Two Continuum Surelite Nd:Yag lasers are used to create a light sheet approximately 80 mm wide to illuminate the seeded flow. The two beams are combined by using a beam splitter. The combined beams are expanded into a sheet of light via a cylindrical lens with focal length $f = -8$ mm. The sheet is subsequently trimmed and made parallel with an elliptical lens of focal length $f = 1000$ mm.

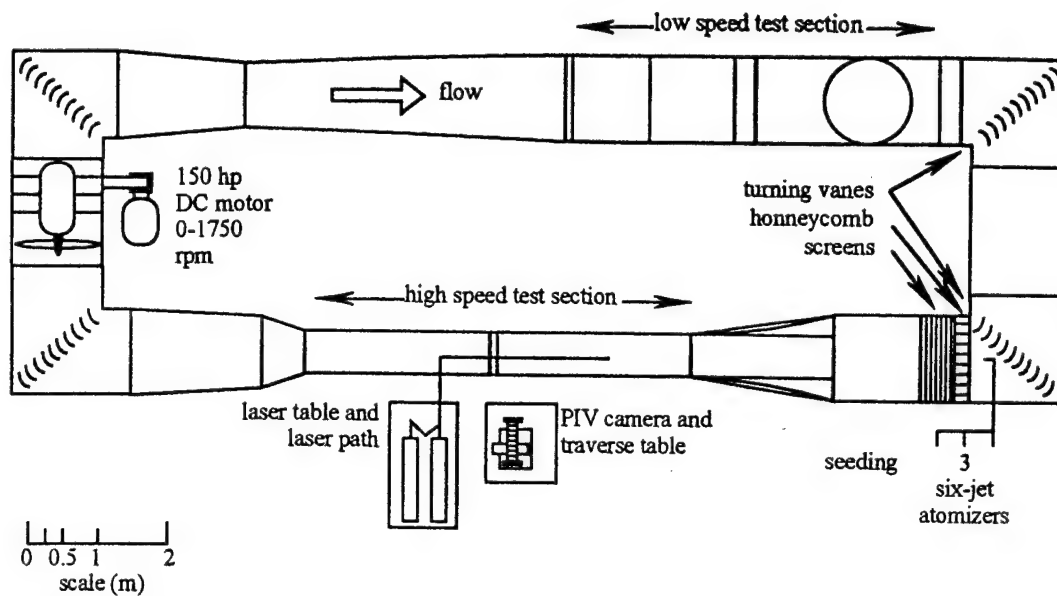


Figure 3.1 Schematic of the Mark V. Morkovin Wind Tunnel

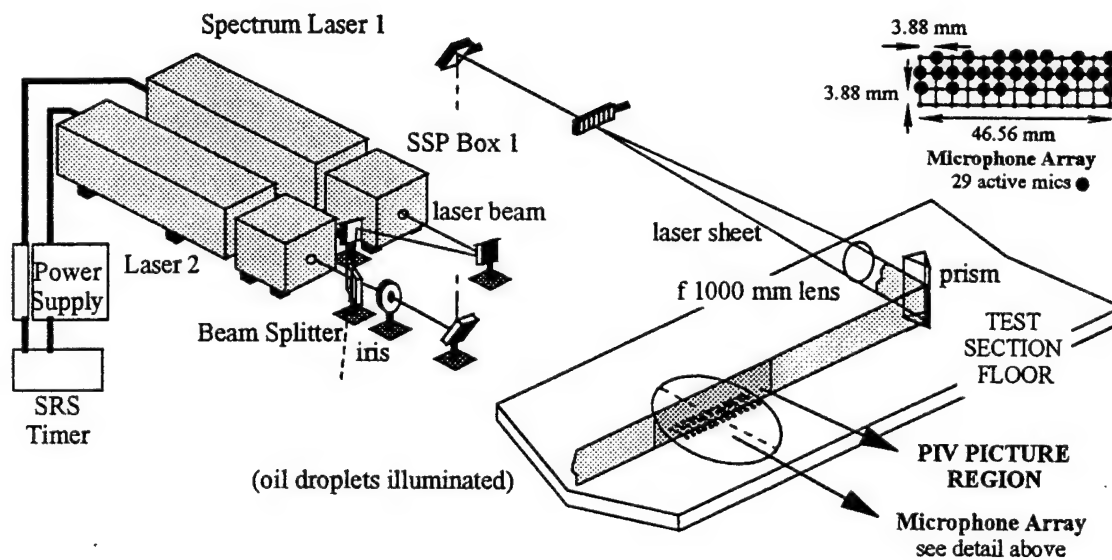


Figure 3.2 Particle Image Velocimetry Set-up and Pressure Array

A prism then deflects the light sheet 90° upstream along the middle of the test section. The disturbance of the prism and lens in the test section was investigated by comparison of hot-wire measurements of the streamwise mean and rms velocity profiles with and without these optics in the test section: no noticeable effects at 500 and 1000 mm upstream from the optics were observed. Both lasers were pulsed at 9.8 Hz and their triggering voltage was adjusted such that each emitted 150 mJ per pulse. The pulse trains from the lasers were synchronized using a Stanford Research System timing box with a time delay that varies according to the freestream speed and ranged from 20 to 55 μ sec. A large format camera (5" x 4") with a 480 mm focal length lens is used to image particles on T-max 400 film. The magnification was determined for each condition and was nominally 1:1.

Seeding was accomplished with 1–2 μ m diameter droplets atomized with three TSI 6-jet units from a 10/90 polyethylene-glycol/water mixture. The seeding is introduced into the windtunnel upstream from the contraction, prior to the screens and honeycomb sections as shown in Figure 3.1.

The negatives were analyzed in the interrogation system described by Ullrich (1993). A schematic of the system used is shown in Figure 3.3. The interrogation system consists of a computer controlled translation stage that holds the negative, a 568 x 415 pixel Pulnix CCD camera (of which only the center 128 x 128 pixels are used) with a Scion frame grabber and a Macintosh IIfx computer with a model MacDSP256kN 256 x 256 array processor of eight bit integers. The imaged area is digitized by the camera and the particle displacement is calculated from the two dimensional auto-correlation of the image in the interrogation spot as illustrated in Figure 3.4. The displacement is calculated from the distance between the self-correlation peak and the centroid of the largest non-central peak in the auto-correlation. The displacement on the film is then converted into the displacement on the flow field through the film and camera magnifications. The negative is translated to the next interrogation position once the interrogation of a spot is

completed. Details regarding the PIV data acquisition and errors involved in the velocity vector calculations are presented in the following chapter.

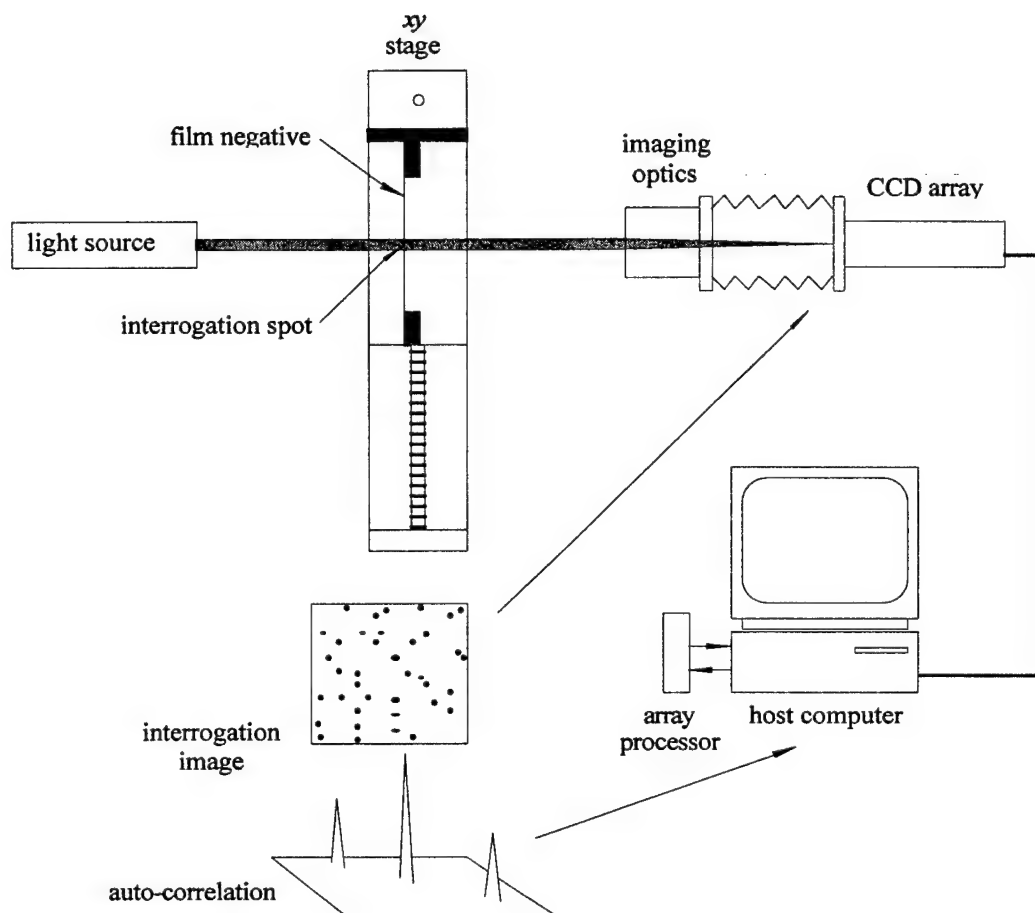


Figure 3.3 Schematic Diagram of the Interrogation System

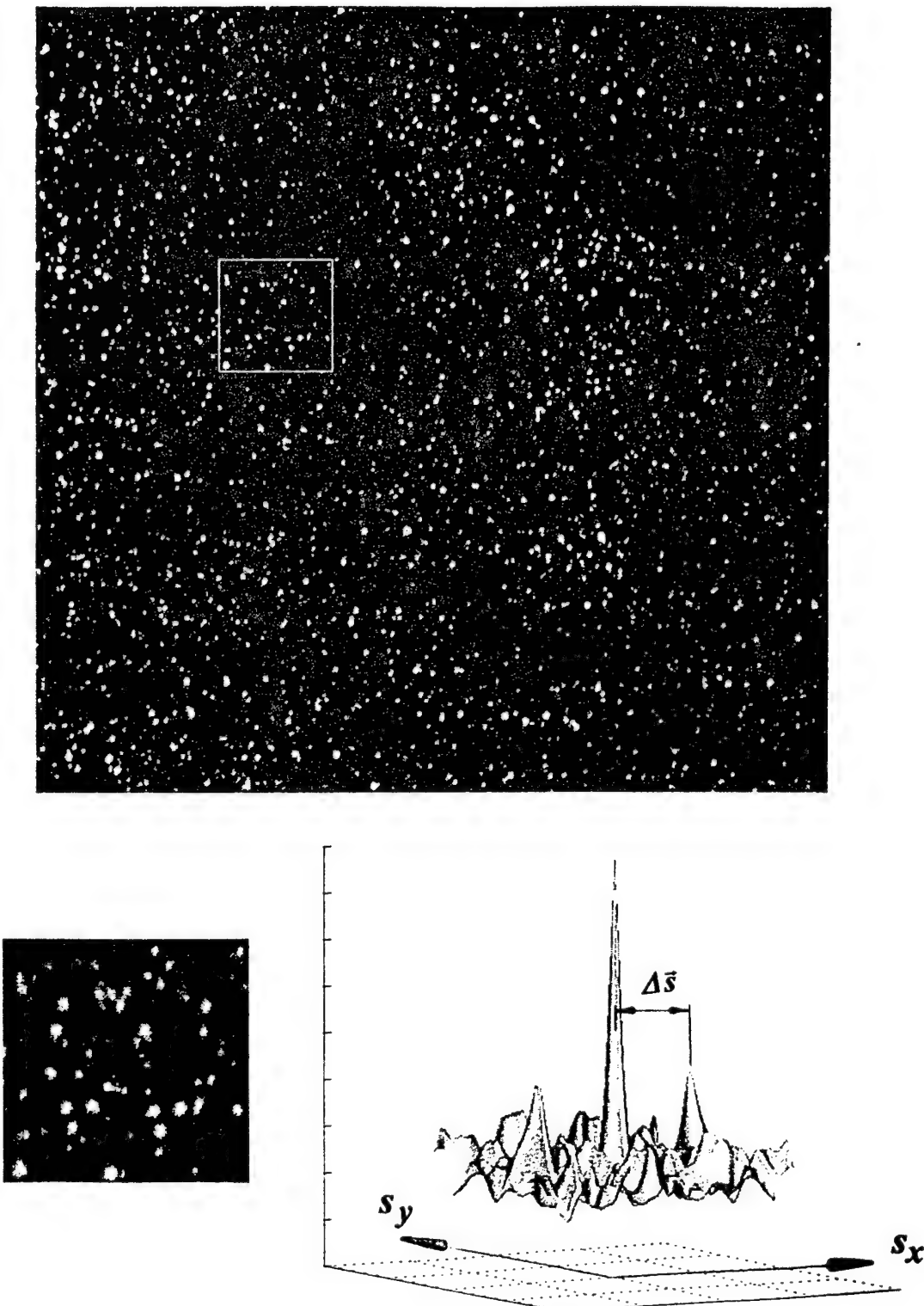


Figure 3.4 Sample of a Single-Frame, Double-Exposed Image Taken in the Turbulent Boundary Layer with a Single Interrogation Region Highlighted and Resultant Two-Dimensional Auto-correlation Field.

3.3 Pressure Measurements

In order to obtain an accurate representation of the turbulent pressure underneath the velocity flow field a plug was designed to house a multiple number of miniature microphones, all equally spaced from one another. The design and assembly of the plug, the method for calibrating the miniature microphones, the pressure data acquisition and reduction are documented in the following subsections. The documentation begins with a description of the microphones.

3.3.1 Miniature Microphones and Supporting Hardware. The fluctuating wall pressure is measured with the subminiature condenser type Knowles EM-3068 model microphone. The housing has dimensions $3.63 \times 3.63 \times 2.28$ mm, with 1.52 mm length sensing probe with a 1.0 and 0.7 mm outer and inner diameter respectively (Knowles, 1992). The microphone diameter nondimensionalized, $d^+ \equiv du/v$, corresponds to 9, 20 and 29 for the three Reynolds numbers considered here. Schew (1983) reviewed a wide range of microphone diameters, and concluded that a $d^+ \approx 20$ is able to resolve the pressure structures essential to turbulence. Recently, Gravante (1995) confirmed this. At the highest Reynolds number tests ($Re_q = 5670$, $d^+ = 29 > 20$) the microphone exhibits a low-pass filtering character which attenuates higher frequencies and larger wavenumbers. The diameter is nevertheless still small: comparison of this diameter to those used by Schew, and consideration of the transducer resolution correction to the power spectra calculated by Corcos* (1967) shows that the losses incurred at this Reynolds number are small (the rms is attenuated in the order of 1–2%).

A Power-Supply Box, a dual purpose DC-Filtering/Amplifying Box, and a Terminal-Connection Board were designed and constructed around the requirements of the microphone array. The array houses a maximum of 65 microphones (Figure 3.5).

* Corcos, G. M., 1967, J. Sound Vib., Vol. 6, pp. 59–70, as cited by Schew, G. 1983, On the Structure and Resolution of Wall-Pressure Fluctuations Associated with Turbulent Boundary Layer Flow, J. Fluid Mech., Vol. 134.

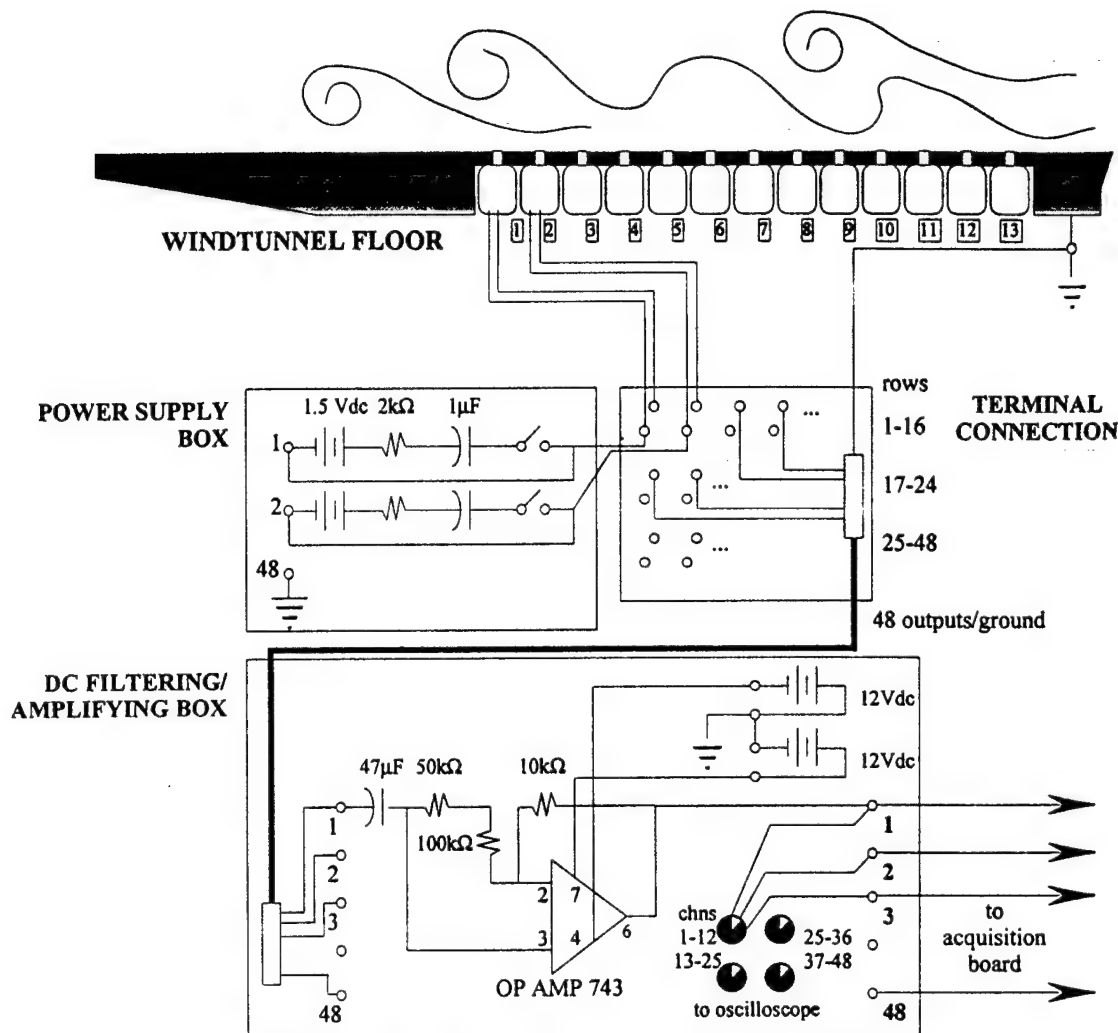


Figure 3.5 Microphone Array and Supporting Hardware

The Power-Supply Box provides 48 independent on/off 1.5 Vdc lines to the Terminal-Connection Board located underneath the array. Independent power supply lines assure easy isolation of a possible malfunctioning microphone. From the Terminal-Connection Board 48 wire pairs, power supply and return output voltage, are directed to 48 microphones in the array. All microphones share the same ground. The microphone casings are grounded through direct contact with the plug. The output leads and ground from the Terminal-Connection Board are then directed by means of a 50-wire cable to the

DC-Filtering/Amplifying-Box. A high-pass filter removes the DC component and a non-inverting amplifying circuit applies a $\times 100$ amplification to each signal. These circuits have a flat frequency response up to and beyond 15 KHz, well within the frequency range of interest here. Each signal is then directed to the acquisition board by means of BNC cables.

3.3.2 Pressure Array and Assembly. The pressure plug consists of a main casing, five miniature-microphone inserts, and two reference microphone inserts (all aluminum construction). The upper surface of the main casing (Figure 3.6) is inserted into one of the available holes in the boundary layer test plate. The lower flange in the plug has a groove machined into it which houses a flexible o-ring. The o-ring surfaces above the groove, permitting the four holding screws in the flange to be tightened to bring the upper surface flush with the floor surface.

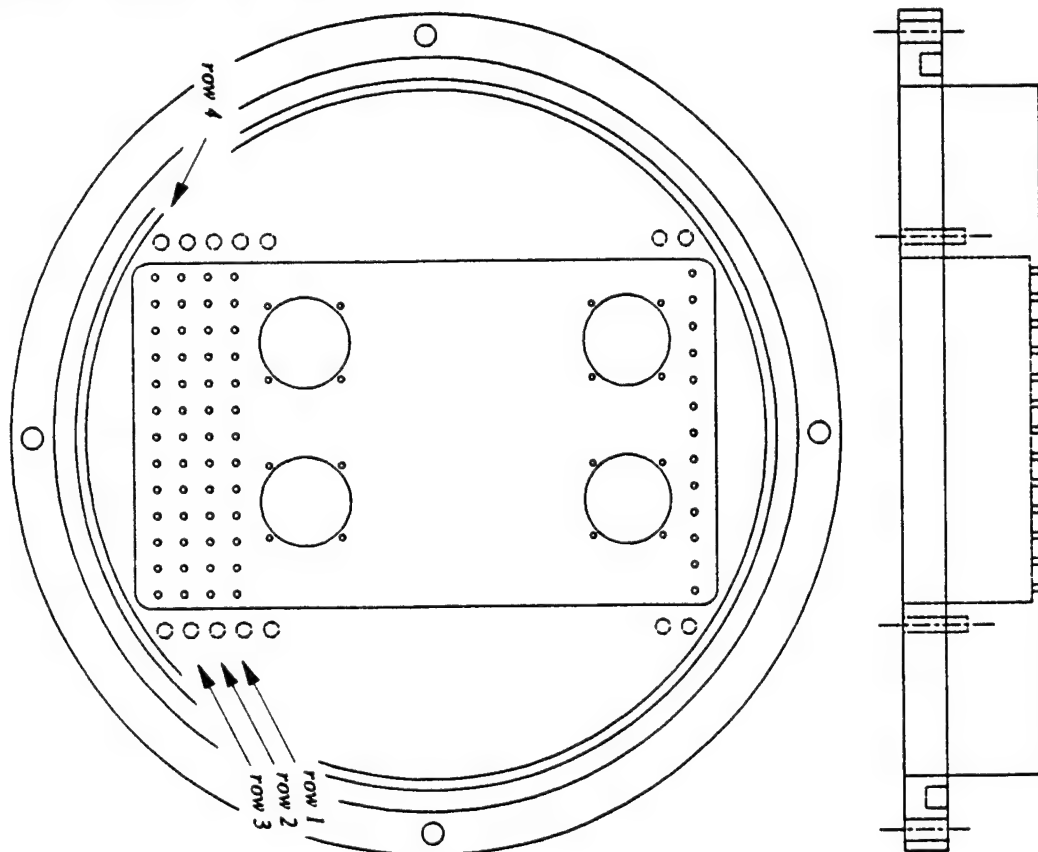


Figure 3.6 Main Casing

The main casing houses five rows, each row encompassing thirteen 1 mm diameter tapered holes. The holes are tapered from underneath to ease insertion of the microphones during assembly. The rows are aligned in the streamwise direction of the flow. All microphones are equally spaced by 3.886 mm. Four of the rows are closely aligned with the PIV realization with one of the rows directly underneath. The fifth row is removed 50 mm, a distance on the order of the boundary layer thickness. Four additional larger holes allow reference microphones to be installed for calibration purposes. The main casing design allows for two size reference microphones, 0.25" (6.35 mm) and 0.50" (12.7 mm).

One of the miniature-microphone inserts (Figure 3.7) holds thirteen microphones, each separated from one another by a 0.010" (0.39 mm) aluminum wall. Two microphone leads, positive power supply and output, run to each microphone along grooves imbedded in the insert. The microphones slip in their mounts, and the leads are secured to the insert with a drop of epoxy. Once all thirteen microphones are assembled and secured, the insert is then gently slipped into the main casing. The insert holding screws are tightened while checking that microphone heads align and enter the tapered perforations in the main casing.

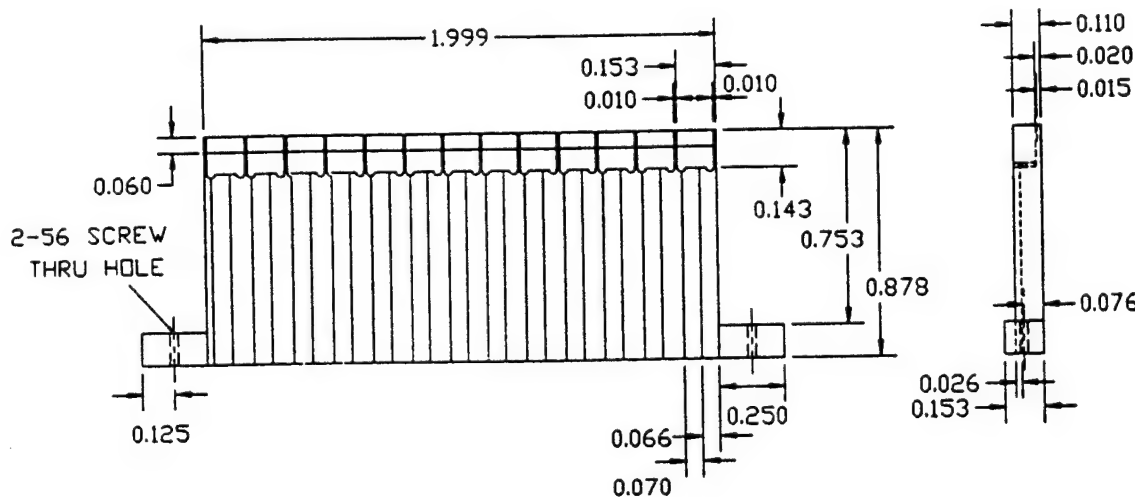


Figure 3.7 Miniature-Microphones Inserts

The array microphones are calibrated by removing the 0.5" (12.7 mm) reference plugs from the main casing and inserting the reference microphone insert (Figure 3.8) with either two 0.25" (6.35 mm) Larson and Davis microphones or with the larger 0.5" Brue and Kjoer (12.7 mm) size microphone insert. The larger size microphone allows for extending the calibration curve to smaller frequencies (not used in this study; see Gravante 1995 for further details).

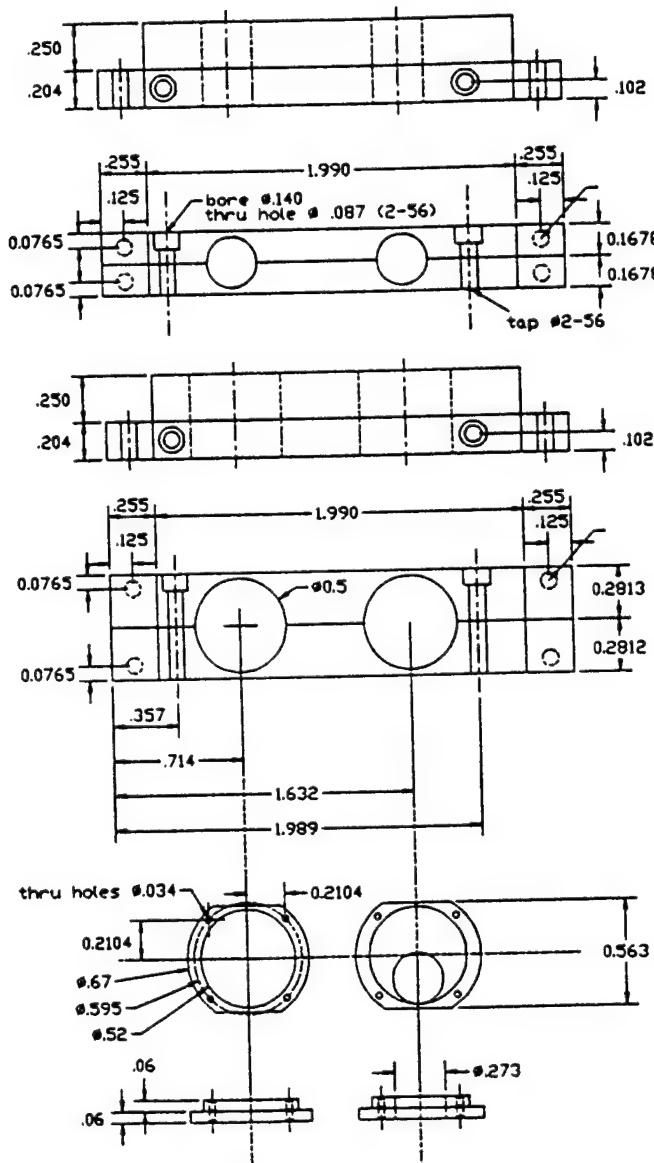


Figure 3.8 Reference Microphone Insert and Plugs

3.3.3 Calibration Microphones. Each miniature microphone is calibrated against a Larson and Davis microphone which is characterized by a flat frequency response in the range of interest. Two 0.25" microphones, LD1203 and LD1222, with preamplifiers 910B-253 and 910B-254, and sensitivities of 767.23 Pa/V and 714.29 Pa/V respectively are used. The Larson and Davis 2200C preamp/power supply with a 100x gain is used to excite and amplify the microphone signals before acquisition. Given the large number of miniature microphones present in the array, the use of two Larson and Davis microphones speeds up the calibration process.

3.3.4 In Situ Calibration. The complex frequency response of the array microphones is obtained by acquiring a white-noise sound field simultaneously with the reference microphones. The response curve is optimized by calibrating for two frequency ranges separately: near and far field calibrations corresponding to low and high frequency ranges respectively.

An Elgenco Incorporated 312A White Noise generator and a Realistic MPA-40 35 Watt P.A. amplifier are used in conjunction with two different speakers to capture a large range of frequencies. A VIFA A17WG two-way speaker, with a 6 1/2" (165 mm) woofer and a 3/4" (19 mm) tweeter provides a flat noise spectrum from 100 to 40,000 Hz. An ASL-1 subwoofer extends the low frequency by providing frequencies between 30 and 10,000 Hz.

The method of calibration follows the work of Gravante (1995), except in the present experimental set-up the procedure involves expanding the technique from one to multiple microphone calibrations. A total of 204,800 points per microphone are recorded. The data for the near field calibration curve is acquired at 4000 Hz. Data for the far field calibration is acquired at 40,000Hz.

Stable calibration curves are obtained with one near field and ten independent far field acquisitions. There is greater scatter in the datapoints from the calibration curve at high frequencies. The scatter is reduced by averaging ten far field calibrations performed with

different speaker orientations with respect to the microphones. The floor plug accommodates four different locations for the calibration microphones so that they are in close proximity to a group of miniature microphones in the array. The four locations correspond to two locations for calibrating the “noise cancellation” row and two locations for calibrating the “active microphones”. Data from the calibration microphone and a prescribed number of miniature microphones in the corresponding group are thus recorded simultaneously. This grouping is denoted as a “block” and is illustrated in Figure 3.9.

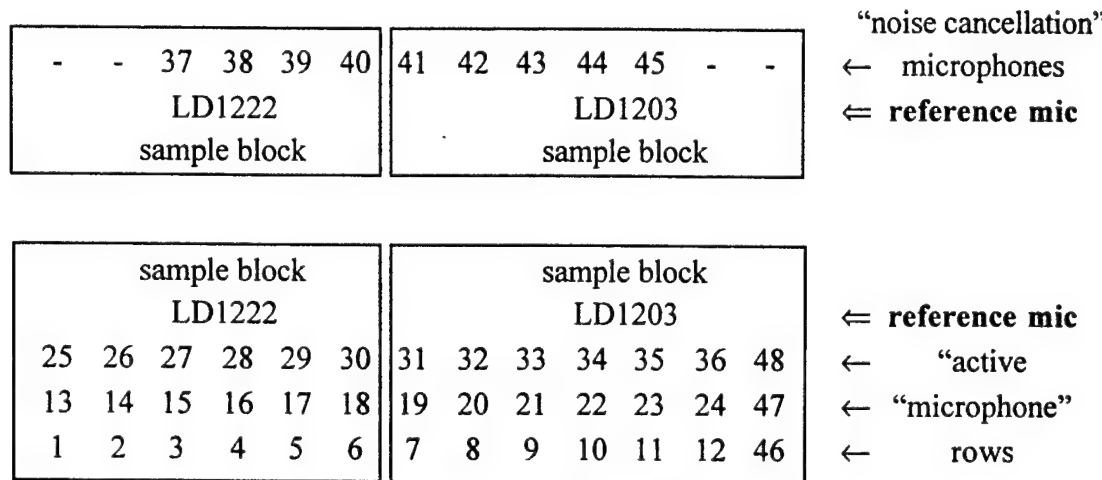


Figure 3.9 Assignment of Array Microphones to Reference Microphone

Individual calibration curves are obtained by pairing each microphone with the corresponding calibration unit. The frequency response is thus composed of the near field calibration and the averaging of ten far field calibrations. A polynomial fit to the magnitude and phase components of the transfer function yields a coefficient file used later to convert voltage data to pressure. Following the work of Gravante (1995), three 4th order polynomials are used to approximate the magnitude and phase, from 30 to 150 Hz for the near field calibration data, and 150 to 4500 Hz and 4500 to 12500 Hz for the far field calibration data. A typical calibration curve is shown in Figure 3.10.

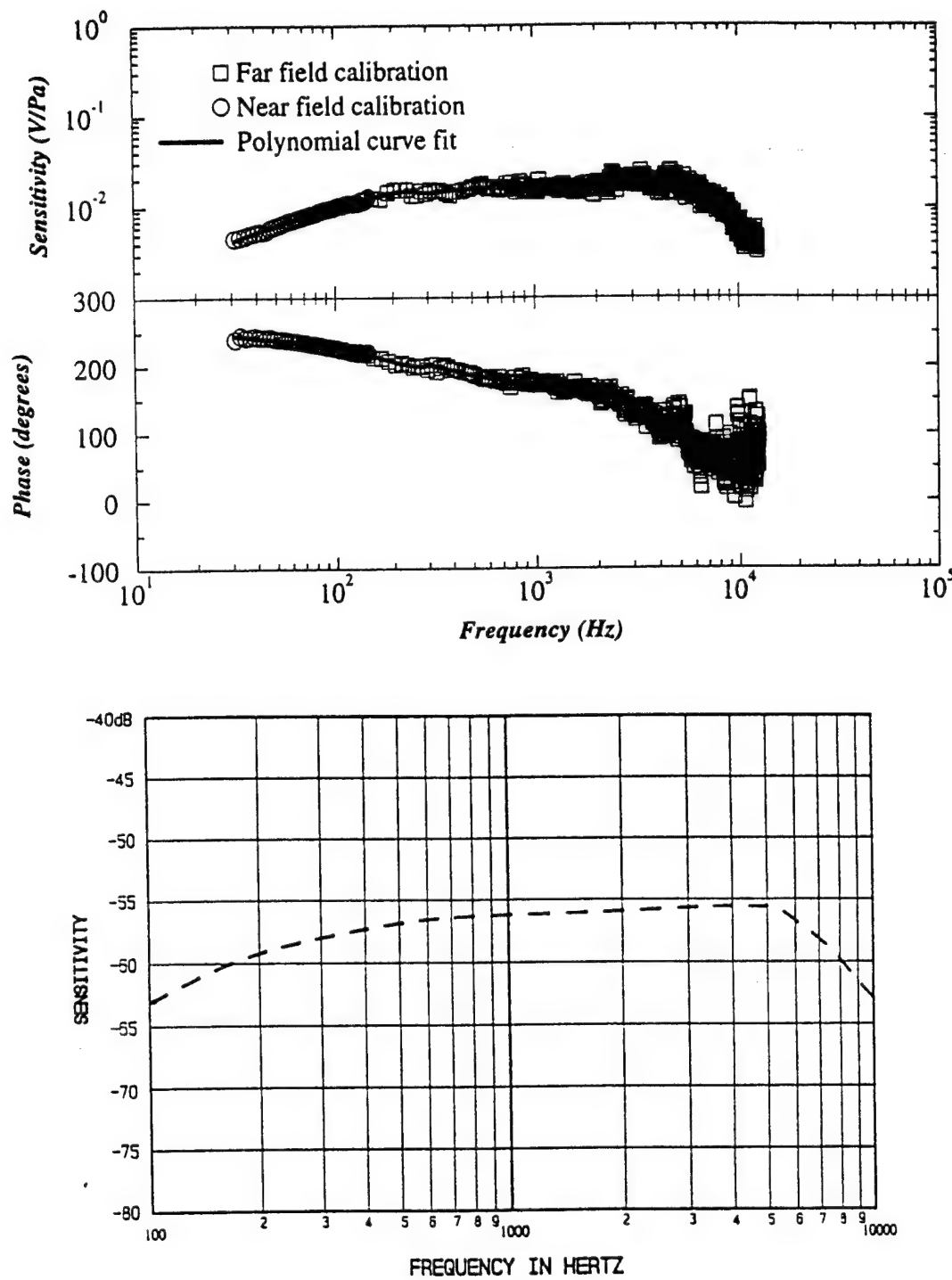


Figure 3.10 Typical Miniature Microphone Calibration Curve (Top) and Knowles Factory Calibration Curve (Bottom)

3.3.5 Noise Cancellation. The contribution of acoustic and electrical noise to measurements of pressure are removed using an optimal filtering technique developed by Naguib et al. (1995) and used by Gravante (1995). Briefly, the optimal filtering technique relies on the “noise” sensed by one microphone (active microphone) being correlated with the “noise” acquired by another microphone (noise cancellation microphone). If the two microphones are separated sufficiently far apart such that no correlation is expected from the turbulence itself then the noise which is common to both sensors can be removed to yield only the signal due to the wall pressure. For the present experiment the noise canceling microphone was placed a sufficient distance away in the spanwise direction. Referring to Figure 3.6 one can see the row for “noise-canceling” microphones.

The following test was conducted throughout the range of Reynolds numbers under consideration to validate the placement of the noise canceling microphone. Several time series from one given active microphone using different noise canceling microphones yielded nearly identical wall pressure statistics. This permits using just one noise canceling microphone in the row while maximizing the number of active microphones in the array to obtain the turbulent pressure field in the vicinity of the PIV picture. Since only 32 channels could be sampled simultaneously with the acquisition hardware, it was desired to maximize the number of active wall pressure sensors in the four rows close to the PIV realization.

An alternative technique commonly used entails digitally filtering the time-series data by applying a rectangular bandpass filter to remove acoustic and electrical noise (Snarski and Lueptow, 1995). The noise is assumed to lie within specified bands of frequency and applying this type of filtering eliminates the frequency information within these bands. However, the disadvantages of this technique are that part of the signal that is removed is likely to include both noise and turbulent wall pressure information alike.

3.4 Synchronization of PIV and Pressure Measurements

The instant in time at which the PIV picture is taken with respect to the measured pressure time series is determined by acquiring simultaneously the microphone voltage signals along with the output from the SRS timing box (which triggers the lasers) and the output from the camera shutter switch. Port A from the SRS box outputs a -3.5 Vdc pulse to the acquisition board every 0.102 sec (1/9.8 Hz) with a duration of 0.010 sec. The lead laser fires on the first, downward, leg of the -3.5 Vdc pulse. A 6 Vdc signal is wired through the camera shutter switch. When the shutter is closed the switch outputs a 0 Vdc signal to the A/D board, when the shutter is open the 6 Vdc signal is output. The time at which the first downward leg of the -3.5 Vdc pulse occurs inside the 6 Vdc pulse corresponds to the time at which the PIV picture was taken.

The camera shutter is triggered electronically through the first channel of the D/A system immediately before the acquisition routine is started. The camera shutter switch shorts, thereby opening the shutter and exposing the film, during acquisition by directing the D/A signal through a low pass filter which delays the shutter opening approximately 1.5 seconds. The net time of acquisition for the current experiments ranges between 3.9 and 12.8 seconds. The camera shutter setting is 0.1 ± 0.01 sec. In this time span only one downward leg of the pulse is expected. Post-processing of the acquired data determines the time when the first downward leg of the -3.5 Vdc pulse occurred while the camera shutter was open. In addition, the possibility that zero or two downward legs occurred during the camera shutter being open is checked for although for the shutter setting of 0.1 ± 0.01 sec this never occurred.

The flashing of the laser is not instantaneous but is subject to 180 μ sec time delay (Surelite, 1992). This delay was checked by simultaneously recording the laser trigger pulses and impact noise produced by the laser sheet on an object near the microphone array to corroborate the specified time delay. This was done prior to the experiments being performed.

3.5 Acquisition System

Acquisition of all signals was performed with a Kinetic Systems Corporation CAMAC mini-crate connected to a Silicon Graphics Indy workstation. Two 16-bit, 16-channel CAMAC 4008 digitizers (75 KHz maximum acquisition rate) are used in conjunction with one 4054 memory module (4Mbyte cache) and a 3660 external clock (with a maximum frequency of 10 MHz). The background electronic noise of the CAMAC crate limits the effective resolution to 12-bit. The maximum and minimum voltage range used for the present experiment was ± 10 Volts. In the present configuration, 102400 samples per channel, for 32 channels, (amounting to the upper limit of the memory module) are recorded. The workstation features 16 Mbytes of RAM, 32 Gbytes of memory and a 100 MHz IP22 processor.

The 32 channels are distributed as follows. Referring to Figure 3.6, CAMAC A/D channels 1-8 record eight microphones in row 1, channels 9-21 record all thirteen microphones in row 2, channels 22-29 record eight microphones in row 3, channel 30 records the noise-canceling microphone, and channels 31 and 32 record the laser and camera pulses respectively.

The frequencies of acquisition for $Re_\theta = 1520, 3950$ and 5720 are $8500, 16000$ and 26000 Hz respectively. These frequencies exceed by a factor of two those corresponding to non-dimensionalized $f^+ = 0.5$ required to resolve the small scales of motion. Power spectra calculations at $8500, 16000$ and 26000 Hz with and without filtering show identical results; thereby, ensuring that no aliasing of the data is present. Figure 3.11 shows voltage spectra for signals acquired with and without analog filtering at each of the above Reynolds numbers. The filtering consisted of low-pass filtering at half of the acquisition frequency. The spectra calculated from the microphones in the array are nearly identical as is illustrated from the data of two separate microphones displayed in Figure 3.11.

In addition to signal acquisition, a CAMAC 3116 16-bit, 8-channel DAC is used to output signals to trigger the camera shutter, a laser diode (which inscribes a reference line for alignment purposes on the film) and to monitor the on/off position of a solenoid valve in the flow seeding supply line.

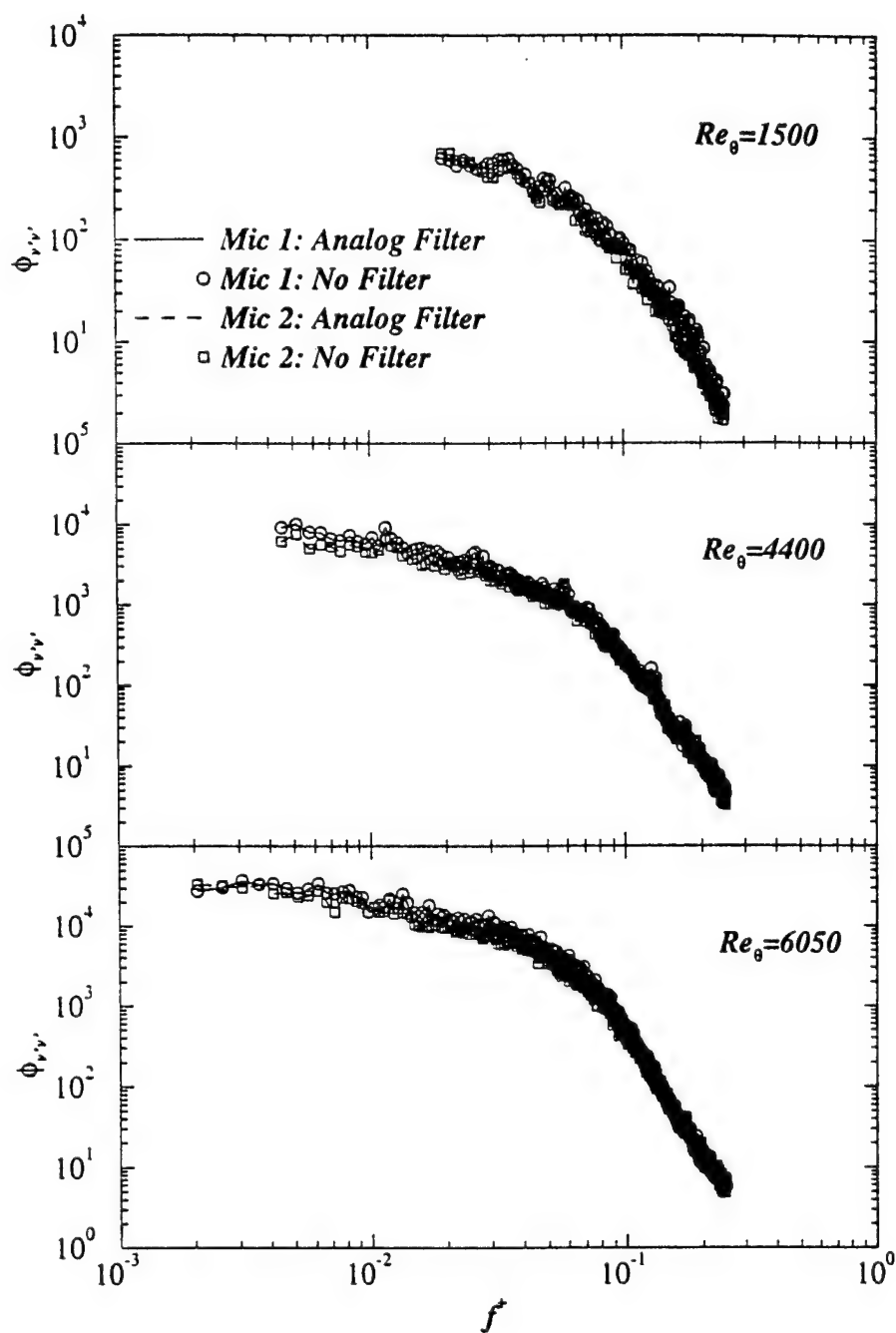


Figure 3.11 Voltage Spectra of Microphone Signals with and without Analog Filtering

CHAPTER IV

DATA PROCESSING AND ERROR ANALYSIS

4.1 PIV Data Processing

A general overview of the Particle Image Velocimetry set-up was presented under the Experimental Set-Up (Section 3.3). This section concentrates on details of the PIV interrogation and PIV data processing.

The analysis of one film negative encompasses 20,000 interrogation positions. Each negative is interrogated with overlapping spots as illustrated in Figure 4.1. The area of overlap is 50%. The spots are $1.09 \times 1.09 \text{ mm}^2$ with a spacing of 0.543 mm in flow field units between subsequent interrogations in both directions. A single interrogation is performed in 0.7 seconds. The interrogated PIV photograph extends 109 by 55 mm of the actual flow field in the streamwise and wall normal directions, comprising 200 and 100 vectors respectively. The non-dimensionalized extent of the velocity fields are $x^+ = 1460$, 3070 and 4390, and $y^+ = 730, 1535, 2195$ for the Reynolds numbers, $Re_\theta = 1520, 3950$

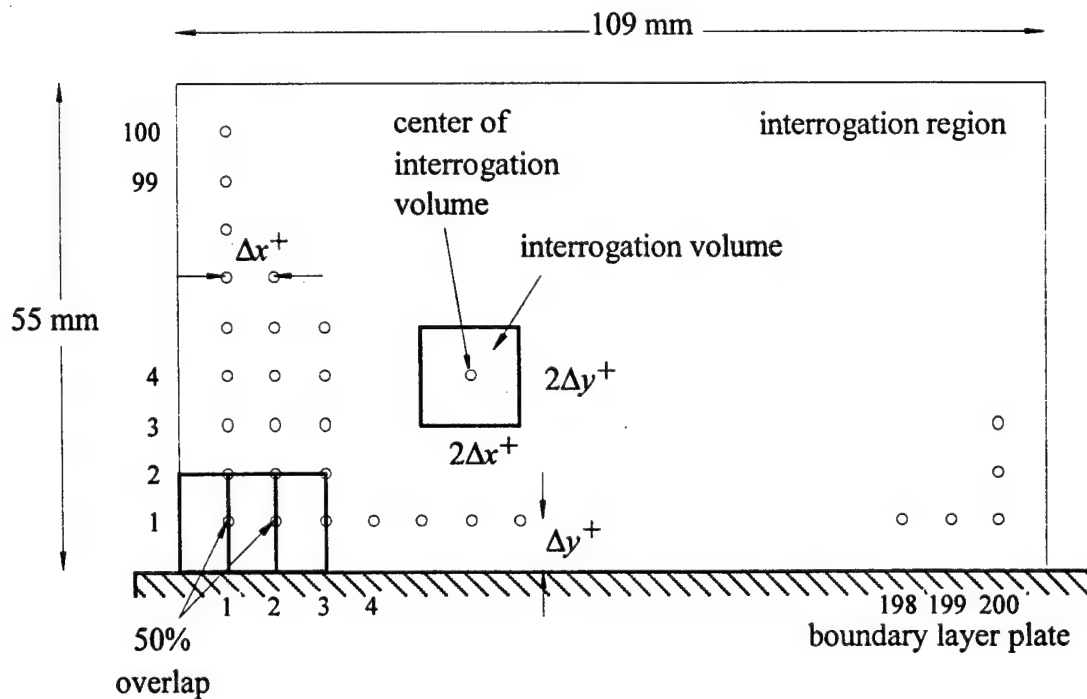


Figure 4.1 Description of Vector Field and Calculation

and 5790 respectively. The resolution in the vector fields are $2\Delta x^+ \times 2\Delta y^+$, where $\Delta x^+ = \Delta y^+ = 8, 16$ and 22 for the above Reynolds numbers. The timing between exposures (the time delay between the pulses from the two lasers) was $\Delta t = 55, 30$ and $20 \mu\text{s}$ ($\Delta t^+ = 0.24, 0.24$ and 0.12) for $Re_\theta = 1520, 3950$ and 5790 respectively. The maximum particle image displacement is about 0.36 mm based upon the maximum velocity expected in the flow field. The maximum velocity is estimated from the mean velocity profile, $\bar{U}(y)$, and the turbulent intensity profile, $u_{rms}(y)$, where the maximum fluctuations from the mean are on the order of $\pm 3u_{rms}(y)$. The number of particle pairs is about 15 in an interrogation spot and the imaged particle diameters are about $30 \mu\text{m}$. These settings are in accordance with the recommendations of Keane and Adrian (1990). The error in the displacement is 0.3 pixel which corresponds to 0.6% of the maximum particle image displacement (0.36 mm in this experiment). The error in the displacement is estimated by locating the centroid of the displacement with sub-pixel accuracy. The displacement of the correlation peak always covers more than one pixel and therefore its centroid may be determined resolving the displacement peak with sub-pixel accuracy. The justification for the rms error in the sub-pixel range is treated by Westerweel, 1993.

Reliable measurements were obtained for distances above 2 mm from the boundary layer wall. Close to the wall the distance between image pairs decreases and the images may overlap. In these cases it is not possible to distinguish the displacement peak from the self-correlated peak. Reliable measurements for the near wall region may have been obtained if an image shifting technique had been implemented or if Δt between the two laser pulses was increased. At the boundary layer interface, i.e. between the region of turbulent and non-turbulent flow, there exists occasionally freestream flow with relatively few seeding particles. The lack of sufficient particle pairs also decreases the number of good vectors obtained at y/δ values close to 1.

Consistent with other investigators experience, sufficient laser power, good laser-sheet/camera alignment and focusing, and proper uniform seeding result in good vector

fields. Occasionally, "noise" within the interrogation volume results in an incorrect determination of the velocity vector. This "noise" can be the result of insufficient particle pairs, shadows or glare on the photograph, etc. Consequently, the second and third highest peak in the autocorrelation field may correspond to the actual velocity. To replace or remove any erroneous vectors, a systematic analysis of the raw data is performed and is presented below.

4.1.1 Vector Clean-up Routine. The methodology to establish that a vector is potentially erroneous consists in comparing the vector with global and localized statistics. The method is highly effective when the number of bad vectors in the field is limited to approximately 5%. The cleaning of vector fields with an excess number of bad vectors is highly unreliable and should be avoided.

The line average, $\bar{U}(y)$ and $\bar{V}(y)$, and standard deviation, $u_{rms}(y)$ and $v_{rms}(y)$, profiles are calculated from the raw data and are used in the evaluation of each vector. Vectors with uncommonly large magnitudes are identified when either the u or v component exceeds a specified threshold, k_g , of standard deviations from the mean; that is,

$$\begin{aligned} |u(x, y) - \bar{U}(y)| &> k_g u_{rms}(y) \\ |v(x, y) - \bar{V}(y)| &> k_g v_{rms}(y) \end{aligned} \quad (4.1)$$

When a vector exceeds either of these criteria, local statistics are performed that consist in calculating 1) the standard deviation of the group of vectors formed by the bad vector and its eight neighbors ($N = 9$) for each velocity component, u_{std} and v_{std} , and 2) the group median velocities u_{median} and v_{median} . The median value is the middle value of the N element sequence when organized in increasing or decreasing order. Vector components of successive correlation peaks in the auto-correlation field are compared to the respective median value to see if they are within a reasonable local threshold, k_l ; that is,

$$\begin{aligned} |u - u_{median}| &< k_l u_{std} \\ |v - v_{median}| &< k_l v_{std} \end{aligned} \quad (4.2)$$

If both criteria are met the vector components of the correlation peak are used to determine the velocity vector. If neither the second or third correlation peak give vector components that meet the criteria of Eqn. 4.2 the median value, $\vec{V} = u_{median}\hat{i} + v_{median}\hat{j}$, is used to replace the bad vector. This first step in the cleaning process minimizes the effect of these few bad vectors on the overall statistics, which are recalculated after the bad vectors are replaced. In the present study $k_g = 3.5$; for a normal distribution this corresponds to a 99.95% probability that a vector will fall within this deviation. The local threshold chosen to identify large localized deviations is $k_l = 2.5$.

The second step in the cleaning process considers a vector, $\vec{V} = u\hat{i} + v\hat{j}$, and its eight neighbors. These are grouped together to yield an updated localized standard deviation for each of its components, u_{std} and v_{std} , and updated group median velocities, u_{median} and v_{median} . The vector components are compared to the respective median value to see if they are within k_l of the standard deviation according to the inequality of Eqn. 4.2. If either u or v components exceed the threshold, the second correlation peak is examined. The second peak is kept if both components meet the criteria. If they fail to meet it, the third correlation peak is examined. Finally if the third velocity fails to meet the criteria, the median vector, $\vec{V} = u_{median}\hat{i} + v_{median}\hat{j}$, is substituted. The threshold value is chosen to identify only large localized deviations. In the present measurements, $k_l = 2.5$ gives an optimum cleaning.

The use of the median versus the group mean significantly improves the process. Spurious data generally have large deviations from the expected value: the group mean therefore would be skewed by the value of any one spurious element. On the other hand, the group median in general takes on the value of one of the “good” elements in the sequence. Typically the number of erroneous vectors is on the order of 2%; a fraction of these (on the order of 40%) are corrected by replacement with the second and third correlation peaks. Figure 4.2 shows (a) the velocity corresponding to the first correlation peak and (b) the velocity field after processing with the vector clean-up routine. The methodology above is similar to that used by Westerweel (1993) and Meinhart (1994), who

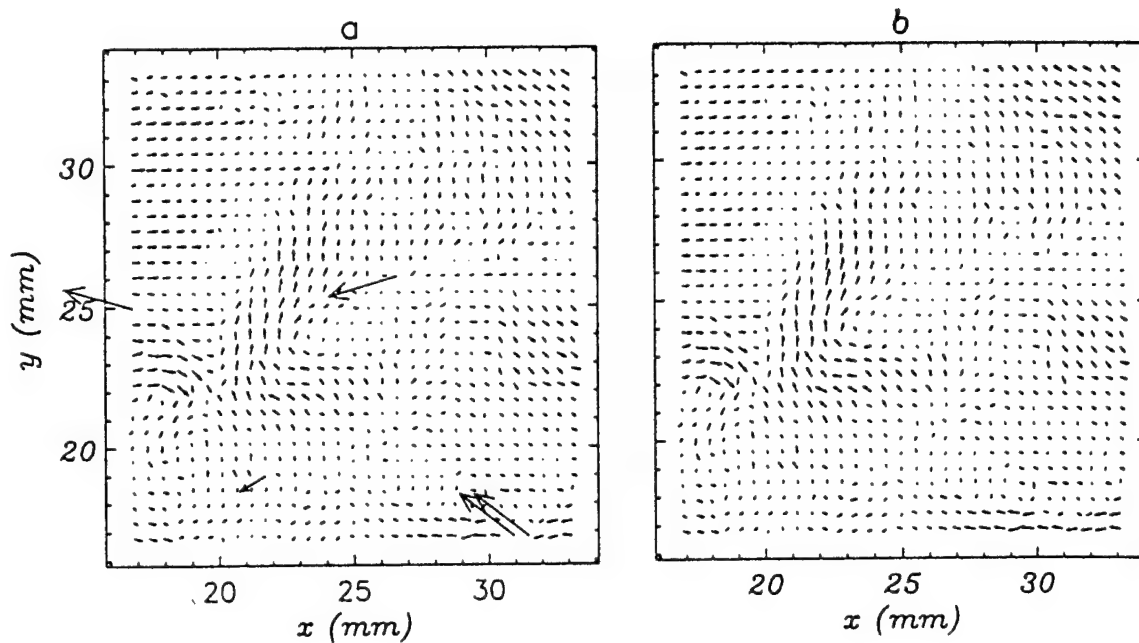


Figure 4.2 Vector Fields, (a) Raw Data and (b) After Clean-up Routine

alternatively use the mean or median, as well as a low pass filtering scheme to clean-up the velocity field.

4.2 Mean and RMS Velocity Profiles

Measurements of velocity and pressure are performed at three Reynolds numbers, at a streamwise location of $x = 3.25$ m from the leading edge of the boundary layer test plate. These and corresponding boundary layer parameters are summarized in Table 4.1. Evaluation of freestream velocity and momentum thickness is done from boundary layer profile measurements with a hot-wire. Estimates of friction velocity are found from the non-dimensionalized mean velocity profiles obtained with both hot-wire and PIV measurements; the percent difference between the two ranges from 5 to 10%. The momentum thickness is evaluated using a hot-wire since the PIV realizations provide valid data only up to $y \approx 50$ mm which is less than the boundary layer thickness. Additionally, Table 4.1 shows the number of PIV realizations used at the respective Re_θ in the determination of u_r .

Table 4.1 Range of Flows

Re_θ^a	U_∞^a m/s	u_r^b m/s	δ^a mm	θ^a mm	no. of PIV realizations
1520	4.9	0.20	51	5.3	32
3950	10.0	0.42	56	6.4	98
5790	14.9	0.60	56	6.4	58

^a based on hot-wire data^b based on PIV data

The hot-wire time-series were processed to obtain profiles of the average velocity, $\langle U(y) \rangle$, and rms of the streamwise velocity fluctuations, $u_{rms}(y)$. Figure 4.3 shows mean velocity and turbulent intensity profiles plotted on a semi-log axis when scaled using wall variables for all three Reynolds numbers tested compared with the log law.

The PIV measurements consist of a large number of realizations (see Table 4.1) at each of the above test conditions. The line averaged streamwise velocity profile calculated from all realizations at a given Reynolds number, $\bar{U}(y)$, is subtracted from each individual realization to find the corresponding fluctuating velocity field, $u'(x,y) = u(x,y) - \bar{U}(y)$. Profiles of line average and rms of streamwise velocity at each Reynolds number are shown in Figure 4.4 and compared with hot-wire measurements. PIV and hot-wire data are consistent with one another except near the wall. As discussed in the previous section, close to the wall the separation between doubly exposed particles is small and makes the PIV vector calculations suspect.

4.3 Velocity, Vorticity and Reynolds Stresses

The instantaneous PIV velocity fields are commonly represented by either the fluctuating component obtained through conventional Reynolds decomposition, or by subtracting a constant velocity, the value of which could represent the convection velocity of the coherent structure present at that instant; for example,

$$u'(x,y) = u(x,y) - \bar{U}(y)$$

or

$$u'(x,y) = u(x,y) - U_c$$

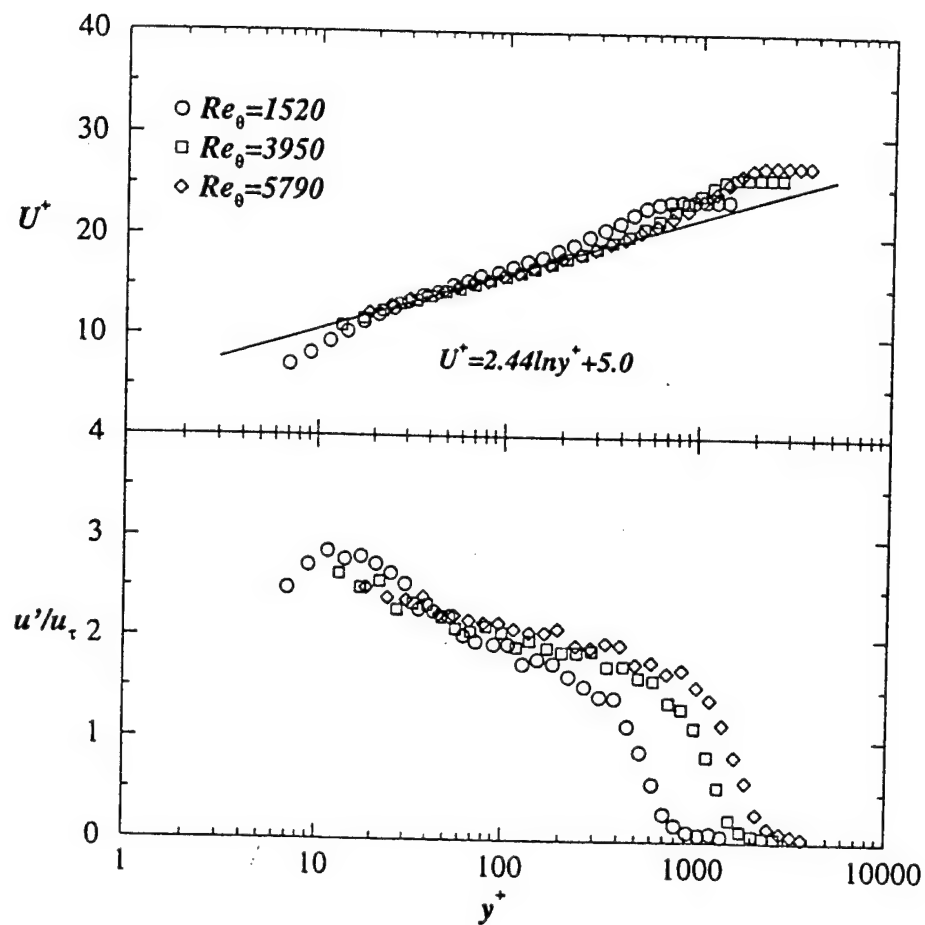


Figure 4.3 Wall Scaling of Boundary Layer Mean (top) and Turbulent Intensity Profiles (bottom)

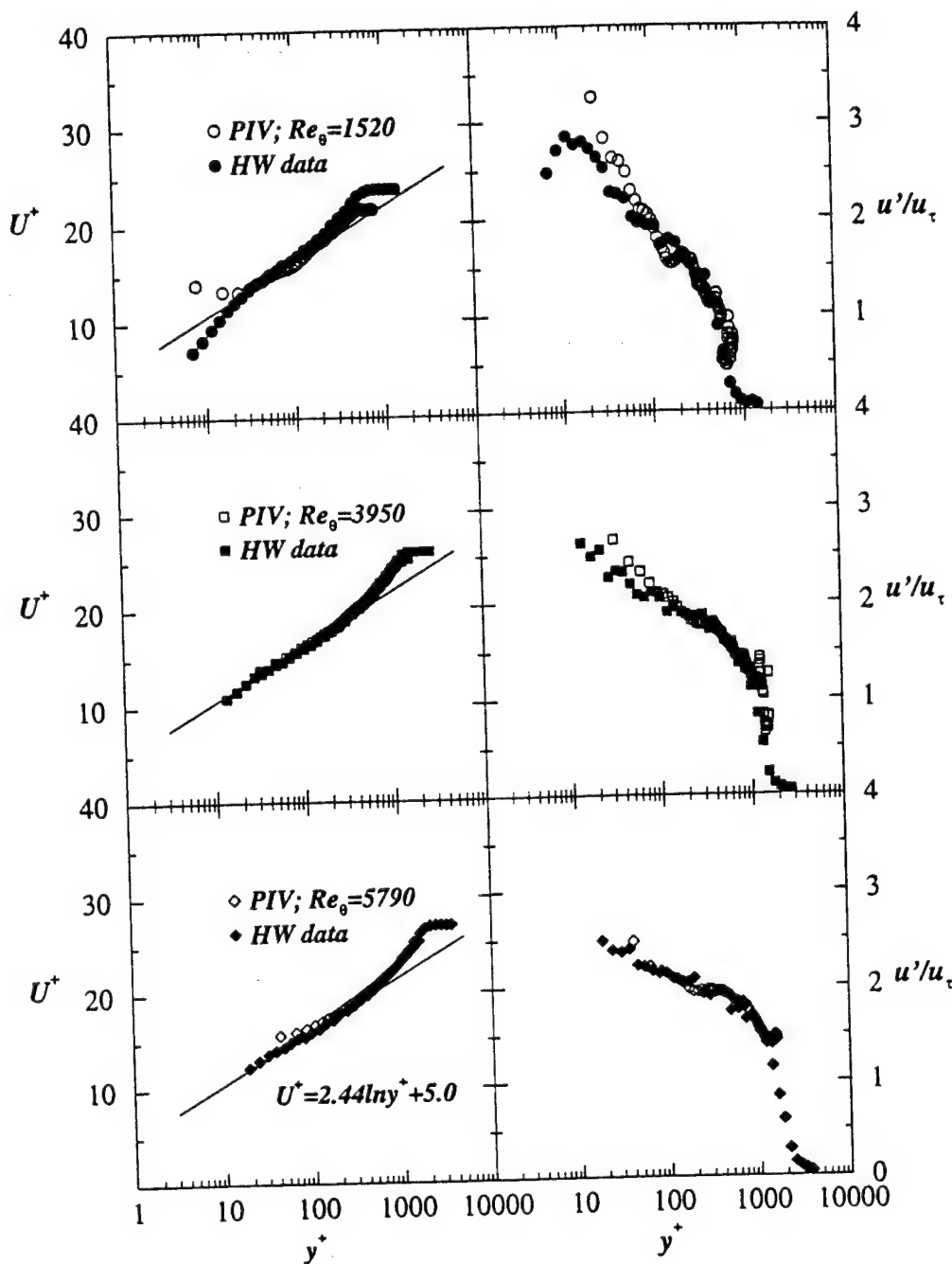


Figure 4.4 Line Average and RMS Profiles

Figure 4.5 shows a sample of fluctuating velocity fields corresponding to convection velocities of $0.7U_\infty$, $0.9U_\infty$ and Reynolds decomposition for $Re_\theta = 3950$. The correct choice for U_c may be used to show distinct clockwise roll-up structures which fit the descriptions of hairpin vortices, where U_c is an approximation of the convection velocity of these structures. The fact that another choice of U_c shows similar structures at other locations suggests that a hierarchy or array of hairpin vortices exist. The Reynolds decomposition typically highlights the same coherent structures that would be brought about by several choices of U_c . In this work, most velocity fields are considered using Reynolds decomposition (it provides a depiction of the turbulent field which is standardized and can be compared with previous investigations that have used standard Reynolds decomposition) though at times the use of U_c is introduced.

Meinhart and Adrian (1995) showed the existence of uniform regions of streamwise momentum in the instantaneous x - y plane of a zero pressure gradient turbulent boundary layer when the flow field was viewed from a moving reference frame or convection velocity. The zones of nearly constant streamwise momentum occur in the wall region, the logarithmic layer and the wake region. The authors conclude that the zones are separated from each other and from the free stream by thin viscous shear layers that contain concentrations of spanwise vorticity. They suggested that the large, nearly constant streamwise momentum structures are created by the alignment of wall vortices and the interaction between them. Instantaneous PIV realizations of the u - v components of the velocity field in the x - y plane reveal the near-wall viscous-inertial layer filled with inclined vortex structures that extend well into the logarithmic layer. The authors indicated that coherent regions of high and low speed fluid are inclined with respect to the wall which is sufficient to transport over one-half of the momentum.

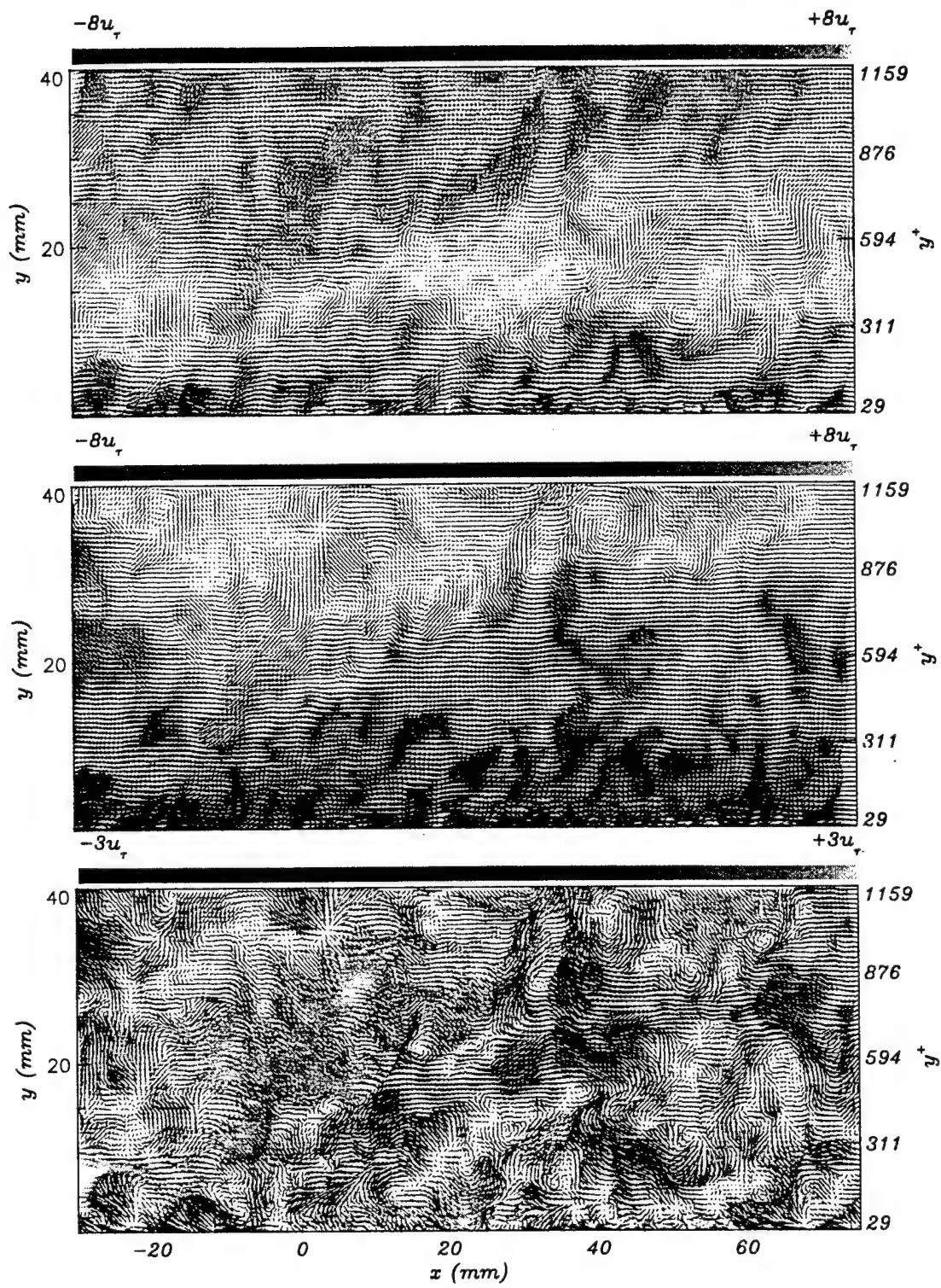


Figure 4.5 Fluctuating Velocity Fields: Top, $U_c = 0.7U_\infty$; Middle, $0.9U_\infty$; Bottom, Reynolds Decomposed. $Re_\theta = 3950$

For this investigation the primary tool for the study of turbulent structures is based on the velocity fields. Velocity fields give a picture of the instantaneous flow patterns, which will later be associated with the wall pressure. A secondary representation of the flow field is obtained by calculating the corresponding vorticity and Reynolds stress fields. Vorticity, from the total and fluctuating components of the velocity vectors, is calculated both through the derivative of the velocity field, and through Stokes' theorem which relates the circulation around a closed contour to the sum of vorticity enclosed within the contour. The total and fluctuating velocity components give different vorticity results arising from the steep velocity gradient near the wall. The calculations included here and in later chapters are based on the total velocity field (see Westerweel, 1993). The integral method yields,

$$\Gamma = \oint_C \vec{V} \cdot d\vec{s} = \int_A \omega_z dA \quad (4.3)$$

$$\oint_C \vec{t} \cdot \vec{V} ds$$

or,

$$\omega_z = \lim_{S \rightarrow 0} \frac{\Gamma}{S} \quad (4.4)$$

where C denotes the contour taken along the 8-connected neighborhood of data point (i,j) as shown on Figure 4.6 and S is the area enclosed.

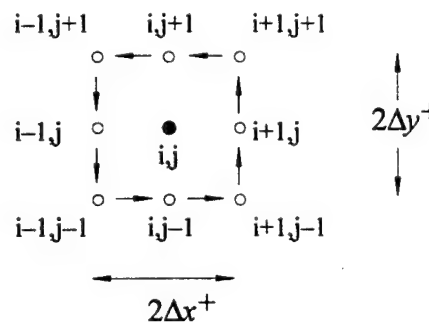


Figure 4.6 Contour of Integration around Data Point (i,j)

The derivative methods yields,

$$\omega_z = \frac{\partial v}{\partial x} - \frac{\partial u}{\partial y} \quad (4.5)$$

Based on the number of data points involved a central first-order derivative is expected to amplify the noise of the measured data (Westerweel, 1993) when calculating ω_z using equation 4.5. Calculations presented hereafter are based on the circulation, where the vorticity at a given vector location is calculated from its eight neighboring velocity vectors. Figure 4.7 shows, for the same flow field of Figure 4.5, total (top) and fluctuating (middle) vorticity fields non-dimensionalized using inner variables, $\omega^+ = \omega v / u_\tau^2$; the bottom plot shows the corresponding instantaneous non-dimensionalized Reynolds-stress field $u'v'/u_\tau^2$.

4.4 Pressure Profiles in Space

The instantaneous pressure distribution is resolved by concatenating the microphone signals in a given row (see Figure 3.5 in Section 3.3). The separation between microphones in non-dimensionalized wall variables is $\Delta x^+ = 53, 112$ and 160 for $Re_\theta = 1520, 3950$ and 5790 respectively. In an attempt to resolve $p(x; t)$ under the PIV realization the “frozen-flow” assumption is used. The accuracy of this frozen-field assumption increases as the distance between the microphones (Δ) decreases. A convection speed, U_c , is calculated by correlating two adjacent microphone signals over a specified time increment which is kept small, on order of $\Delta/0.6U_\infty$, to assure a local convective speed. The assumption of $0.6U_\infty$ is based on a common convection speed of wall pressure structures reported by Eckelmann (1990). On the other hand, a longer time increment, on the order of $3\Delta/U_c$, yields a higher correlation coefficient but loses the small scale or local character of the computation. The wall pressure profile $p(\Delta x)$ centered about a microphone for a given time, t_o , is calculated by applying the frozen field assumption on the time series immediately preceding and following the time t_o . That is,

$$p(\Delta x_j; t_o) \approx p((t_j - t_o)U_c) \quad (4.6)$$

where t_j represents the discrete times the microphone signal was acquired and Δx_j would range from $-\Delta/2$ to $+\Delta/2$.

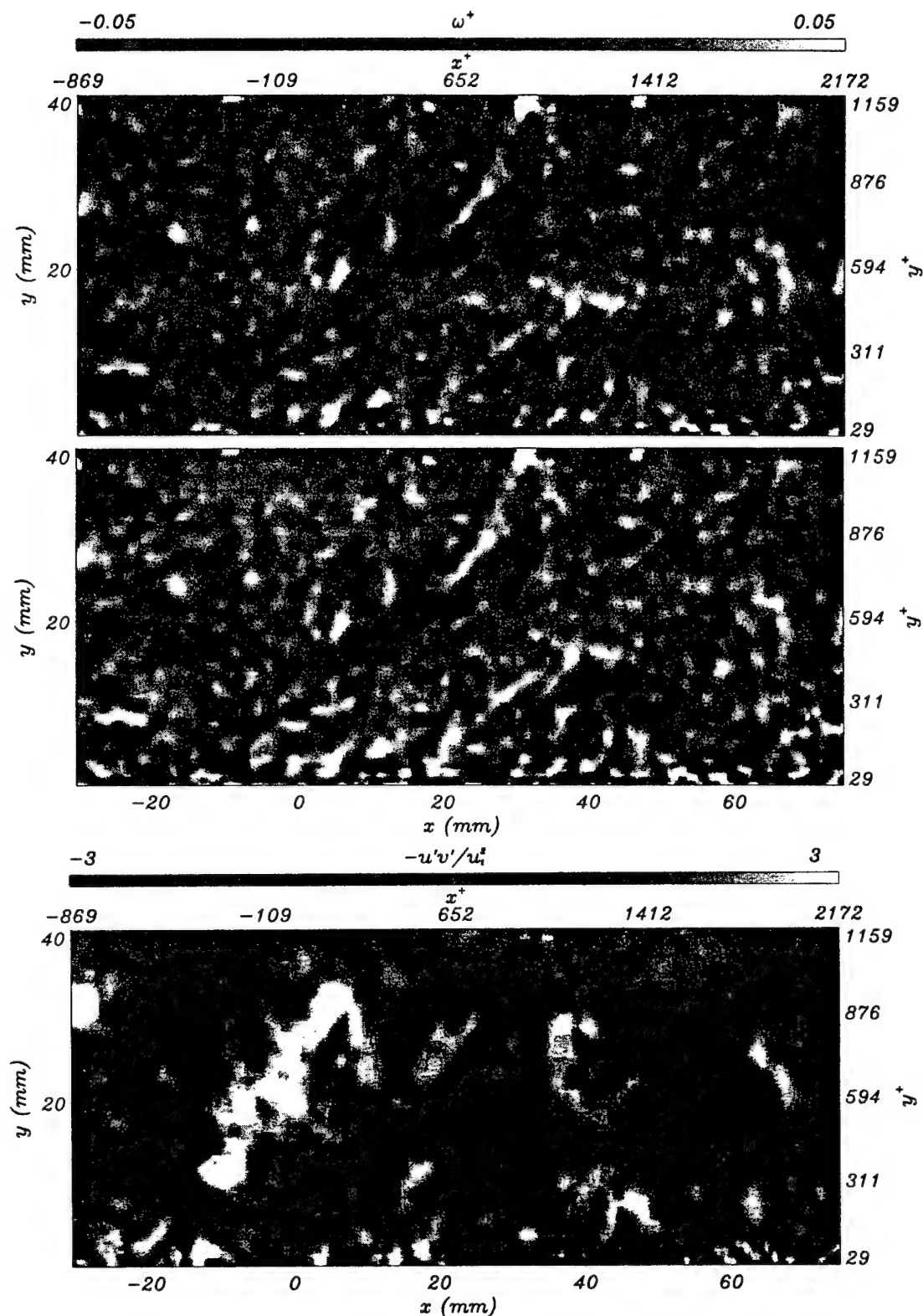


Figure 4.7 Total (Top) and Fluctuating (Middle) Non-dimensionalized Vorticity Fields $\omega^+ = \omega v / u_r^2$ and Reynolds Stresses $u'v'/u_r^2$ (Bottom) for the Instantaneous Flow Field of Figure 4.5

Generally the resulting profile exhibits minor discontinuities where the individual segments are connected to one another, that is, half way between the microphones at $\Delta x_j = \pm \Delta/2$. An effective method to remove these discontinuities consists in curvefitting the concatenation profiles. A total of $n-1$ curvefits are performed in a row with n microphones. The curvefit spans Δ , from one active microphone location to the next and eliminates the discontinuities which occur half-way between the microphones, while faithfully preserving the pressure profile in the immediate vicinity of the microphones. In the case of the first and last microphones the curvefit extends $-\Delta$ to $\Delta/2$ and $-\Delta/2$ to Δ referenced to each microphone respectively. This is illustrated in Figure 4.8.

The microphone locations are indicated by an arrow. Three rows of microphones, each showing the concatenated profile, with and without curvefit are indicated. The middle row carries the greatest number of microphones, minimally spaced, and the pressure profile is well concatenated. The profile before and after the curvefit are nearly identical. The offset rows have less microphones and larger deviation between the simple and curvefit concatenation. In the present case, the middle row of microphones consists of 13 microphones separated each by 3.886 mm, sufficient to resolve the pressure profile at the three Reynolds numbers tested here. The extreme rows contain eight active microphones each (due to limitations on the acquisition system); the largest distance between two microphones is 7.772 mm.

Figure 4.9 illustrates the limitations of Taylor's hypothesis or frozen flow assumption. The figure contains seven plots, each plot containing one time signal corresponding to the microphone indicated by the arrow. A convection velocity of $0.6 U_\infty$ was used to convert the time series to a spatial profile. This profile is compared with the concatenated profile obtained from the thirteen microphones as described above. The figure clearly illustrates the pressure signal is "nearly-frozen" only over a small convecting distance. In the present experiment data was processed from a row of microphones in which signals were acquired from all microphones in the row.

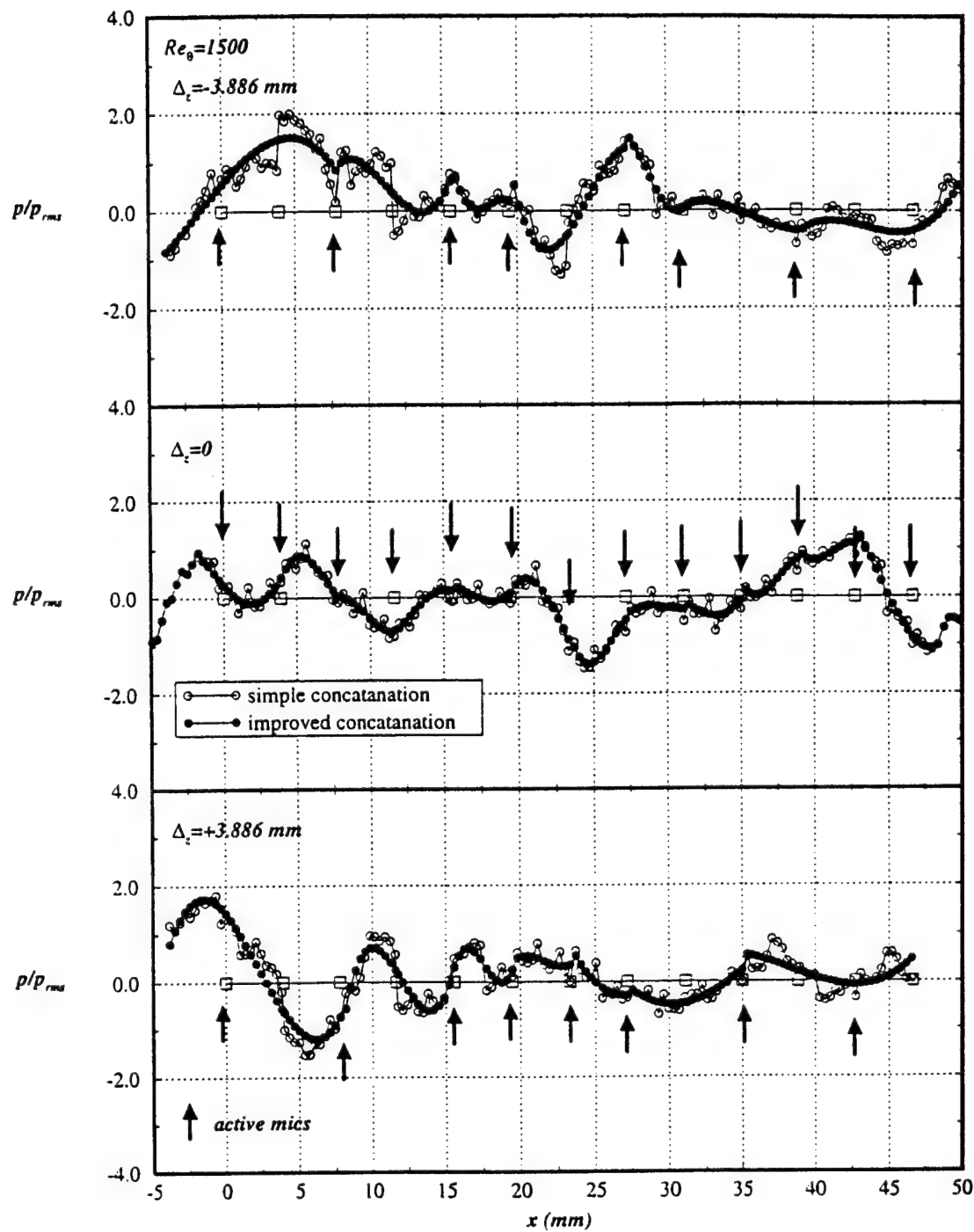


Figure 4.8 Simple and Improved Concatenation for Three Rows of Microphones.

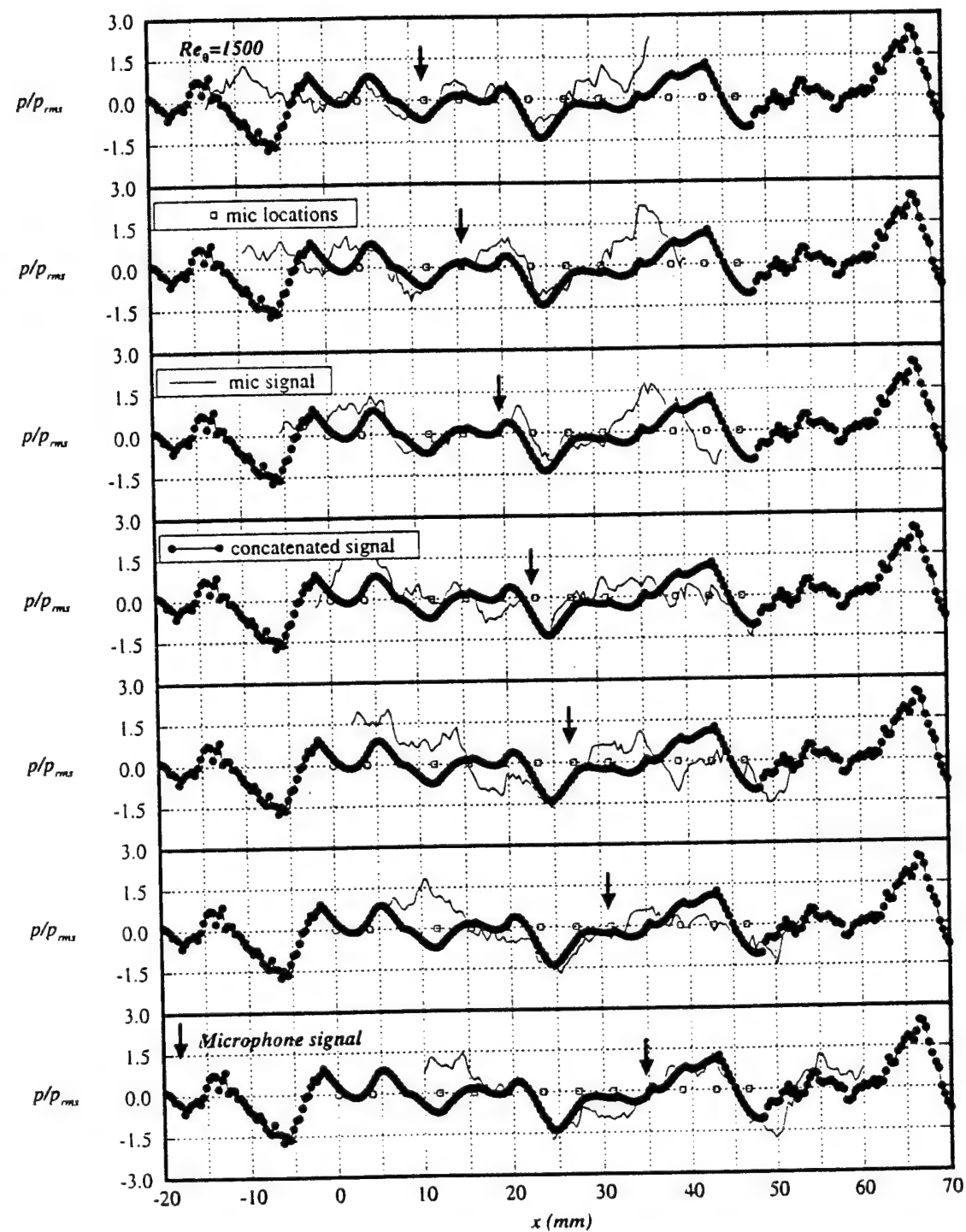


Figure 4.9 Taylor's Hypothesis versus Spatial Distribution of Pressure

Since the pressure measurements consist of a long time series, a time history of the concatenated spatial evolution of wall pressure is reproduced signaling the formation and dissipation of pressure structures in the streamwise location. Interesting to study in itself, it takes on special significance when compared to an instantaneous velocity field. A sample is illustrated in Figure 4.10 for $Re_\theta = 3950$ where the gray level corresponds to the magnitude of the fluctuating pressure. The inclination of the “structure” in the plot would provide the convection velocity. These figures will be discussed and related to the PIV realizations in Chapter 5.

4.5 Conditional Averages and Spectra of Pressure

The quality of the concatenation, by which individual microphone signals $p'(t;x)$ are combined to reproduce the wall pressure $p'(x;t)$, is estimated by comparing statistical quantities calculated from individual microphones and from the concatenated signal itself.

The character of the wall pressure is often represented through a large amplitude peak detection scheme. In a single point pressure measurement both positive ($p' \geq \kappa p_{rms}$) and negative ($p' \leq -\kappa p_{rms}$) events are identified occurring at times $t = t_i$. Where several data points consecutively exceed the threshold, the detection point corresponds to where the pressure magnitude is maximum, $t = t_{i*}$. The conditional average of the pressure is determined by averaging around the detection point: $\langle p'(\tau) \rangle = \sum_1^N p'(t_{i*} + \tau)$, where N is the number of detections, $-\tau_o \leq \tau \leq +\tau_o$, and τ_o is sufficiently large to resolve the integral scales of motion.

This conditional averaging is performed on both the time series from a given microphone, $p(t;x)$, and on the concatenated pressure series of the middle row of microphones, $p(x;t)$. For the case of the concatenated signal, large peaks are detected from a continuous sequence of 60,000 wall profiles (stored each in 72 MB files, 300 times the size as the sequence record of Figure 4.10); independent peaks are identified and centered about their local maximum or minimum, now referenced to $t^+ = 0, x^+ = 0$, and averaged.

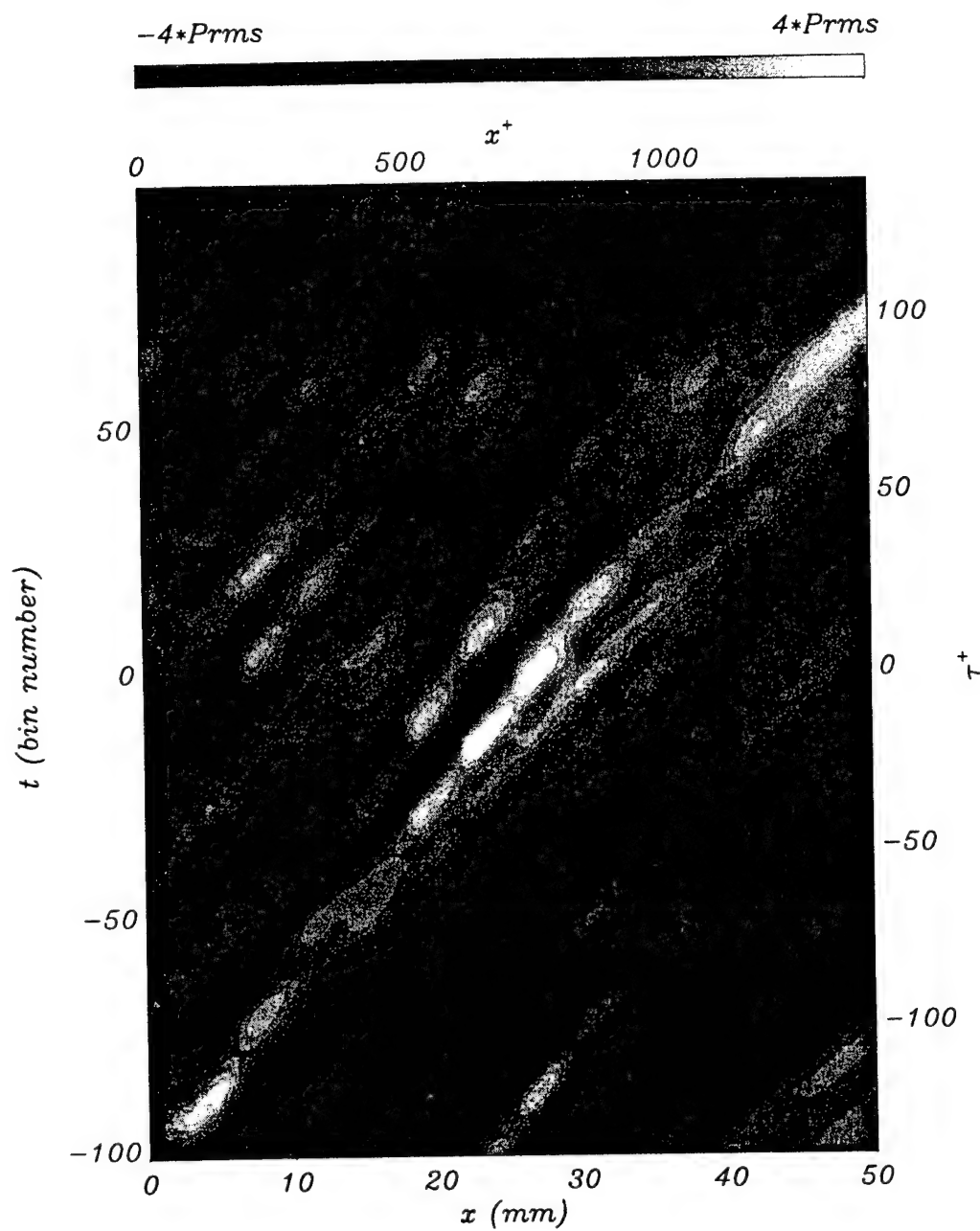


Figure 4.10 Time Evolution of the Wall Pressure

The threshold level is $\kappa = 2.5$. Figure 4.11 shows the comparison between the conditional pressure field from a single microphone, $\langle p'(\tau) \rangle$, and that calculated from the concatenated profile, $\langle p'(x^+ = 0, \tau) \rangle$. The conditional average from both calculations are nearly identical.

The quality of the concatenated signal is also considered by comparing the energy content calculated from a single microphone and from a long sequence of the concatenated wall pressure at an arbitrary x location. The power spectra is calculated as,

$$\phi_{p'p'}(f) = \frac{P * P^*}{\Delta f} \quad (4.7)$$

where P is the Fast Fourier transform of pressure $p'(t; x)$ (single microphones) or $p'(x; t)$ (concatenated signal), and P^* is its complex conjugate. The spectra non-dimensionalized with inner variables yields,

$$\phi_{p'p'}^+ \left(f^+ = f \frac{V}{u_r^2} \right) = \phi_{p'p'}(f^+) \frac{u_r^2}{\tau_w^2 V} \quad (4.8)$$

Figure 4.12 shows the power spectra calculated for the time series from a given microphone and for the concatenated signal. Data are displayed for frequencies greater than 40 Hz (lower limit of the microphones) and up to $f^+ = 0.25$, above which the contribution to the energy in the signal is negligible. Both signals show very good agreement for all Reynolds numbers thus verifying there is no loss of energy in transposing the data from individual microphones to the concatenated signal.

4.6 Spatial Filtering and Spectra of Pressure

Spectra calculations, shown in Figure 4.13, based on the concatenated pressure signal shows for $Re_\theta = 1520$ and 3950 the predominance of an extraneous wave number corresponding to the distance between microphones, $k_c = 1/\Delta$ ($\Delta = 3.886$ mm). The extraneous wave number appears as a certain waviness in the concatenated profiles and can be seen in Figure 4.10.

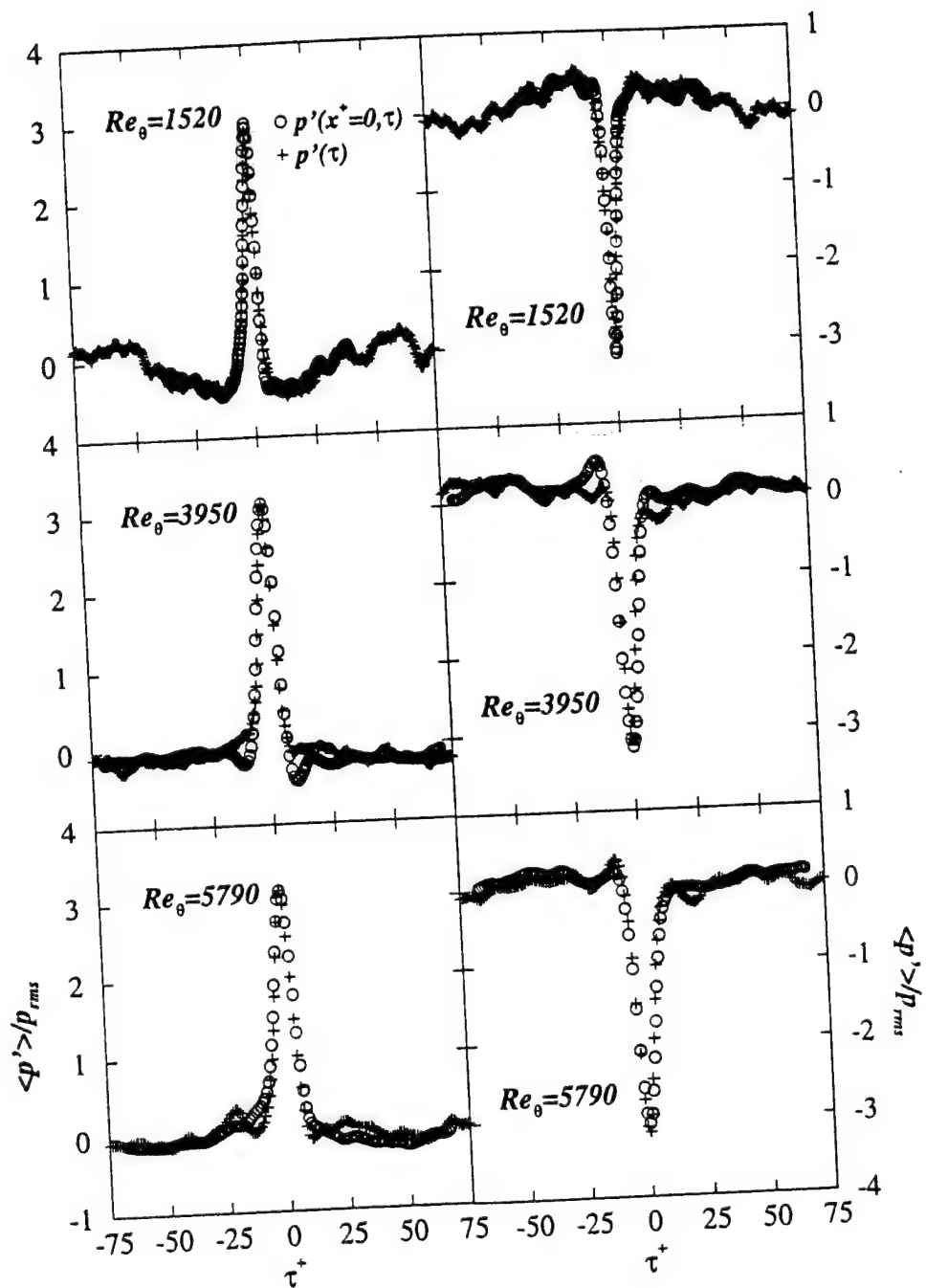


Figure 4.11 Conditional Average of Pressure for Positive ($p' \geq \kappa p_{rms}$) and Negative ($p' \leq -\kappa p_{rms}$) Events for an Individual Microphone, $\langle p'(\tau) \rangle$, and for the Concatenated Wall Pressure Signal, $\langle p'(x^+ = 0, \tau) \rangle$; $\kappa = 2.5$

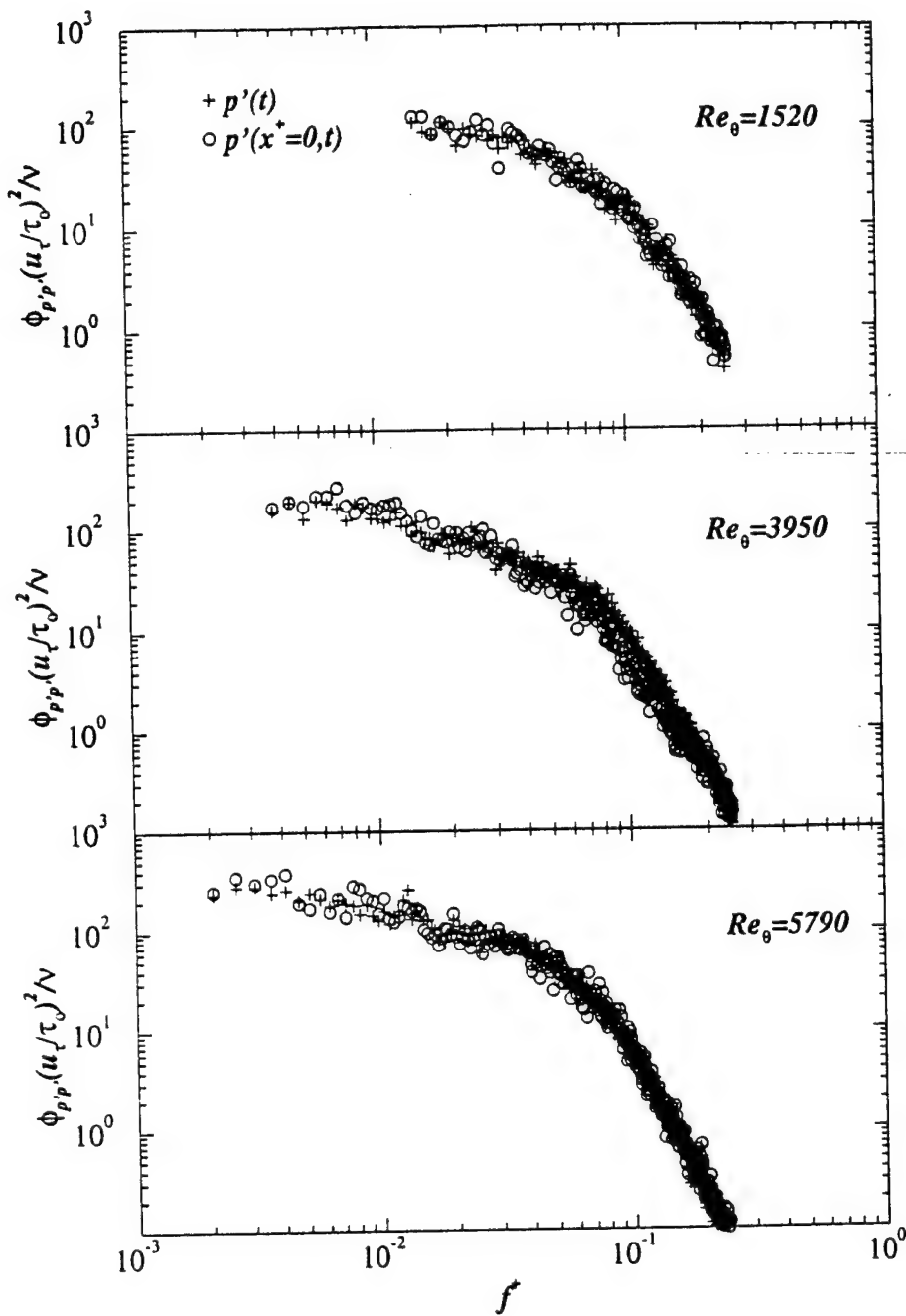


Figure 4.12 Power Spectra of Pressure for an Individual Microphone, $\phi_{p'(\tau)p'(\tau)}$, and for the Concatenated Wall Pressure Signal, $\phi_{p'(x^+ = 0; \tau)p'(x^+ = 0; \tau)}$

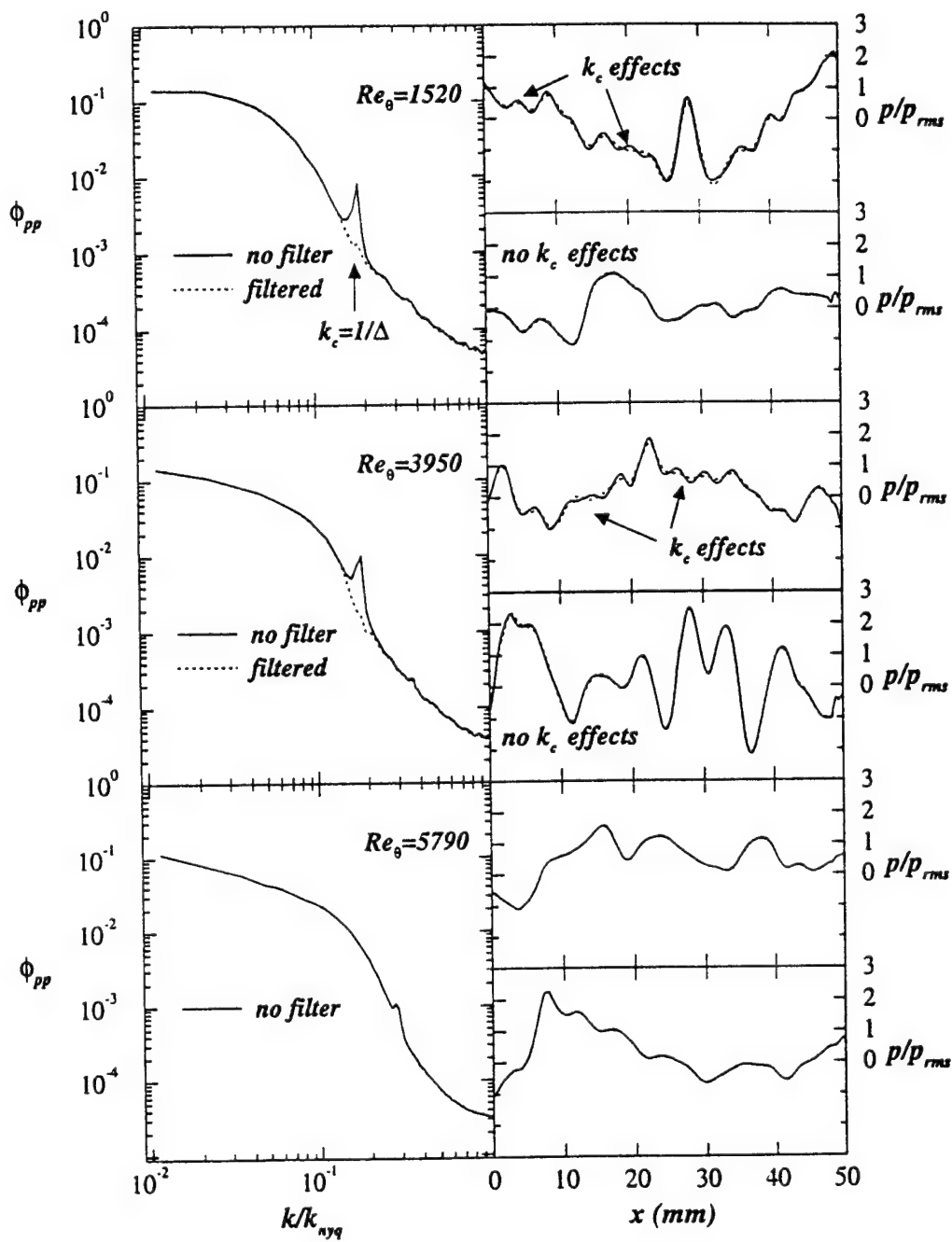


Figure 4.13 Power Spectra of the Concatenated Spatial Pressure Profiles with and without Filtering

Physically it is a result of failing to calculate the correct local convection velocity between two adjacent microphones as well as relying on Taylor's hypothesis which assumes the flow to convect without changing. Section 4.4 pointed out the difficulties in calculating local convection velocities —mostly arising from the short time sequences requirements. The extraneous wave number does not appear in the higher $Re_\theta = 5790$.

The digital filter applied is a Finite Impulse Response type (finite number of coefficients, zero time delay). The filter coefficients, $h(n)$, are obtained from a filter design software (McClellan et al., 1972) where the number of pass bands and cut-off frequencies are specified. The values for low and high cut-off k/k_{nyq} values are 0.165 and 0.192 respectively. The number of filter coefficients M is 51. The filtered profile is obtained by the convolution,

$$\tilde{p}(n) = \sum_{k=-(M-1)/2}^{k=(M-1)/2} h(k)p(n-k) \quad (4.9)$$

To ensure that no distortions are introduced into the resulting signal, the filtered spatial spectra and the concatenated profile before and after filtering is examined. Spectra and sample of pressure profiles are shown in Figure 4.13.

CHAPTER V

INSTANTANEOUS VELOCITY AND PRESSURE FIELDS AND TEMPORAL EVOLUTION OF PRESSURE STRUCTURES

Independent instantaneous pictures of the two dimensional velocity field in the xy plane are combined with wall pressure measurements to address some of the fundamental issues of turbulence, those concerning its production, sustenance, transport and dissipation.

Realizations where the level of activity involves a characteristic pressure signature at the time the instantaneous velocity field is recorded on film are selected and presented in this chapter. Instantaneous pressure and velocity fields are combined and shown alongside each other in the following set of figures. Accompanying each PIV realization is the corresponding instantaneous wall pressure profile. A detail of the same PIV realization (the region immediately above the microphones) is then shown accompanied by the time evolution of the wall pressure. A brief summary of the relationships documented in Chapter 2 between the wall pressure and the velocity field is given below; they are instrumental in that they provide average relations between pressure and velocity events which are helpful when examining the instantaneous fields. An outline of the goals precedes the selected images and discussion on the instantaneous character of the turbulent boundary layer flow.

5.1 Review of Conditional Pressure and Velocity Calculations

Conditional averaging results are used to consider separately, prominent positive and negative pressure peaks and how these are correlated to the velocity field.

Based upon previous investigators (Langeheineken, 1981, Thomas and Bull, 1983, Johansson et al., 1987, Snarski and Lueptow, 1995, Jukenhoefel, 1995) large positive pressures are associated with the presence of a convecting, inclined shear layer with high momentum flow upstream of flow with momentum deficit. Conditional averaging and

other statistical tools (e.g. stochastic estimation, Variable Integral Time Average) show that the location of the shear layer near the wall roughly coincides with the streamwise location point of positive pressure detection.

No clear consensus exists among the above investigators in regards to large amplitude negative pressures. Measurements from Juckenhoefel (1995) show that large amplitude negative pressure events are associated with an inclined shear layer; the streamwise location of the shear layer occurs downstream of the negative pressure detection point. Additionally, a small region of fluid with streamwise momentum deficit is appreciable in the near vicinity of the negative pressure detection point.

5.2 Present Goals

A typical turbulent flow can vary significantly from one realization to another. Ideally, the three dimensional, time varying velocity and pressure fields would be measured but to date such a goal is not realistic. For the present experiment, two components of the velocity in a two dimensional xy plane are measured along with the 2-D array of wall pressure sensors.

The objective of the discussion below is to synthesize, from independent realizations, common patterns occurring in the velocity and pressure data. These realizations are examined carefully to discern prominent characteristic features and more importantly to document relationships among them. Little work has been attempted to date to study instantaneous structures present in the velocity field. An exception to this is Meinhart (1994), Adrian and Meinhart (1995) and Adrian et al. (1995) who have documented that regions in the boundary layer, with a streamwise extent on the order of δ , have fairly constant momentum. The information provided herein by pressure measurements however yields a significant contribution when interpreting the velocity field. A number of very defining traits, including that suggested by Adrian, are made apparent. Of special interest is the cause-effect relationship that the velocity field has on the wall pressure; previous

statistical averaging results are enhanced by looking at true, instantaneous images encompassing a wide range of scales of motion from integral scales of the turbulent field to small scale features which are lost in the averaging methods.

5.3 Instantaneous Correlations

The velocity fields in the figures below display Reynolds decomposed turbulent fluctuations. The gray scale coloring of vectors is used to distinguish negative from positive streamwise component fluctuations, where black and white correspond to $-3u_t$ and $+3u_t$, respectively. The instantaneous pressure profile is resolved using the thirteen microphones indicated by the square symbols as discussed in Section 4.4. At the upstream and downstream end of the array the pressure profile shown is simply the result of using the frozen field assumption on the first and last microphones. This portion of the signal is not considered to be an accurate representation of the wall pressure and thus no interpretation is attempted in this region. Pressures are nondimensionalized with p_{rms} .

5.3.1 $Re_\theta = 1520$. Three events are selected at this Re_θ . The operating free stream is $U_\infty = 4.9$ m/s. The velocity field is resolved from 1 mm above the tunnel floor to 40 mm in the wall normal direction, and 105 mm along the streamwise direction; these correspond to 14 to 552 y^+ and 1450 x^+ units respectively. The thirteen wall pressure measurement locations extend 660 wall units in the streamwise direction.

(i) Figure 5.1a shows an instantaneous realization of the turbulent boundary layer. In event i, the instantaneous wall pressure shows a negative pressure peak at $x^+ \approx 350$, labeled N_1 on the figure. A strong counterclockwise (ccw) eddy* with sense of rotation opposite to that of the mean spanwise vorticity, labeled **A**, exists above the negative pressure N_1 . Downstream of structure **A** a clockwise (cw) eddy with same sense of rotation as the spanwise vorticity, **B**, occurs at $x^+ \approx 550$, $y^+ \approx 150$. Further downstream three other cw

* The term “eddy” is used here rather than vortex. A precise definition of a vortex and its relation with vorticity are given in Chapter 7.

eddies are present, at **C** and **D** and **E**. It may be conjectured that eddies **A** through **E** form the interface of a large scale shear layer: this line of eddies (in particular **A** through **C**) separates a flow region upstream with mostly positive streamwise momentum from a flow region downstream with negative streamwise momentum. The convection of the negative pressure **N**₁ is shown in Figure 5.1b. The eddy **A** is located above **N**₁, while downstream of **N**₁ there exists a region of positive streamwise momentum (indicated by the symbol \Rightarrow).

Figure 5.1b also shows the convection of another negative pressure, **N**₂. Referring back to Figure 5.1a one can see an eddy (**F**) and a large region of positive momentum (indicated by a \Rightarrow) above and downstream of **N**₂ respectively. Presently, the high streamwise component flow regions in the vicinity of **N**₁ and **N**₂ seem to be part of the roll-up structures **A** and **F**. Generally, an eddy (with sense of rotation opposite to the mean spanwise vorticity) and near wall positive streamwise momentum flow are also observed in other realizations as flow features associated with a negative pressure peak.

Event i also shows two eddies with opposite vorticity located at $(x^+, y^+) \approx (100, 210)$ and $(180, 280)$ labeled **I** and **II** respectively in Figure 5.1a. There is flow with negative wall normal velocity between these structures that extends from the freestream down to $y^+ \approx 200$. Downstream of **I-II** exists a cw eddy, **III**, with positive wall normal velocity upstream of it. It is interesting to observe a relatively “strong” ejection (Q2 event: $u < 0, v > 0$) of fluid from the wall region to the logarithmic layer occurring directly above the negative pressure peak **N1**.

(ii) The instantaneous velocity from a second PIV realization and associated wall pressure profile is given in Figure 5.2a. This $p(x)$ profile shows a positive wall pressure region extending from $x^+ \approx 200$ to 500. The positive pressure oscillates about $2p_{rms}$ and peaks to $3p_{rms}$ around $x^+ \approx 430$. The time history of the wall pressure as seen from Figure 5.2b depicts the “large-scale” pressure structure at $t^+ \approx 0$ from $x^+ \approx 200$ to 500. As this structure convects the two positive pressure peaks **P**₁ and **P**₂ become distinct with the

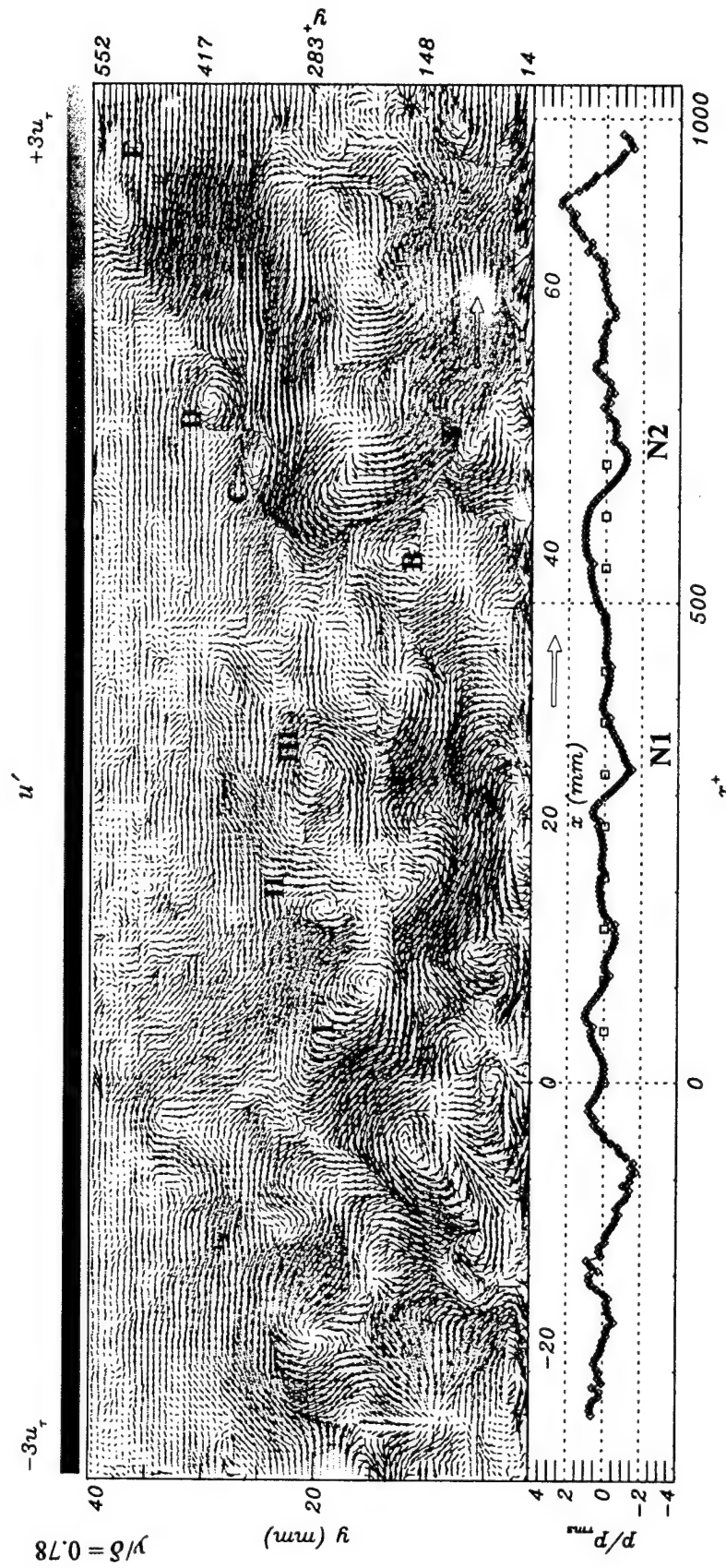


Figure 5.1a Instantaneous Velocity and Pressure Fields, Event i, $Re_\theta = 1520$

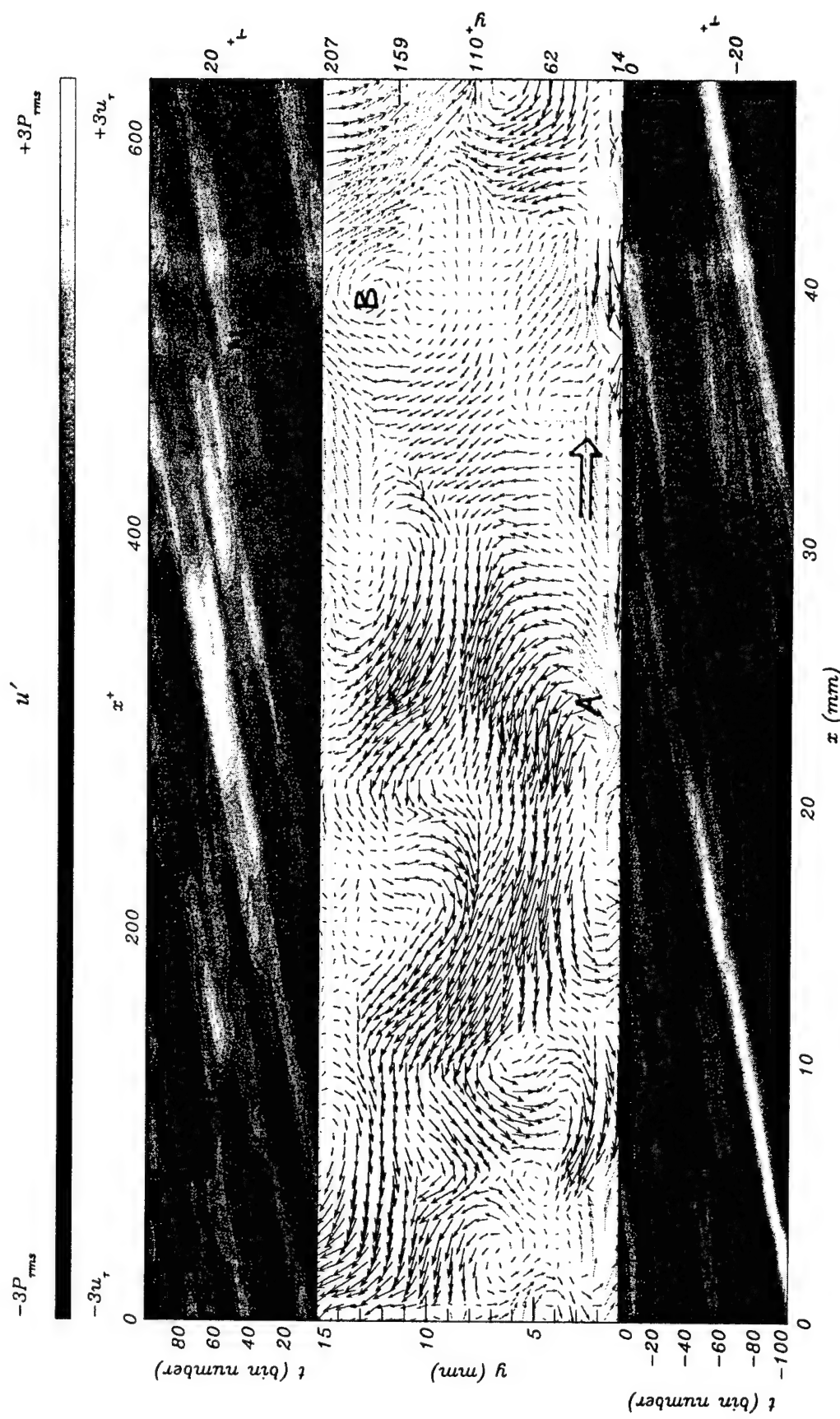


Figure 5.1b Detail of the Instantaneous Velocity Field and Contours of the Wall Pressure History Underneath from Event i

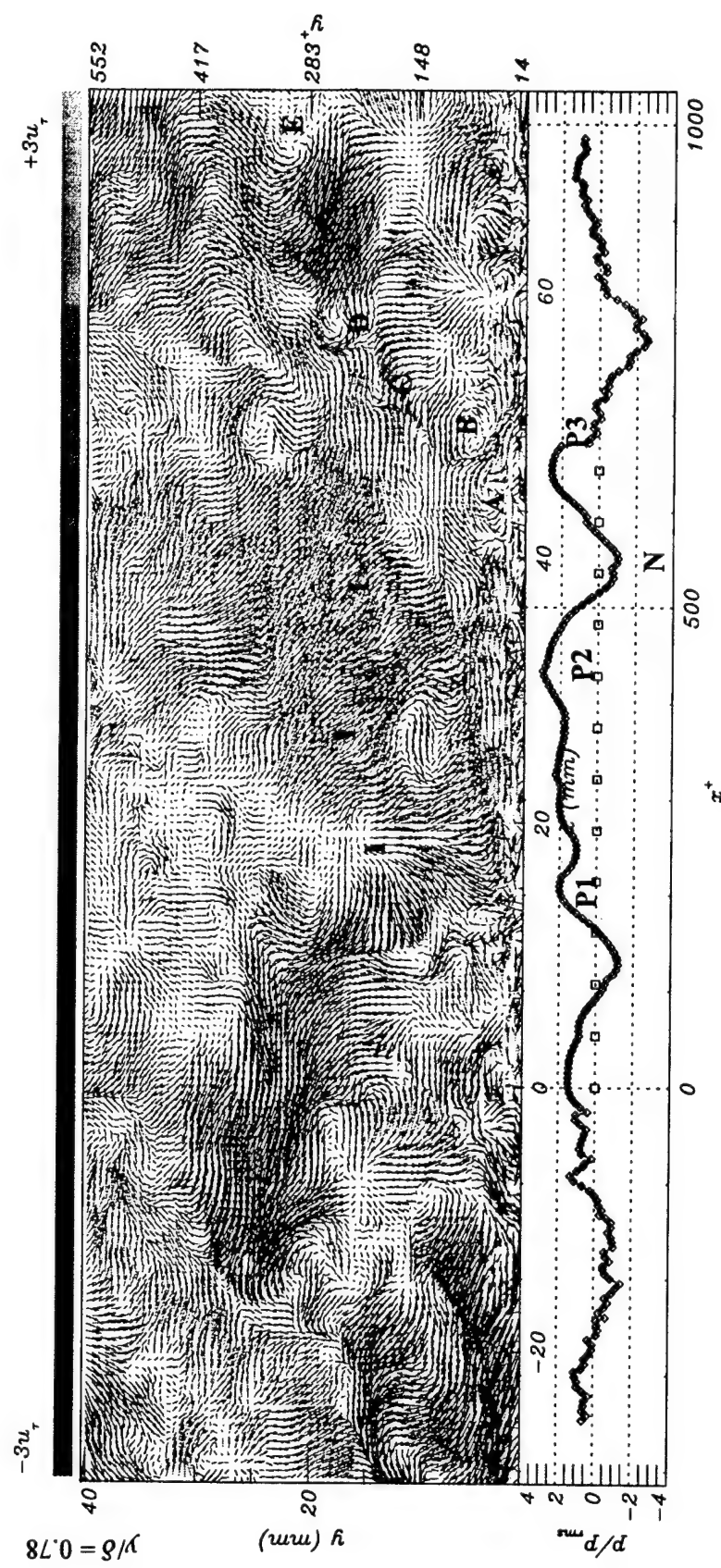


Figure 5.2a Instantaneous Velocity and Pressure Fields, Event ii, $Re_\theta = 1520$

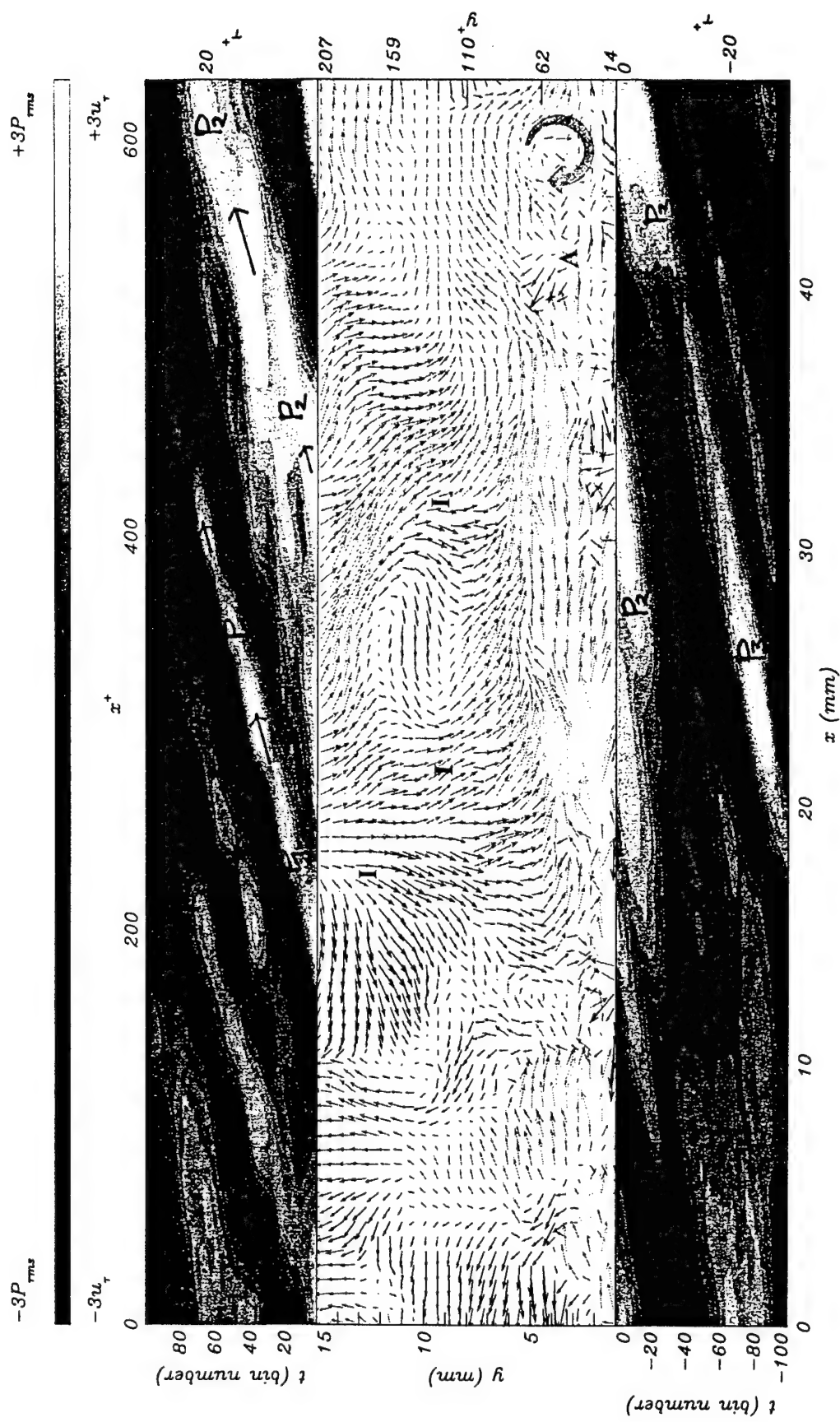


Figure 5.2b Detail of the Instantaneous Velocity Field and Contours of the Wall Pressure History Underneath from Event ii

magnitude of \mathbf{P}_2 remaining high (at $t^+ = 15$ it is $\approx 3p_{rms}$) and convecting over a large distance. A large scale motion, indicated as **I** on Figure 5.2a, of flow with negative wall normal velocity exists above the region of positive wall pressure. Downstream of **I**, at $x^+ \approx 600$, a shear layer occurs.

Two eddies (**A** and **B**) with opposite sense of rotation are located at $(x^+, y^+) \approx (600, 50)$ and $(680, 80)$ respectively. Other cw eddies are present further downstream at $y^+ \approx 210$, 240 and 310 (**C**, **D**, **E**). Underneath structures **A** and **B** a large amplitude positive pressure (\mathbf{P}_3) was captured at $t^+ = 0$. A negative pressures peak (**N**) also appears upstream of **A** and **B**. Both \mathbf{P}_3 and **N** are observed between $-30 < t^+ < 0$ before they convect out of the viewing window of Figure 5.2b.

(iii) Figure 5.3a shows a negative pressure peak (**N**), $p \approx -2p_{rms}$, at $x^+ \approx 200$. The velocity field above and downstream of **N**, shown between **I-II**, exhibits a region of high streamwise momentum with a positive wall normal velocity component as indicated with the arrows \rightarrow . Recall that in event i a small region with positive streamwise momentum was also observed downstream of the negative pressure. Downstream of the high momentum region, in the current event iii, a small shear layer is observed where eddies **A** and **B** are distinguished around the interface.

The flow region of positive streamwise momentum fluid downstream of **N** extends from **I** to **II**, where the flow displays a positive v component, and it further extends from **II** to **III**, where the sign of v becomes negative. A detail of the wall region is presented in Figure 5.3b. In addition to eddies **A** and **B**, other eddies indicated as **C**, **D**, **E** and **F** are positioned along the region with positive streamwise momentum. The flow field also shows a large cw structure (**G**) at $(x^+, y^+) \approx (150, 280)$. Upstream of the large roll-up structure **G**, at $(x^+, y^+) \approx (-150, 200)$, there is a region (**H**) where the velocity fluctuations vanish while exhibiting large radially outward flow from this spot. The outward velocities are indicative of a mass deficit which would be supplanted by a strong spanwise velocity component.

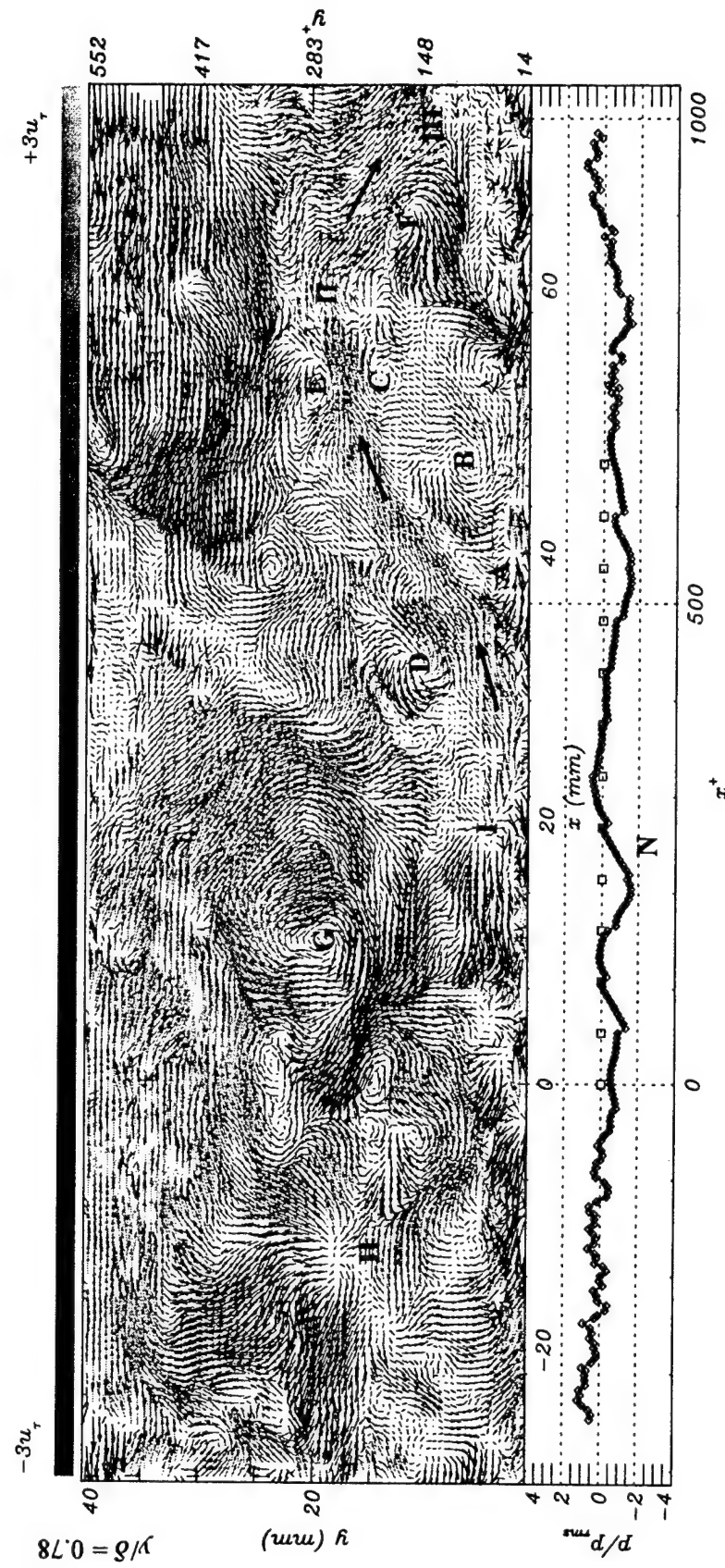


Figure 5.3a Instantaneous Velocity and Pressure Fields, Event iii, $Re_\theta = 1520$

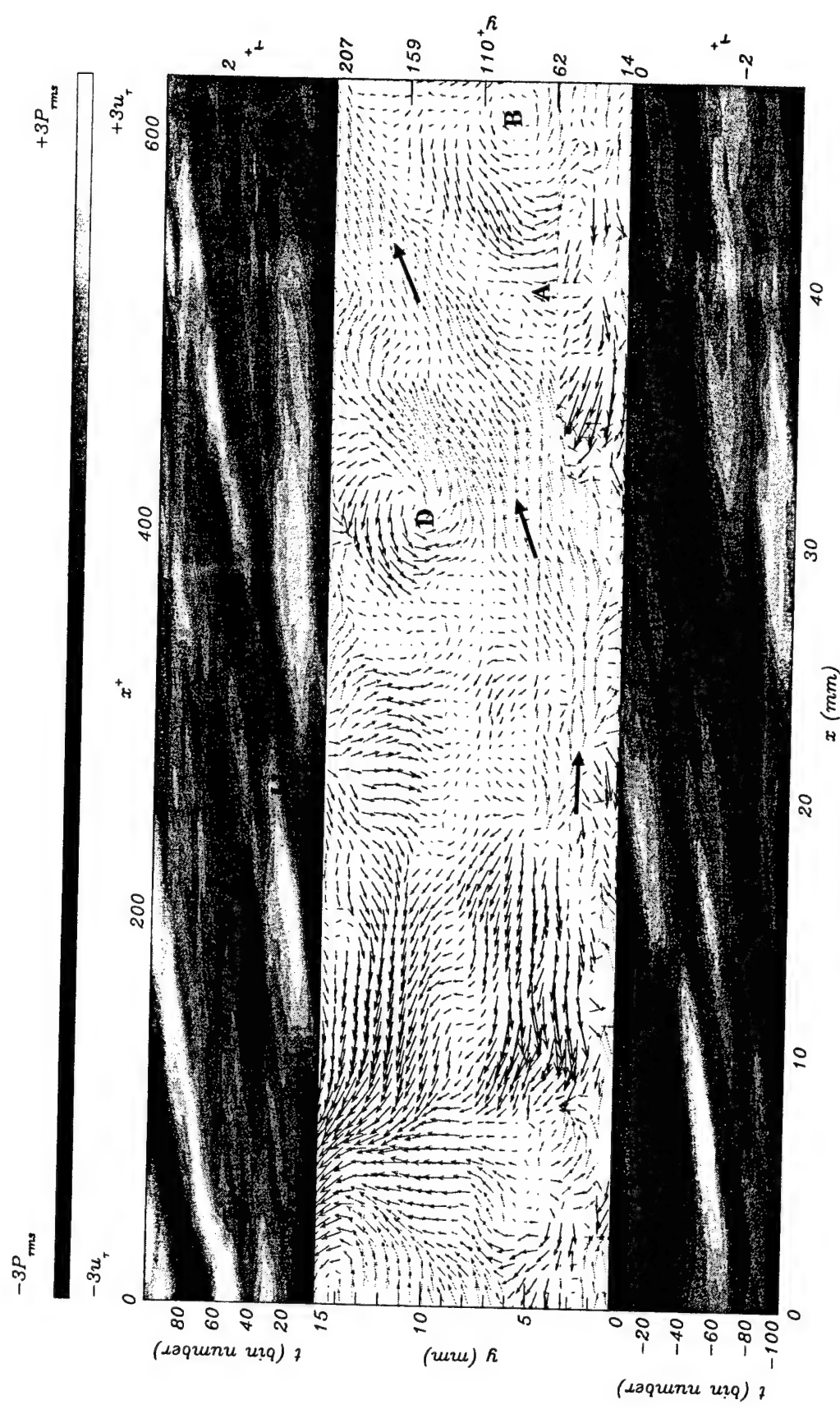


Figure 5.3b Detail of the Instantaneous Velocity Field and Contours of the Wall Pressure History Underneath from Event iii

5.3.2 $Re_\theta = 3950$. Realizations iv–vi correspond to $U_\infty = 10$ m/s. The physical dimensions of the velocity fields along the streamwise and wall normal directions and the location of the microphone array are the same as in events i–iii. The nondimensional extent of the velocity field is 3000×1160 in x^+ and y^+ respectively. The thirteen wall pressure measurements extend $1350 x^+$ units.

(iv) Figure 5.4a shows a large positive pressure peak (\mathbf{P}_1) of $4p_{rms}$, located at $x^+ \approx 775$. The pressure time history of Figure 5.4b shows that the positive structure \mathbf{P}_1 existed for at least $60 t^+$ units before and after the PIV realization. A second large magnitude positive pressure (\mathbf{P}_2) occurs upstream of \mathbf{P}_1 at $x^+ \approx 600$ around $t^+ = 0$. Between $200 < x^+ < 900$ the pressure is consistently positive also around $t^+ = 0$. The large region of positive pressure occurs beneath a region of the flow characterized by a negative wall normal velocity indicated by **I** on Fig. 5.4a. A large scale shear layer occurs downstream of region **I**. The shear layer is indicated by eddies **A**, **B**, **C**, and **D**. The shear layer near the wall is located in the vicinity of the large positive pressure structure \mathbf{P}_1 .

Above the negative wall pressure peak which occurs at $x^+ \approx 150$ an ejection of fluid (Q2 event) from the wall region is observed. Although this is smaller in scale than that seen in Figure 5.1a above N1 the magnitude of the ejection is comparable.

(v) The realization of Figure 5.5a shows a large scale shear layer extending from near the wall at $x^+ \approx -500$, towards the outer edge of the boundary layer near $x^+ \approx 1250$. Although the positive pressure peak that is plotted at $x^+ \approx -500$ was calculated using Taylor's hypothesis on the signal from the microphone at $x^+ = 0$, it is consistent with the findings of Figures 5.2 and 5.4. Namely, a positive pressure peak is indicative of an inclined shear layer in the flow. Numerous eddies with sense of rotation equal to the mean spanwise vorticity (**A**, **B**, **C**, **D**, **E** and **F**) exist along the interface. The interface separates two distinct regions of high and low streamwise momentum. Only near the wall at **I** the high speed flow seems to have extended into the interface.

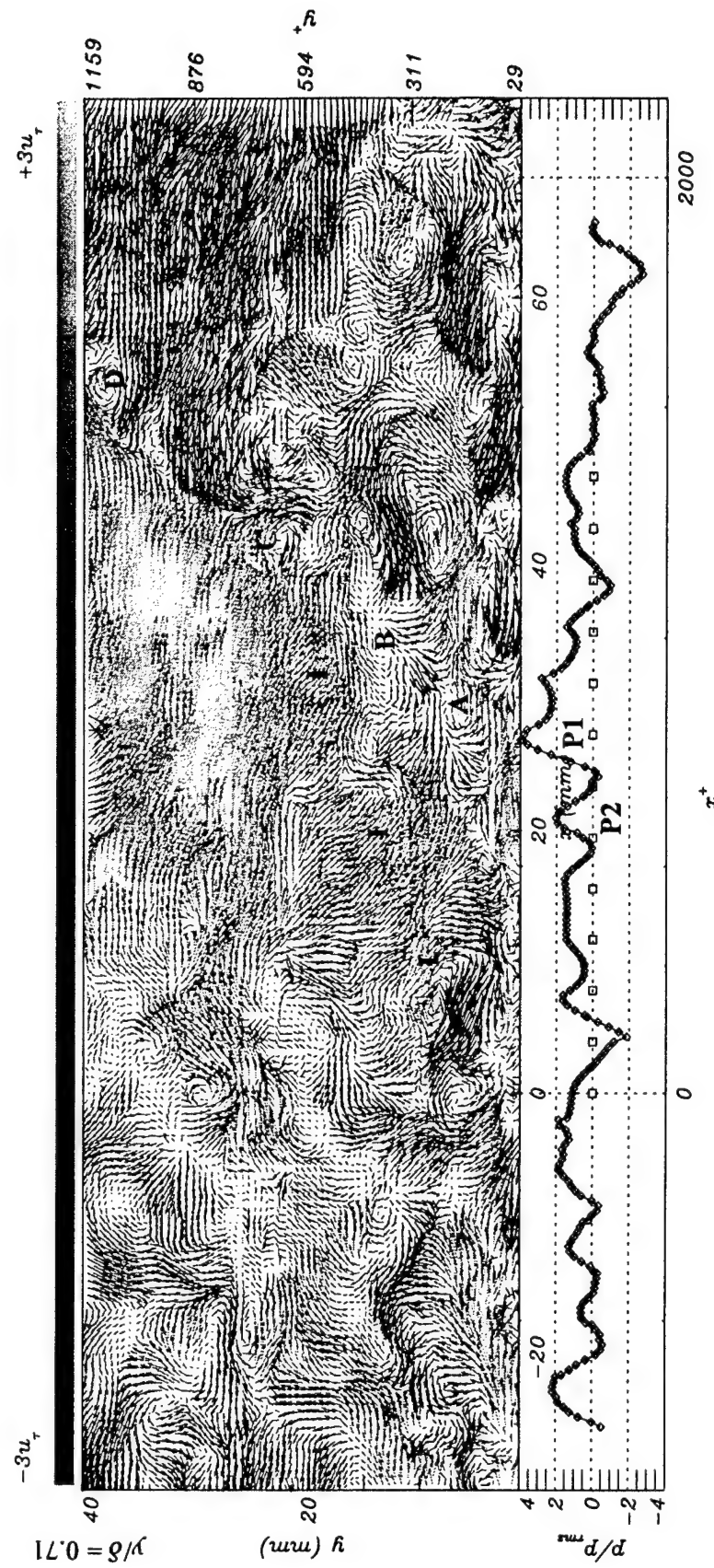


Figure 5.4a Instantaneous Velocity and Pressure Fields, Event iv, $Re_\theta = 3950$

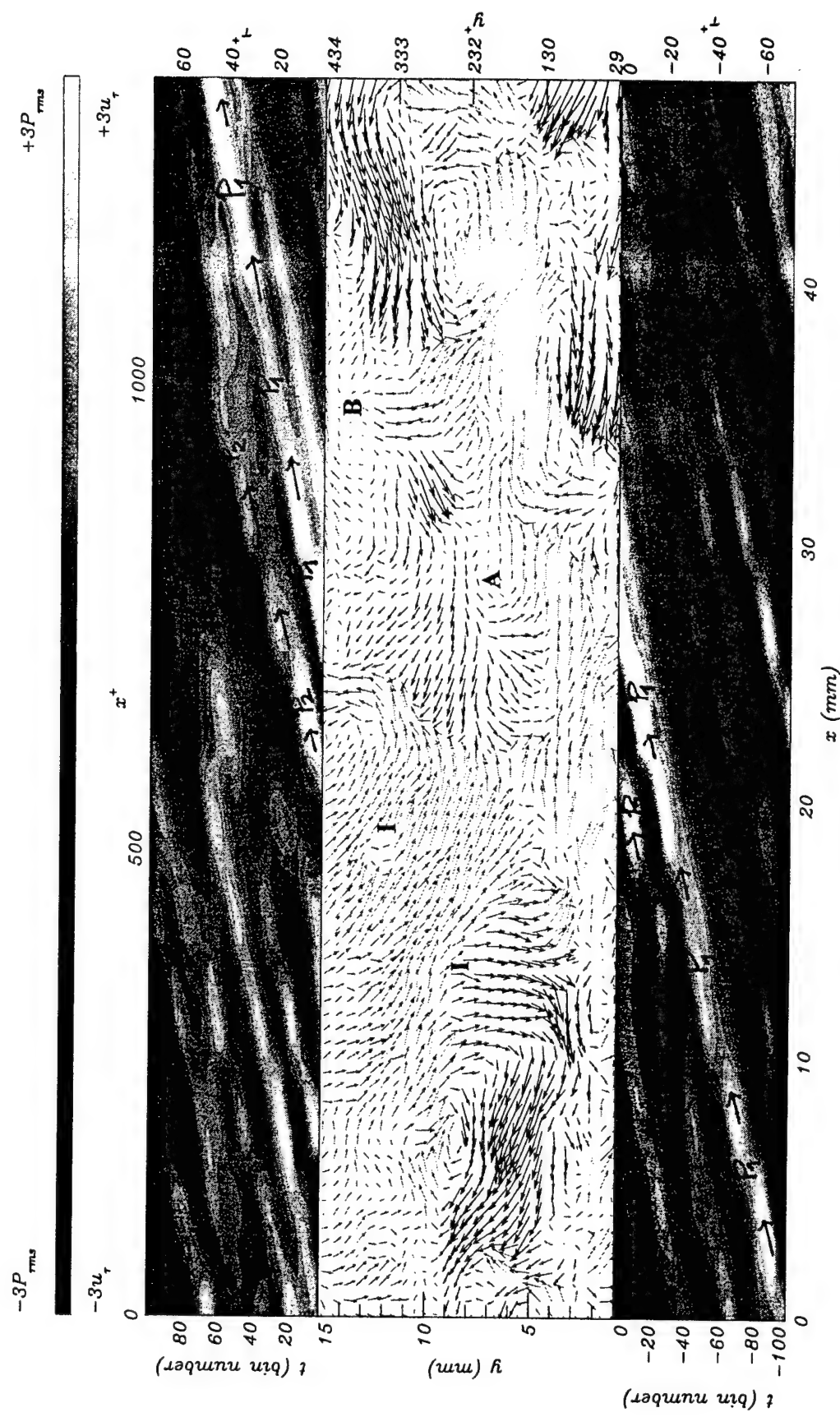


Figure 5.4b Detail of the Instantaneous Velocity Field and Contours of the Wall Pressure History Underneath from Event iv

A second shear layer is observed at $x^* \approx 100$ where eddies **G** and **H** are observed at the interface. This shear layer, unlike the shear layers observed previously, shows slow flow upstream of flow with positive momentum; also, structures **G** and **H** have opposite vorticity to the structures represented in **B-F**.

The region of positive momentum located between **I-II** extends from the shear layer marked by structures **G** and **H** downstream to another shear layer indicated by structure **J**. The shear layer indicated by structure **J** extends to 500 y^* units at an angle of 45° . The region of positive momentum, indicated by a \Rightarrow symbol, is present above a large magnitude negative pressure (**N**), $p \approx -4p_{rms}$, centered around $x^* \approx -300$ in Figure 5.5a. The presence of a negative pressure beneath a region of positive momentum flow is consistent with Figures 5.1 and 5.3 ($Re_\theta = 1520$) described earlier. Figure 5.5b shows a detail of the flow field associated with the shear layers delineated by structures **G** and **H**, and **J**. Between them the region of positive streamwise momentum is indicated (from **I** to **II**). The convection of the negative pressure structure **N** underneath the high streamwise momentum region is also indicated.

(vi) The pressure profile of Figure 5.6a shows a very strong favorable pressure gradient formed by consecutive positive (**P**) and negative (**N**) pressure peaks located at $x^* \approx 800$ and 900 respectively. The magnitude of the positive pressure peak is largest, reaching $4p_{rms}$; the negative pressure reaches $-3p_{rms}$, and remains downstream of the positive peak as is shown in Figure 5.6b. A region of positive streamwise momentum velocity between $x^* \approx 500$ and 1100 (**I-II**) exists above the pressure structure. The detail view of Figure 5.6b shows that there is an eddy (**A**) very near the wall between **P** and **N** with sense of rotation equal to that of the mean spanwise vorticity. Further away from the wall other structures such as **B** and **C** are present.

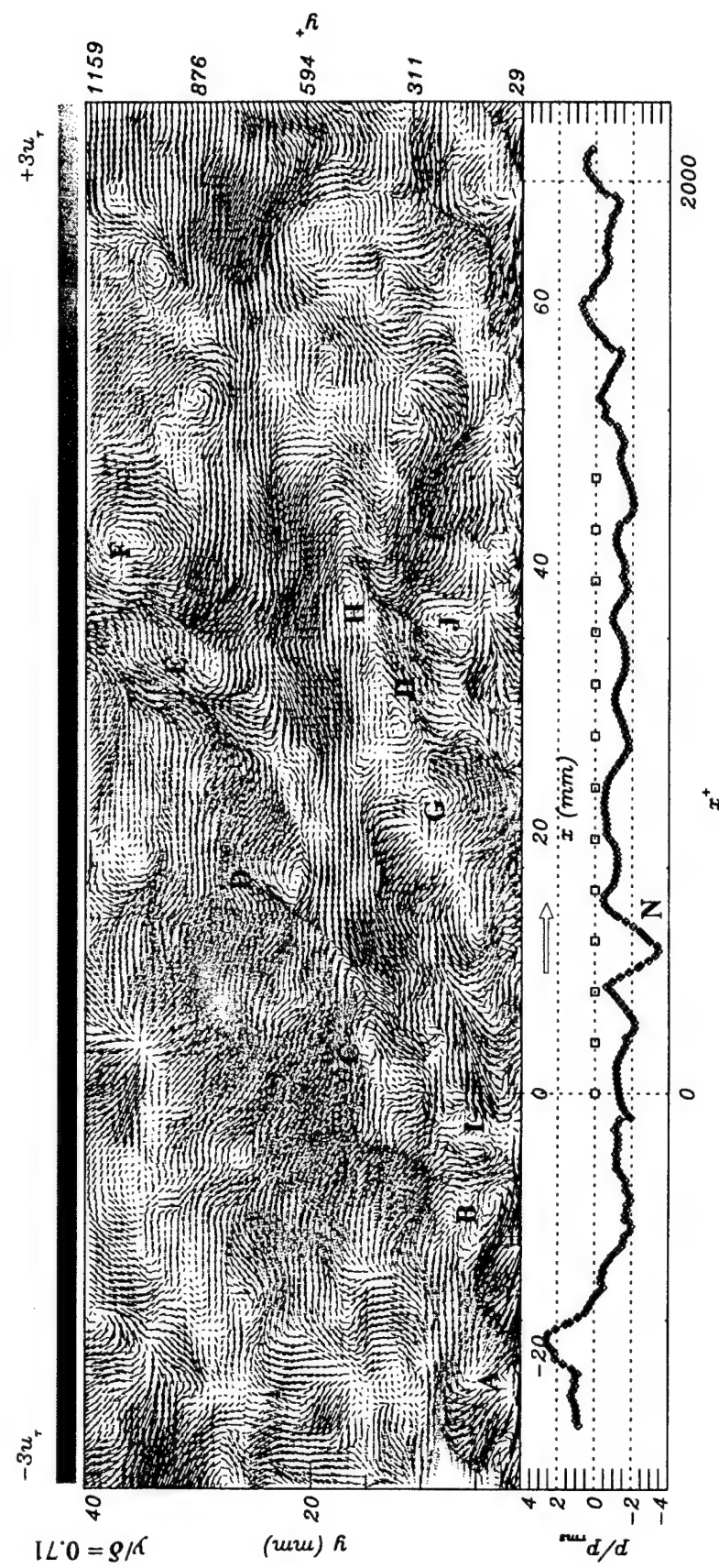


Figure 5.5a Instantaneous Velocity and Pressure Field, Event v, $Re_\theta = 3950$

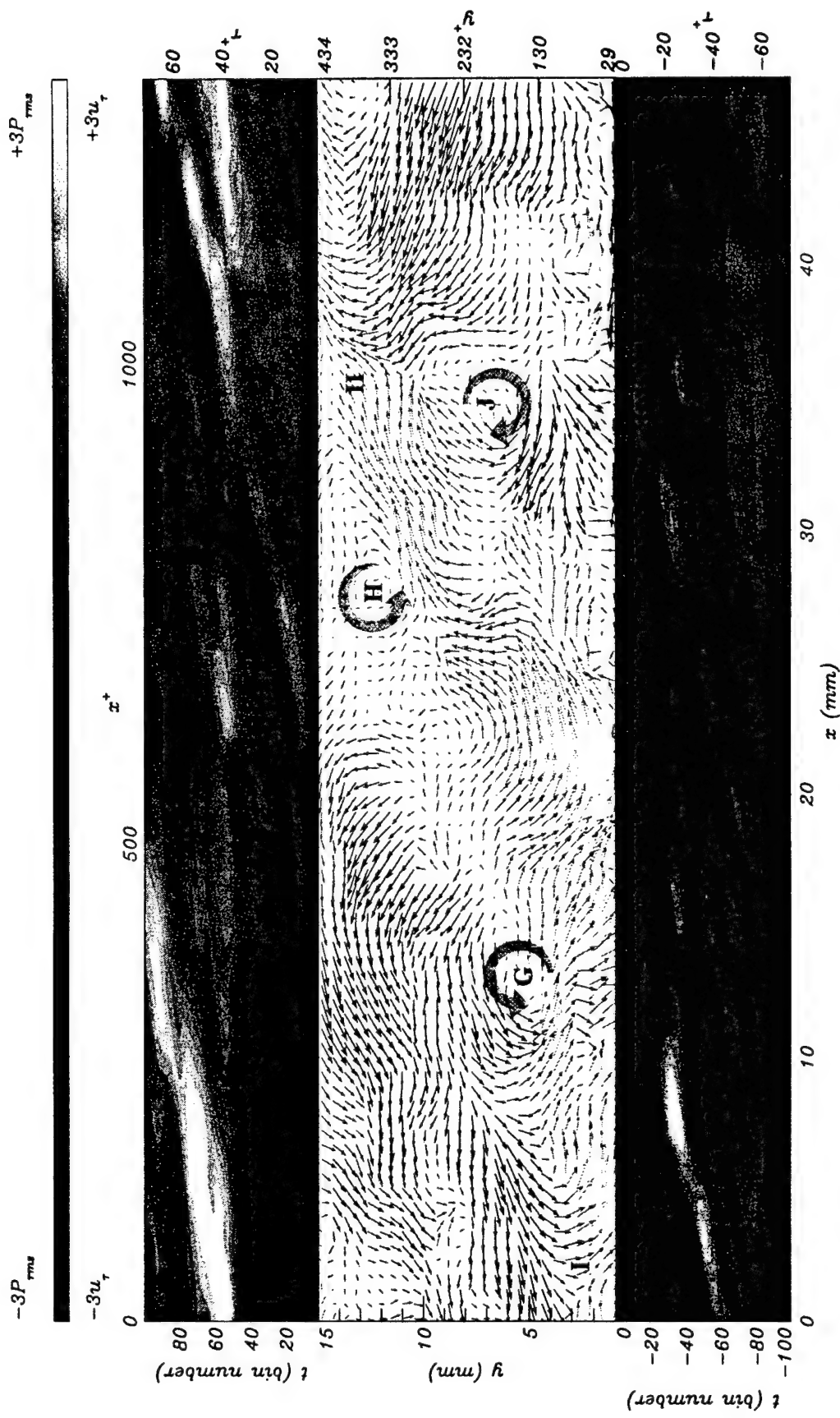


Figure 5.5b Detail of the Instantaneous Velocity Field and Contours of the Wall Pressure History Underneath from Event v

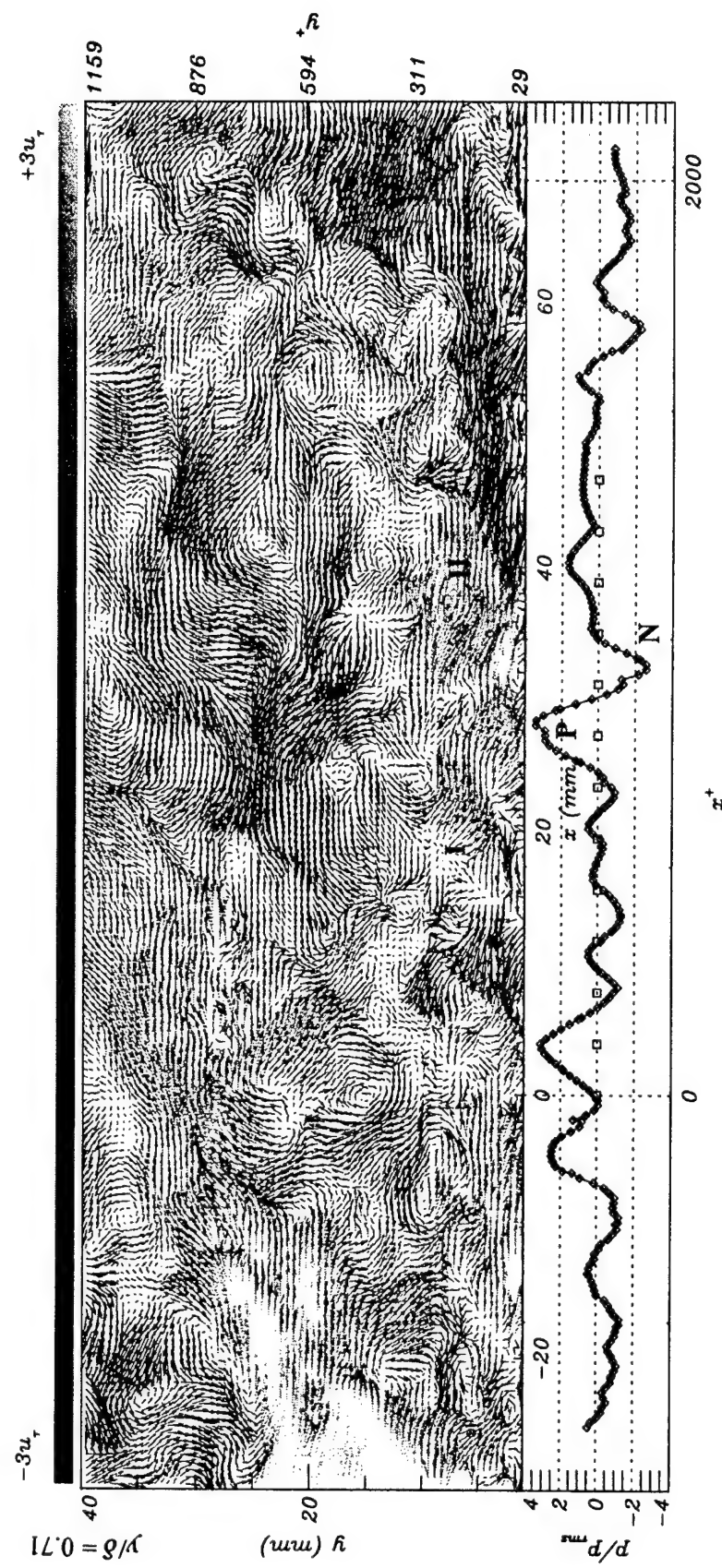


Figure 5.6a Instantaneous Velocity and Pressure Fields, Event vi, $Re_\theta = 3950$



Figure 5.6b Detail of the Instantaneous Velocity Field and Contours of the Wall Pressure History Underneath from Event vi

5.3.3 $Re_\theta=5790$. Events vii–ix show a selection of velocity fields and wall pressure at this Reynolds number. The freestream velocity is 14.9 m/s. The velocity fields extend 4200 and 1650 wall units in x^+ and y^+ respectively. The location of the wall pressure measurement locations extend approximately 1800 wall units in x^+ .

(vii) Two large shear layers are distinguished in Figure 5.7a. They are indicated as **I-II** and **III-IV**. Both the “ejection” like event downstream of **I-II** and the “sweep” type event upstream of **III-IV** appear as large scales in the figure; both regions also contain within numerous eddies. The pressure of Figure 5.7b is resolved in between these shear layers. Positive (**P**) and negative (**N₁**) pressures exist at $x^+ \approx 800$ and 900 respectively. Above **P** there occurs a small shear layer indicated by eddies **A**, **B**, and **C**. The presence of the shear layer above **P** in event vii is consistent with the positive pressures observed under the shear layers of event ii ($Re_\theta = 1520$) and of event iv ($Re_\theta = 3950$).

Upstream of the pressure structure **N₁-P** a negative pressure peak **N₂** occurs. The flow downstream of **N₂** is characterized by a positive streamwise momentum. It is indicated by the symbol \Rightarrow . The presence of the high speed flow above **N₂** in event vii is consistent with the high speed flow observed over the negative pressures of events i and iii at $Re_\theta = 1520$ and of event vi at $Re_\theta = 3950$.

(viii) The velocity field of Figure 5.8a shows a large region of high momentum flow with a downward component upstream of a shear layer. Numerous eddies are present along the shear layer interface (some have been labeled **A-G**). A region of high speed flow extends downstream of the shear layer along the wall, from $x^+ \approx 600$ to 2000. It is indicated by the symbol \Rightarrow . Beneath this positive streamwise velocity region a large negative pressure exists, $-4p_{rms}$ (labeled **N** in the figure). Figure 5.8b shows that there are other negative pressures associated with this velocity region.

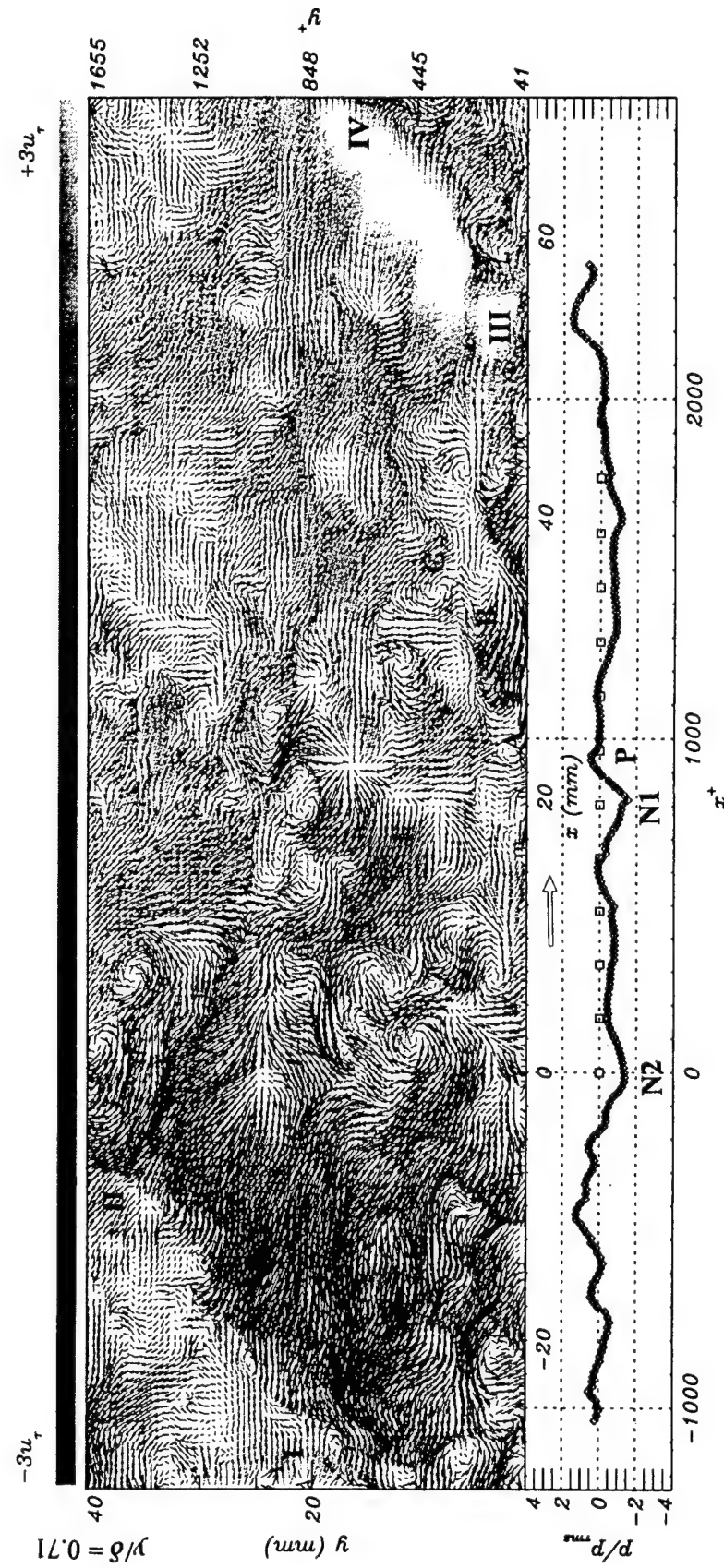


Figure 5.7a Instantaneous Velocity and Pressure Fields, Event vii, $Re_\theta = 5790$

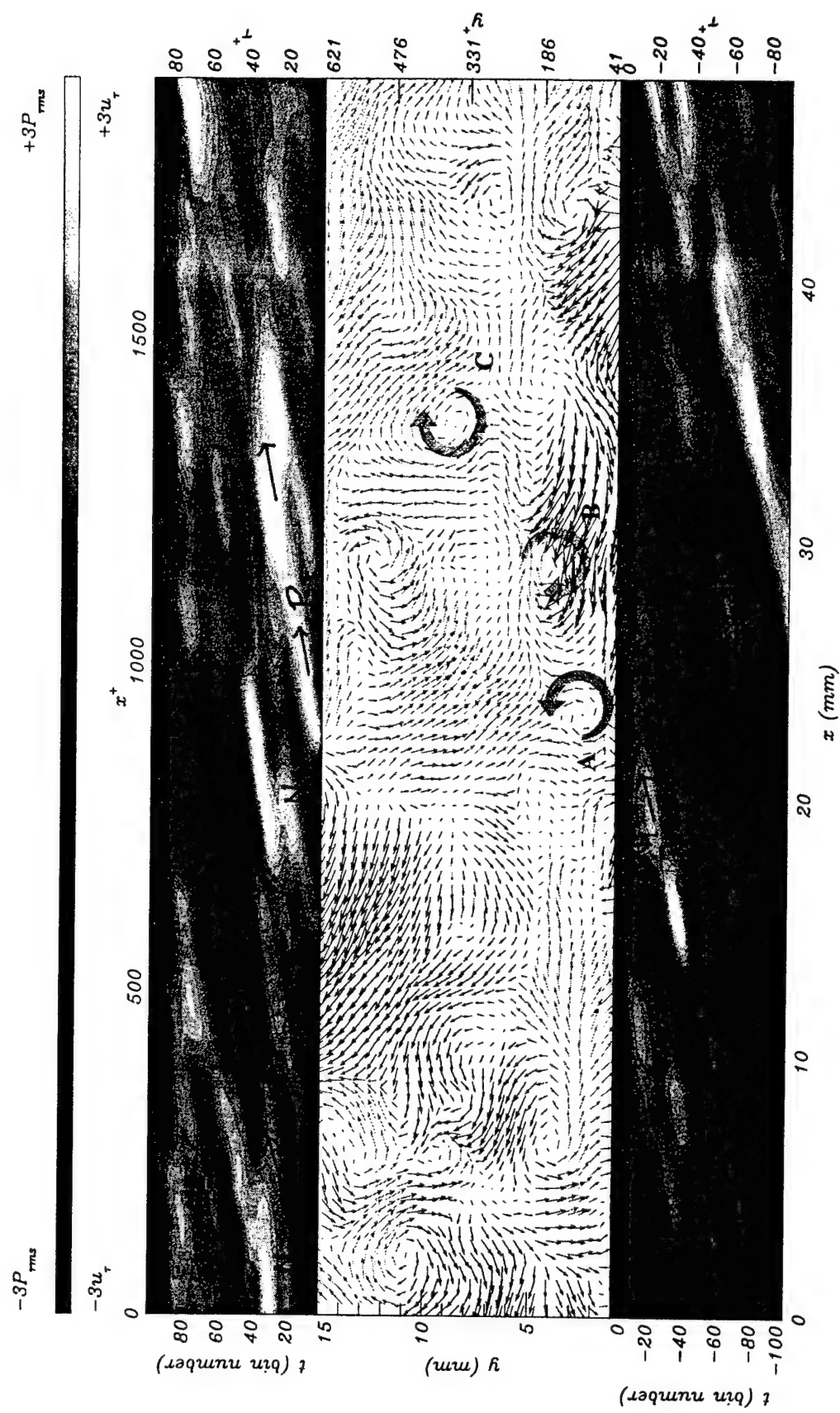


Figure 5.7b Detail of the Instantaneous Velocity Field and Contours of the Wall Pressure History Underneath from Event vii

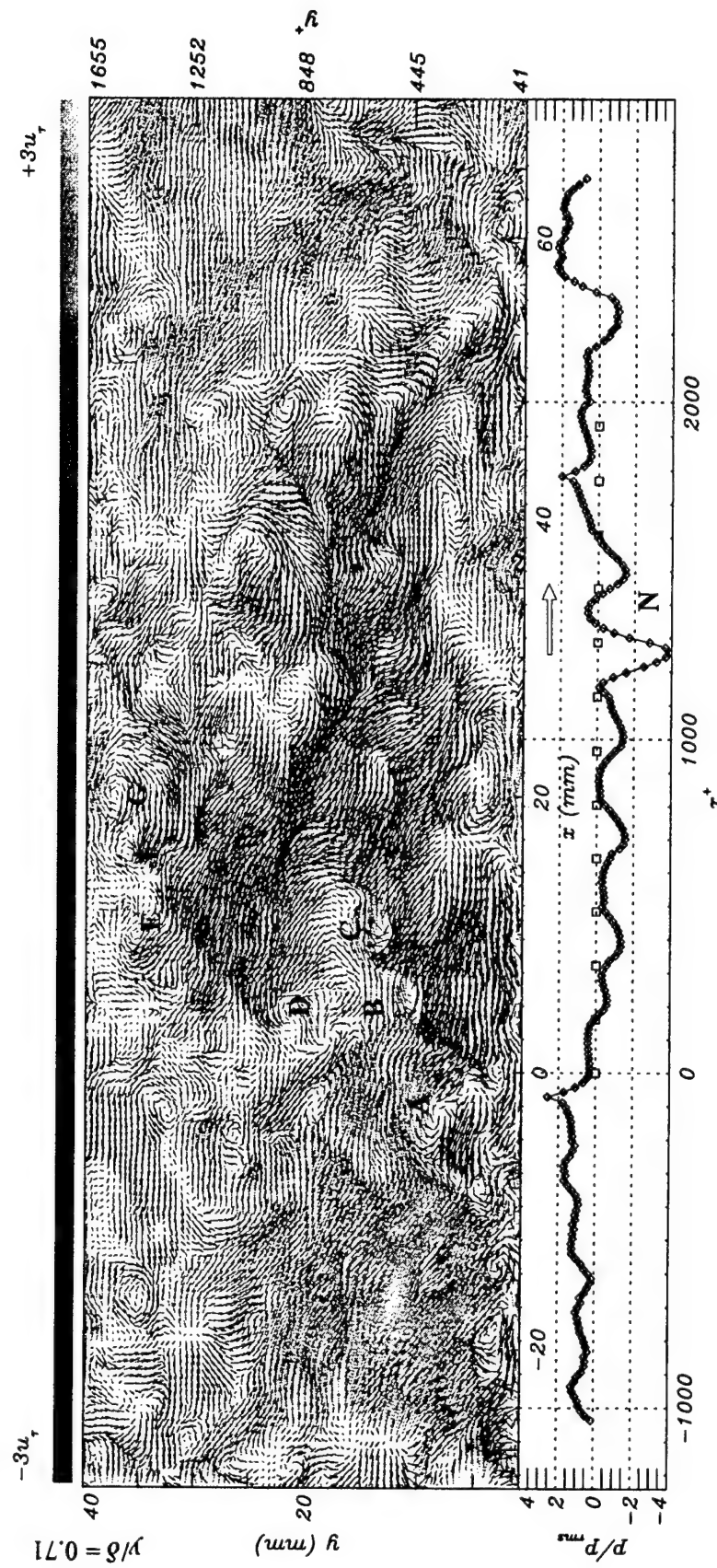


Figure 5.8a Instantaneous Velocity and Pressure Fields, Event viii, $Re\theta = 5790$

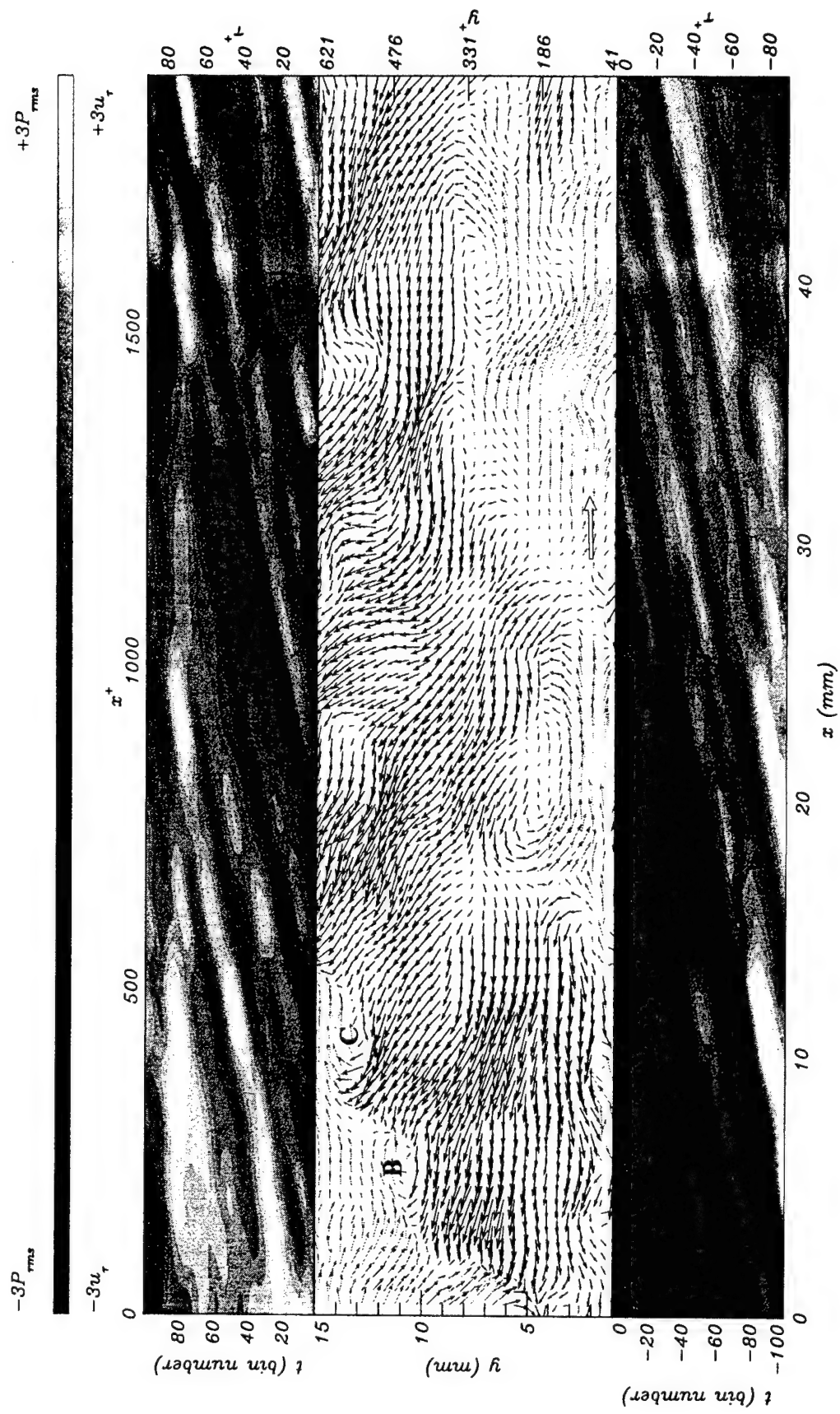


Figure 5.8b Detail of the Instantaneous Velocity Field and Contours of the Wall Pressure History Underneath from Event viii

(ix) Figure 5.9a shows a large flow region of low streamwise momentum upstream of another large region of high streamwise velocity component. The large scale regions contain numerous smaller scale eddy-like structures. The wall pressure underneath the interface that separates the above regions is negative. The pressure time history of Figure 5.9b shows two large amplitude negative pressure structures (N_1 and N_2) within the region where the pressure is mostly negative. Above N_1 and N_2 several eddies with sense of rotation opposite to that of the mean spanwise vorticity are identified as **A**, **B**, **C** and **D**. The eddies are associated with predominately positive wall normal velocity components with negative streamwise velocity (i.e. ejections or Q2 events) flow near the wall and above the negative pressure structures.

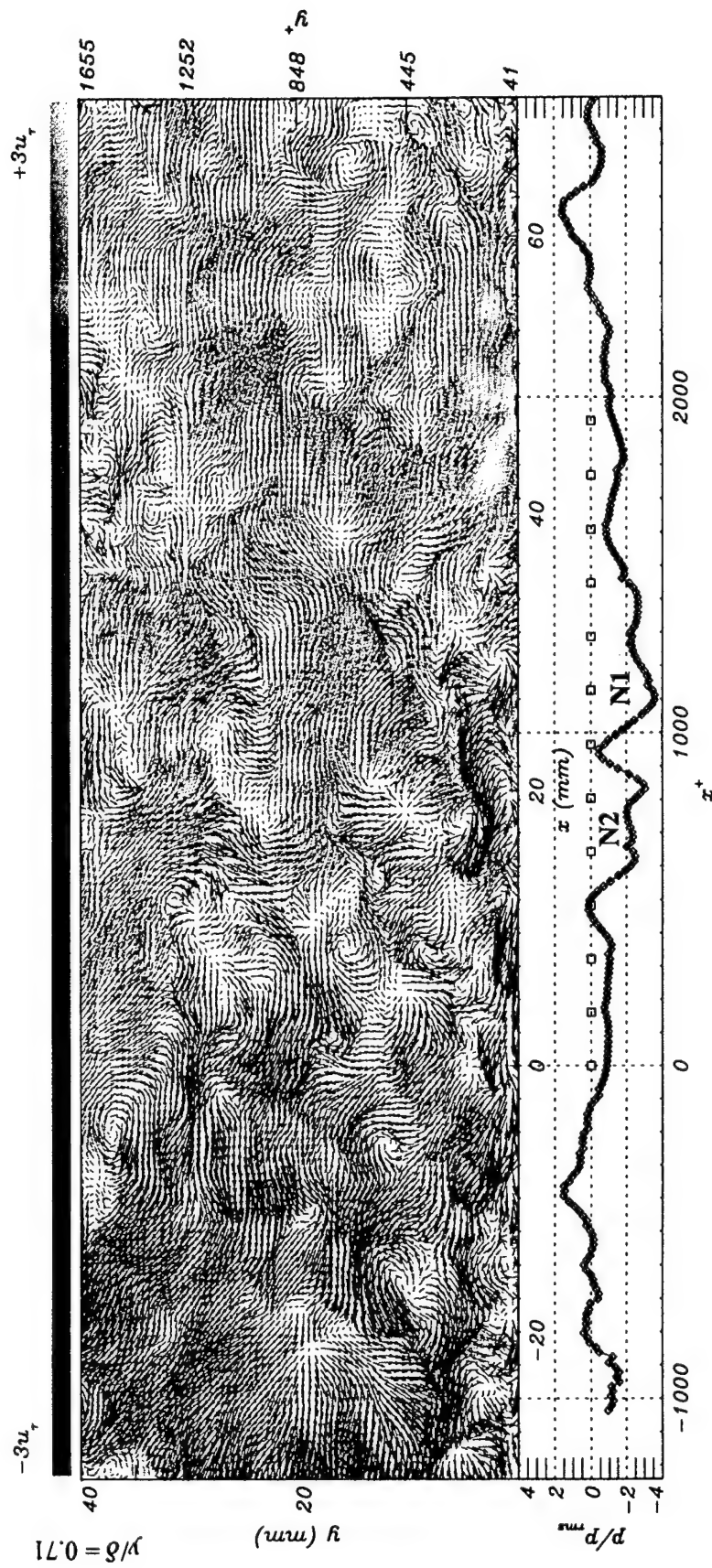


Figure 5.9a Instantaneous Velocity and Pressure Fields, Event ix, $Re_\theta = 5790$

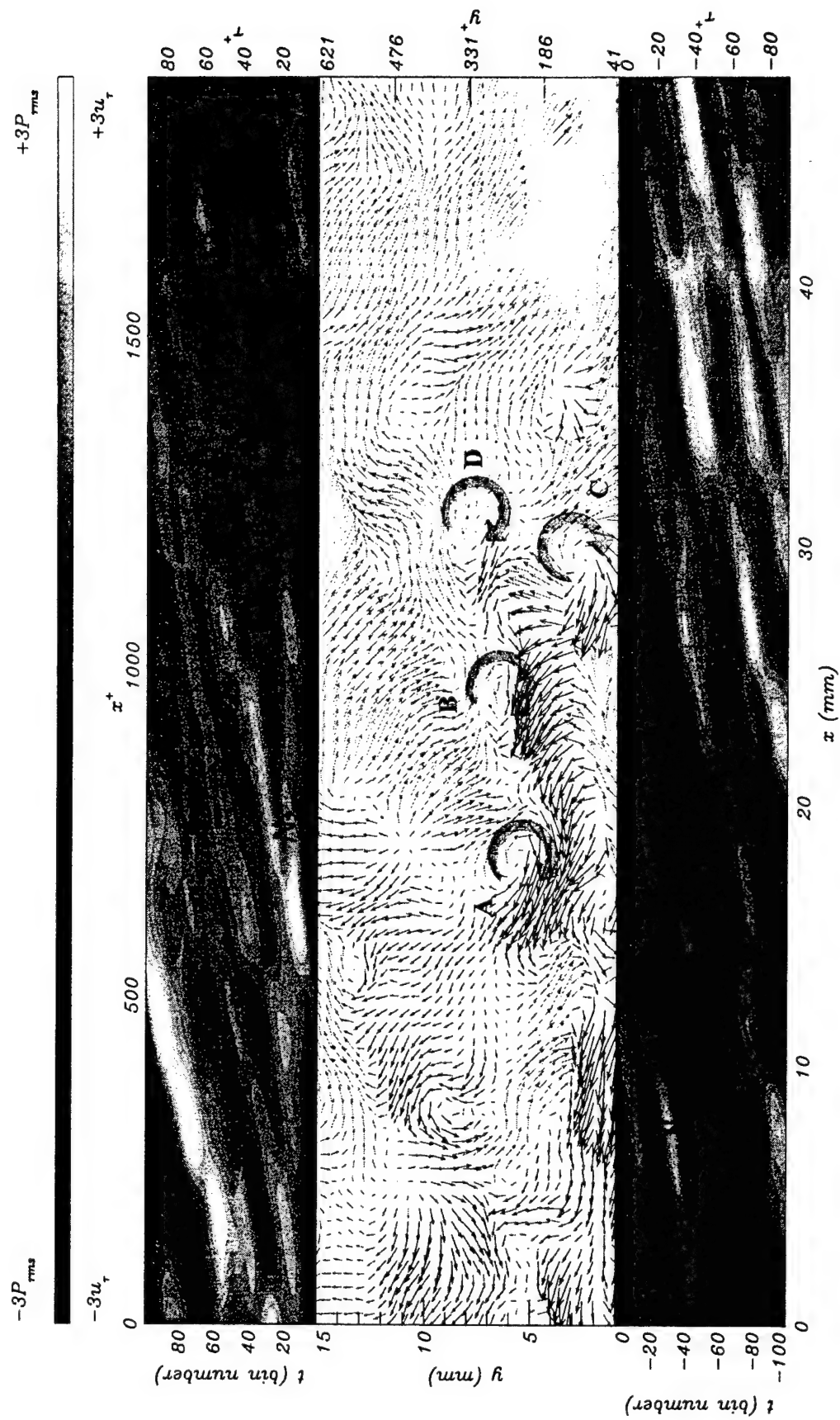


Figure 5.9b Detail of the Instantaneous Velocity Field and Contours of the Wall Pressure History Underneath from Event ix

CHAPTER VI

WALL PRESSURE MEASUREMENTS

As the Poisson equation (equation 2.6) for the pressure shows, all the points of the velocity field contribute to the wall pressure. The integral effect of the velocity on the pressure at a given wall location (Section 2.3) is dominated by the strength of the velocity structures about the point in question in such a way that the closer they are the greater their contribution. The wall pressure time-history underneath the PIV realization may give an indication of the life of the coherent motions in the velocity field. For example, one eddy structure above a large magnitude negative pressure peak in one of the figures of Chapter 5 may be assumed to convect and retain at least partly some of its original character if the pressure time history shows that the negative pressure structure is well preserved. The pressure-to-pressure interaction captured in the time-history may thus be used to gain insight as to which coherent structures are mostly responsible for the large amplitude wall-pressure events.

The conditional averages of the velocity field were calculated by Juckenhoefel (1995) to resolve the salient features associated with large amplitude wall pressure events. Measurements presented in Chapter 5 showed that positive pressure events were associated with an inclined shear layer commencing immediately above the positive pressure peak. Negative pressure structures were associated with a roll-up flow structure and positive wall normal velocities above as well as a region of positive streamwise momentum downstream of the negative pressure. The following section considers conditional averages calculated from streamwise wall pressure profiles. Subsequently the consideration of a long time sequence of the wall pressure field demonstrates that only a very localized structure is resolved in the conditional averaging and that there are other important events that emerge as a repeated pattern but are washed out in the conditional averaging process.

6.1. Conditional Averages

A conditional sampling procedure is utilized to identify a repeated pattern or salient feature in the signal. Conditional averages of the pressure are constructed from large-amplitude short-duration wall pressure fluctuations in the following,

$$\begin{aligned} \langle p'(\chi^+, y^+ = 0, z^+, \tau^+) \rangle = \\ \frac{\sum_{n=b}^{N-b} \sum_{k=a}^{K-a} \sum_{i=-a}^{+a} \sum_{j=-b}^{+b} D(k\Delta x_{acq}^+, 0, z^+, n\Delta t_{acq}^+) p'((k+i)\Delta x_{acq}^+, 0, z^+, (n+j)\Delta t_{acq}^+) }{\sum_{n=b}^{N-b} \sum_{k=a}^{K-a} D(x^+ = k\Delta x_{acq}^+, y^+ = 0, z^+, t^+ = n\Delta t_{acq}^+)} \end{aligned} \quad (6.1)$$

where N ($N = 60,000$) is the number of points in the time series, K ($K = 276$) is the number of discrete data points obtained from the concatenated $p(x)$ signal. The detection function D is a discrete function centered upon the detection point and takes the value of one when a detection is established and zero at any other time. In the above equation, $k(\Delta x_{acq})^+$ and $n(\Delta t_{acq})^+$ set the reference space and time for the occurrence of the event that corresponds to $\chi^+ = \tau^+ = 0$. To facilitate comparison with measurements in flat plate boundary layers a threshold of $2.5 p_{rms}$ is used in the present study (Juckenhoefel, 1995, Snarski and Lueptow, 1995).

The space-time resolution of the wall pressure measurements permits the conditionally averaged structure to be resolved in time and space as illustrated in Figure 6.1. A long time sequence of wall pressure was measured along $K\Delta x_{acq}$ in the streamwise direction (indicated as step 1 on the figure). A large peak is identified, typically convecting downstream, and distinguished from other peaks (step 2). The location of maximum or minimum pressure in the vicinity of the peak just detected (step 3) is assigned as the detection point ($\chi^+ = 0, \tau^+ = 0$). A window is established around each detection point (step 4). The size of the window, $2a(\Delta x_{acq})^+ \times 2b(\Delta t_{acq})^+$ is selected to resolve the averaged structure. The time-space pressure field in the window is stored and then averaged over the number of detections. The size in the streamwise direction of the

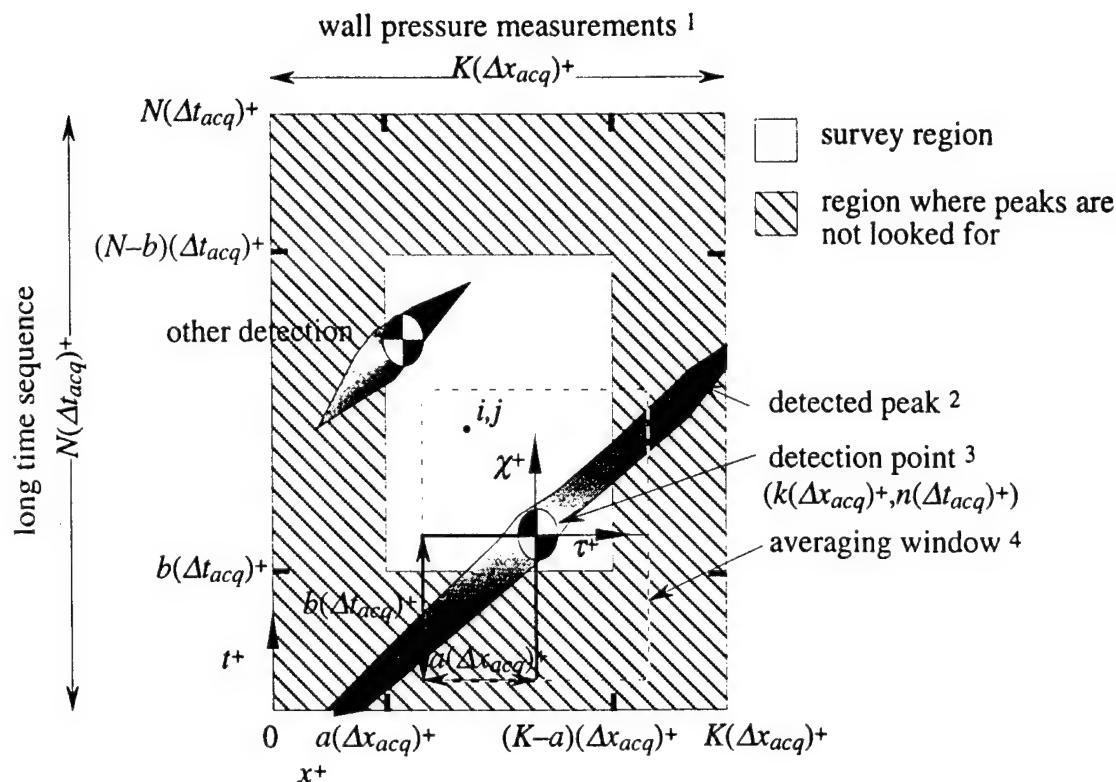


Figure 6.1 Illustration of Space-Time Averaging

averaging window establishes the region wherein the peaks are surveyed $(K - 2a)(\Delta x_{acq})^+$. A typical average is calculated from 300 detections.

The positive (or negative) signatures calculated in the conditional averages are nearly identical for $Re_\theta = 1520, 3950$ and 5790 . The conditional averages are non-dimensionalized by the respective rms and are shown as shaded contours in Figures 6.2–6.4 for $Re_\theta = 1520, 3950$ and 5790 respectively. The shaded contours are resolved as spatial profiles of pressure at various t^+ in the following Figures 6.5–6.7.

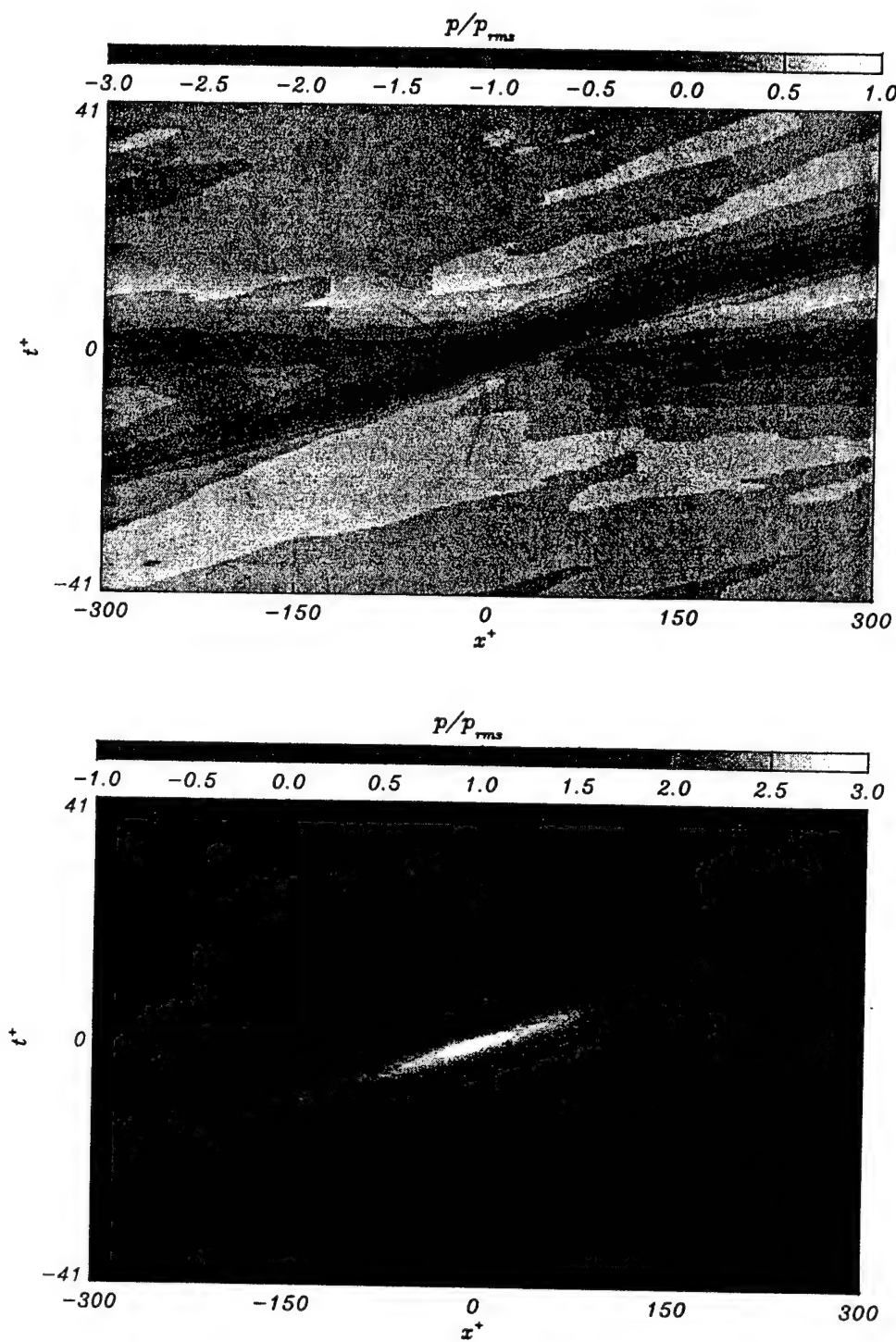


Figure 6.2 Time-Space Conditional Average for Negative (Top) and Positive (Bottom) Pressure Events. $Re_\theta = 1520$ and Threshold $\kappa = 2.5$

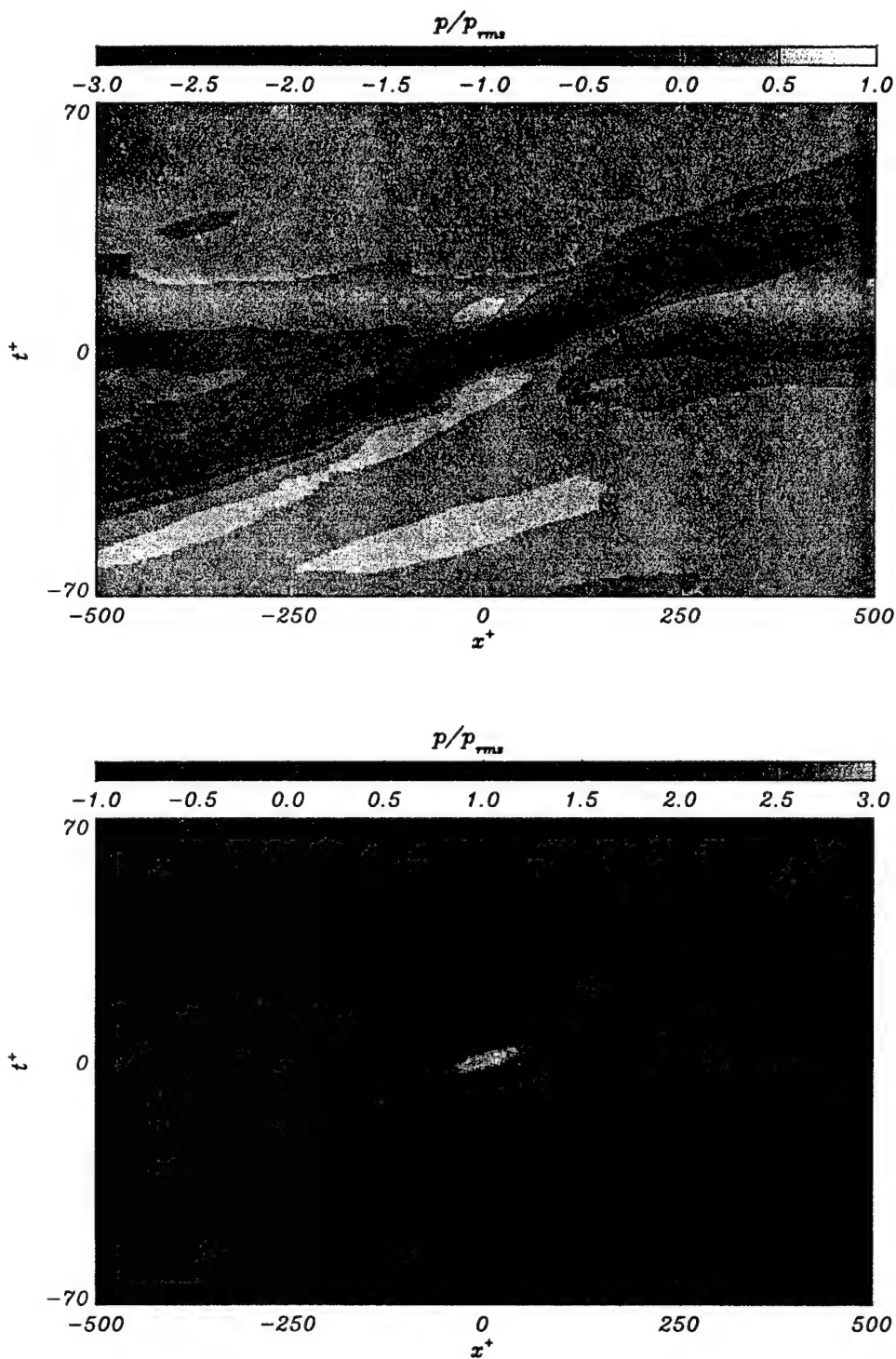


Figure 6.3 Time-Space Conditional Average for Negative (Top) and Positive (Bottom) Pressure Events. $Re_\theta = 3950$ and Threshold $\kappa = 2.5$

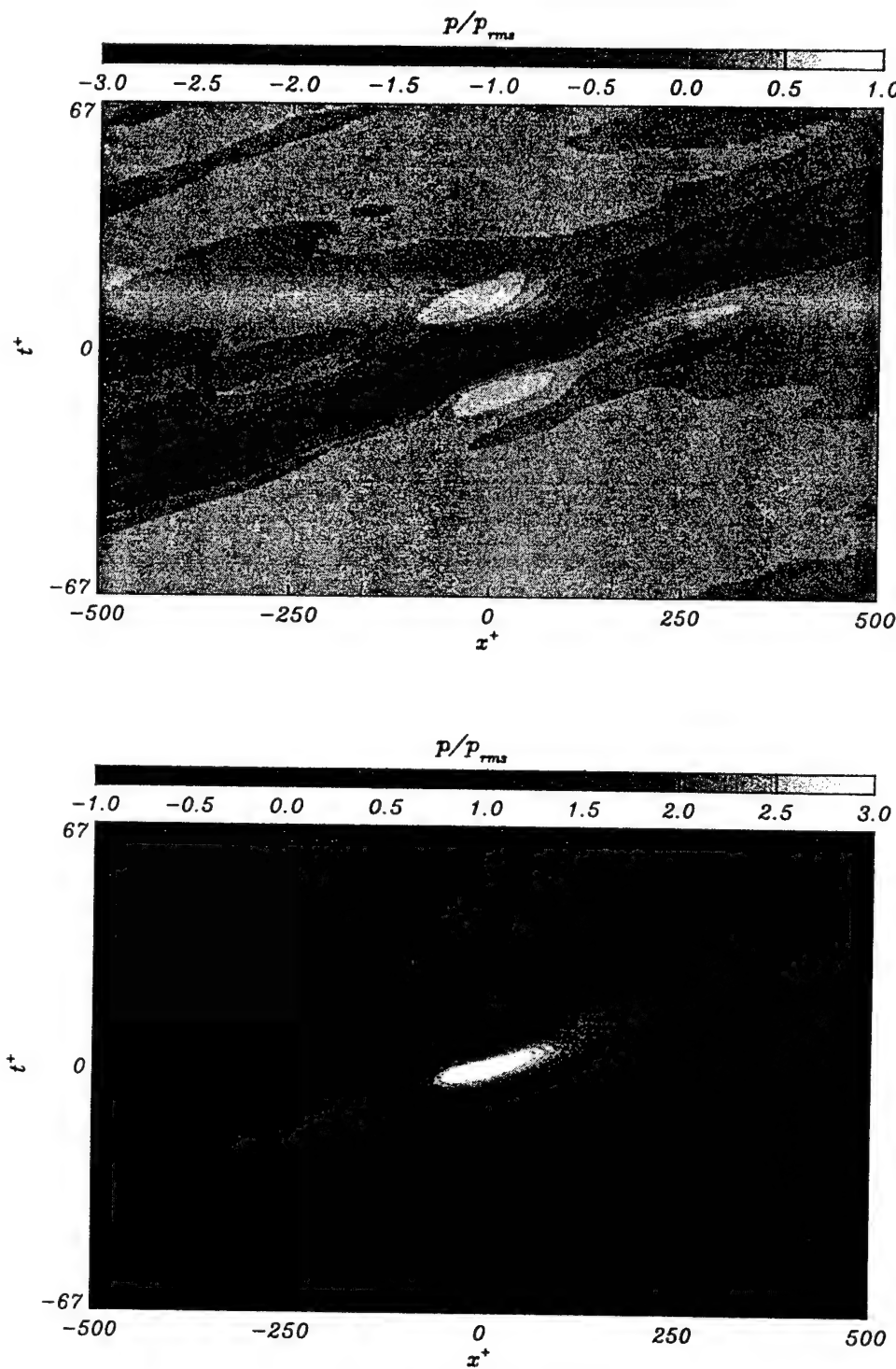


Figure 6.4 Time-Space Conditional Average for Negative (Top) and Positive (Bottom) Pressure Events. $Re_\theta = 5790$ and Threshold $\kappa = 2.5$

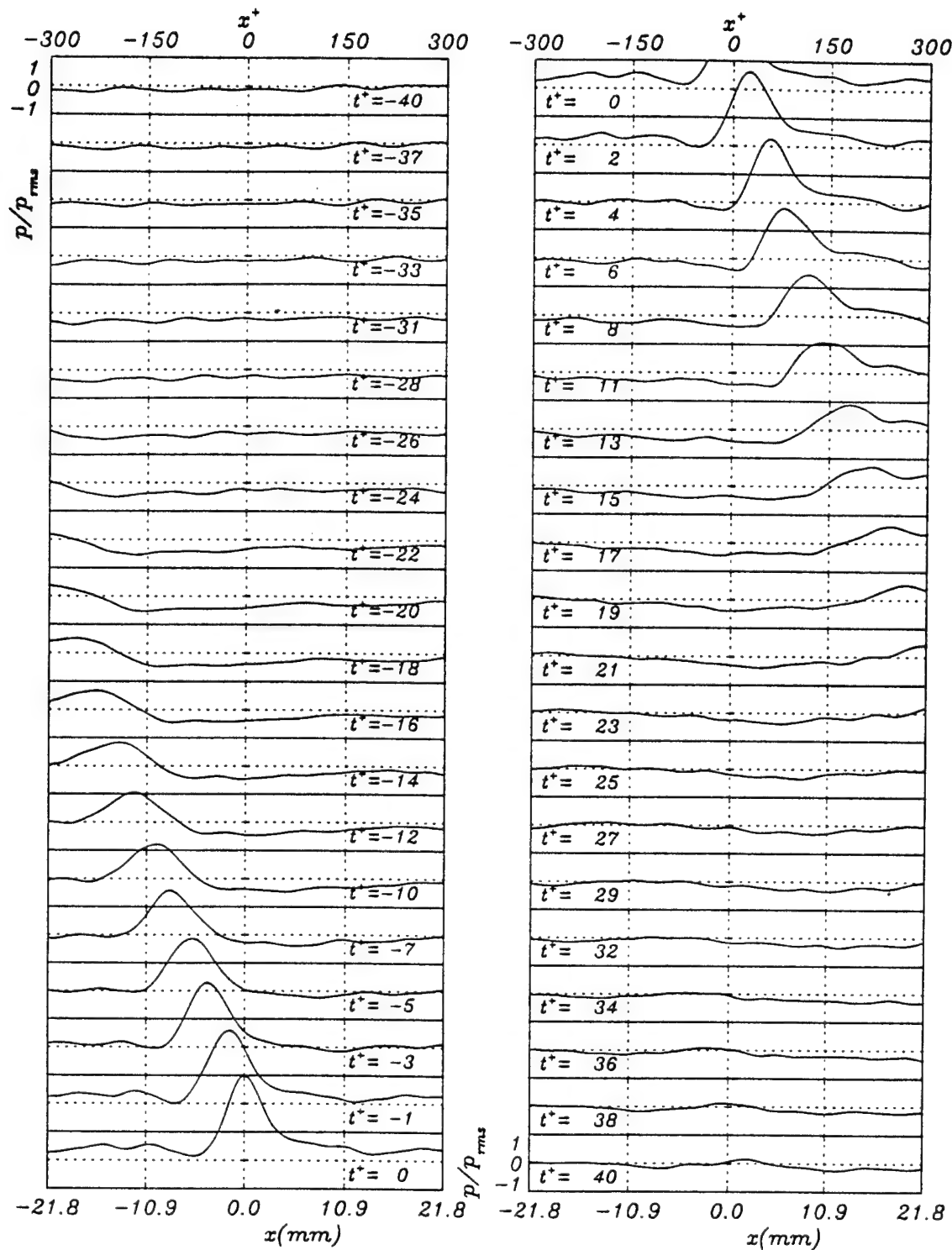


Figure 6.5a Time-Space Average for Positive Pressures. $Re_g = 1520$, $\kappa = 2.5$

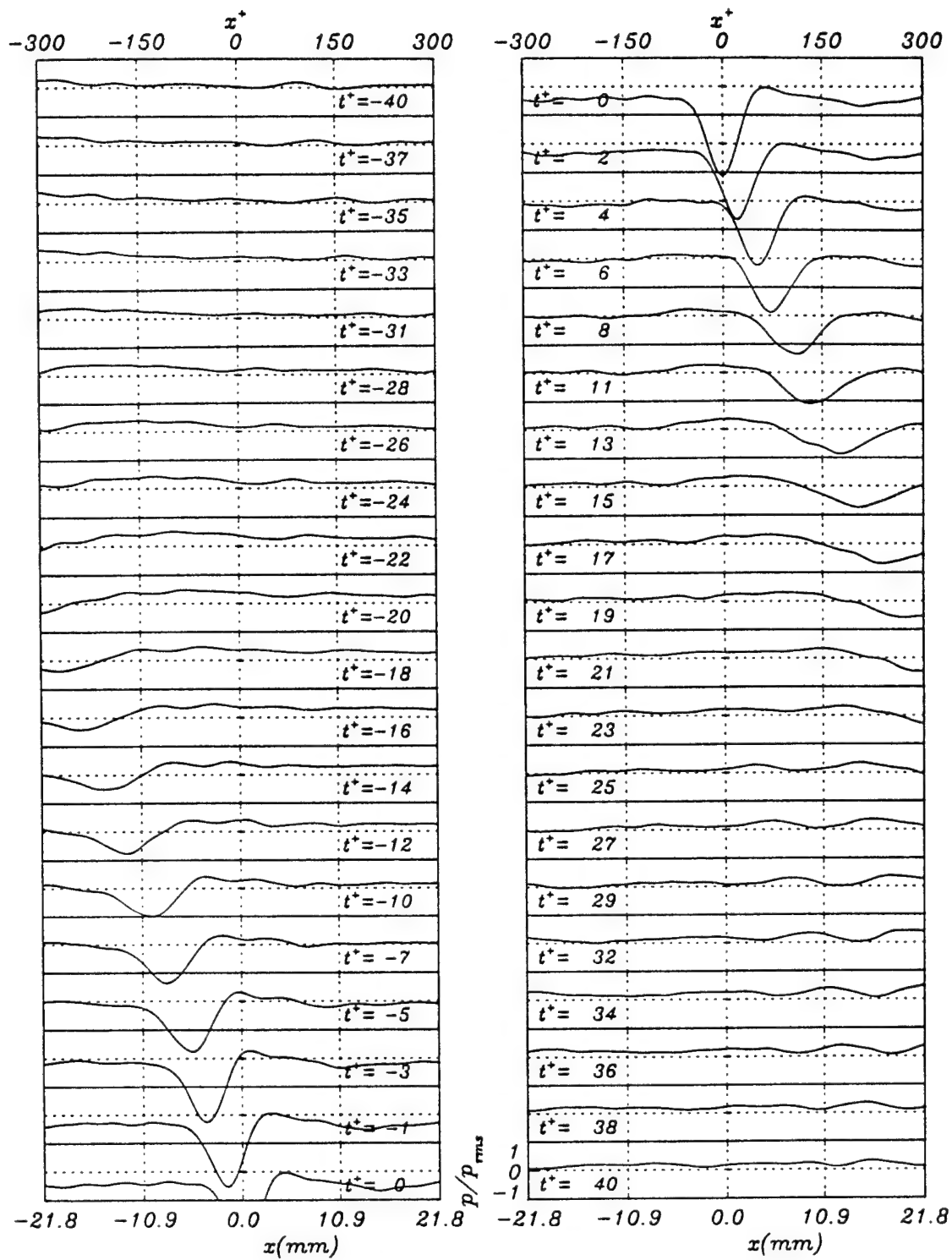


Figure 6.5b Time-Space Average for Negative Pressures. $Re_\theta = 1520$, $\kappa = 2.5$

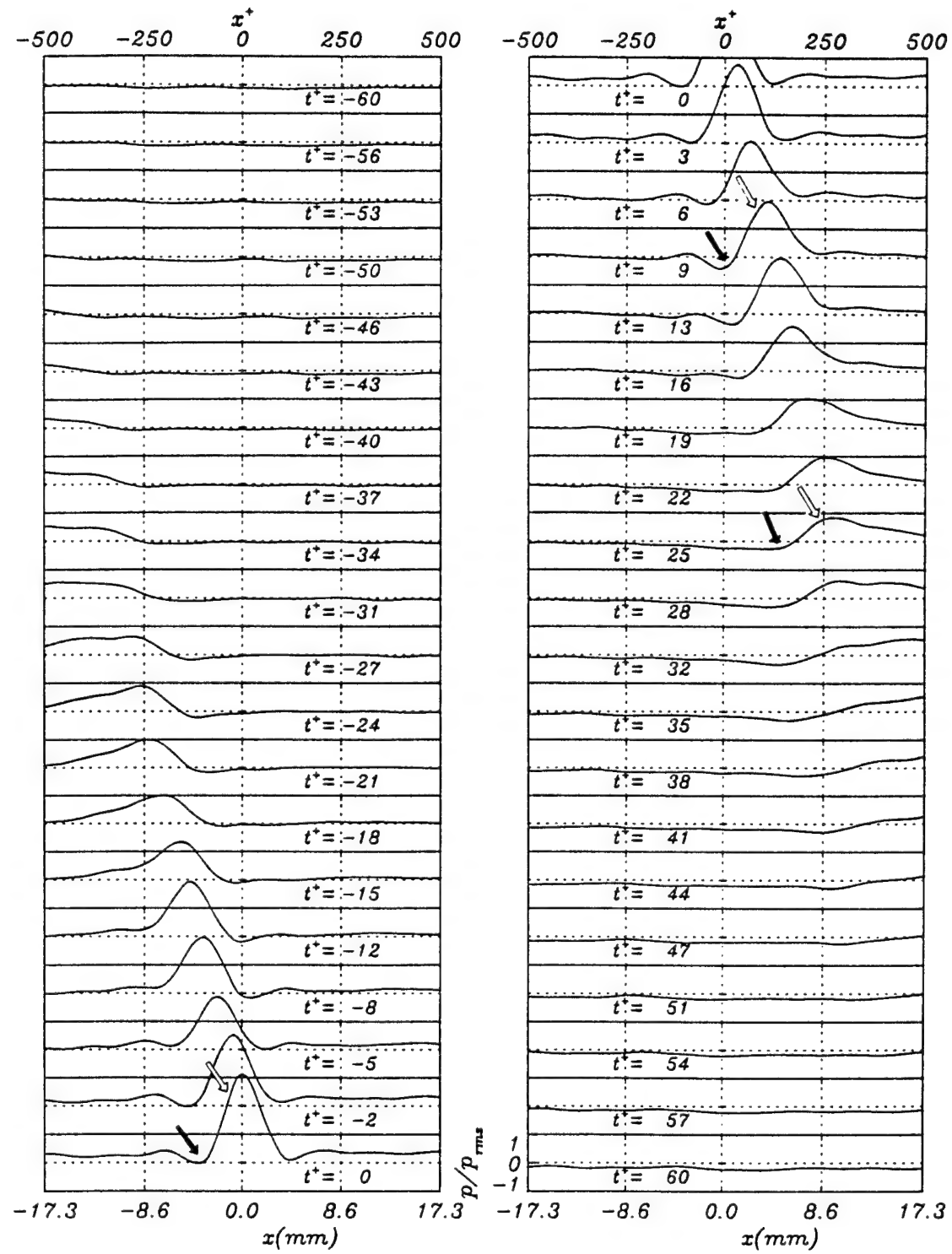


Figure 6.6a Time-Space Average for Positive Pressures. $Re_\theta = 3950$, $\kappa = 2.5$

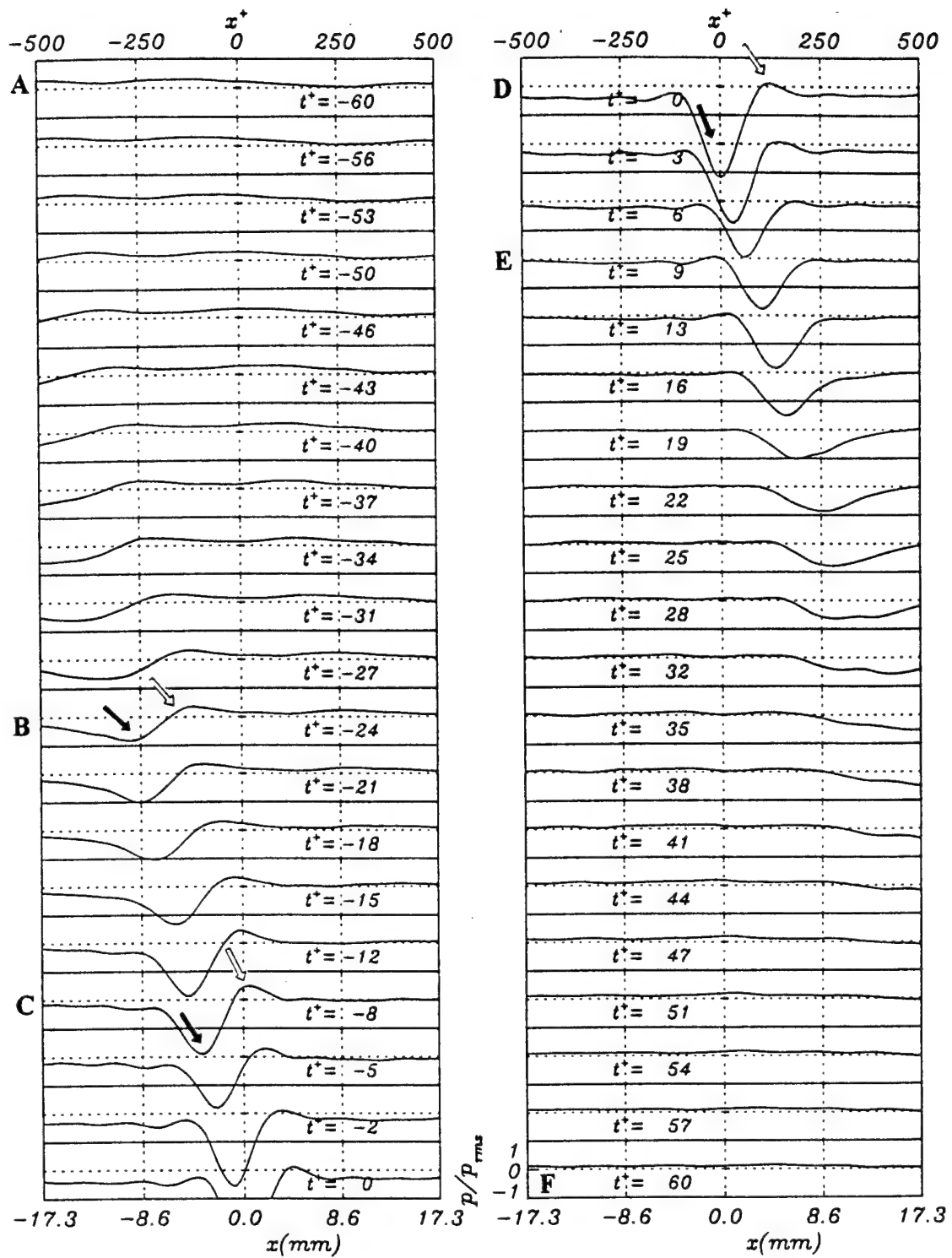


Figure 6.6b Time-Space Average for Negative Pressures. $Re_0 = 3950$, $\kappa = 2.5$

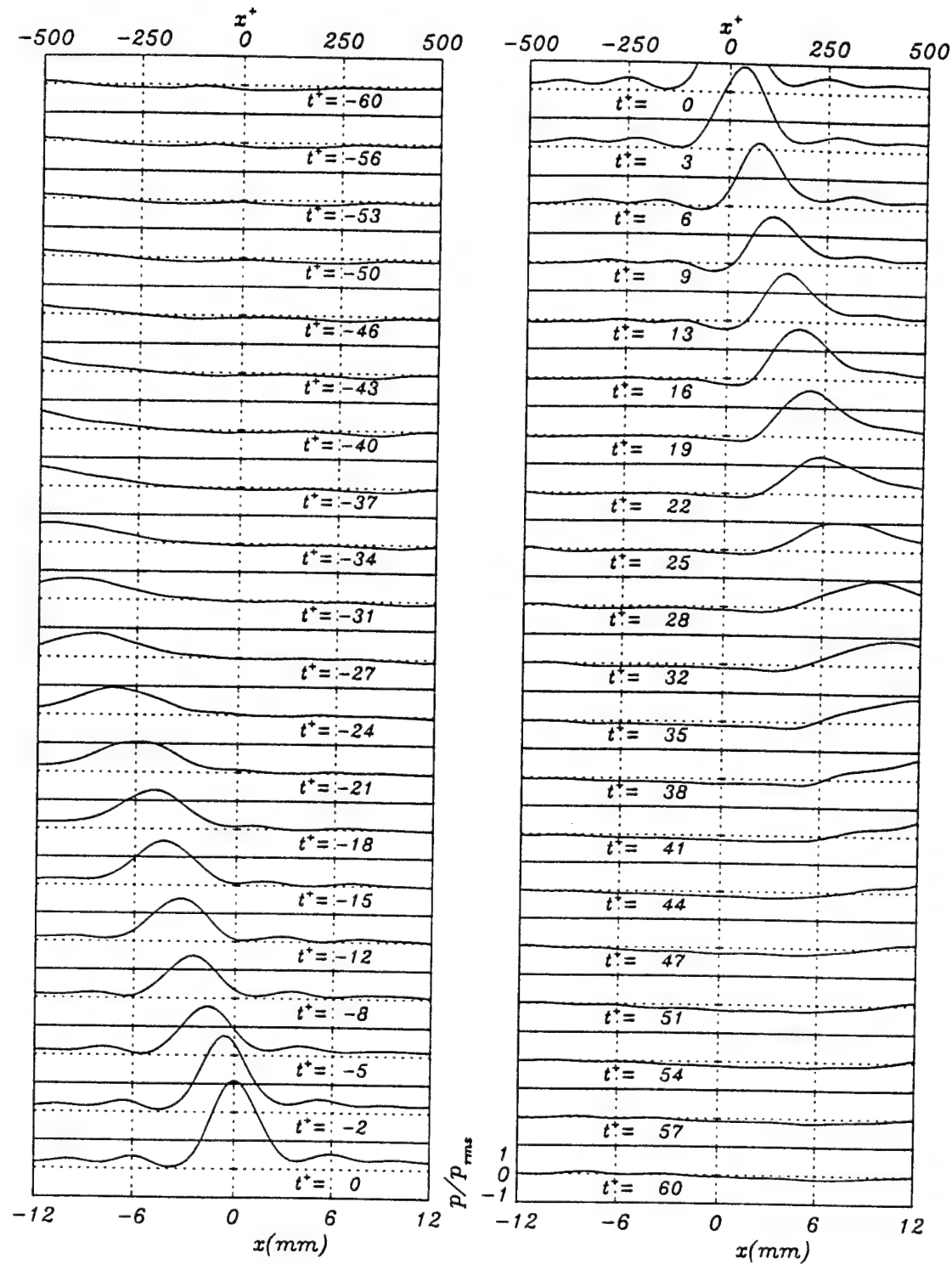


Figure 6.7a Time-Space Average for Positive Pressures. $Re_\theta = 5790$, $\kappa = 2.5$

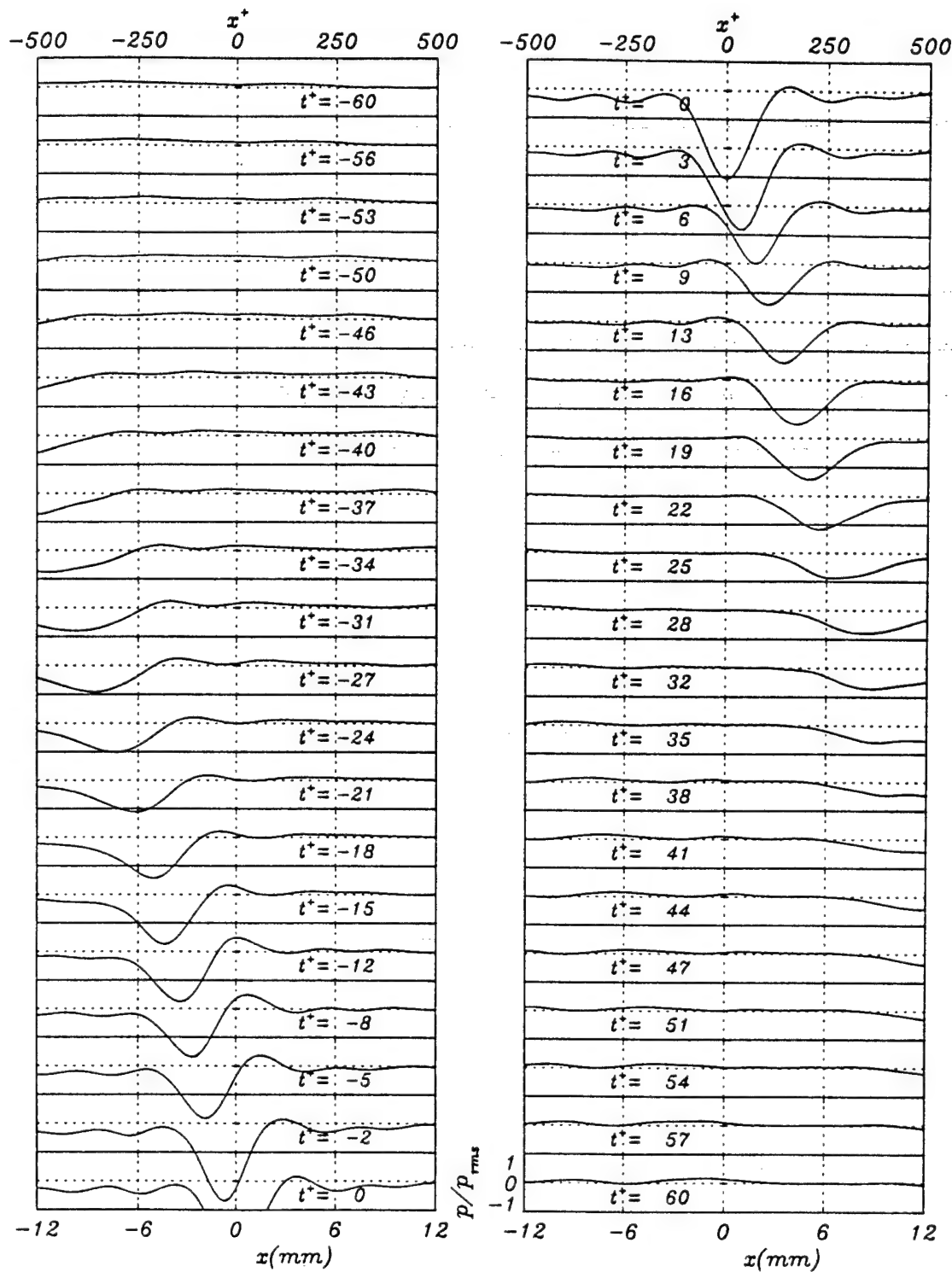


Figure 6.7b Time-Space Average for Negative Pressures. $Re_\theta = 5790$, $\kappa = 2.5$

The structure obtained from the conditional average is centered (in x^+ and t^+) about the detection point. By tracking the maximum magnitude of $\langle p(\chi^+, t^+) \rangle / p_{rms}$ (which from here on it is designated as $\langle p(x^+, t^+) \rangle / p_{rms}$) one can calculate a convection speed U_c . For all Reynolds numbers, U_c was determined to be $0.50U_\infty = 12.0u_\tau$ for the characteristic positive and negative pressure structures. There is an uncertainty of $\pm 0.05U_\infty$, $\pm 0.1u_\tau$ associated with the calculation of the convection velocity that arises from a small variation in the slope of the maximum magnitude of $\langle p(x^+, t^+) \rangle / p_{rms}$ away from the detection point obtained from Figures 6.2-4. Schewe (1983) reported a convection velocity of $11.9u_\tau$ for the characteristic pressure pattern in a flat plate boundary layer deduced from streamwise separated pressure transducers for $Re_\theta = 1400$. Krepling and Eckelmann (1979) determined the mean propagation velocity of perturbations in the viscous sublayer by space-time correlations of the velocity gradient at the wall for a turbulent channel flow at a Reynolds number of 7700 based upon the width of the channel and the center line velocity. They measured a convection velocity $c_x = 12.1u_\tau$ for streamwise fluctuations at the wall. Both of these values agree with the convection velocity of the characteristic pressure structure in the present investigation.

The conditional average calculations show the amplitude of the averaged pressure at the detection point ($x^+ = 0, t^+ = 0$) for both large amplitude positive and negative events to be $3p_{rms}$. The "size" of the conditionally averaged pressure structure for both large amplitude positive and negative events is determined by the width of the pressure peak at $t^+ = 0$. The size is approximately 225 in x^+ units. The distance convected by the large amplitude positive and negative events is $x^+ \approx 1000$ units, comparable with the characteristic pressure pattern of Schewe (1983) and consistent also with the convection of the near-wall vortex structure documented by Kline and Robinson (1990) and Robinson (1990). The data from the two rows offset in the streamwise direction in the current experiment are not sufficient to resolve the spanwise extent of the structure.

6.1.1 Negative Pressure Detections. The structure calculated from the conditional average is not symmetric about the detection point in the streamwise direction. In fact there exists a characteristic shape which is revealed in the negative and positive detections alike. For a negative pressure detection the shape of the structure is described by considering separate regions preceding and following the negative detection point. Referring to Figure 6.6b ($Re_\theta = 3950$) these regions will be described below.

- Region A–B, $-60 \leq t^* < -25$. A wide positive pressure region is distinguished along the streamwise extent of the averaging window ($-500 \leq x^* \leq 500$) where the pressure is on the average $+0.25p_{rms}$. The negative pressure peak, convecting through the region shown in the figure, is upstream of the wide positive pressure region and takes a value of $-0.75p_{rms}$ at station **B** ($t^* = -24$).
- Region B–C, $-25 \leq t^* < -8$. At $t^* \approx -25$ the positive pressure region begins to narrow (\Rightarrow) immediately downstream of the negative pressure peak (\rightarrow). The magnitude of the positive pressure increases to $+0.5p_{rms}$ at station **C** ($t^* = -8$).
- Region C–D, $-8 \leq t^* < 0$. The magnitude of the detection event increases from $-2p_{rms}$ to $-3p_{rms}$ between these stations. The pressure profile at $t^* = 0$ away from the detection event is negative, $-0.3p_{rms}$, with exception of the positive pressure peak which has convected to $x^* \approx 125$.
- Region D–E, $0 \leq t^* < 9$. The magnitude of the negative pressure decreases to $-2p_{rms}$ at station **E** ($t^* = 9$). The positive pressure observed at earlier t^* values has diminished and is no longer observed. The pressure upstream and downstream of the main event is nominally zero.
- Region E–F, $9 \leq t^* \leq 60$. The negative pressure peak convects downstream and decreases in magnitude.

6.1.2 Positive Pressure Detections. For a positive pressure detection, such as the one considered in Figure 6.6a, a negative peak (\rightarrow) is resolved on the upstream side of the positive pressure detection (\Rightarrow), from $t^* = 0$ to $t^* = 25$. The largest magnitude of

the negative pressure peak is approximately $-0.5p_{rms}$, and it is observed at $t^+ = 9$. In the average, the distance between the positive detection pressure peak ($2p_{rms}$ at $t^+ = 9$) and the negative pressure peak ($-0.5p_{rms}$ at $t^+ = 9$) revealed in the averaging is $125 x^+$ units. The distance that separated the negative detection pressure peak ($-2p_{rms}$ at $t^+ = -8$) from the positive pressure peak ($0.5p_{rms}$ at $t^+ = -8$) was also $125 x^+$ units. For $t^+ > 25$ there exists a wide negative pressure region (albeit smaller in magnitude) upstream of the detection event.

In summary, the averaging calculations indicate that events involving large negative wall pressure events are accompanied by regions with lower magnitude positive pressure occurring downstream and likewise high magnitude positive wall pressure events have lower magnitude negative pressure regions occurring upstream. For both cases the streamwise separation between positive and negative peaks is on the average of $125 x^+$ units.

The calculations also yield relatively large regions extending in the streamwise direction where the magnitude of wall pressure is above or below the nominal zero pressure level (on the order of $0.25p_{rms}$). These regions occur for $t^+ < -25$ in the negative detection and for $t^+ > 25$ in the positive detection averages. It is conjectured that flow structures exist alongside the detection event; the large extension of the $0.25p_{rms}$ pressure region in the averages is due to the decay of the structures away from the detection point and also to the different convection velocity of individual events.

The negative pressure detection reveals a broad positive pressure region (segment **A–B** in Fig. 6.6b) and a relatively large positive pressure structure (segment **B–D**) downstream of the negative pressure prior to the detection time $t^+ = 0$. Similarly, the positive pressure detection reveals a negative pressure structure and a broad negative pressure region upstream of the positive pressure after the detection time $t^+ = 0$ (Fig. 6.6a). It may thus be conjectured that in the average positive pressures precede (in time) negative pressures. This coincides with the conceptual model of Pratney and Brodkey (1978). In the model

large scale spanwise vortices are generated on the shear layer interface between high and low speed flow; the roll-up motions induce ejections and streamwise vortices above the wall. The spanwise vorticity at the interface is responsible for the positive pressure structures directly beneath (documented by Johansson et al., 1987, Eckelmann, 1990, Juckenhofel, 1995, Snarski and Lueptow, 1995, and including the results of Chapter 5); the shear layer then induces ejections at the interface near the wall which are responsible for the negative pressures.

The fact that pressure events further away from the detection point are not resolved in the conditional averaging (except in the very broad regions discussed earlier) is considered in the next section by examining a long time sequence.

6.2. Long Time Sequence of Wall Pressure

Figure 6.8 shows 6000 consecutive pressure profiles acquired at $Re_\theta = 5970$; pressures are non-dimensionalized by p_{rms} . The entire time sequence lasts 0.2308 seconds. For presentation purposes the entire time sequence is divided into six shorter sequences. The gray shading indicates the magnitude of pressure; -2 and $+2p_{rms}$ correspond to black and white respectively.

Figure 6.8 emphasizes that the conditional average (Figs. 6.2–7) washes out many important features of the flow. The physical importance of these may be answered by examining the convection or evolution of the structures that resemble the salient features obtained in the conditional average calculation. Repeating patterns in the vicinity of the conditional structure are then sought. The times of interest with respect to the occurrence of an event correspond to the locations where the broad pressure peaks were observed in the conditional averages ($t^* < -25$ in the negative and $t^* > 25$ in the positive detection).

Several events in Figure 6.8, where a large negative pressure occurs upstream of a large positive pressure, corroborate the result obtained in the conditional average calculations of Section 6.1. The typical separation between these peaks is close to the separation

calculated in the conditional averages (on the order of $x^* \approx 125$). Some of these events are labeled SL_1 , through SL_{14} . The labeling of these sequences as SL (explained in the following chapter) signify that a pressure signature of this form may be related to the occurrence of a shear layer.

SL phenomena highlighted in Figure 6.8 are observed to follow close behind another SL event. Events SL_1 – SL_2 , SL_3 – SL_5 and SL_7 – SL_{10} form three separate groups. The magnitude of pressure in these events is large, the pressures typically span across the viewing window and are good candidates for study. In each case, the pressure structures in the SL groups convect downstream. The separation between one SL and another SL structure ranges typically from 400 to 800 x^* units. There are relatively long intervals during which two or more SL structures coexist, up to $t^* \approx 150$.

In the case of SL_1 a large negative pressure upstream of a large positive pressure comes about at approximately $x^* \approx 0$. The unfavorable pressure gradient of this structure takes on particularly large values when it convects past $x^* \approx 500$ (the magnitude between the positive and negative pressure peaks exceeds $4p_{rms}$). The magnitude difference of $4p_{rms}$ continues to exist by the time it exits the viewing window at $x^* \approx 2000$. At approximately $x^* \approx 1600$, the negative pressure part of the structure detaches and convects at a slower speed. Upstream of SL_1 event SL_2 is observed. Like SL_1 , SL_2 also has a favorable pressure gradient associated with it. The positive pressure part of the structure dissipates at $x^* \approx 1300$. The negative part of the pressure structure convects beyond $x^* \approx 1300$ and appears to continue beyond the viewing window. There are 500 x^* units separating SL_1 and SL_2 .

A wide region of negative pressure, denoted as p_1 , convects along the row of microphones preceding the series of SL events denoted as 3, 4 and 5. Event SL_3 features a strong negative pressure peak upstream of a positive pressure peak. As in the case of SL_1 , SL_3 extends the entire viewing window (2100 x^* units). Event SL_4 features a quick succession of negative and positive pressure sequences, among them a negative pressure

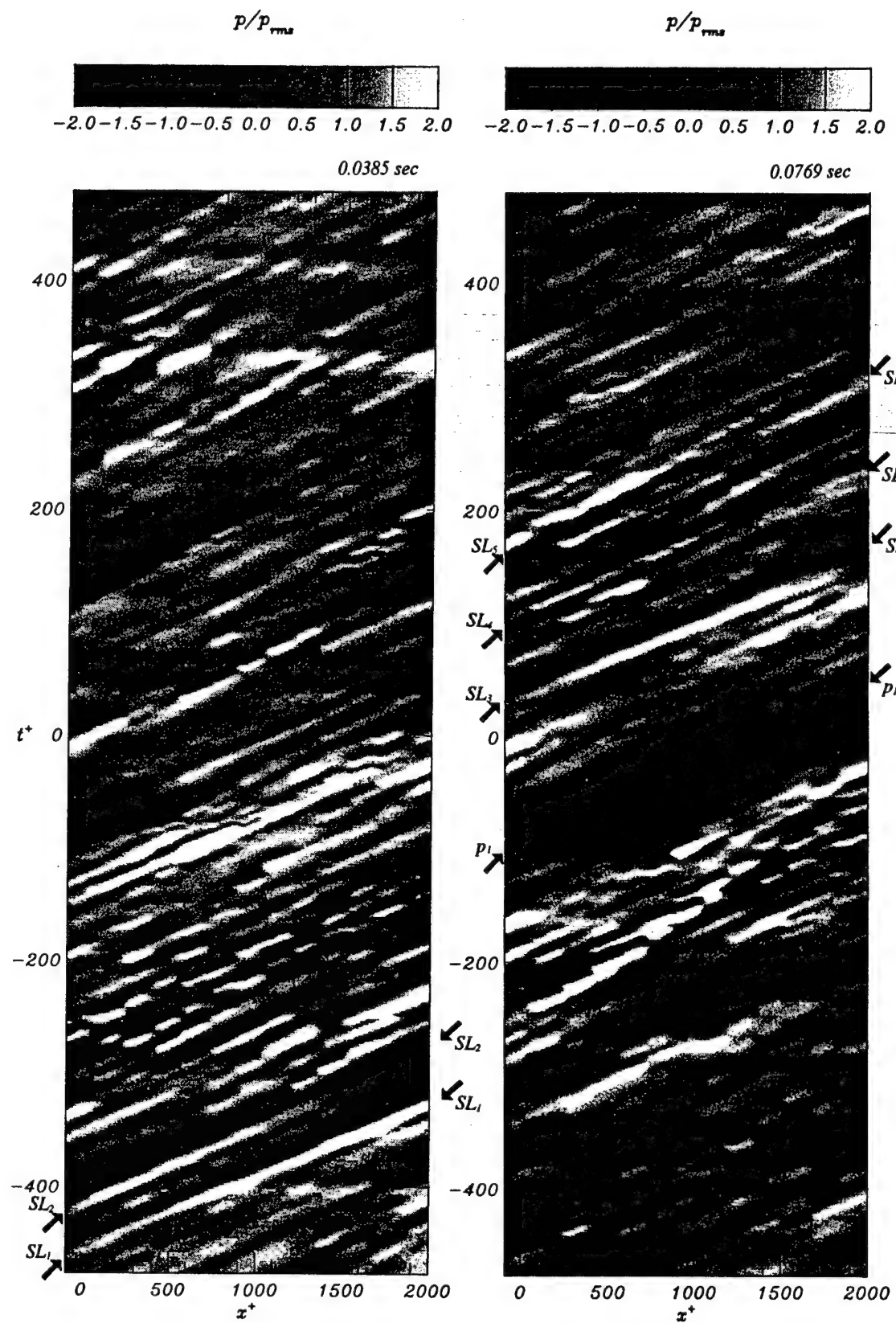


Figure 6.8 History of Wall Pressure at $Re_\theta = 5790$ (page one of three)

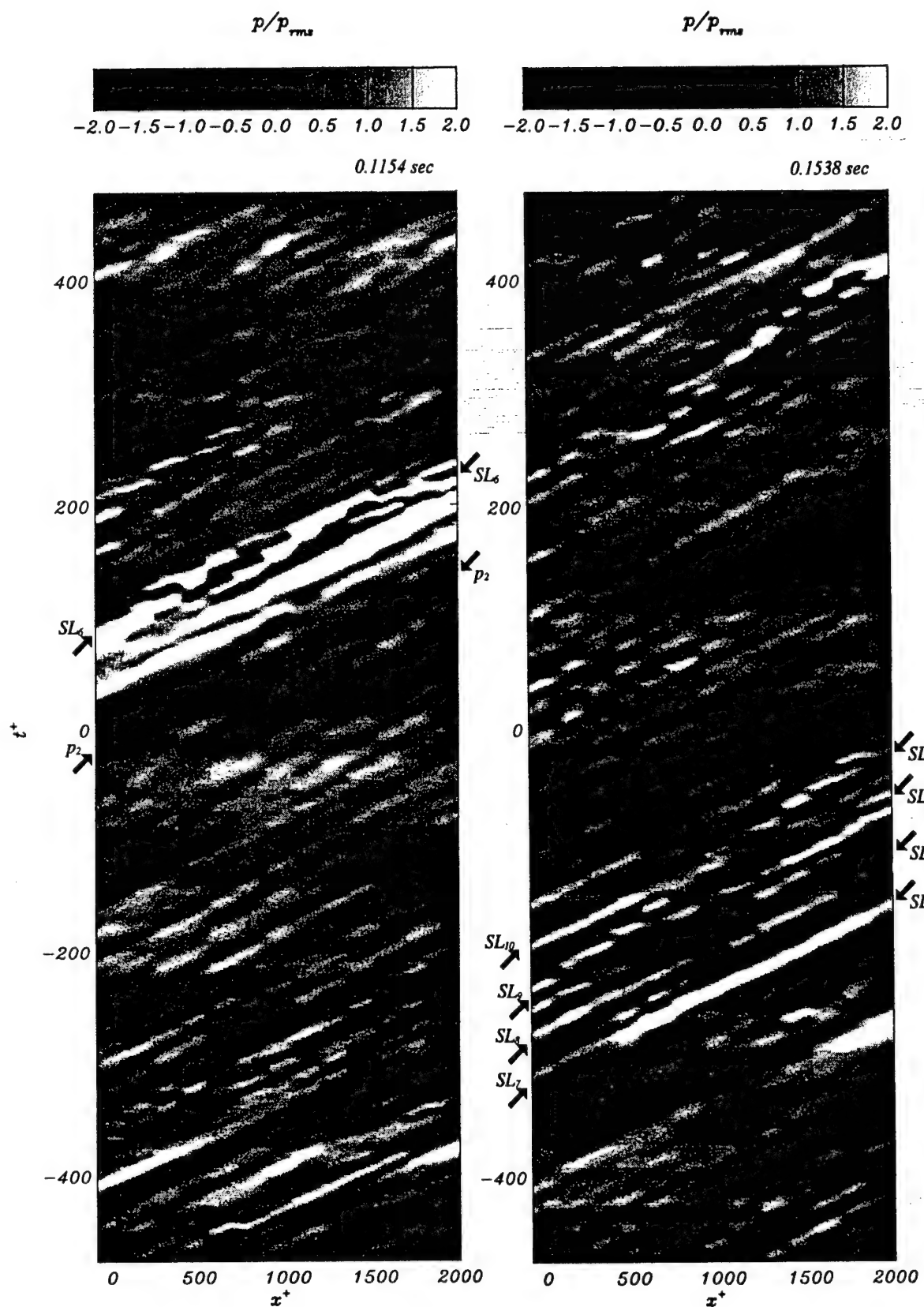


Figure 6.8 (continued, page two of three)

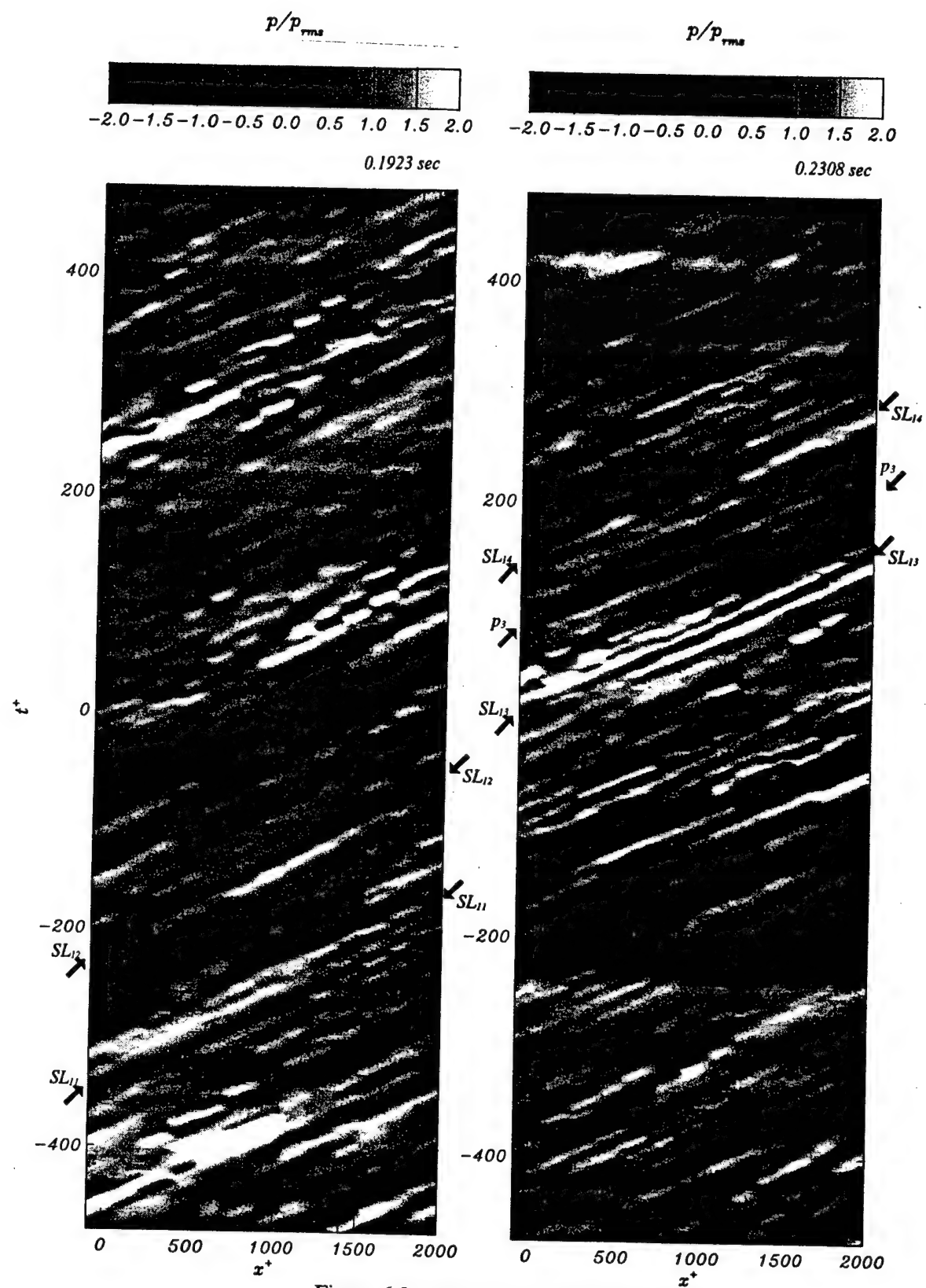


Figure 6.8 (continued; page three of three)

peak extending $x^+ \approx 2100$. Upstream and at a latter time several *SL* events are recorded and indicated as SL_5 . In between SL_4 and SL_5 , and after SL_5 , negative pressure structures are observed convecting at a speed lower than the convective speed of the *SL* phenomena themselves. The *SL* phenomena convect typically at $0.6U_\infty$. The slower events, such as these negative pressure events, convect as slow as $0.4U_\infty$.

On page two of Figure 6.8, a negative pressure event expands across the entire viewing window and is indicated as p_2 . The convection speed of this negative pressure decreases between 5–10% as the structure moves downstream. A very large magnitude and wide positive pressure structure denoted as SL_6 is observed upstream of p_2 . The positive pressure structure also extends the entire viewing window. It is composed of several distinct pressure peaks; these peaks are relatively close to one another and are separated by large negative pressures. Individual segments of this region display different convection speeds.

In the same page, the right hand side frame shows a succession of events denoted as SL_7 – SL_{10} . The close-spaced succession, approximately 125 x^+ units, of negative and positive pressures that characterize *SL* phenomena is present here. Event SL_7 exhibits a $p' > 3p_{rms}$ over 1500 viscous units. Event SL_8 exhibits a negative pressure peak over 2000 viscous units. Events SL_9 and SL_{10} interact with a positive pressure structure that spans the entire viewing window and convects at a much lower speed, approximately $0.35U_\infty$, compared with the larger $0.6U_\infty$ of the *SL* phenomena. The lower speed structure is similar to that observed in events SL_3 – SL_5 .

Page three of Figure 6.8 shows two other *SL* events, SL_{11} and SL_{12} . These are separated approximately by $t^+ \approx 100$ (or 1200 wall units). The first event convects at $0.65U_\infty$ the second event convects at $0.55U_\infty$. An issue for further study is whether these events are correlated to one another given their larger separation compared with that observed in previous *SL* groupings. In other words, how far may these events be separated and be related to one another.

Finally, in the same page, the second frame shows event SL_{13} characterized by a strong and positive pressure peak which already exists when it enters the viewing window; downstream of it, at $x^+ \approx 600$ in the viewing window coordinates, a negative and positive pressure structure comes about. The strength of this downstream structure is maintained throughout the viewing window. At a latter time small scale negative pressures occur in the viewing window before another SL type event appears. These are denoted as p_3 and SL_{14} respectively.

In summary, the events described above stress the difference between the characteristic flow structure obtained through conditional averaging and the instantaneous feature of the flow. The averaging calculations reveal a structure composed of a negative pressure upstream of a positive pressure separated by 125 x^+ units (SL phenomena). The average structure is readily appreciated in the instantaneous pressure profiles. The instantaneous profiles show that negative pressures also occur with significant number downstream of the positive pressure. It is difficult to establish whether in the SL phenomena the positive pressure precedes (in time) the negative or the negative precedes the positive. It was reasoned in Section 6.1, from the results obtained in the averaging calculations, that positive pressures precede negative pressures. The sequences observed from the pressure history show several instances where this is the case, although it does also show the contrary. The close succession of positive and negative pressure structures occurs with certain periodicity, suggesting that these are not isolated events but are related in some way. Related to SL phenomena is the presence of a negative pressure structure (when no positive pressure is observed in the immediate vicinity, approximately 300 x^+ units) observed downstream of the SL phenomena. Finally visual inspection of the evolution of the wall pressure is useful in distinguishing the overlapping of distinct structures with different speeds. Occasionally a slower convection velocity is superimposed across several structures with faster convection velocities. The slower velocities have been observed to be as low as $0.35U_\infty$. More characteristic velocities range from $0.50-0.60U_\infty = 12.0-14u_r$.

The average wall distance for the flow structures related to the characteristic wall pressure structure may be estimated assuming the velocity sources move with the mean local velocity. Reference to the velocity profile of Figure 4.3 shows that for $U_c = 0.50U_\infty = 12u_\tau$, the velocity calculated in the conditional average, the wall distance is $y^+ = 20$. The average distance of these velocity structures therefore lay in the buffer layer. The occurrence of the bursting phenomena is most probable in the buffer layer (Kim et al., 1971) where the maximum rates of turbulent production and the largest rms values of velocity also occur.

CHAPTER VII

STRUCTURES IN THE TURBULENT BOUNDARY LAYER

7.1 Coherent Structures

The effectiveness of predictive turbulent models and turbulent control mechanisms relies upon accurate knowledge of the processes responsible for the creation and maintenance of turbulence. Complete knowledge of the flow dynamics in a turbulent boundary layer over a flat plate requires the identification of all coherent structures, detailed descriptions of their spatial character and determination of the space-time relationships between them. The relative importance of each coherent structure is determined by calculating space and time probability distribution functions, conditional average statistics and the contribution of each structure to terms in the Reynolds average momentum equation such as the Reynolds stress term $-\overline{u'v'}$. The generation and evolution of coherent structures, a description of recurring sequences in the flow field, are the foundation to understanding the flow interactions. The cause and effect roles in the flow dynamics become the foundation for significant contributions to turbulent models and turbulence control methods.

A comprehensive organization of the various coherent structures and events in a turbulent boundary layer was presented by Robinson et al. (1988). Robinson et al. provide a classification that includes all types of non-random events which have been the object of analysis by researchers. This classification includes the following phenomena:

1. Near-wall low-speed streaks
2. Ejections of low-speed fluid outward from the wall
3. Sweeps of high-speed fluid inward to the wall
4. Vortical structures of various forms
5. Near-wall shear layers exhibiting strong spanwise vorticity and $\partial u' / \partial x$
6. Near-wall "pockets" or regions swept clean of near-wall marked fluid

7. Large (δ -scale) discontinuity in the streamwise velocity or “backs”
8. Large (δ -scale) motions capped by bulges in the outer turb/potential interface

Robinson et al. (1988) explored Spalart’s direct numerical simulations at $Re_\theta = U_\infty \theta / \nu = 670$ of a flat plate turbulent boundary layer (Spalart, 1988). The authors presented examples of all the above classes of boundary layer structure. The authors also simulated some experimental techniques in the databases to clarify probe based or visualization results.

The study of coherent structures in databases obtained from the direct numerical simulations are however limited to small Reynolds numbers. At the present moment, costs and time requirements make calculations at larger Reynolds number not feasible. Many practical flow applications involve much higher Reynolds numbers. The rest of the chapter will carefully discuss measurements of velocity and pressure in a turbulent boundary layer over a flat plate. The measurements comprise the simultaneous use of Particle Image Velocimetry and an array of miniature microphones at the wall. This set-up is able to resolve the spatial character of the flow in the streamwise and wall normal directions as in the direct numerical simulations above with the exception of the near-wall region (Section 4.1). In addition the experiments extend to Re_θ above those used in the simulations.

7.2 Objectives of the Current Measurements

The current study considers a select number of the turbulent structures from the classification of Robinson et al. (1988) as well as others that have been deduced from the current measurements. The effect of Reynolds number on boundary layer structures is also investigated. The Reynolds numbers considered (Re_θ) extend from 1520 to 5790.

The study is based on measurements that combine the use of Particle Image Velocimetry and an array of microphones to capture simultaneously two components of the velocity field in the xy plane and the wall pressure in the x direction underneath the

velocity plane. The x and y coordinates correspond to the streamwise and wall normal coordinates respectively. The velocity measurements extend from the buffer layer to the turbulent/nonturbulent or vortical/nonvortical interface and 2δ in the streamwise direction. The wall pressure measurements extend δ in the streamwise direction (refer to Chapter 3 for details on the experimental set-up).

A typical velocity-pressure realization exhibits several structures simultaneously which allows for spatial relationships between co-existing structures to be considered. The figures presented herein are considered examples and do not necessarily illustrate all realizations. An advantage of considering the instantaneous velocity-pressure field as compared with the averaged or filtered field obtained by most statistical techniques is that significant features may be identified that otherwise would be "washed-out".

The next section will explore in detail the spatial character and selected spatial relationships of the following key structures,

- Near wall shear layers
- Near wall shear layers with strong spanwise vorticity
- Near wall shear layers with concentrated Reynolds stress
- Backs or large scale shear layers
- Backs and concentrations of strong spanwise vorticity
- Bulges in the outer interface and large scale motions

as well as characteristic wall pressure fluctuations that include,

- Convection of large amplitude wall pressure events
- Large amplitude positive pressures beneath shear layers
- Large amplitude negative pressures beneath local high momentum flow

The current experimental configuration does not capture the sublayer streaky structure since the velocity field is not resolved in the immediate wall region where the wall low-speed streaks have been observed (i.e., at $y^+ = 10$.)

7.3 Selected Structural Features

The treatment of coherent structures, particularly in turbulent flows, has often been associated with vortices. What constitutes a vortex however has been of considerable concern. A significant number of definitions for a vortex have been proposed, which have resulted in separate identification criteria. Jeong and Hussain (1995) review vortex definitions, and propose a refined criteria that is able to identify a vortex for a wide range of Reynolds numbers. The reader is referred to Jeong and Hussain for a thorough review of this issue. In the present study, the word eddy is used to describe closed or spiral pathlines. The identification of eddies are performed from visual analysis of the instantaneous velocity fields. Additional criteria would require a more reliable assessment that the structure be a vortex and for this reason the word eddy and not vortex is used.

7.3.1 Near Wall Shear Layers. Flow visualization studies (Corino and Broadkey, 1969), multiple probe measurements (Johansson et al., 1987, Snarski and Lueptow, 1995, Juckenhoefel, 1995) and direct numerical simulations (Spalart, 1988, Robinson et al., 1988) have demonstrated the existence of sloping $\partial u' / \partial x$ shear layers near the wall ($y^+ < 80$) in wall bounded turbulent flows.

Analysis by Robinson et al. (1988) of direct numerical simulations performed at $Re_\theta = 670$ showed the near wall region (particularly below $y^+ = 100$) well populated with near wall shear layers. The structures were nearly parallel to the wall in the sublayer and sloped at an increasing but shallow ($< 20^\circ$) angle farther away from the wall. The spanwise dimension of the near wall shear layer ranged from 30 to 60 viscous lengths. Johansson et al. (1987) calculated the propagation velocity of the near wall shear layers to be $10.6 u_r$; the coherence of the near wall shear layers was estimated to extend over 1000 viscous units.

In the current study numerous random instantaneous velocity fields have been examined. The velocity fields show the predominance of shear layers near the wall inclined at shallow angles with respect to the wall, similar to those exhibited in the

simulations of Robinson et al. at much lower Reynolds numbers. Examples at $Re_\theta = 1520, 3950$ and 5790 are shown in Figure 7.1. The instantaneous velocity fields are represented by the Reynolds decomposed fluctuation velocities u', v' (top) and by the instantaneous u, v vectors in an xy plane moving at a specified convection velocity U_c (bottom). The convection velocity U_c was chosen to highlight the same shear layer features, such as slope of the interface and eddies along the interface, in both representations and was chosen to be $U_c = 0.70 U_\infty$ for $Re_\theta = 1520$ and $0.85 U_\infty$ for $Re_\theta = 3950$ and 5790 . The shear layer represented at $Re_\theta = 1520$ occurs in the near wall region, $y^+ < 60$, where the inclination angle of the interface is less than 20° . The shear layer interface further away from the wall exhibits an angle of 45° . The realizations shown from the higher Reynolds number cases, $Re_\theta = 3950$ and 5790 , exhibit shear layers with slopes on the order of 20° . The angle of 20° coincides with angles obtained in the numerical calculations although the present shear layers contrast with the numerical calculations in that structures such as those of Figure 7.1 extend further in the wall normal direction and well into the logarithmic region.

7.3.2 Near wall Shear Layers with Strong Spanwise Vorticity. Eddies are identified when the instantaneous, Reynolds decomposed, velocity field displays a roughly circular or spiral pattern as shown in the top plots of Fig. 7.1a, b and c. The convection velocity of the eddy is estimated using the mean flow velocity profile at the y -normal location where the circular structure is located. Alternatively, a reference frame convecting with the velocity of the eddy itself may be chosen to display the eddy structure (bottom plots of Fig. 7.1a, b and c).

Based upon the above definition of an eddy, the near wall shear layers of Figure 7.1 exhibit mostly spanwise eddies with their sense of rotation the same as the mean vorticity. At $Re_\theta = 1520$ (Fig. 7.1a), eddies **A** and **B** are identified. At $Re_\theta = 3950$ (Fig. 7.1b), eddies **A** and **B** are identified approximately at the same y location. For $Re_\theta = 1520$ and 3950 the Reynolds decomposed and the moving reference frame velocity fields exhibit

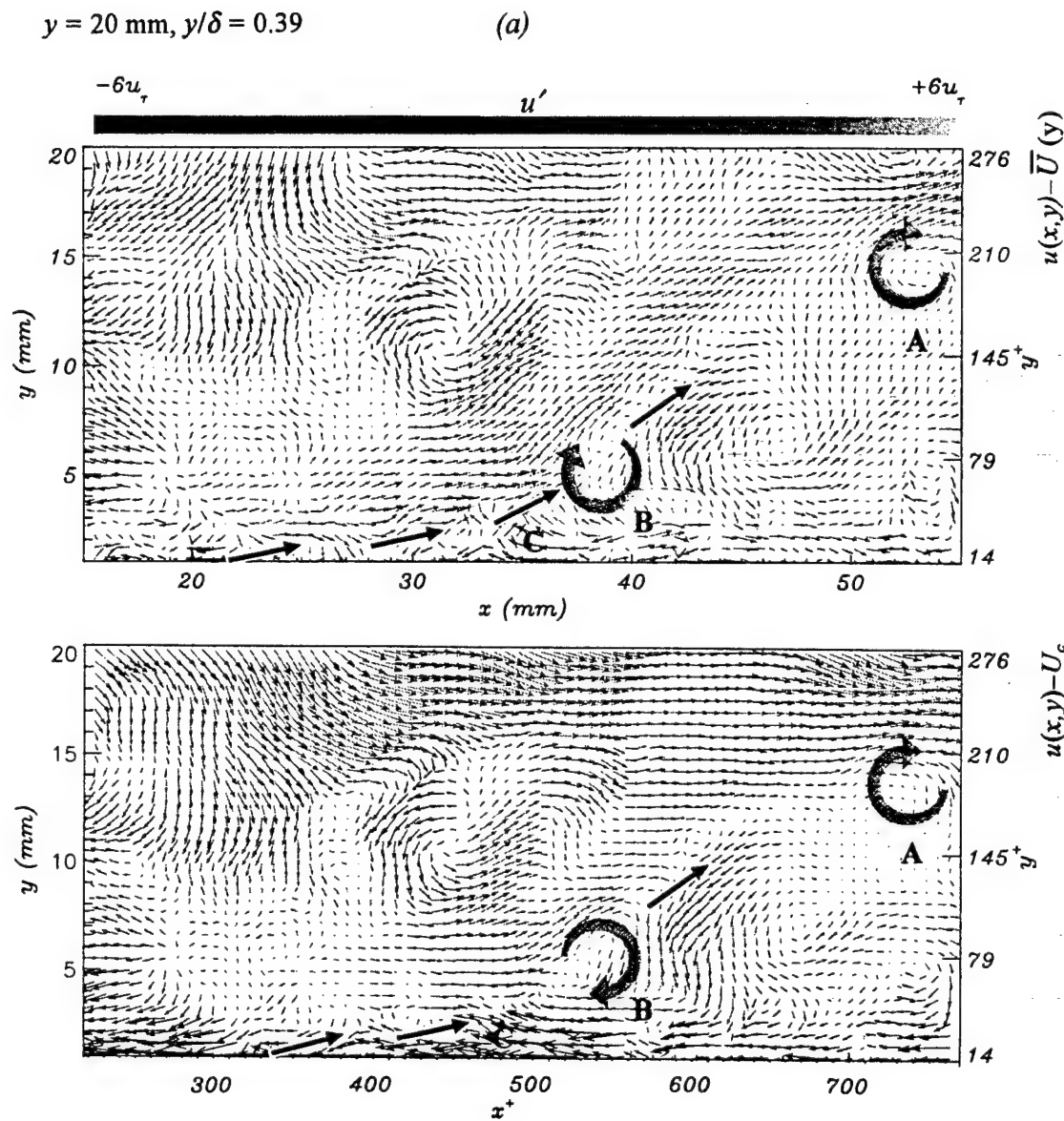


Figure 7.1 Near Wall Shear Layers (a) $Re_\theta = 1520$, $U_c = 0.70 U_\infty$, (b) $Re_\theta = 3950$, $U_c = 0.85 U_\infty$, (c) $Re_\theta = 5790$, $U_c = 0.85 U_\infty$: Reynolds Decomposed Vector Field (Top) and Vector Field in a Plane Moving at U_c (bottom)

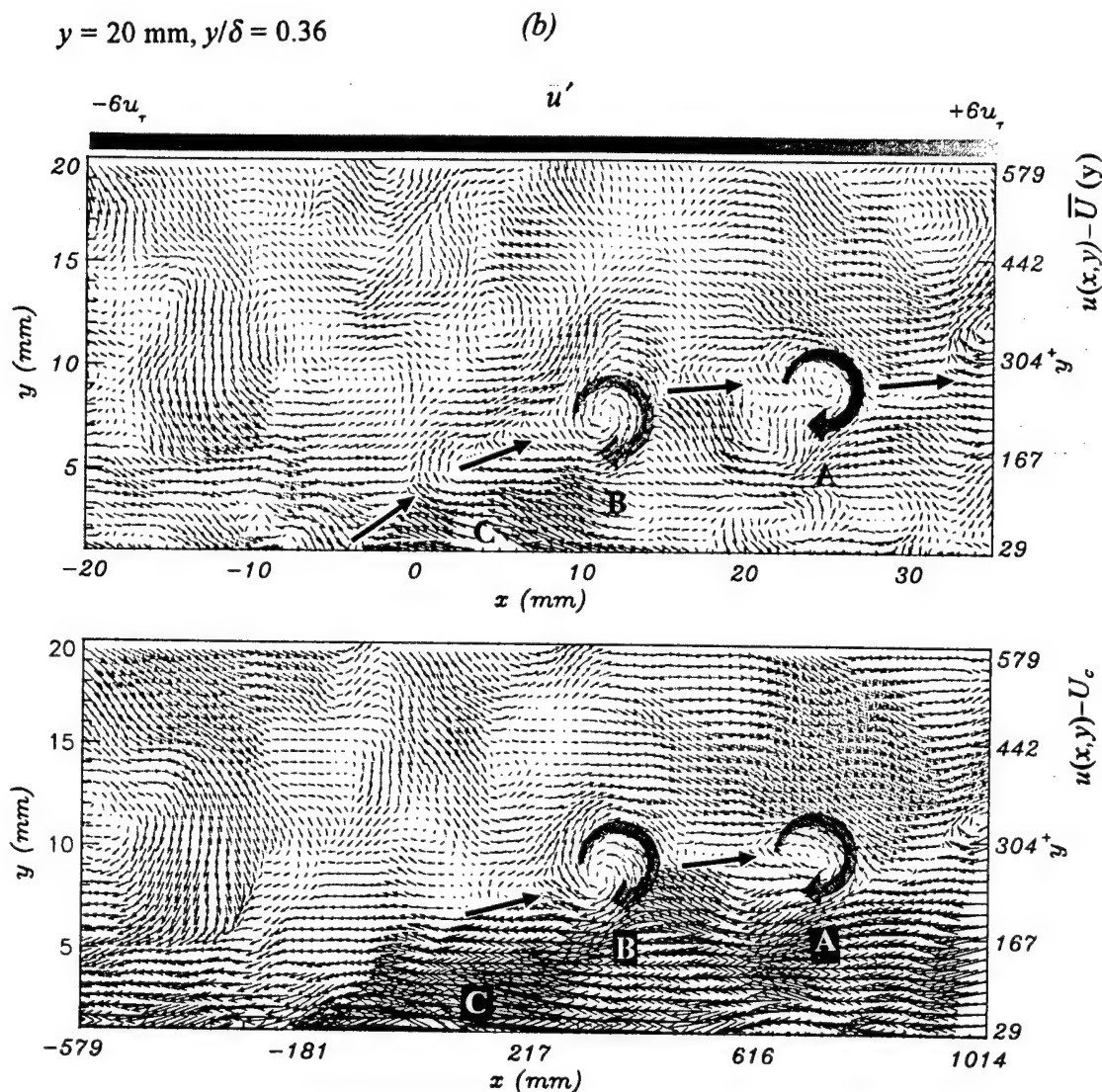


Figure 7.1 (continued, page two of three)

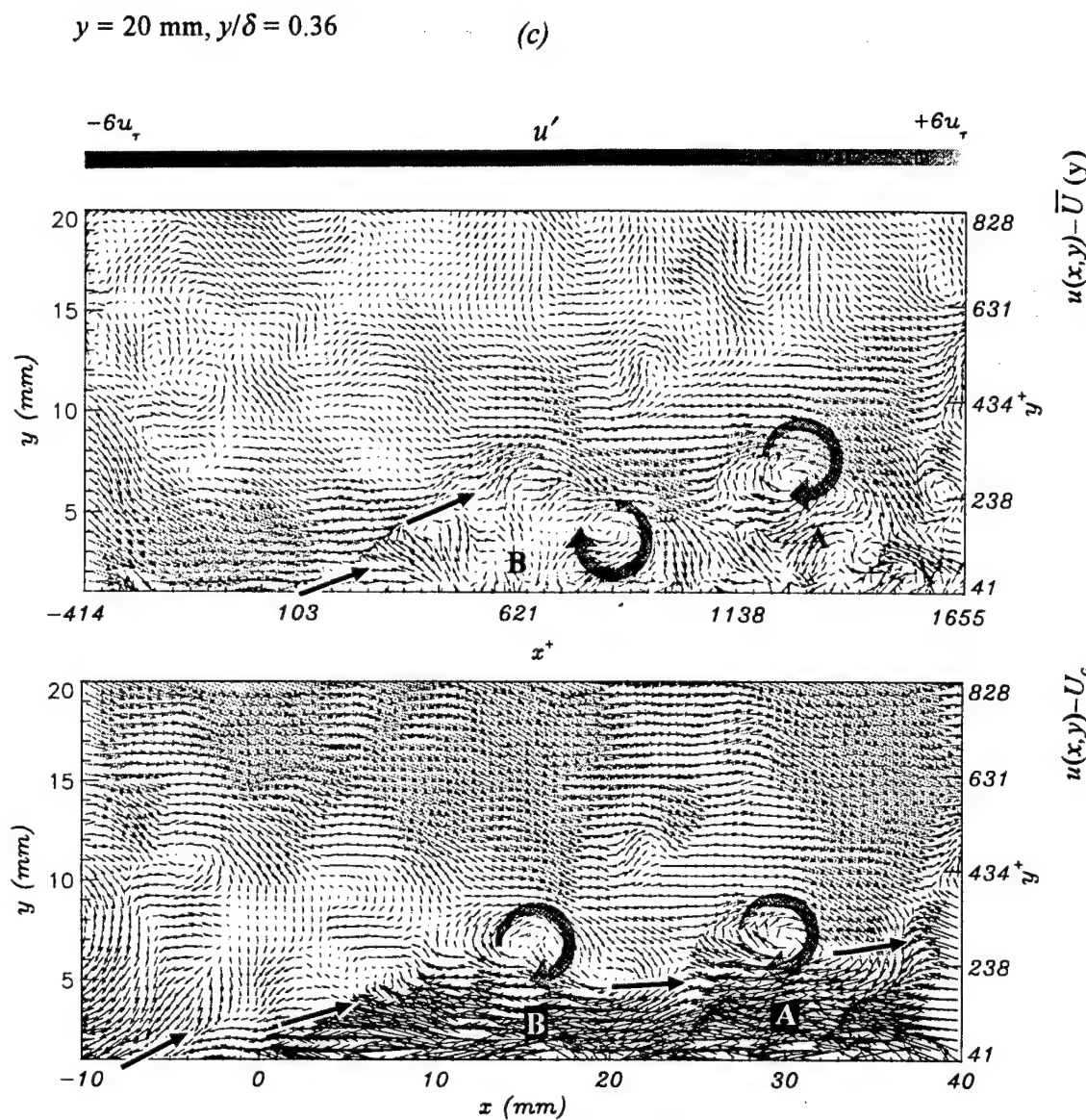


Figure 7.1 (continued, page three of three)

nearly identical eddies. At $Re_\theta = 5790$ (Fig. 7.1c), eddies **A** and **B** are identified nearly parallel to the wall in the case of the moving reference frame; in the case of the Reynolds decomposed field the eddies are noted at different heights.

Regions of significant vorticity may not necessarily correspond to vortex structures. It is important to distinguish between regions of distributed vorticity and vortical structures. Total vorticity is calculated for each of the respective velocity fields of Figure 7.1. Figure 7.2 shows total vorticity for $Re_\theta = 1520$ (top), 3950 (middle) and 5790 (bottom). The vorticity contours are displayed for levels of total vorticity $\omega^+ < -0.07$. The threshold, $\omega^+ = -0.07$, corresponds to three times the rms value of the vorticity in the velocity region considered. The structures calculated therefore correspond to strong contributions of spiral motions with sense of rotation the same as the mean vorticity. The vorticity is high along the shear layer interface for each of the Reynolds numbers. The regions of more pronounced vorticity occur near where the eddies are located. The locations of the eddies identified in Figure 7.1 are indicated in the plots of Figure 7.2.

A number of studies (beginning with Theodorsen, 1952) have conjectured that the loop-like eddies of Figure 7.1 are the heads of horseshoe structures (sometimes known as hairpins at higher Reynolds numbers). Successive eddies at the interface may suggest that an array of hairpin vortices exists, where one hairpin vortex rides on the back of another. Data obtained by Adrian et al. (1995) supports the existence of arrays of hairpin vortices. The DNS calculations contrast with the present work in that only one vortex occurs along the shear layer interface and it is located at the outer tip of the shear layer.

7.3.3 Near wall Shear Layers and Concentration of Reynolds Stress. The Reynolds shear stress, $-\overline{u'v'}$, is defined as a time average and differs from the instantaneous distribution of $u'v'$. Following Robinson et al. (1988) the value of $u'v'$ is denoted as the “shear product”. The shear product is classified into four categories depending on the signs of u' and v' according to the quadrant method introduced by Wallace et al. (1977) and Willmarth and Lu (1972).

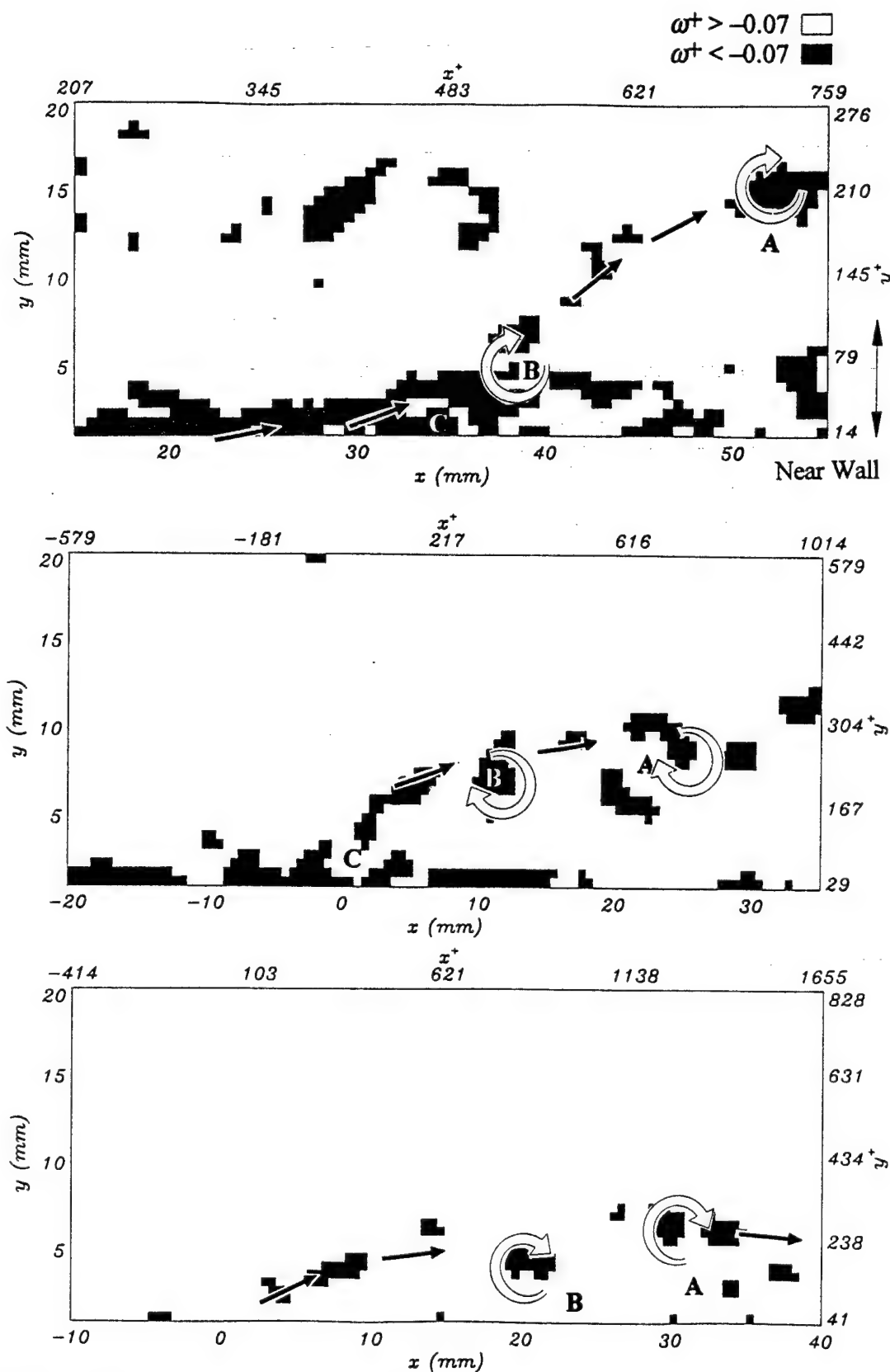


Figure 7.2 Instantaneous Spanwise Total Vorticity in the Same Velocity Fields as Fig. 7.1: $Re_\theta = 1520$ (Top), $Re_\theta = 3950$ (Middle), $Re_\theta = 5790$ (Bottom)

The quadrant technique establishes characteristic motions that contribute significantly to the Reynolds shear stress: ejections are regions of low streamwise velocity with motion away from the wall, whereas sweeps are regions of high streamwise velocity with motions towards the wall. Ejections are defined by $u' < 0, v' > 0$ and sweeps are defined by $u' > 0, v' < 0$. In the case of ejections and sweeps the shear product takes negative values and both are largely responsible for the production of turbulence.

Figure 7.3 shows regions of negative shear product corresponding to the velocity fields of Figure 7.1. The shear product is displayed for levels of $u'v' \leq \kappa u_\tau^2$. Regions of negative shear product (white regions) are distinguished in the vicinity of the spanwise eddies. Strong contributions to the stress product are not present however along the shear layer interface. Threshold values of $\kappa = -1, -1.5$ and -3 are used in the plots of Figure 7.3a to illustrate the effect of the threshold value at $Re_\theta = 1520$. For $\kappa = -1$ (top plot) a large number of small regions of distributed stress product are distinguished, including above the eddy at **A** and upstream of the eddy at **B**. A threshold of $\kappa = -1.5$ (middle plot), eliminates many of the regions on the top plot of Figure 7.3a. A threshold of $\kappa = -3$ (bottom plot) reveals only the region near the wall labeled **C** where very localized flow ejections are present at the shear layer interface, underneath eddy **B**. Figures 7.3b and 7.3c shows contours of negative shear product corresponding to $Re_\theta = 3950$ and 5790 respectively. Like the $Re_\theta = 1520$ case, the larger threshold value $\kappa = -3$ shows that the stronger negative shear product regions are associated with the spanwise spiral structures along the shear layer.

7.3.4 Backs or Large Scale Shear Layers. In addition to the shear layers encountered in the near wall region, Blackwelder and Kovasznay (1972), Praturi and Brodkey (1978) and others have shown that larger size shear layers exist on the upstream or “back” side of large scale outer motions stemming from freestream flow being entrained into the boundary layer. The large size shear layers may span most of the boundary layer, even at high Reynolds numbers.

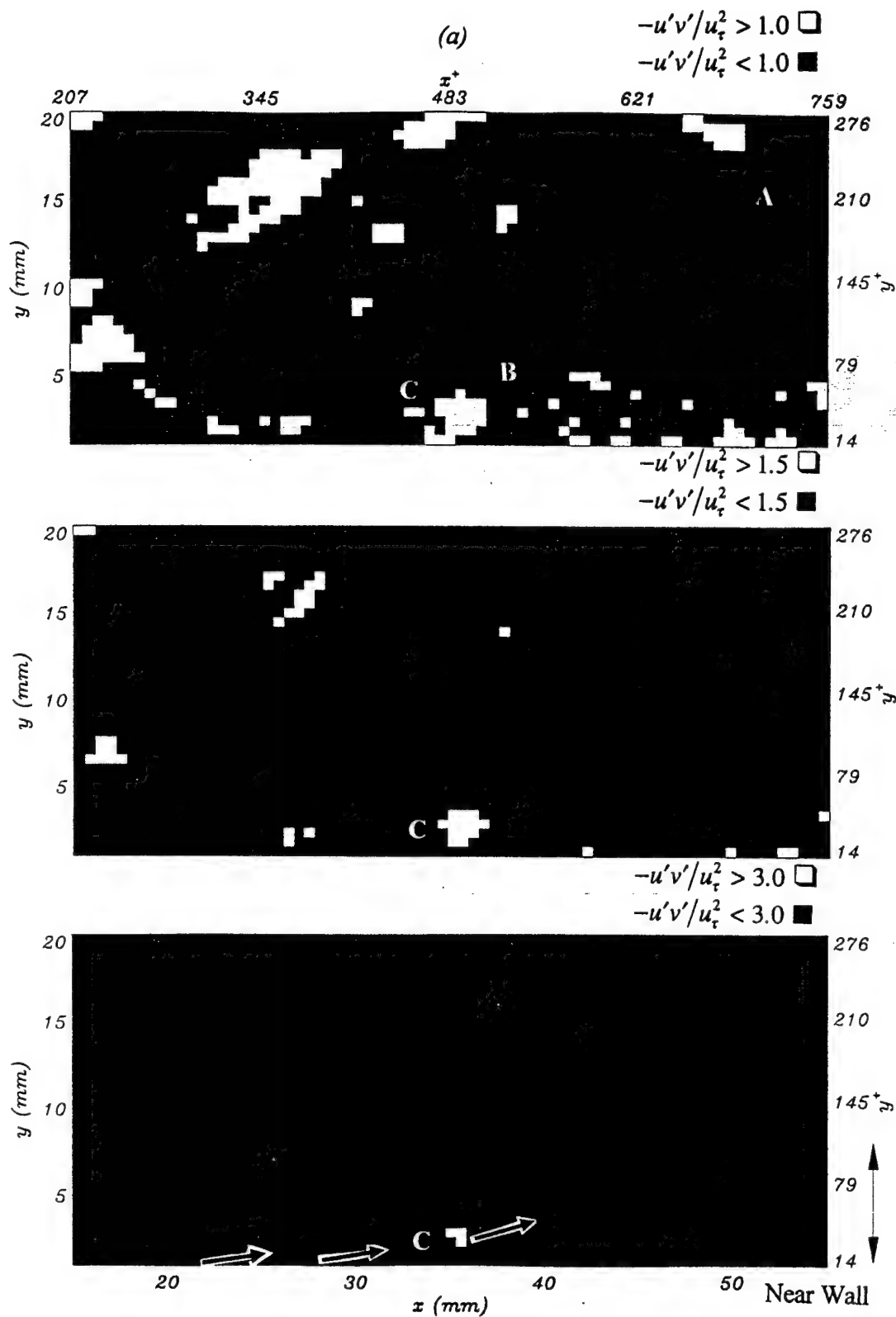


Figure 7.3 Instantaneous Shear Product in the Same Velocity Fields as Fig. 7.1: (a) $Re_\theta = 1520$, (b) $Re_\theta = 3950$, (c) $Re_\theta = 5790$

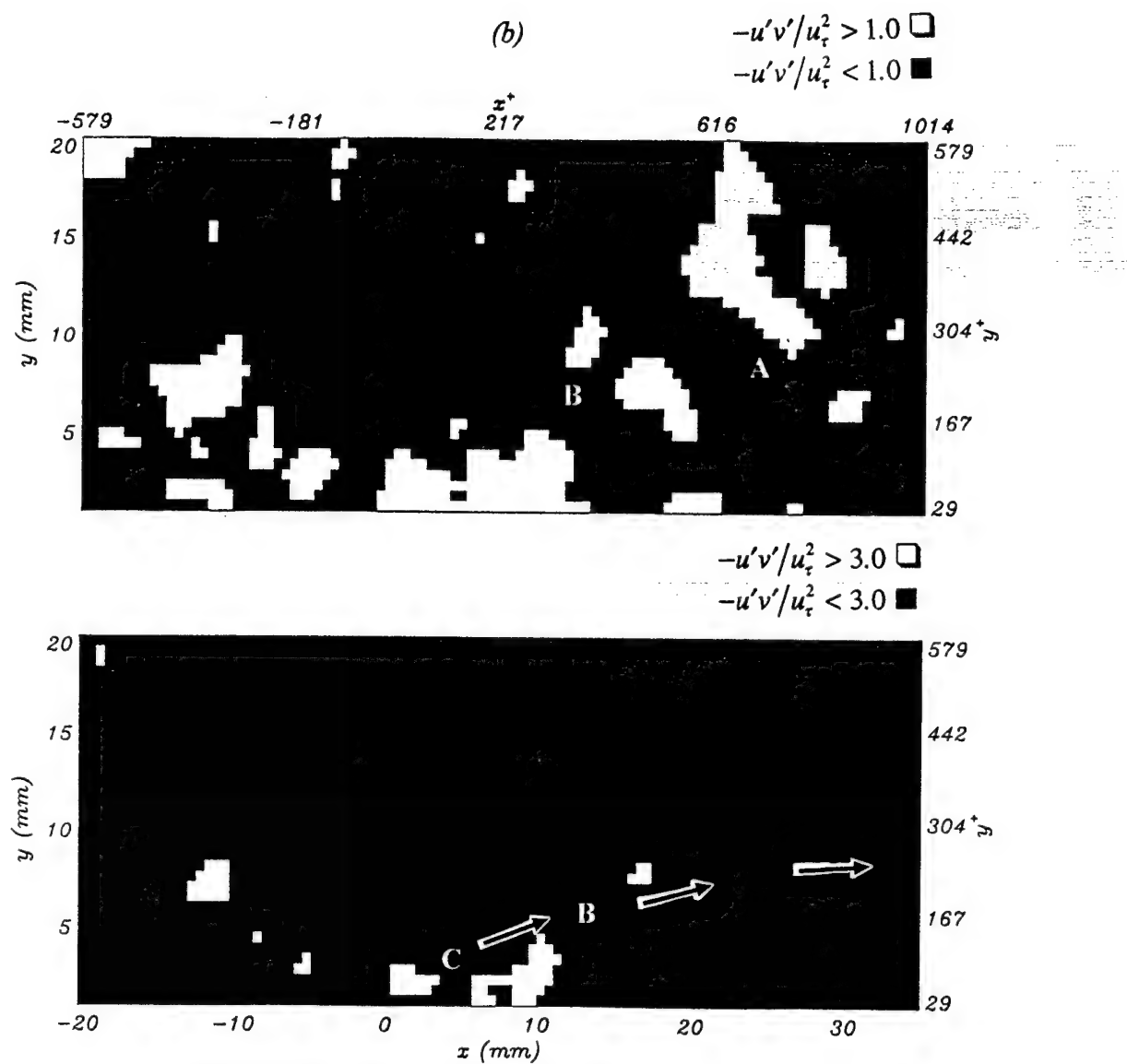


Figure 7.3 (continued, page two of three)

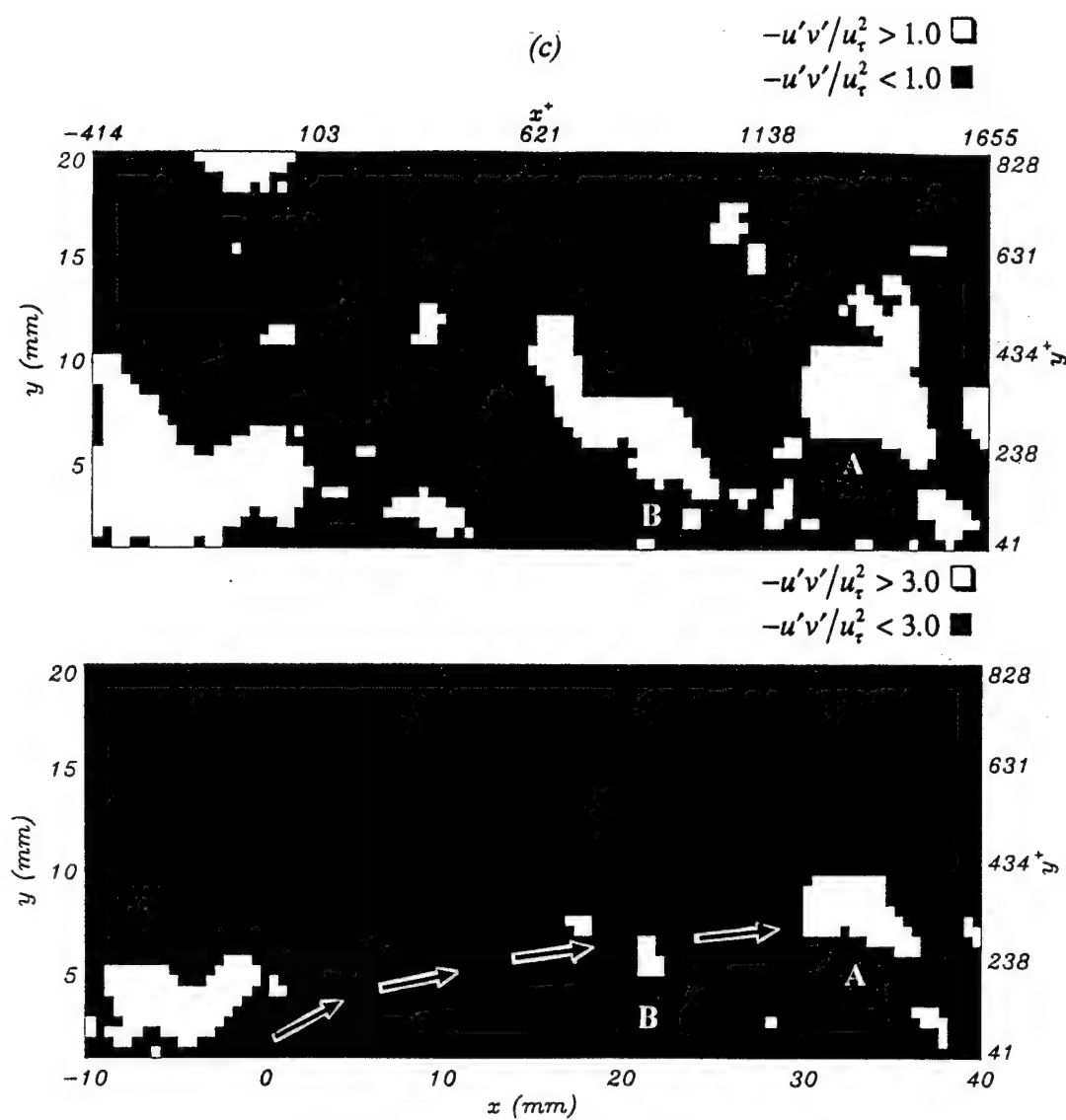


Figure 7.3 (continued, page three of three)

Figure 7.4a, b, and c shows back structures for $Re_\theta = 1520, 3950$ and 5790 respectively. The back structures are large scale, sloping shear layers with coherent spanwise eddies along the interface.

The plots on top of Figure 7.4a, b, and c show the instantaneous Reynolds decomposed u' and v' velocity fluctuation fields. Eddies **A** through **D** delineate the interface for $Re_\theta = 1520$ velocity field; eddies **A** through **E** delineate the interface for $Re_\theta = 3950$; and eddies **A** through **F** mark the interface for $Re_\theta = 5790$.

The middle plots of Figure 7.4a, b, and c show contours of fluctuating streamwise velocity, u'/u_τ . The dark contours signify low streamwise velocity; the lighter contours represent high streamwise velocity. The contrast between light and dark colors highlight strong values of $\partial u'/\partial x$. The slope of the backs in the three Reynolds number events represented in the middle plots are very similar and are approximately 35° .

The bottom plots of Figure 7.4a, b, and c show selected contours of the fluctuating streamwise velocity for values of $u' > u_\tau$ and $u' < -u_\tau$. The white ($u' > u_\tau$) and black ($u' < -u_\tau$) contours show that for all Re_θ cases the size of the structures extend on the order of the boundary layer thickness in both the streamwise and wall normal direction.

7.3.5 Backs and Concentrations of Strong Spanwise Vorticity. A new two-fold assessment made in the present study concerns the slope of the shear layer interface and spanwise eddies associated with the shear layer. A slope of approximately 35° characterizes large shear layer structures for Re_θ cases between 1520 and 5790. Distinct spanwise eddies, ranging from three to six, are typically present along the interface of large scale shear layers.

The numerical simulations of Spalart (1988) and Robinson et al. (1988) at $Re_\theta = 670$ identified a characteristic 18° to 30° angle for a large scale shear layer interface. The simulations showed a single large scale vortical structure, hook-like in shape at the end of the shear layer. Head and Bandyopadhyay (1981) and Kim and Moin (1986) reported an inclination of 45° for the outer flow vortical structures.

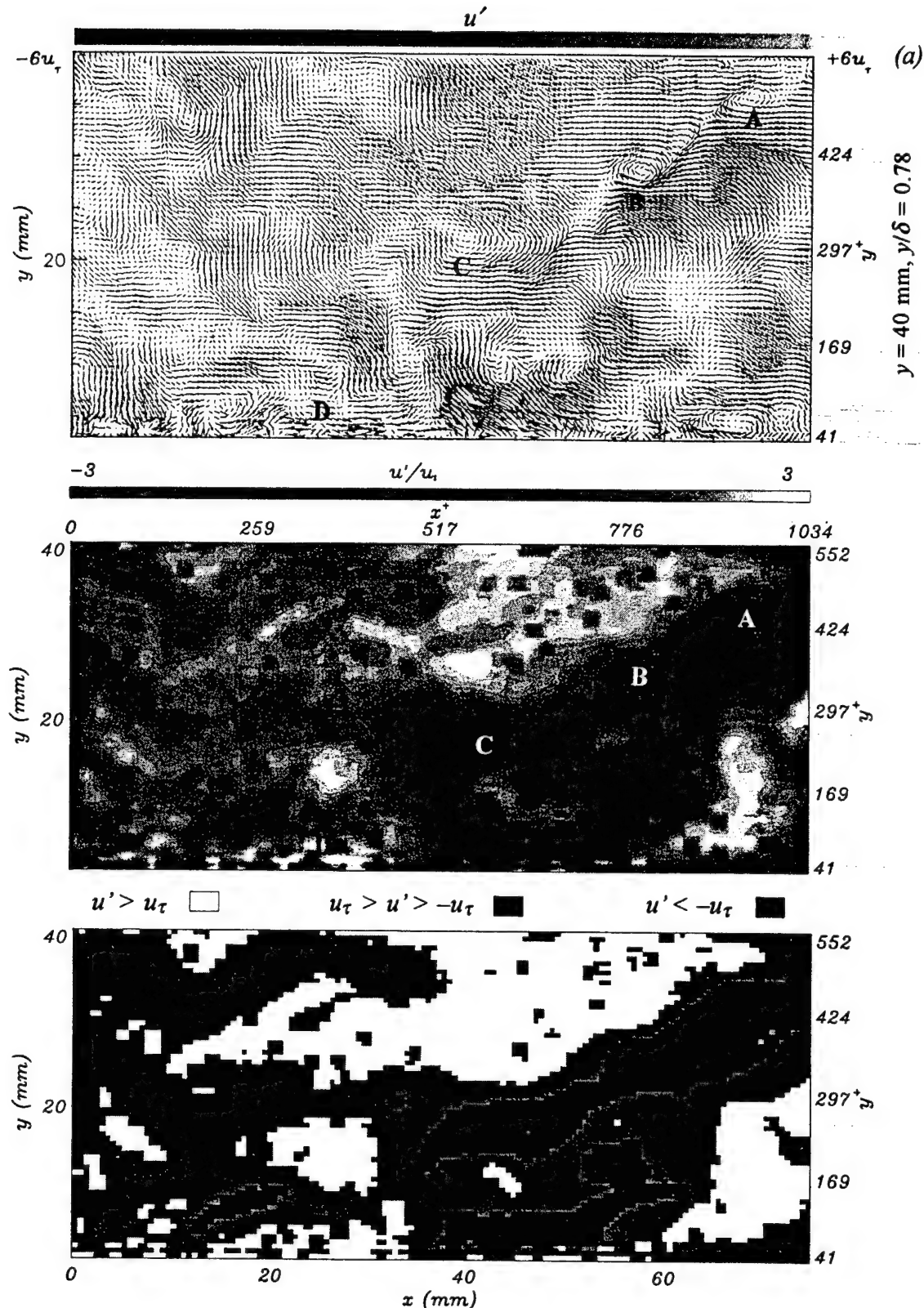


Figure 7.4 Backs and Large Scale Shear Layers (a) $Re_\theta = 1520$, (b) $Re_\theta = 3950$, (c) $Re_\theta = 5790$: u', v' Field (Top); Contours of Fluctuating Streamwise Velocity (Middle); Selected Contours (Bottom)

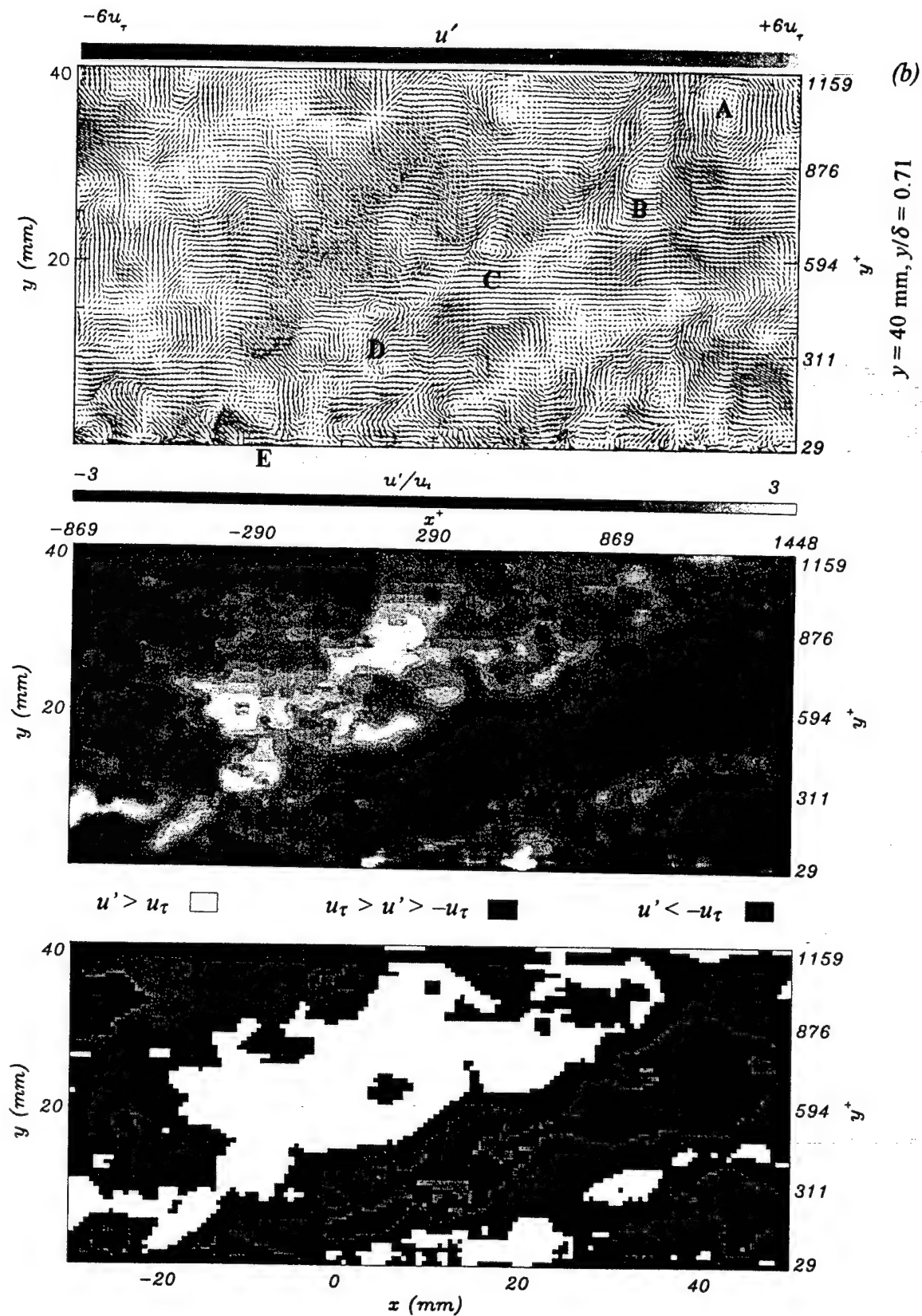


Figure 7.4 (continued, page two of three)

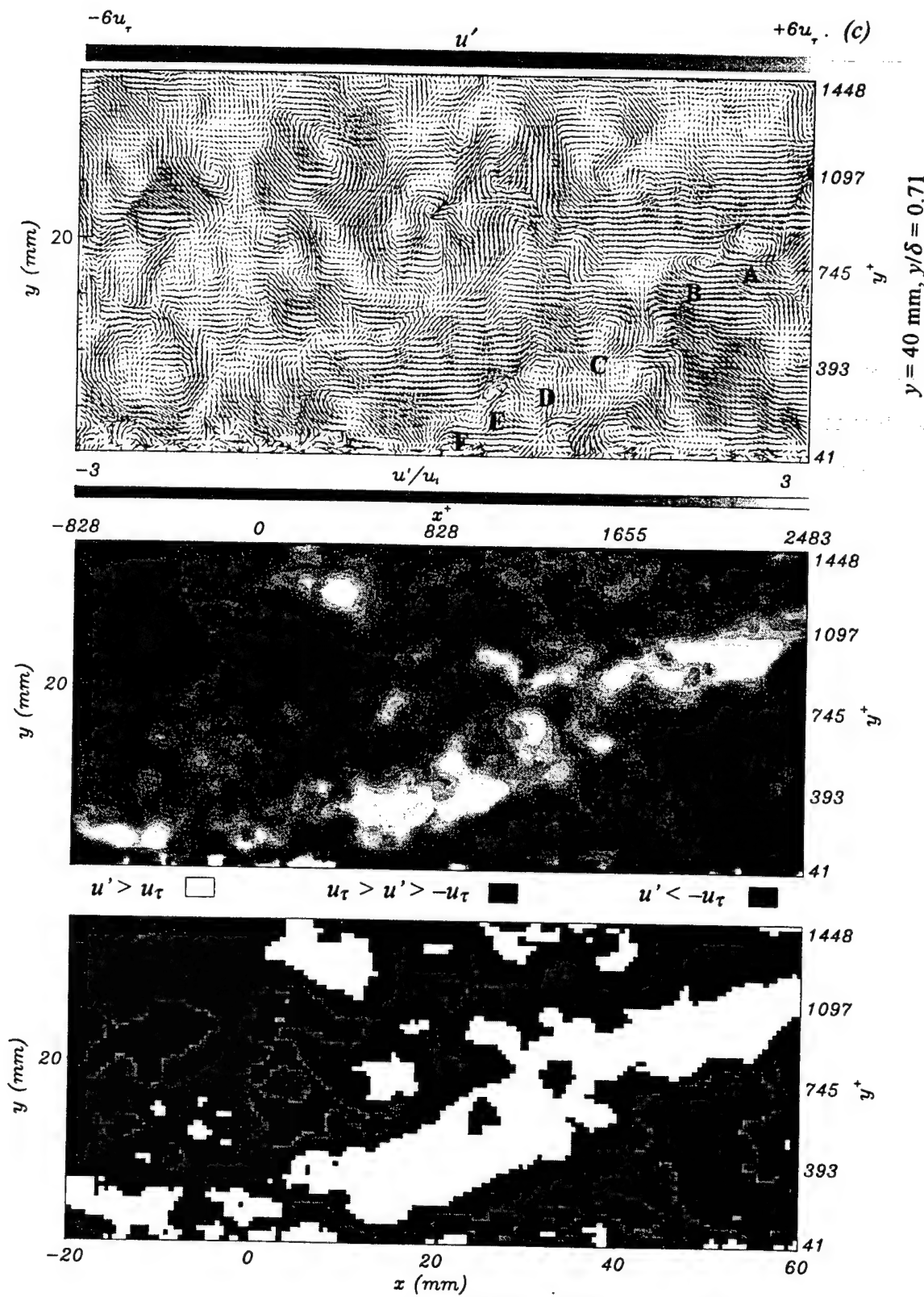


Figure 7.4 (continued, page three of three)

Figure 7.5 shows selected portions of the shear layers presented in Figure 7.4. The top plot in Figure 7.5a, b, c displays the fluctuating velocity field and discrete eddies for $Re_\theta = 1520$ (structures **B**, **C**), 3950 (structures **B**, **C**, **D**) and 5790 (structures **A**, **B**, **C**) respectively.

The middle plot of Figure 7.5a, b, c shows the total vorticity corresponding to the velocity field above. The bottom plot of Figure 7.5a, b, c shows selected contours of the total vorticity ($\omega^+ < -0.035$). Vorticity stretches along the interface of the shear layer, and is greatest in the vicinity of the spiral structures identified in the velocity fields.

7.3.6 Bulges in the Outer Interface and Large Scale Motions. The outer interface between the turbulent boundary layer flow and the free stream is characterized by large scale, bulges and narrow incursions of flow into the boundary layer. The flow incursions are characterized by negative streamwise and wall normal fluctuations localized downstream of large scale backs. The large scale backs associated with the upstream side of the large scale motions considered in Figure 7.4 are reviewed to estimate the narrow regions of fluid entrainment.

The fluctuating velocity fields and contours of $u'v'$ are shown on Figure 7.6a, b, c for $Re_\theta = 1520$, 3950 and 5790 respectively. The regions of incursion are illustrated by selecting regions where $u' < 0$ and $v' < 0$. Selected contours are shown for $u'v' > u_\tau^2$ and $u_\tau^2 > u'v' > 0$. The velocity fields for the range of Re_θ considered here shows a distinctive region of entrained flow downstream of the large bulges and shear layer interface. It is unclear however whether this fluid proceeds from the freestream or from flow within the boundary layer.

The above results illustrated coherent structures present in a range of Reynolds numbers between 1520 and 5790. Differences with numerical simulations were evident in the existence of multiple eddies along a shear layer interface, which were observed in the present study and in the experimental study of Adrian et al. (1995). The following section considers wall pressure signatures of coherent motions in the flow field.

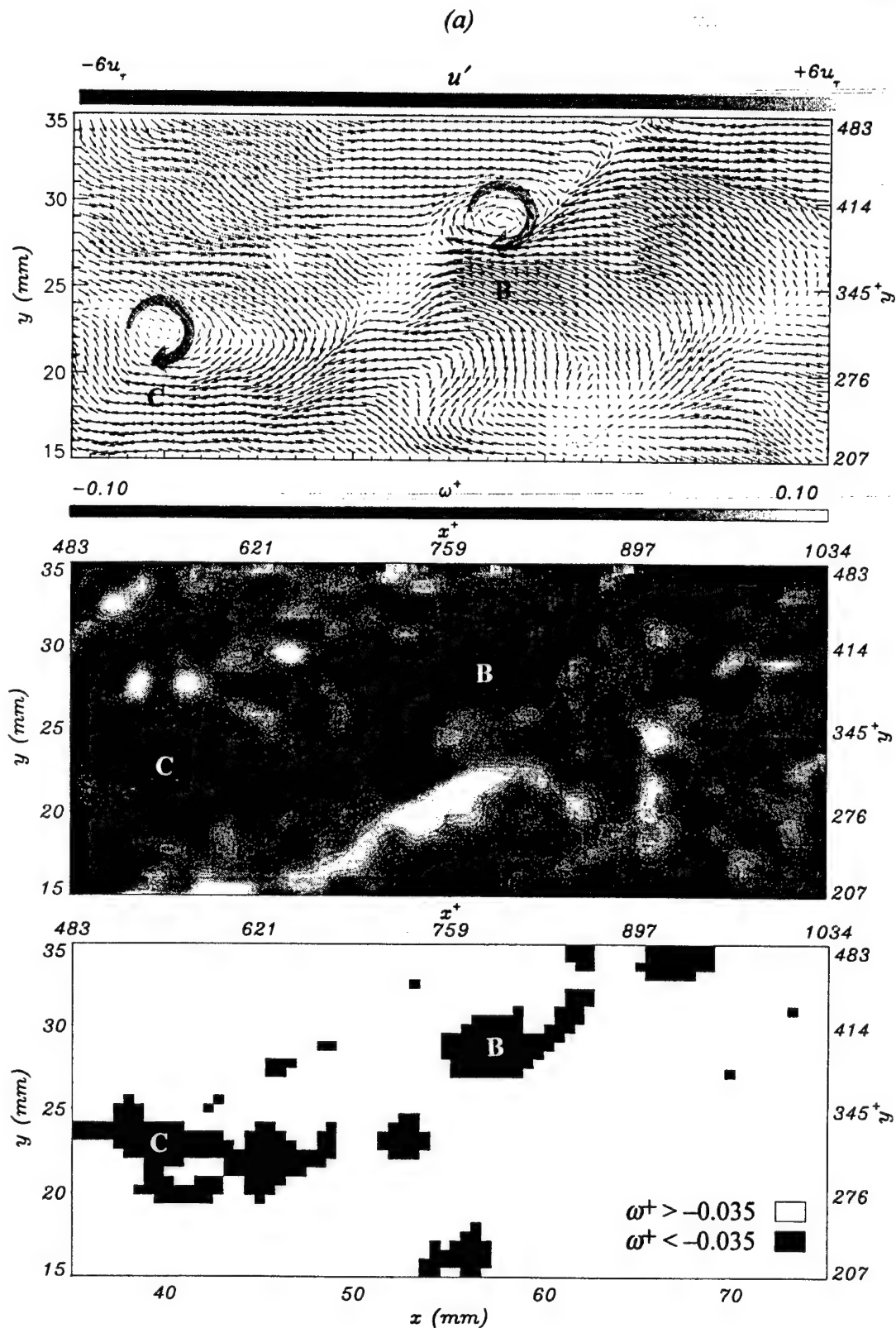


Figure 7.5 Large Scale Shear Layers and Vortex Structures (a) $Re_\theta = 1520$, (b) $Re_\theta = 3950$, (c) $Re_\theta = 5790$: u', v' Field (Top); Contours of Spanwise Total Vorticity (Middle); Selected Contours (Bottom)

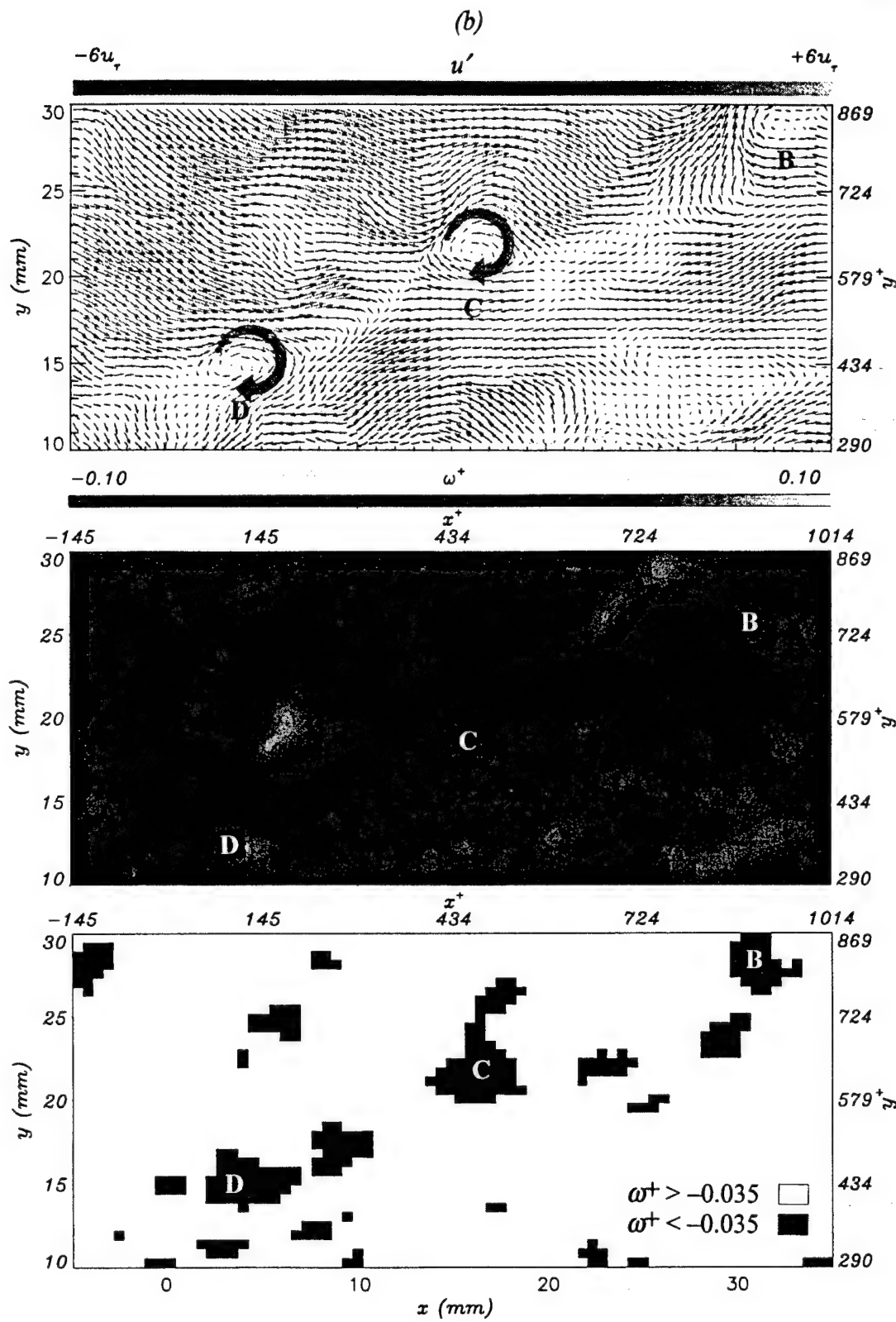


Figure 7.5 (continued, page two of three)

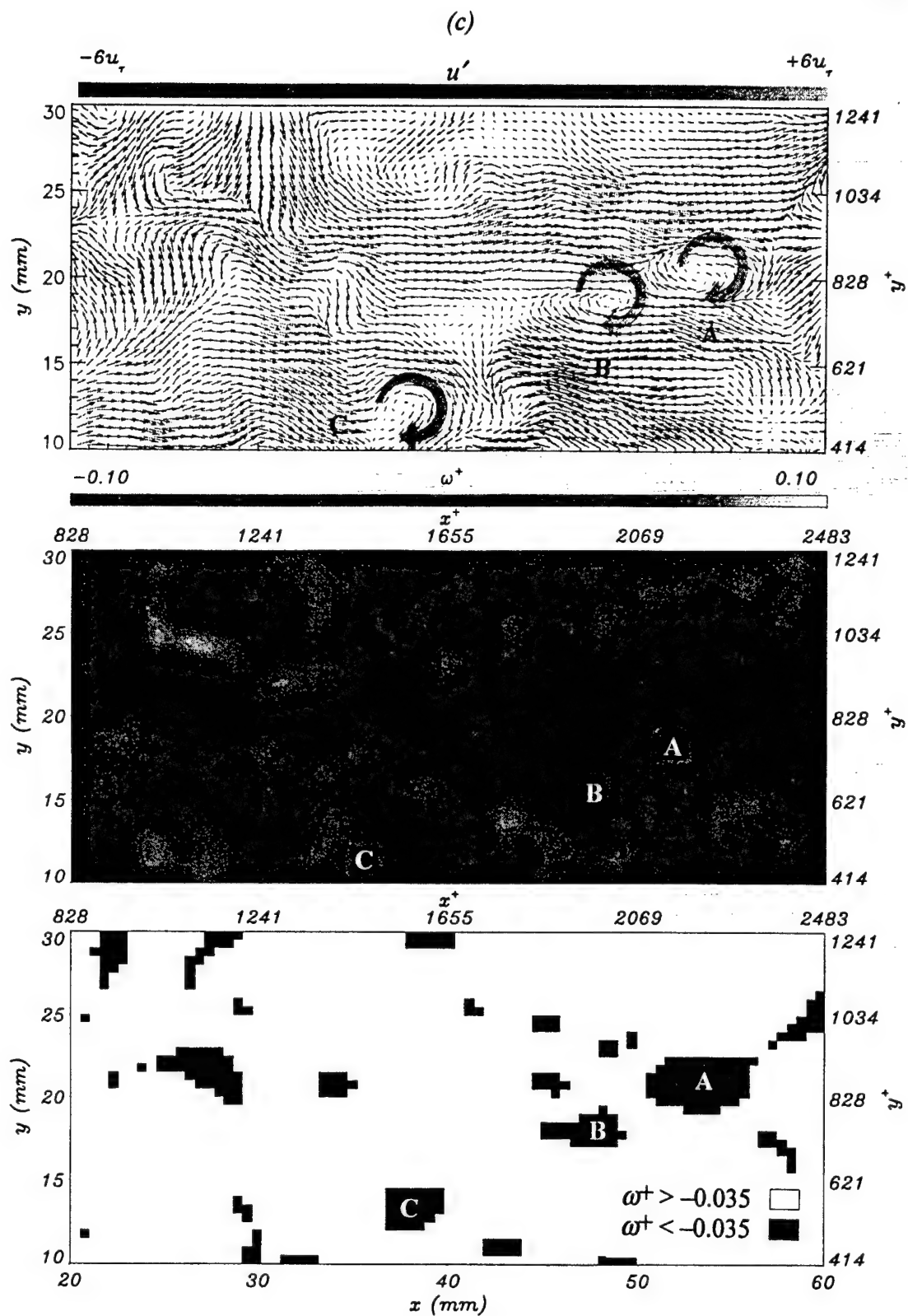


Figure 7.5 (continued, page three of three)

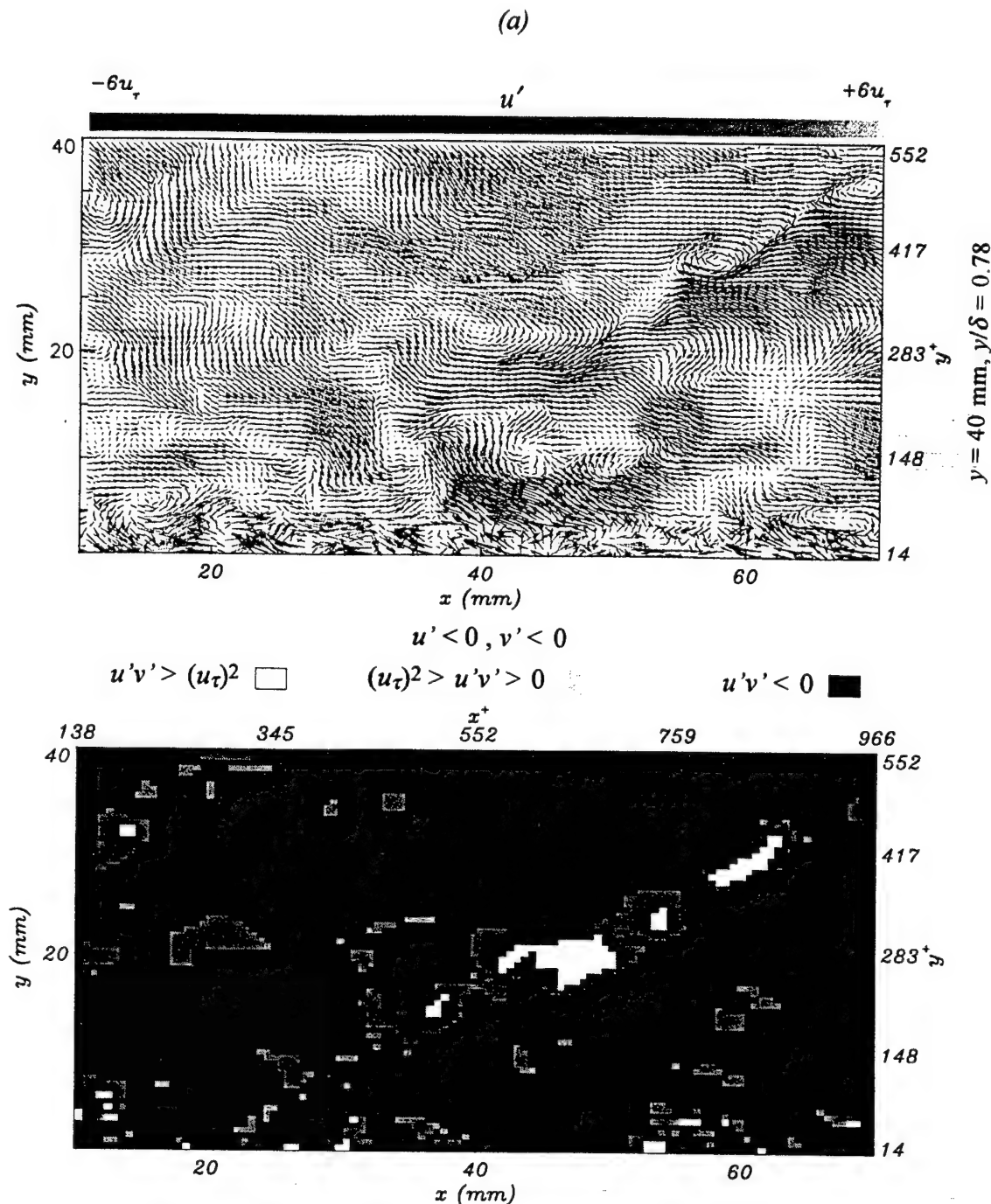


Figure 7.6 Large Scale Velocity Incursions (a) $Re_\theta = 1520$, (b) $Re_\theta = 3950$, (c) $Re_\theta = 5790$: u', v' Field (Top); Contours of $u_\tau^2 > u'v' > 0$ Fluctuations (Bottom)

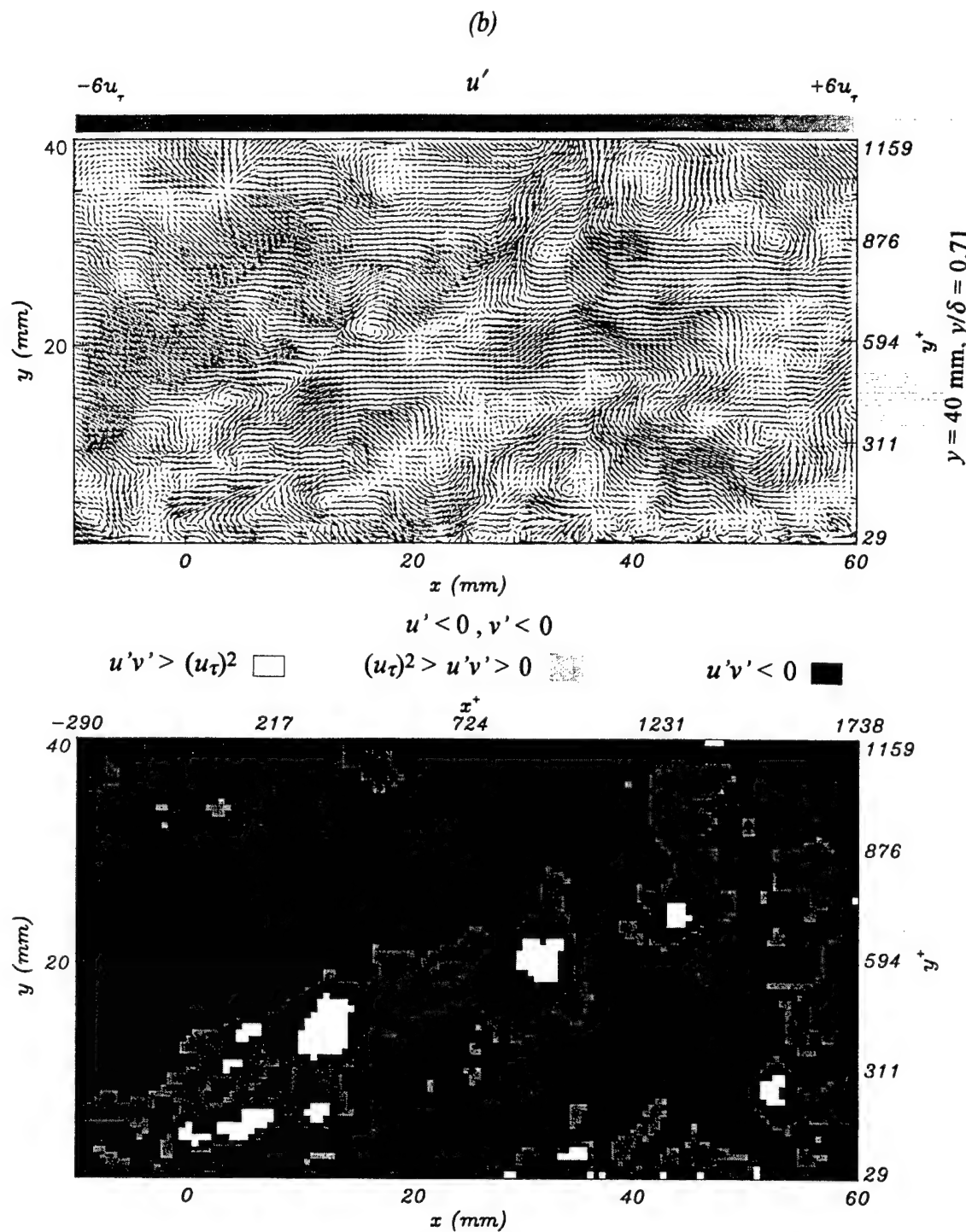


Figure 7.6 (continued, page two of three)

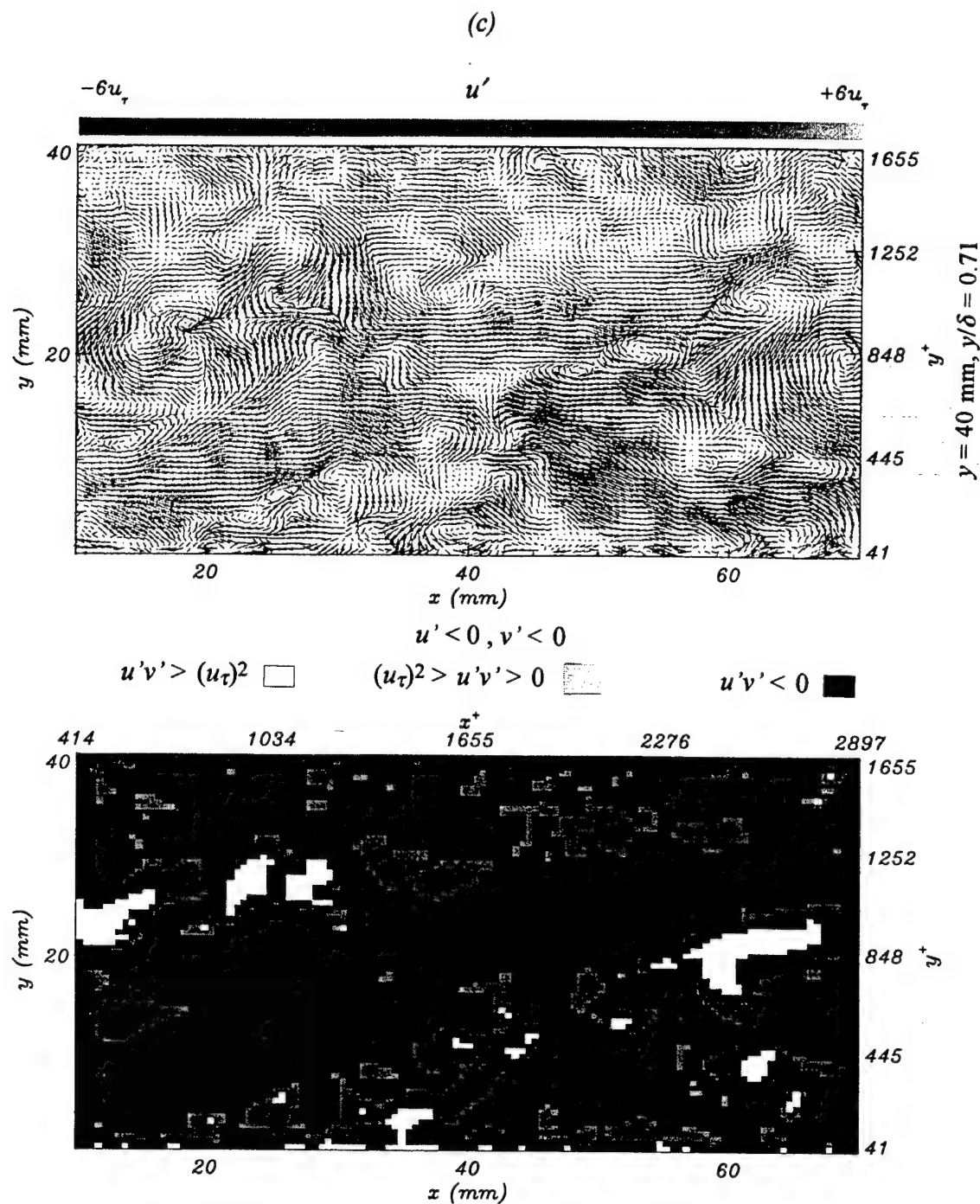


Figure 7.6 (continued, page three of three)

7.4 Characteristic Wall Pressure Fluctuations.

The time sequence of the wall pressure along the streamwise direction is represented in Figure 7.7a, b, c for $Re_\theta = 1520, 3950$ and 5790 respectively. In each case the time sequence encompasses 1000 viscous time units, which correspond to 3081, 1315 and 1047 consecutive wall pressure profiles for the respective Reynolds numbers above. Plots *a* through *c* display the same t^+ to x^+ scale. The following sections consider large amplitude wall pressure events characteristic in the time sequences of Figure 7.7. The larger amplitude wall pressure events are then related to the velocity field through examples of the instantaneous pressure-velocity fields.

7.4.1 Convection of Large Amplitude Wall Pressure Events. The slope of dark and light structures corresponding to large magnitude values of $p'(x,t)/p_{rms}$ signify the convection velocity of negative and positive pressure events. The range of convection velocities is similar for $Re_\theta = 1520$ through 5790. The convection velocities for most structures (indicated as \Rightarrow) range from 0.5 to 0.6 U_∞ or 12 to 14 u_τ . Occasionally other structures (indicated as \rightarrow) appear with lower convection velocities on the order of 0.35 U_∞ . The instantaneous dimension of large amplitude wall pressure patterns in the streamwise direction (for any given t^+ value) range typically from 50 to 400 viscous units. Instantaneous high and low pressure regions however may extend over 800 viscous units. The size in inner units of the large amplitude pressure structures coincide with the sizes documented by Robinson et al. (1988) in numerical simulations performed at $Re_\theta = 670$. The space-time pressure development of Figure 7.7 show that large amplitude events convect over large distances, ranging from 600 to over 2000 viscous units. Johansson et al. (1988) show contours of the wall pressure, $p(x,z)$, separated by equal time intervals calculated from the direct numerical simulation of a turbulent channel flow; the distances along which large amplitude events convect are similar to the distances found in the

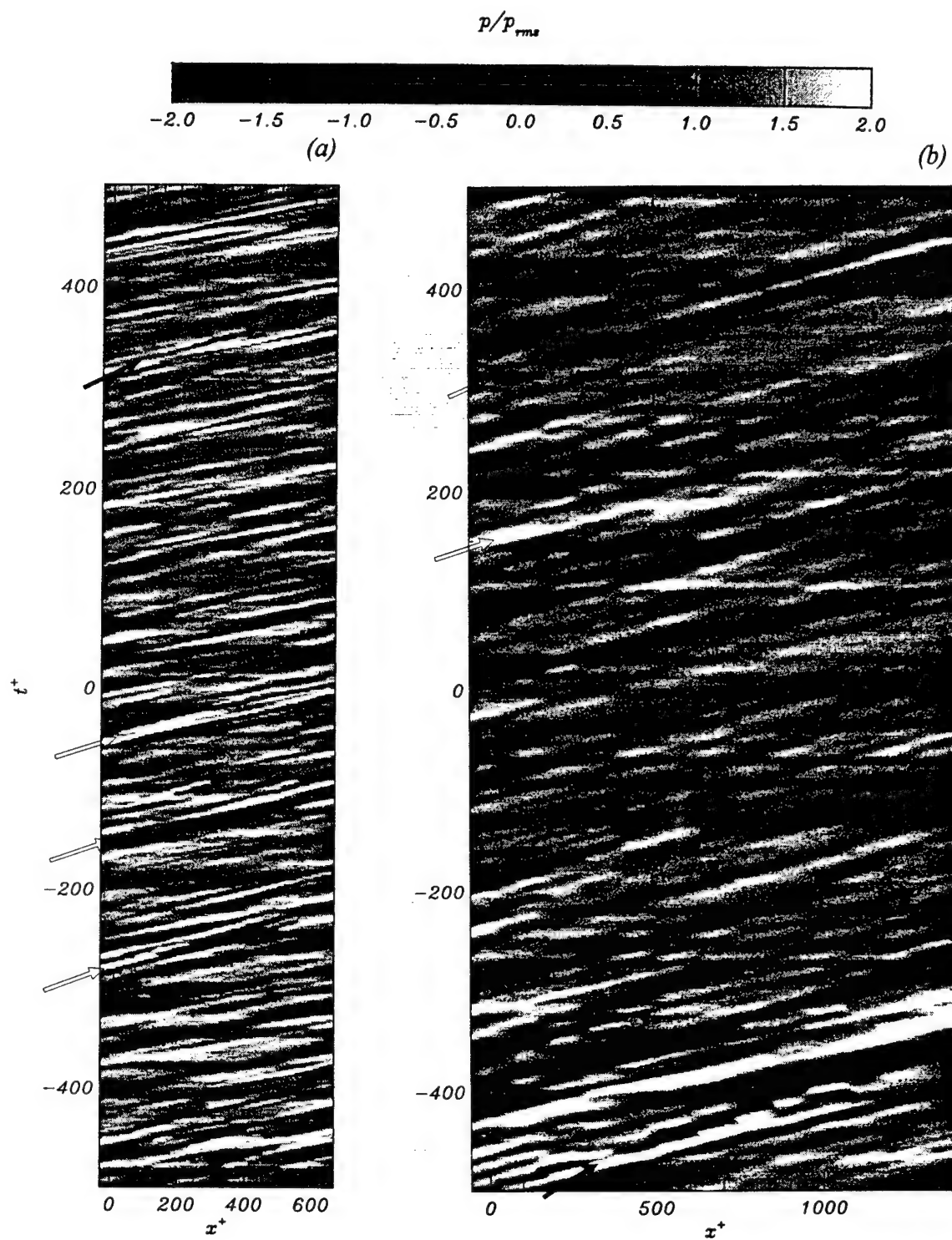


Figure 7.7 Time-Space Development of the Wall Pressure along the Streamwise Direction
 (a) $Re_\theta = 1520$, (b) $Re_\theta = 3950$, (c) $Re_\theta = 5790$

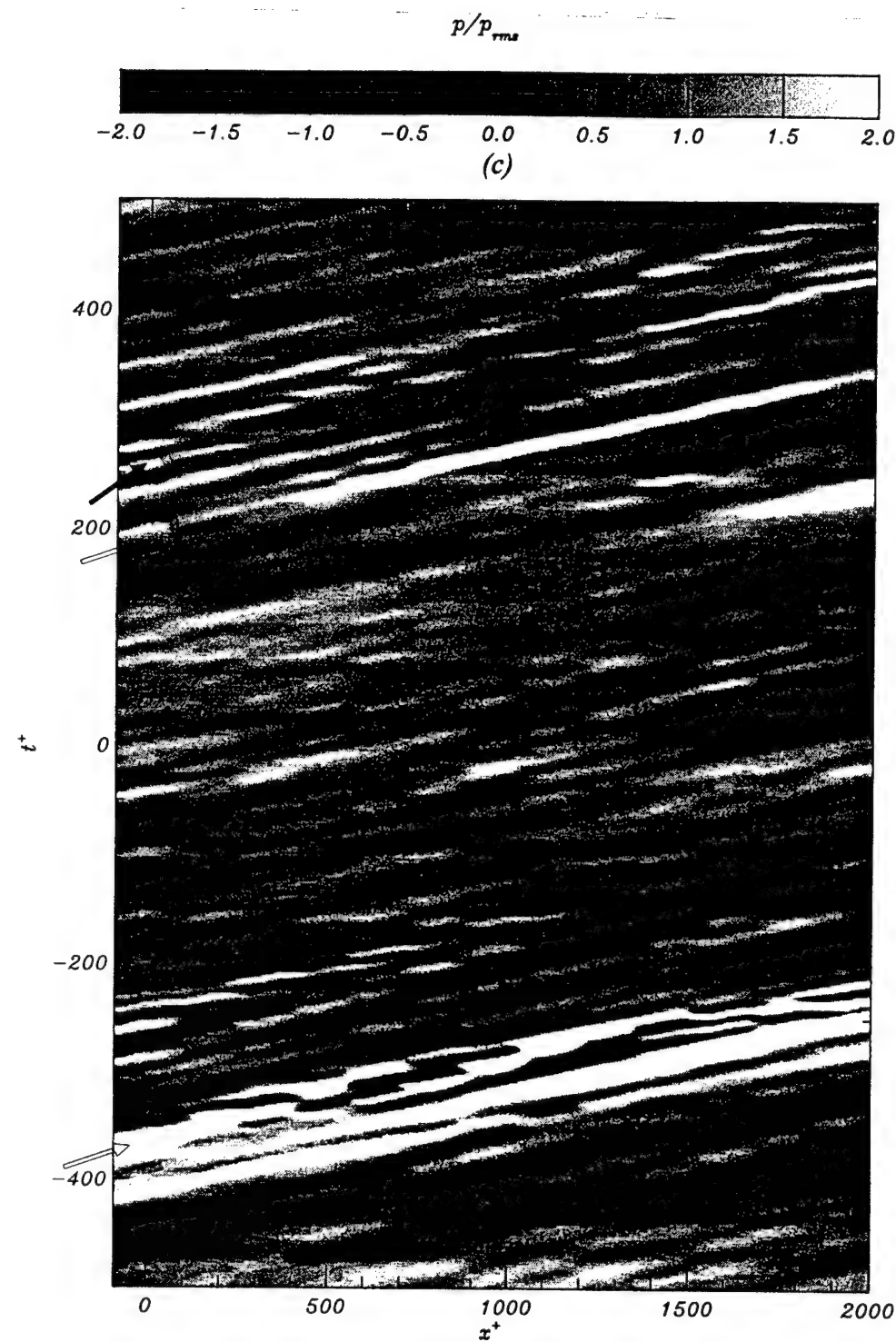


Figure 7.7 (continued, page two of two)

present pressure measurements. Comparison of the time-space wall pressure in Figure 7.7a, b and c shows a Re_θ dependence on the "size" of the pressure structures.

7.4.2 Positive Pressures Beneath Shear Layers. Conditional sampling of large amplitude pressure fluctuations calculated by numerous researchers (reviewed by Eckelmann, 1990, corroborated more recently by Juckenhoefel, 1995, and Snarski and Lueptow, 1995) has shown that a large amplitude positive pressure is related to the convective stagnation line of a shear layer in the averaged velocity field. The stagnation line where high speed fluid is found upstream of low speed fluid occurs above the large positive pressure event in the near wall region.

Figure 7.8a shows the wall pressure underneath an instantaneous flow field at $Re_\theta = 3950$. The positive pressure at $t^+ = 0$ downstream of the adverse pressure gradient structure ($x^+ \approx 600$) occurs beneath with the stagnation line of a shear layer in the near wall region. Two additional wall pressure profiles obtained at $t^+ = +4, -4$ are also shown. The additional profiles show that the pressure structure is generally preserved around the instant when the flow field was captured. Consecutive negative and positive pressure peaks are predominant wall pressure structures and are observed in the time sequences of Figure 7.7. The conditionally averaged wall pressure signal constructed from large amplitude pressure fluctuations also exhibits negative and positive pressure peaks similar to the instantaneous profiles of Figure 7.8 (already documented in Chapter 6, e.g. Fig. 6.6). A second independent realization involving an adverse pressure gradient and a shear layer structure is shown in Figure 7.8b.

Positive pressure structures may extend in space over significantly larger streamwise distances than the pressure gradient structure of Figure 7.8. Pressure structures that extend large distances in the streamwise direction are related to large scale motions in the boundary layer. The top plot of Figure 7.9 shows a positive pressure region extending from $x^+ = 150$ to 500 associated with a large scale structure with predominately negative

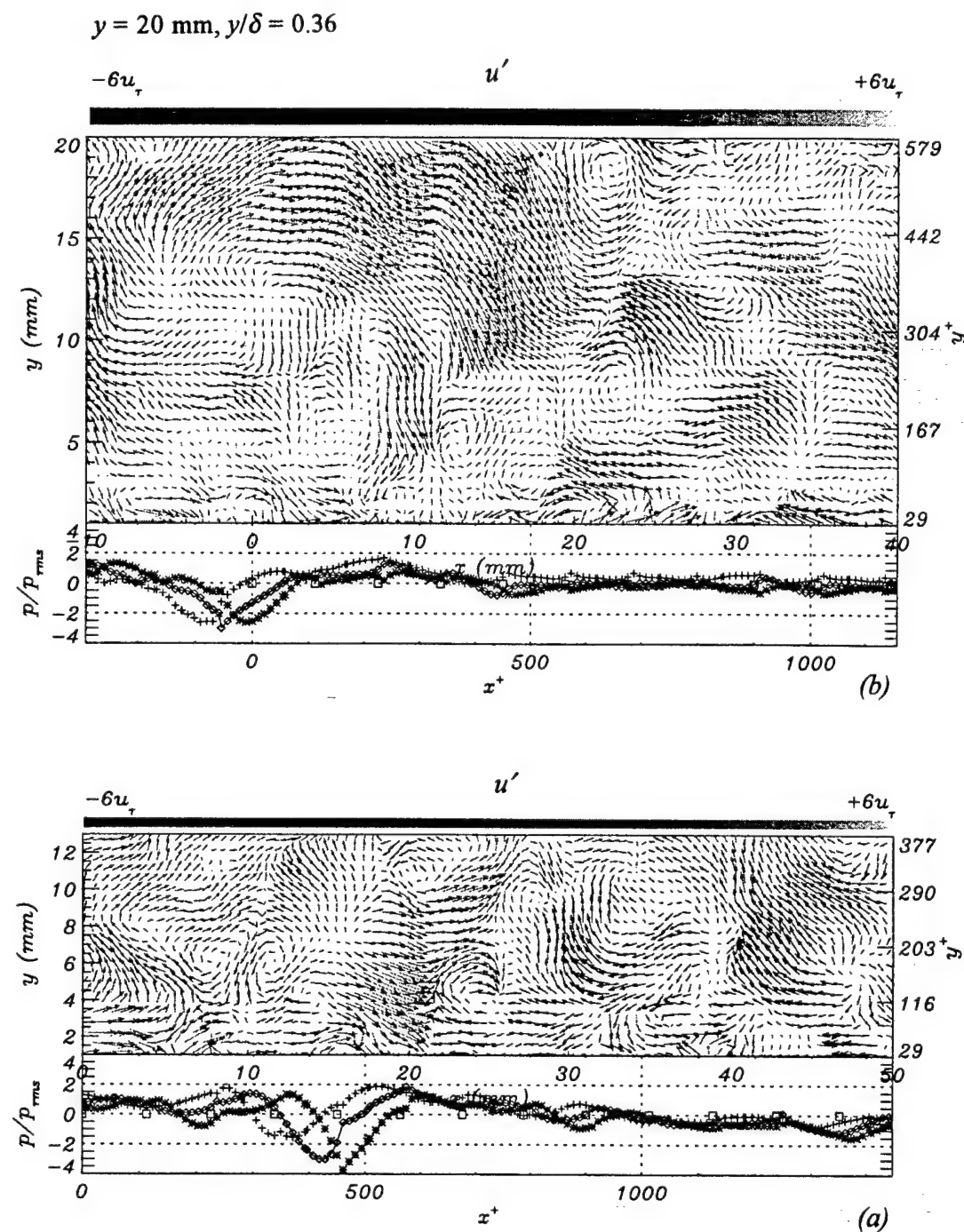


Figure 7.8 Instantaneous $u'v'$ Fields and Wall Pressure at $Re_\theta = 3950$. Wall Pressure Profiles with Respect to the Flow Field Include (+) $t^+ = -4$, (\diamond) $t^+ = 0$, (*) $t^+ = +4$. Microphone Locations Indicated as (\square)

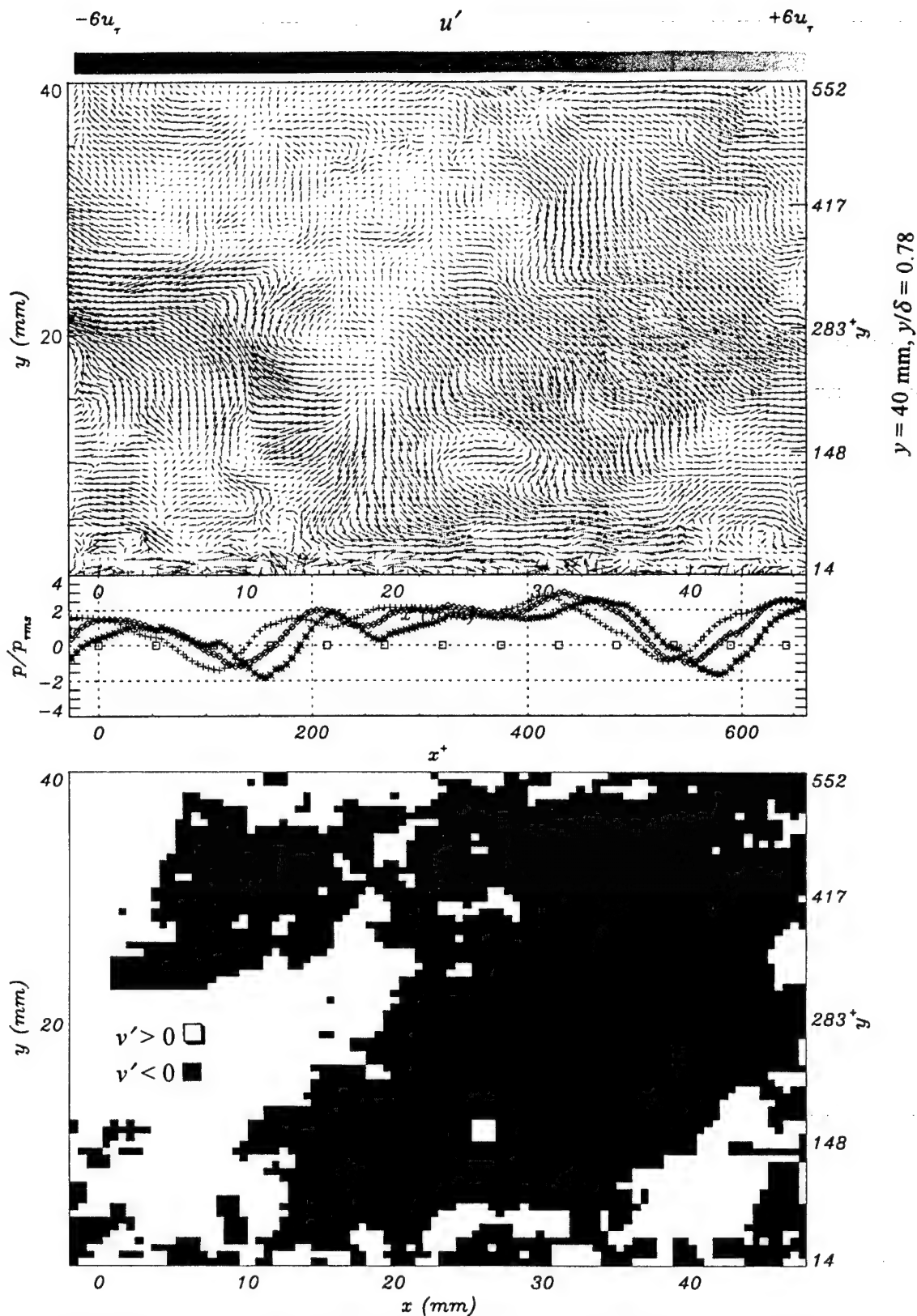


Figure 7.9 Instantaneous $u'v'$ Field and Wall Pressure Associated with a Large Velocity Structure (Top), Large Scale Indicated by Contours of $v' < 0$ (Bottom)

wall normal velocity for $Re_\theta = 3950$ (a sweep like structure). Two additional wall pressure profiles obtained at $t^+ = +2, -2$ are also shown. The bottom of Figure 7.9 shows contours of $v' < 0$ for the velocity field on the top of Figure 7.9; the large scale motion is manifested in the large region of $v' < 0$.

7.4.3 Negative Pressures beneath Local High Momentum Flow. The simultaneous measurements of pressure and velocity in the current study highlight two distinct negative pressures events associated with shear layer structures in the flow field.

The first negative pressure event observed lies underneath a shear layer interface, upstream of a positive pressure. The streamwise distance, normalized by inner units, was found to be 125 and was consistent for Re_θ between 1520 and 5790 (refer to Chapter 6). It is speculated that the negative pressure peak arises from low speed fluid near the wall being overtaken by high speed flow. An eddy-like motion, with sense of rotation same as the mean spanwise vorticity, is formed that ejects flow from the wall and induces a negative pressure.

The time sequence of the wall pressure showed that large negative pressures may occur downstream of a positive pressure peak as well (refer to Fig. 7.7). The pattern of negative pressure downstream of positive pressure however is less noticeable in the conditionally-averaged calculations. Praturi and Brodkey (1978) suggested that flow removal away from the wall occurs downstream of a shear layer interface and is associated with ejection type events ($u' < 0, v' > 0$).

The present study however shows that negative pressures are more commonly encountered upstream of positive pressures. This is corroborated by histograms of large amplitude negative pressure peaks accompanying positive pressures. Positive and negative thresholds of $2.5p_{rms}$ are used in the calculations. When a positive pressure is detected in the space-time pressure field, the locations of negative pressure peaks that exceed the threshold are recorded. A sample corresponding to $Re_\theta = 3950$ is illustrated on

the top of Figure 7.10. At the center of the plot, $t^+ = 0$, $x^+ = 0$, no negative events are detected since this corresponds to the positive pressure detection nor are negative events recorded along the convection line of the positive structure. Most negative pressure events detected are concentrated near the detection point, aligned upstream of the positive pressure structure convection line. The histogram of positive pressure events present at the moment of a negative detection is shown on the bottom of Figure 7.10. Both indicate that a common wall pressure structure is formed by negative and positive pressure events, both of large magnitudes, existing adjacent to one another, located upstream and downstream respectively.

The second negative pressure event considered in this section is found typically beneath a structure rotating in the opposite sense of the mean spanwise vorticity. Figure 7.11a, b, c shows a negative pressure, for $Re_\theta = 1520, 3950$ and 5790 respectively, beneath a counterclockwise (ccw) eddy centered in each case about $y^+ \approx 100$.

Generally a region of positive $\partial u' / \partial x$ gradient is found downstream of the ccw eddy which is inclined towards the wall, represented in Figure 7.11 by symbols . Because of its similarities and at the same time its dissimilarities with the previously discussed shear layer it is denoted as an “inverse” shear layer. In addition to the difference in sign for $\partial u' / \partial x$ between the shear layer and the inverse shear layer, the inverse structure does not exhibit eddies along the interface. Common classifications of boundary layer turbulent structures, as well as reports of numerical simulations and experimental data have not identified the inverse shear layer. Nonetheless, this is not the first time that a sequence of structures with opposite trends such as the one established here between the shear layer and the inverse shear layer is introduced. Williams (1985) showed an organized pattern of vortex lines consisting of hairpins and inverted hairpins from experimental data obtained from boundary layer transition experiments in a water channel.

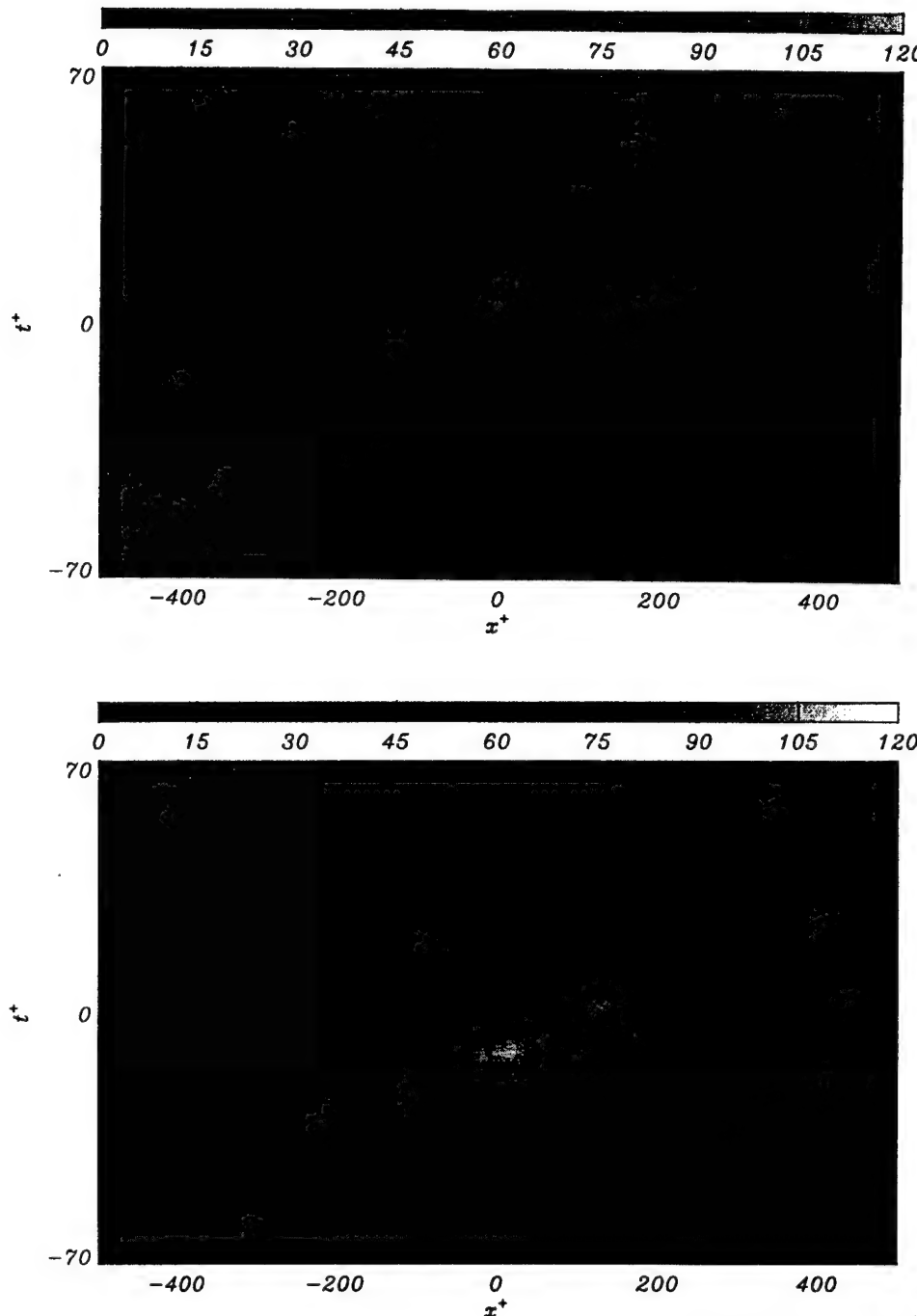


Figure 7.10 Histogram of Negative Pressure Events, $p < -2.5p_{rms}$, Present at the Moment of a Positive Pressure Detection, $p > +2.5p_{rms}$, for $Re_\theta = 3950$ (Top); Histogram of Positive Pressure Events Present at the Moment of a Negative Detection (Bottom)

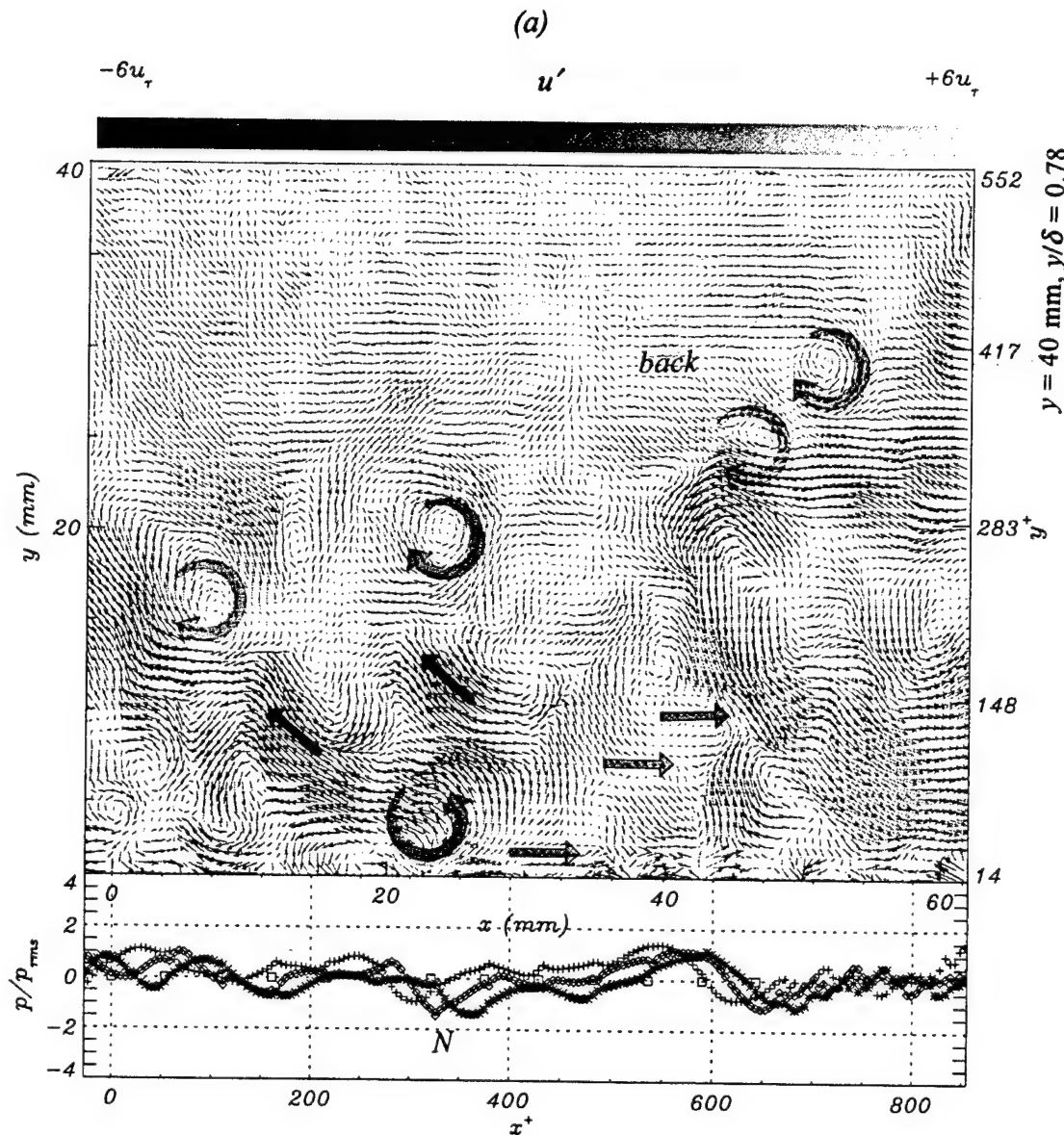


Figure 7.11 Instantaneous $u'v'$ Fields and Wall Pressure Associated with a Negative Pressure Structure (a) $Re_\theta = 1520$, $\Delta = 2$, (b) $Re_\theta = 3950$, $\Delta = 2$ (c) $Re_\theta = 5790$, $\Delta = 4$. Wall Pressure Profiles with Respect to the Flow Field Include (+) $t^+ = -\Delta$, (0) $t^+ = 0$, (*) $t^+ = +\Delta$. Microphone Locations Indicated as (\square)

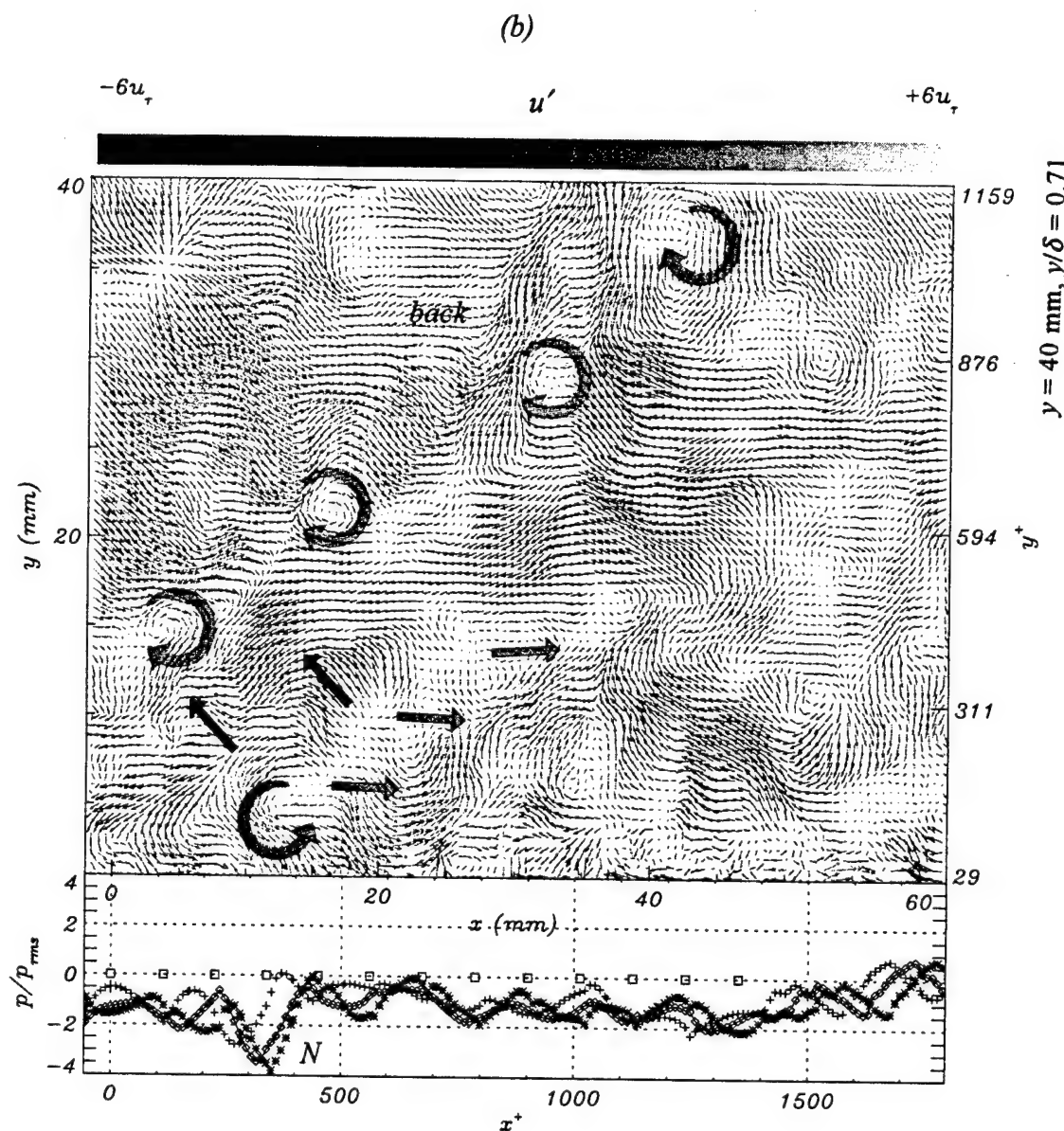


Figure 7.11 (continued, page two of three)

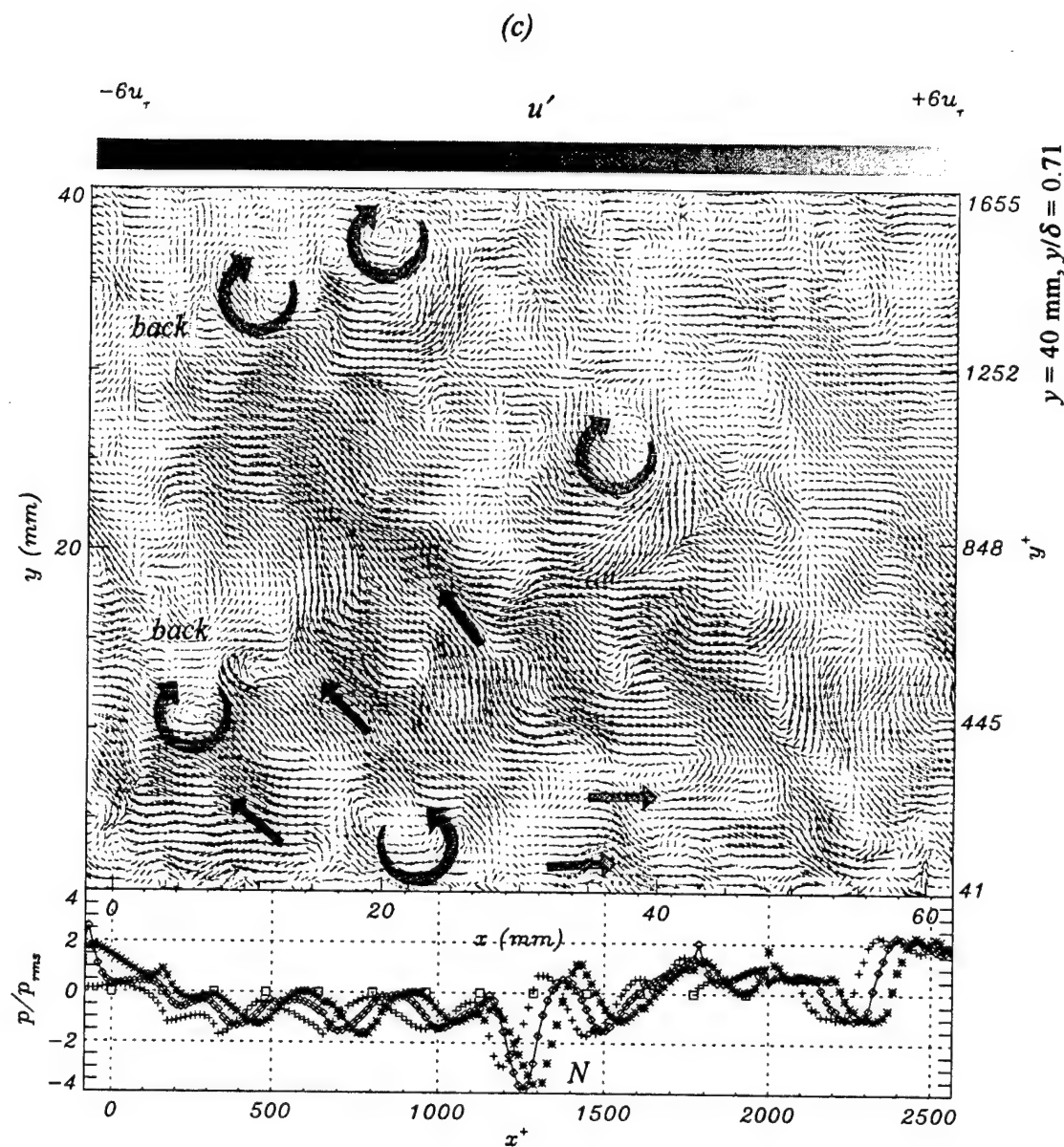


Figure 7.11 (continued, page three of three)

A region of ejections is typically found upstream of the roll-up structure, represented in Figure 7.11 by symbols  . Furthermore, each realization of Figure 7.11 shows that the eddy with rotation opposite to the mean vorticity is present downstream of a large shear layer interface labeled “back”. The eddies present along the interface ($y^+ > 300$) have predominately same rotation as the mean vorticity. The typical distance that separates the shear layer structure and the eddy with rotation opposite to the mean vorticity is on the order of 1000 wall units.

The conditional u' velocity field in the xy plane related to large amplitude negative pressure events was documented by Juckenhoefel (1995). Juckenhoefel resolved two distinct structures: a small region of momentum deficit very close to the wall near the detection point; and a large scale shear layer 400 wall units downstream of the detection point. Data from Juckenhoefel ($Re_\theta = 4035$) is plotted as a function of the streamwise coordinate x in Figure 7.12. The top of Figure 7.12 corresponds to the conditional average of the streamwise velocity at various y^+ locations associated with the detection of negative pressures ($\kappa = 2.5$). The x locations where the velocity was measured are indicated by dashed lines (data between dotted lines was interpolated; not all points are shown here to avoid crowding of symbols). The gradient $\partial u' / \partial x$ is greatest closer to the wall but is still significant for distances of y^+ around 200. The shear layer at $x^+ = 400$ consists of a gradual transition originating from the large positive streamwise velocity, $\langle u \rangle \approx 0.5 u_\tau$ near the detection point to $\langle u \rangle = 0$ at $x^+ > 400$. The bottom of Figure 7.12 shows the conditional velocity field associated with a positive amplitude pressure event ($\kappa = 2.5$). The shear layer for a positive pressure detection starts at $x^+ \approx 0$. Top and bottom plots show strong gradients of $\partial u' / \partial x$ at $x^+ \approx 0$ but of opposite signs. The fact that the magnitude of $\partial u' / \partial x$ is strongest at the detection point for both positive and negative detection schemes suggests that the more active motion associated with the negative detection lies close to the detection point rather than away from it.

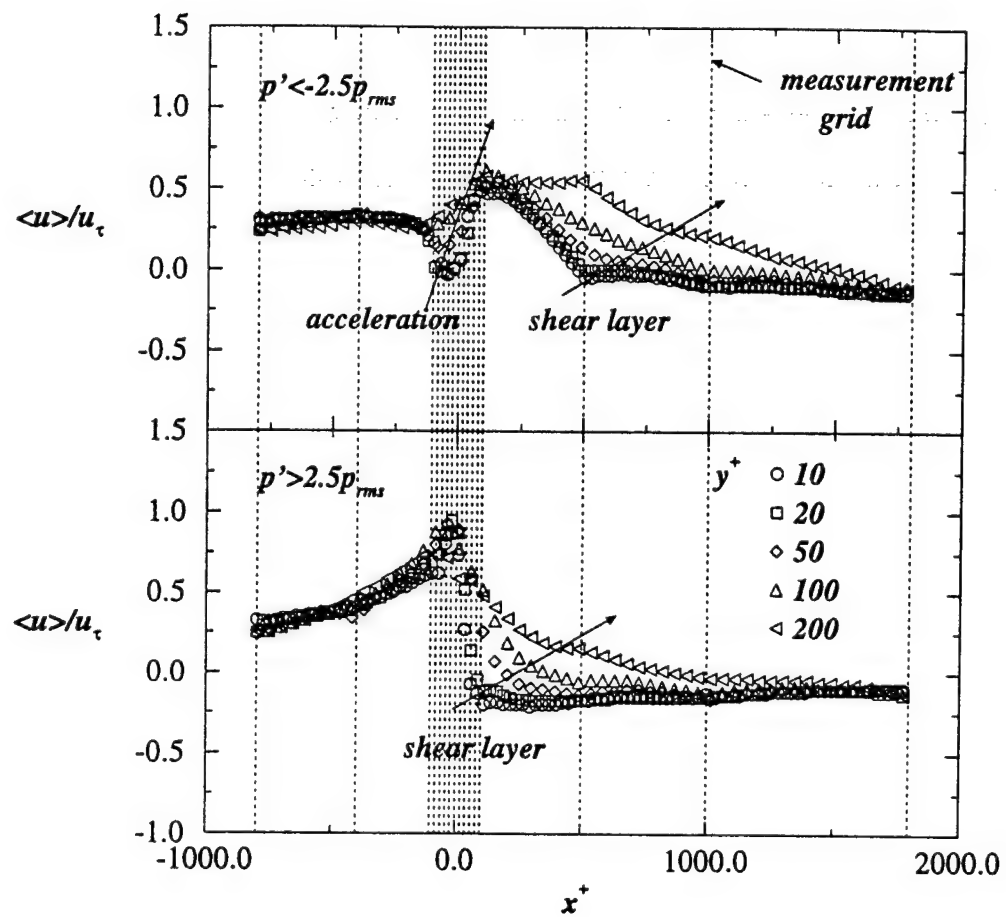


Figure 7.12 Conditional Average of Streamwise Velocity Associated with Negative (Top) and Positive (Bottom) Pressure Events for $Re_\theta = 4035$, $\kappa = 2.5$. Data of Juckenhöfel (1995)

The wall pressure associated with distinct motions of the velocity field may be summarized as follows. Consecutive negative and positive pressures (adverse pressure gradient) separated by $\Delta x^+ \approx 125$ in the streamwise direction are likely manifestations of a shear layer structure immediately above. Large amplitude negative pressures (distinct from the consecutive negative/positive pressures) are associated with an inverse shear layer as well as an eddy with sense of rotation opposite to the mean spanwise vorticity and flow ejections all of which are present downstream of a large scale shear layer structure. A negative $\partial u'/\partial x$ gradient is associated with an adverse pressure gradient at the wall (i.e. positive followed by negative pressure), whereas a positive $\partial u'/\partial x$ gradient is associated with a negative pressure structure.

CHAPTER VIII

CONCLUSIONS AND RECOMMENDATIONS

8.1. Conclusions

Instantaneous realizations by means of Particle Image Velocimetry of the flow in a turbulent boundary layer over a smooth plate show that an inclined shear layer is a common structure of the flow when a high wall pressure is observed. The shear layer separates regions of high momentum flow from fluid with momentum deficit. Typically the high momentum fluid is upstream of the low momentum fluid. The sizes of these shear layers vary, ranging from shear layers that are confined to the near wall region, $y^+ < 100$, to some that span several hundred y^+ . A characteristic signature of small or large scale shear layers is a positive, large magnitude, wall pressure beneath the convective stagnation line of the shear layer structure in the near wall region. The pressure-velocity relation confirms results published in the literature, though differences between the shear layers observed here and those reported from numerical simulations exist and are reported next.

Shear layers closer to the wall exhibit a typical inclination angle of 20° , which is consistent with inclination angles of shear layers obtained from numerical simulations. The simulations however differ from the current experimental findings in two ways. First, shear layers that exhibit a characteristic 20° slope from the computations are confined to $y^+ < 100$, whereas the experiments have shown that these may extend to $y^+ \approx 300$ while still preserving the 20° angle of inclination. Secondly, the numerical studies show near wall shear layers roll-up into a single transverse eddy located at the shear layer outer tip, whereas the experiments have shown consistently for Re_θ between 1500 and 6000 several distinct eddies present along the shear layer interface.

Larger scale shear layers obtained from the instantaneous PIV realizations exhibit larger inclination angles compared to the near wall shear layers, typically 35° to 45° with respect to the wall. The numerical simulations also show larger scale shear layers with similar inclination angles. The size of the shear layers obtained in the numerical computations however is limited by the computation domain (typically $y^+ < 250$). In the present study shear layers have been documented that extend to $y^+ \approx 1300$ or $y/\delta \approx 0.8$. A similar distinction is observed here between numerical simulations and the experiments as noted in the near wall shear layer structure. That is, several coherent eddies are typically encountered along the shear layer interface of the instantaneous PIV picture. Indeed, the experimental study shows that the turbulent flow at the higher Reynolds numbers is composed of a hierarchy of structures as compared to the lower Reynolds number simulations.

A significant contribution of the present work has been the spatial and temporal resolution of the wall pressure. When the pressure is resolved in the streamwise direction, instantaneous wall pressure profiles show that a negative pressure occurs both upstream and downstream of a large magnitude positive pressure. Conditional averaging calculations performed on detections of large positive and negative pressure events (threshold of $\kappa = 2.5$) corroborate the findings from the instantaneous profiles. In addition, histograms show that negative pressures upstream of large positive pressures are more common than those occurring downstream of large positive pressures. The streamwise separation between adjacent negative and positive pressure peaks was found to be $x^+ \approx 125$ for $1500 < Re_\theta < 6000$. Furthermore, the conditional calculations indicate that, on average, the negative pressure reaches its maximum magnitude a short time after a large positive pressure is detected, about $\Delta t^+ \approx 8$. The x location of the maximum negative pressure coincides with the x location of the positive pressure detection.

In the dynamics of a shear layer, the convective stagnation point is marked by a positive pressure peak at the wall. The action of the high momentum fluid upstream of

the low momentum fluid sets up a roll-up motion with a sense of rotation equal to the mean spanwise vorticity of the flow with fluid directed to and ejected from the wall. The signature of the roll-up motion is two consecutive, positive and negative, pressure peaks. The time delay between the maximum positive and negative pressures may suggest that the high momentum flow is responsible for the onset of a shear layer and the positive pressure, and secondly, the subsequent interaction between the high momentum fluid and the flow with momentum deficit near the wall induces a roll-up structure, which is responsible for flow ejected from the wall and the negative pressure.

The positive and negative pressure combination that signals the presence of a shear layer is in general well preserved. This signature persists and convects for distances on the order of δ . Long time sequences of the wall pressure also show that the adjacent positive and negative pressure structure is common, and that there are groups formed by this recurring pairing of positive and negative pressures. Typically the positive and negative pairs are separated in time by a $\Delta t^+ \approx 50-100$. Corresponding realizations of the instantaneous velocity field suggest that these correspond to shear layers at different stages in their life history.

A second negative pressure structure was identified by inspection of the instantaneous wall pressure. It appears that it is not associated with a positive pressure peak adjacent to the negative pressure. The negative pressure structure however is associated with a roll-up motion (with a sense of rotation opposite to that of the mean spanwise vorticity) located above the negative pressure and centered about $y^+ \approx 100$. Realizations for Re_θ between 1500 and 6000 have shown that the negative pressure and flow pattern consistently occur downstream of a shear layer interface. The distance between the shear layer structure and the negative pressure and roll-up motion vary typically between $\Delta x^+ = 400$ and 1500. The variation in distances away from the shear layer interface is attributed to the unique details of each particular shear layer. This is consistent with the conditional averaging calculations which do not reveal a negative pressure peak (except as

a very broad region of slightly negative pressure) when detecting on a positive pressure structure (associated with a shear layer interface).

The flow region above the counterclockwise roll-up motion is dominated by ejections whereas the flow downstream is characterized by an “inverse” shear layer. The inverse shear layer is a structure inclined towards the wall which is defined by a positive $\partial u' / \partial x$ gradient, different from the earlier shear layer structure which is characterized by a strong negative $\partial u' / \partial x$ gradient and large negative vorticity along the interface. The inverse shear layer consistently appears in the instantaneous PIV realizations associated with an eddy that exhibits a sense of rotation opposite to the mean spanwise vorticity and a negative wall pressure for the range of Reynolds numbers considered in the study. The inverse shear layer has not been mentioned in previous classifications of boundary layer turbulent structures nor identified in surveys from Direct Numerical Simulation databases.

The time history of the wall pressure is used to estimate the propagation speed of various wall pressure structures. The speed associated with a positive followed by a negative pressure structure ranges between 0.5 and $0.6U_\infty$, though the convection speed may vary along the course of its trajectory. The convection speed of the conditionally averaged positive followed by negative pressure structure was approximately $0.5U_\infty$. Another convective speed that predominates in the wall pressure sequence is $0.4U_\infty$. Structures with $0.4U_\infty$ convection velocity have been observed to be overtaken by a pressure structure convecting at $0.6U_\infty$. Structures convecting at $0.4U_\infty$ speeds have been encountered both with positive and negative magnitudes of pressure. How these are related to the dynamics of the flow field is yet to be understood.

In summary, the shear layer structure has been associated with distinctive smaller scale motions and wall pressure signatures. The small scale motions are eddies, typically with a sense of rotation equal to the mean spanwise vorticity. Calculation of vorticity shows that the interface contributes significantly to total vorticity, although the total vorticity is more pronounced in the vicinity of the eddies. Calculations of the Reynolds product $u'v'$

however shows that significant contribution to the Reynolds stress term occurs only in the vicinity of the eddies, typically upstream of them. The calculations therefore suggest that the shear layer structure is related to the production of turbulence through significant contribution to the Reynolds stress term.

8.2. Recommendations

The velocity fields measured in the present study resolve many of the large-scale features in the boundary layer. The near wall motions however are poorly resolved and this is mainly due to the low signal to noise ratio caused by the large near-wall velocity gradients. Using a magnification factor of greater than one when acquiring the PIV photographs in the near wall region may prove useful to further uncover the velocity-pressure interactions, and to deduce the role that the small scale structures have on the wall-pressure signature.

The current velocity realizations compared well with conditional averaging of the streamwise velocity which proved useful when first studying the instantaneous flow features. Similar analysis of long time series of the wall normal velocity component v' could be undertaken to resolve the vortex structure upstream of the shear layer interface. This structure is likely to be responsible for production of turbulence, owing to the ejection of flow away from the wall. Additionally, the v' component is immediately responsible for transfer of momentum across the boundary layer and interacts with the pressure through the pressure-strain product, $\overline{p' \partial v' / \partial y}$, from which it receives its energy. Measurements of v' could be performed with an LDV system given the difficulties using an X-wire probe owing to spatial resolution requirements.

Further conditional average calculations could be performed from the pressure-velocity data of Juckenhoefel (1995). Averages were calculated based on detections of large positive and negative pressure thresholds. The new calculations would aim at isolating two separate large negative pressures events. The one would be associated with a quick

sequence of positive and negative pressures, which has been shown to be the signature of a shear layer above. The second negative pressure event would not be associated with any positive pressure in the immediate vicinity. This second pressure event was shown in this presentation to be a result of high momentum flow that is initiated downstream of a coherent, well preserved, shear layer interface. The conditional velocity field may thus be represented for these separate negative amplitude pressure events.

The first velocity field would intuitively resemble that obtained with a positive detection. Additionally however, other than the shear layer interface, the present calculations may shed further insight into the region where flow ejections were observed in the instantaneous realizations. The second, detecting solely on a negative pressure, would be compared with flow configuration observed in the instantaneous PIV realizations and wall pressure measurements documented in this work.

BIBLIOGRAPHY

Adrian, R. J., 1991. Particle-Imaging Techniques for Experimental Fluid Mechanics. Ann. Rev. Mech., Vol. 23, pp. 261-304.

Adrian, R. J., Meinhart, C. D., Liu, Z., Hanratty, T. J., 1995. New Observations of Structures in Turbulent Wall Flows, ONR Turbulence Contractors Meeting, 23-25 October 1995, Dulles.

Blackwelder, R. F. and Kovasznay, L. S. G., 1972. Time Scales and Correlations in a Turbulent Boundary Layer. Phys. Fluids, Vol. 15, pp. 1545-1554.

Bradshaw, P., Ferriss, D. H. and Atwell, N.P., 1967. Calculation of Boundary Layer Development Using the Turbulent Energy Equation, in S.J. Kline, M. V. Morkovin, G.S. Sovran and D.J. Cockrell, Computation of Turbulent Boundary Layers—1968 AFOSR-IFP-Standford Conference, Standford University Press, Standford, CA (Original Paper Published in J. Fluid Mech., Vol. 28, pp. 539-616 (1967).)

Boussinesq, J., 1877. Théorie de L'écoulement Tourbillant. Mém. Prés. Acad. Sci., Vol. 23, p. 46.

Clauer, F. H., 1956. The Turbulent Boundary Layer. Advances in Applied Mechanics, Vol. IV, Academic Press, New York.

Continuum. Operation and Maintenance Manual Surelite II, 1992. Santa Clara, CA.

Corino, E. R. and Brodkey, R. S., 1969. A Visual Investigation of the Wall Region in Turbulent Flow. J. Fluid Mech., Vol. 37, pp. 1-30.

Corrsin, S., 1943. Investigation of flow in an Axially Symmetric Heated Jet of Air. NACA Adv. Conf. Rep. 3123.

Dinkelaker, A., Hessel, M., Meier, G. E. A. and Schewe, G., 1977. Investigation of the Pressure Fluctuations Beneath a Turbulent Boundary Layer by Means of an Optical Method. Phys. Fluids Suppl., S216.

Eckelmann, H., 1990. A Review of Knowledge on Pressure Fluctuations. Near Wall Turbulence, ed. by Kline and Afgan, pp 328-347.

Falco, R. E., 1977. Coherent Motions in the Outer Region of Turbulent Boundary Layers. Phys. Fluids, Vol. 20, pp. 124-132.

Favre, A. L., Gaviglio, J.J. and Dumas, R., 1957. Space-Time Double Correlation and Spectra in a Turbulent Boundary Layer. J. Fluid Mech., Vol. 2, pp. 313-341.

Head, M. R. and Bandyopadhyay, P., 1981. New Aspects of Turbulent Boundary Layer Structure. J. Fluid Mech., Vol. 107, pp. 297-338.

Hinze, J. O., 1959. Turbulence. New York, McGraw-Hill.

Hinze, J. O., 1975. Turbulence. New York, McGraw-Hill.

Johansson, A. V., Her, J. Y. and Haritonidis, J. H., 1987. On the Generation of High-Amplitude Wall-Pressure Peaks in Turbulent Boundary Layers and Spots. *J. Fluid Mech.*, Vol. 175, pp. 119–142.

Johansson, A. V. and Kim, J., 1988. Velocity and Pressure Fields Associated with Near-Wall Turbulence Structures. *Near Wall Turbulence*, ed. by Kline and Afgan, pp 368–380.

Juckenhoefer, O. J. H., 1995. Stochastic Estimation of the Velocity Field Associated with High-Amplitude Wall-Pressure Events Beneath a Turbulent Boundary Layer, Fluid Dynamics Research Center Report. Illinois Institute of Technology, Chicago, IL.

Keane, R. D., and Adrian, R. J., 1990. Optimization of Particle Image Velocimeters. Part I: Double Pulsed Systems. *Meas. Sci. Technol.*, Vol. 1, pp. 1202–1215.

Kim, H. T., Kline, S. J., Reynolds, W. C., 1971. The Production of the Wall Region in Turbulent Flow. *J. Fluid Mech.*, Vol. 50, pp. 133–160.

Klebanoff, P. S., 1954. Characteristics of Turbulence in a Boundary Layer with Zero Pressure Gradient. NACA Rep. 1247.

Kline, S. J., Reynolds, W. C., Schraub, F. A., and Runstadler, P. W., 1967. The Structure of Turbulent Boundary Layers. *J. Fluid Mech.*, Vol. 30, pp. 741–773.

Kline, S. J., and Robinson, S. K., 1990. Quasi-Coherent Structures in a Turbulent Boundary Layer: Part I. Status Report on a Community-Wide Summary of the Data. Summary Lecture. *Near Wall Turbulence*, ed. by Kline and Afgan, pp 200–217.

Knowles Electronics, Inc., 1992. Data Performance Documentation. Itasca, IL 60143.

Kolmogoroff, A. N., 1941. The Local Structure of Turbulence in Incompressible Flow for Very Large Reynolds Number. *C. R. Acad. U.R.S.S.* Vol. 30, p. 301.

Landau, B. E., and Spalding, D. B., 1974. The Numerical Computation of Turbulent Flows. Computer Methods and Applications in Mechanical Engineering, Vol. 3.

Laufer, J., 1954. The Structure of Turbulence in Fully Developed Pipe Flow. NACA TR 1174.

Mansour, N. N., Kim, J. and Moin, P. 1988. Reynolds Stress and Dissipation-Rate Budgets in a Turbulent Channel Flow. *J. Fluid Mech.*, Vol. 194, pp. 15–44.

Meinhart, C. D., 1994. A PIV Investigation of Turbulent Boundary Layer Structure. Ph.D. Thesis, University of Illinois at Urbana-Champaign, IL.

Meinhart, C. D., and Adrian, R. J., 1995. On the Existance of Uniform Momentum Zones in a Turbulent Boundary Layer. *Phys. Fluids*, Vol. 7, pp. 694–696.

Panton, R. L., Goldman, A. L., Lowery, R. L., and Reischman, M. M., 1980. Low Frequency Pressure Fluctuations in Axis-Symmetric Turbulent Boundary Layers. *J. Fluid Mech.*, Vol. 97, pp. 299–319.

Perry, A. E., and Chong, M. S., 1982. On the Mechanisms of Wall Turbulence, J. Fluid Mech., Vol. 119, pp. 173–217.

Perry, A. E., Henbest, S., and Chong, 1986. A Theoretical and Experimental Study of Wall Turbulence. J. Fluid Mech., Vol. 165, pp. 163–199.

Prandtl, L., 1925. Bericht Über Untersuchungen Zur Ausgebildeten Turbulenz. Z. Angew. Math. Mech., Vol. 5, pp. 136–139.

Prandtl, L., 1945. Über Eine Neues Formelsystem für die Ausgebildete Turbulenz. Nachr. Akad. Wiss., Göttingen, Math. Phys. Klasse., pp. 6–9.

Prasad, A. K. and Adrian, R. J., 1993. Stereoscopic Particle Image Velocimetry Applied to Liquid Flows. Experiments in Fluids, Vol. 15, pp. 49–60.

Praturi, A. K., and Brodkey, R. S., 1978. A Sterioscopic Visual Study of Coherent Structures in a Turbulent Shear Flow. J. Fluid Mech., Vol. 89, pp. 215–272.

Robinson, S. K., Kline S. J., Spalart, P. R., 1988. Quasi-Coherent Structures in a Turbulent Boundary Layer: Part II. Verification and New Information from a Numerically Simulated Flat-Plate Layer. Near Wall Turbulence, ed. by Kline and Afgan, pp 218–247.

Robinson, S. K., 1990. The Kinematics of Turbulent Boundary Layer Structure. NASA Tech. Memorandum 103859.

Robinson, S. K., 1991. Coherent Motions in the Turbulent Boundary Layer. Ann. Rev. Mech., Vol. 23, pp. 601–639.

Rodi, W., 1980. Turbulence Models and Their Application in Hydraulics, Int. Assoc. Hydraulics Res., Delft, Netherlands.

Rogallo, R. S. and Moin, P., 1984. Numerical Simulation of Turbulent Flows. Ann. Rev. Mech., Vol. 16, pp. 99–138.

Schew, G. 1983. On the Structure and Resolution of Wall-Pressure Fluctuations Associated with Turbulent Boundary Layer Flow. J. Fluid Mech., Vol. 134, 311–328.

Snarski, S. and Lueptow, R. M., 1995. Wall Pressure and Coherent Structures in a Turbulent Boundary Layer on a Cylinder in an Axial Flow. J. Fluid Mech., Vol. 286, pp. 137–171.

Spalding D. B., 1961, A Single Formula for the Law of the Wall. J. Fluid Mech., Vol. 28, pp. 455–457.

Spalart P. R., 1988. Direct Simulation of a Turbulent Boundary Layer up to $Re_\theta=1410$. J. Fluid Mech., Vol. 187, pp. 61–98.

Tennekes, H. and Lumley, J. L., 1972. A First Course in Turbulence. The MIT Press.

Thomas, A. S. W. and Bull, M. K., 1983. On the Role of Wall-Pressure Fluctuations in Deterministic Motions in the Turbulent Boundary Layer. *J. Fluid Mech.*, Vol. 128, pp. 283–322.

Taylor, G. I., 1935. The Statistical Theory of Turbulence, Parts I–IV, *Proc. R. Soc. London Ser. A*, Vol. 151, pp. 421–511.

Townsend, A. A., 1947. Measurements in the Turbulent Wake of a Cylinder. *Proc. R. Soc. London Ser. A*, Vol. 190, pp. 551–561.

Townsend, A. A., 1956. The Structure of Turbulent Shear Flow. Cambridge Univ. Press. 1st ed.

Townsend, A. A., 1970. Entrainment and the Structure of Turbulent Shear Flow. *J. Fluid Mech.*, Vol. 41, pp. 13–46.

Townsend, A. A., 1976. The Structure of Turbulent Shear Flow. Cambridge Univ. Press. 2nd ed.

Ullrich, S. A., Development of Particle Image Velocimetry Interrogation System. MSc. Thesis, Illinois Institute of Technology, Chicago, IL.

Van Dyke, M., 1982. An Album of Fluid Motion. Standford, California.

Wallace, J. M., Broadkey, R. S. and Eckelmann, H., 1977. Pattern-Recognized Structures in Bounded Turbulent Shear Flows, *J. Fluid Mech.*, Vol. 83, pp. 673–694.

Westerwheel, J., 1993. Digital Particle Image Velocimetry: Theory and Application. Delft University Press.

Williams, D. R., 1985. Vortex Structures in the Breakdown Stage of Transition. Proceedings of ICASE/NASA Workshop on Stability of Time Dependent and Spatially Varying Flows. Springer.

Willmarth, W. W., 1975. Pressure Fluctuations beneath Turbulent Boundary Layers. *Ann. Rev. Mech.*, Vol. 7, pp. 13–37.

Willmarth, W. W. and Lu, S. S., 1972. Structure of the Reynolds Stress Near the Wall. *J. Fluid Mech.*, Vol. 55, pp. 65–69.

Willmarth, W. W. and Wooldridge, C. E., 1962. Measurements of the Fluctuating Pressure at the Wall beneath a Thick Turbulent Boundary Layer. *J. Fluid Mech.*, Vol. 14, pp. 187–210.

Willmarth, W. W. and Wooldridge, C. E., 1963. Measurements of the Correlation between the Fluctuating Velocities and the Fluctuating Wall Pressure in a Thick Turbulent Boundary Layer. AGARD Rep. 456.